

Measuring the Higgs Self-coupling at the International Linear Collider

Dissertation

zur

Erlangung des Doktorgrades (Dr. rer. nat.)

an der

Fakultät für Mathematik, Informatik und Naturwissenschaften

Fachbereich Physik

der

Universität Hamburg

vorgelegt von

Claude Fabienne Dürig

Hamburg 2016

Tag der Disputation: 13.10.2016

Folgende Gutachter empfehlen die Annahme der Dissertation:

1. Gutachterin: Dr. Jenny List
2. Gutachterin: Prof. Dr. Erika Garutti

To my Mother.

Abstract

In this thesis, the experimental prospects of measuring the Standard Model (SM) Higgs self-coupling λ_{SM} at the International Linear Collider (ILC) are investigated. The observation of double Higgs production is necessary to directly establish a non-zero Higgs self-coupling. Information on λ_{SM} can be extracted from a measurement of the cross section for this process. At a centre-of-mass energy of $\sqrt{s} = 500$ GeV double Higgs-strahlung is the dominant Higgs-pair production process. This measurement is extremely challenging due to very small production cross sections and multi-jet final states which pose large challenges to detector technologies and event reconstruction techniques.

A detailed full detector simulation of the International Large Detector is performed for a Higgs boson with a mass of 125 GeV. The analysis is based on ILC beam parameters according to the Technical Design Report and investigates several improvements compared to earlier studies. These include an isolated lepton selection strategy and the application of kinematic fits to final states with heavy-flavoured jets. Depending on the decay mode of the Z boson, relative improvements of up to 25% are obtained in the selection of ZHH ($HH \rightarrow bbbb$) events. This results in a relative improvement of 10% in the measurement of σ_{ZHH} when combining all channels. For the SM scenario, an evidence of 3.5σ for the observation of double Higgs-strahlung and a measurement precision of 30% on σ_{ZHH} is reached with an integrated luminosity of $\mathcal{L} = 2 \text{ ab}^{-1}$ and a beam polarisation of $P(e^+e^-) = (0.3, -0.8)$. The result extrapolates to an achievable precision of 21% on σ_{ZHH} after the full ILC running scenario, which corresponds to a 5.9σ discovery for the observation of double Higgs-strahlung. Combined with the channel $HH \rightarrow bbWW$, σ_{ZHH} can even be measured to a precision of 16%, which corresponds to a precision of 26% on λ_{SM} . Additionally, the impact of $\gamma\gamma \rightarrow \text{low-}p_T$ hadrons background is investigated, which proves the need of advanced removal strategies, which include a detailed modelling of the background and exploit the full power of high-granularity detectors.

Zusammenfassung

In der vorliegenden Arbeit werden die experimentellen Möglichkeiten untersucht die Higgselbstkopplung des Standardmodells λ_{SM} am International Linear Collider (ILC) zu beobachten. Um die Existenz der Higgselbstkopplung direkt nachweisen zu können, muss die Produktion von Higgspaaren beobachtet werden. Durch die Messung des Wirkungsquerschnitts solcher Prozesse können Rückschlüsse auf λ_{SM} gezogen werden. Bei einer Schwerpunktsenergie von $\sqrt{s} = 500$ GeV ist doppelte Higgsstrahlung der dominante Produktionsprozess. Die Messung stellt jedoch große Anforderungen an Detekorttechnologien und Methoden zur Ereignisrekonstruktion aufgrund der sehr kleinen Produktionswirkungsquerschnitte und Endzuständen mit vielen Jets.

Zu diesem Zweck wird eine detaillierte Detektorsimulation des International Large Detectors für ein Higgsboson mit einer Masse von 125 GeV durchgeführt. Die Studie basiert auf ILC Strahlparametern gemäß des Technical Design Reports. In der Studie werden verschiedene Ansatzpunkte für mögliche Verbesserungen untersucht. Diese beinhalten eine Strategie für die Identifizierung isolierter Leptonen und die Anwendung kinematischer Anpassungen in Endzuständen mit schweren Quarks. Die Untersuchungen dieser Arbeit erreichen relative Verbesserungen von bis zu 25% in der Ereignis Selektion von ZHH ($HH \rightarrow bbbb$) und von 10% in der Messung des Wirkungsquerschnitts. Unter der Annahme einer standardmodellartigen Kopplung kann die Existenz von doppelter Higgsstrahlung mit 3.5σ Genauigkeit bewiesen sowie σ_{ZHH} zu 30% Genauigkeit bestimmt werden. Die Ergebnisse beruhen auf einer integrierten Luminosität von $\mathcal{L} = 2 \text{ ab}^{-1}$ und einer Strahlpolarisation von $P(e^+e^-) = (0.3, -0.8)$. Daraus ergibt sich eine Genauigkeit von 21% in der Messung von σ_{ZHH} nach der vollen Laufzeit des ILC. Dies entspricht einer Entdeckung von doppelter Higgsstrahlung mit einer Signifikanz von 5.9 Standardabweichungen. In Kombination mit $HH \rightarrow bbWW$ kann σ_{ZHH} zu 16% und λ_{SM} zu 26% Genauigkeit bestimmt werden. Zusätzlich wird der Einfluss des Untergrundes aus Photoproduktion von niederenergetischen Hadronen auf die Analyse untersucht. Die Untersuchung zeigt, dass anspruchsvolle Methoden zur Unterdrückung des Untergrundes benötigt werden, die ein detailliertes Modell der Ereignisse beinhalten und die hohe Detailgenauigkeit der Detektoren ausnutzen.

Contents

1	Introduction	1
2	Higgs Self-coupling in the Standard Model of Particle Physics	5
2.1	Standard Model of Particle Physics	5
2.2	Electroweak Symmetry Breaking	8
2.3	The Standard Model Higgs Boson	13
2.3.1	Higgs Production in Hadron and e^+e^- Collisions	13
2.3.2	Higgs Couplings and Decays	17
2.3.3	Higgs Boson Search	19
2.4	Shortcomings of the Standard Model	22
2.5	The Measurement of the Higgs Self-coupling	25
2.5.1	Special Role of the Top Quark in the SM	26
2.5.2	Indications of Physics Beyond the Standard Model	28
2.5.3	Sensitivity of the Higgs Self-coupling	32
2.5.4	Measurement Prospects of the HL-LHC	35
2.5.5	Linear Collider Studies	37
3	The International Linear Collider and Experimental Environment	41
3.1	Reasons for an e^+e^- Linear Collider	41
3.1.1	Experimental Features of Lepton Colliders	41
3.1.2	Advantages of Linear Colliders	42
3.2	The International Linear Collider Project	43
3.3	ILC Operating Scenario	43
3.4	Experimental Environment	46
3.4.1	Beam Parameters	46
3.4.2	Backgrounds	48
3.5	Overview of the Accelerator	49
4	The International Large Detector Concept	53
4.1	Detector Design Challenges	53
4.1.1	Jet-Energy Resolution	54
4.1.2	Track Momentum Resolution	56
4.1.3	Impact Parameter Resolution	56
4.1.4	Precise Knowledge of Machine Backgrounds	57

4.2	Particle Flow Concept	57
4.3	The International Large Detector	59
4.3.1	Vertex Detector and Flavour Tagging Performance	60
4.3.2	Tracking System and Performance	61
4.3.3	Calorimeter System	63
4.3.4	Particle Flow Performance	64
4.4	Event Generation	66
4.5	Software Framework	66
4.5.1	Detector Simulation	67
4.5.2	Beam-Background Overlay	67
4.5.3	Standard Event Reconstruction	68
5	Event Reconstruction and Analysis Strategy	69
5.1	Signal and Background Processes	69
5.1.1	Signal Process	70
5.1.2	Background Processes	72
5.2	Analysis Strategy	74
5.2.1	Preselection	74
5.2.2	Challenges in Higgs Mass Reconstruction	77
5.2.3	Final Selection	78
5.3	Standard Analysis Tools	80
5.3.1	Jet Clustering	81
5.3.2	Standard Overlay Removal	82
5.3.3	Vertex Finding and Flavour Tagging	83
6	Reconstruction Improvements	85
6.1	Isolated Lepton Tagging	85
6.2	Optimised Overlay Removal	90
6.3	Kinematic Fitting	92
6.3.1	Motivation	92
6.3.2	General Concept and Working Principle	94
6.3.3	Fit Performance Measures	98
6.3.4	Building of Fit Hypotheses	100
6.4	Fit Performance of Default Setup	103
6.5	Application of Fits to the Analysis Concepts	104
6.5.1	Hypothesis Testing	104
6.5.2	Mass Reconstruction	105
7	Considering ISR and Semi-leptonic Decays in Kinematic Fits	107
7.1	Considering ISR in the Fit	108
7.2	Fit Performance with ISR	109
7.3	Strategy for an Event-specific ISR Treatment	112
7.3.1	Event Identification using ISR Properties	112

7.3.2	Optimised Event Categorisation	114
7.3.3	Results of the Mass Reconstruction	116
7.4	Impact of Semi-leptonic Decays	118
7.4.1	Effect on ISR Consideration and Mass Reconstruction	118
7.4.2	Effect on Energy Error Parametrisation	119
7.5	Strategy of Jet Energy Correction	120
7.6	Lepton Identification	122
7.7	Improvements due to the Energy Correction	126
7.7.1	Jet Energy Uncertainties	126
7.7.2	Fit Performance	127
7.7.3	Automatic ISR Recognition	129
7.7.4	Mass Reconstruction	130
7.8	Hypothesis testing in both Strategies	133
8	Event Selection	135
8.1	Lepton Channel	135
8.1.1	Preselection	135
8.1.2	MVA Training and Final Selection	139
8.1.3	Flavour Tag Information	149
8.2	Neutrino Channel	150
8.2.1	Preselection	150
8.2.2	MVA Training and Final Selection	152
8.2.3	Flavour Tag Information	157
8.3	Hadron Channel	158
8.3.1	Mass Reconstruction and Jet Pairing	160
8.3.2	Additional Preselection Cuts	161
8.3.3	MVA Training and Final Selection	161
8.3.4	Flavour Tag Information	169
8.4	Event Selection Summary	172
8.4.1	Signal Significance	174
8.4.2	Event Selection Improvements	175
9	Analysis and Results	179
9.1	Prospects for Discovery and Measurement of Higgs-Pair Production	179
9.1.1	Combined Excess Significance	179
9.1.2	Cross-section Measurement	181
9.1.3	Effects of Analysis Improvements	182
9.1.4	Effect of different Beam Polarisations	183
9.1.5	Prospects for the Full ILC Running Scenario at 500 GeV	185
9.1.6	Effect of Overlay	185
9.2	Determination of the Higgs Self-coupling	186
9.2.1	Extracting λ_{SM} at 500 GeV	186
9.2.2	Prospects for λ_{SM} after Energy Upgrade	187

9.2.3	Measurement Prospects for $\lambda \neq \lambda_{SM}$ at the ILC	187
9.3	Outlook on further Ideas for Improvement	189
10	Conclusion	195
A	Appendix	199
A.1	Neutrino Channel	199
A.1.1	Input variables of first BDTG	199
A.1.2	Input variables of second BDTG	200
A.1.3	Input variables of third BDTG	202
A.2	Hadron Channel	204
A.2.1	Input variables of first BDTG	204
A.2.2	Input variables of second BDTG	206
A.2.3	Input variables of third BDTG	208
A.2.4	Final selection variables	208
A.3	Results for Analysis with Overlay	211
	Bibliography	217

Chapter 1

Introduction

The Standard Model (SM) of particle physics currently is the most complete description of the subatomic world, since this theory is consistent with the majority of all observed phenomena. One of the key building blocks in the SM is the Higgs sector, which is believed to be the origin of fermion and gauge boson masses by the mechanism of spontaneous electroweak symmetry breaking [1–3]. In the so-called Higgs mechanism, the neutral component of an isodoublet scalar field acquires a non-zero vacuum expectation value which gives rise to the non-zero masses of fermions and gauge bosons while preserving the $SU(2) \times U(1)$ gauge symmetry. In the SM, the couplings of the Higgs boson to the fermions and gauge bosons are predicted as a function of the respective fermion or gauge boson mass and the Higgs mass, which represents the only free parameter of the SM Higgs sector.

Now that a Higgs boson candidate was discovered at the Large Hadron Collider (LHC) in 2012 [4, 5], it is crucial to investigate its properties and compatibility with the SM. This requires a precise and model-independent reconstruction of the electroweak symmetry breaking sector and the verification of theoretical predictions, any deviation of which could indicate new physics beyond the SM. While precise measurements of the mass-coupling relation represent a test of the SM electroweak symmetry breaking sector, precision measurements of the Higgs mass and couplings are not enough to establish the Higgs mechanism experimentally. In particular the measurement of the Higgs self-coupling allows to reconstruct the potential of the Higgs field. The model-independent measurement of double Higgs production is necessary to establish a non-zero Higgs self-coupling.

Higgs-pair production plays the key role as the production process which is sensitive to the Higgs self-coupling. Moreover, by discovering deviations from its SM prediction it provides indirect possibilities for probing new physics scenarios and the existence of heavy new particles. A measurement precision in the order of 20% could allow to observe deviations from the SM and to directly reveal the nature of extended Higgs sectors [6]. For example, in the parameter region of the Two Higgs Doublet Model (2HDM) in which the theory of Electroweak Baryogenesis is possible, a minimal deviation of 20% from

the SM value is expected [7]. A precise measurement of the double Higgs production cross section, and thus the Higgs self-coupling, can be an important probe of such a cosmological scenario. The SM cross sections for double Higgs production are very small and unless new physics produces sizeable enhancements, the measurement is quite challenging. Combined with multi-jet final states the measurement places many challenges on detector technologies and on event reconstruction techniques. Hence, it is crucial to investigate the possibilities of measuring the Higgs self-coupling at particle colliders.

Direct and model-independent precision measurements can be performed at e^+e^- colliders with sufficient energy. The International Linear Collider (ILC) is one of the largest next generation collider projects, operating at energies up to 500 GeV with possible options for an energy upgrade to 1 TeV. It is planned as a complement to the LHC to perform precision measurements of known and possibly new particles. The ILC detector performance goals are driven by optimisation studies in full detector simulations which are based on the precise knowledge of particle properties and their behaviour in the detector, and on the current knowledge of technologies. The ILC detector concepts target the best possible particle detection and reconstruction of events with multi-jet final states.

At a centre-of-mass energy of $\sqrt{s} = 500$ GeV, the dominant double Higgs production process at an e^+e^- collider is double Higgs-strahlung ZHH . The signal events have to be reconstructed as precisely as possible. The invariant mass reconstruction drives the overall physics performance at the ILC and relies on an excellent jet-energy resolution. Moreover, at a Higgs mass of 125 GeV the Higgs boson predominantly decays into a pair of b quarks. Therefore, ZHH can result in up to six-jet final states which result in complex signatures in the detector. At 500 GeV these events are produced near the kinematic threshold and thus, the jets have significant overlap with each other. High flavour-tagging efficiencies are required, while being robust against mis-clustering of particles into jets. Leptonic decays of the Z boson need high track momentum resolutions which can help in the event reconstruction. Therefore, the Higgs self-coupling measurement is directly linked to the performance requirements of ILC detectors and event reconstruction techniques. The experimental prospects of observing the SM Higgs self-coupling at the ILC need to be investigated in order to study further improvements in detector optimisation and event reconstruction. Therefore, we perform the Higgs self-coupling measurement for a Higgs boson with a mass of $m_H = 125$ GeV and investigate starting points for improvement as indicated by former linear collider studies.

This thesis is organised as follows:

In chapter 2, the theoretical foundations are introduced, mainly focussing on double Higgs production and the Higgs self-coupling. The measurement capabilities at hadron and e^+e^- colliders are discussed, which serves as motivation for this thesis. In chapter 3, an overview of the ILC is given. Herein, the experimental environment and the machine backgrounds are introduced. The wide range of high precision measurements in the ILC physics programme sets new standards on detector technologies and their physics perfor-

mance. In chapter 4, the ILC detector design goals and challenges are discussed. An overview on the performance of the International Large Detector (ILD) concept is given.

The subsequent part of the thesis is dedicated to the Higgs self-coupling analysis at the ILC. In chapter 5, the signal and background processes used in the analysis are discussed and an overview on the analysis strategy is given. ILD physics studies are based on the interplay of detector performance and analysis techniques. In chapter 6, analysis techniques are discussed, which have been investigated and optimised in this thesis. There are several starting points for improvement which can have large effects on the precision of the Higgs self-coupling measurement. This concerns the isolated lepton selection, which requires large efficiencies and purities, the $\gamma\gamma \rightarrow \text{low-}p_T$ hadrons background removal, and most importantly the application of kinematic fits. In chapter 7, the application of kinematic fits to final states with heavy-flavoured jets is evaluated. The kinematic fit performance is studied in the presence of large missing four-momentum. This includes the investigation of the ISR treatment in the presence of missing four-momentum from semi-leptonic decays. Two strategies are explained which solve issues with the automatic ISR treatment in final states with b and c quarks. In chapter 8, the improvements are included to the event selection and the latter is optimised and described in detail. In chapter 9, the results of the cross-section measurement of double Higgs-strahlung and the determination of the Higgs self-coupling for the full ILC running scenario is discussed. This is outlined in terms of the SM and Beyond the SM theories. An outlook is given on further improvements to enhance the measurement precisions. Finally, the work of this thesis is concluded and summarised in chapter 10.

Chapter 2

Higgs Self-coupling in the Standard Model of Particle Physics

In this chapter, the theoretical foundations of this thesis are discussed with regard to the Standard Model of particle physics (SM) and the SM Higgs boson, focussing on the Higgs self-coupling measurement. In sec. 2.1, an overview of the SM is given, which is followed by a description of electroweak symmetry breaking and the Higgs mechanism in sec. 2.2. The SM Higgs boson and its properties are introduced in sec. 2.3 and a historical overview of the Higgs search is presented. In sec. 2.4 the shortcomings of the SM are discussed. In sec. 2.5, the measurement of the Higgs self-coupling is introduced. An overview on possible indications to new physics is given, which can be detected as deviations from SM Higgs self-coupling predictions. Finally, the measurement capabilities at hadron and e^+e^- colliders are discussed. This serves as motivation of this thesis.

2.1 Standard Model of Particle Physics

In the 1960s and 1970s the Standard Model (SM) of particle physics emerged which described all of the known elementary particle interactions, except gravity. The SM includes quantum chromodynamics (QCD) and the Glashow–Salam–Weinberg theory of electroweak interactions [8–12], which contains quantum electrodynamics (QED). It is based on two types of elementary matter particles, fermions and bosons. Elementary particles appear to be structureless and point-like. Fermions are matter particles of half-integer spin, which satisfy Fermi-Dirac statistics [13, 14]. To each fermion there is an antiparticle with the same properties, but additive quantum numbers of opposite sign. Bosons are responsible for the interaction between matter particles. They follow Bose-Einstein statistics [15, 16] and have integer spin.

Mathematically, the SM is built upon the requirement of local gauge invariance under the gauge group $SU(3)_C \times SU(2)_L \times U(1)_Y$, accounting for the strong, weak and electromagnetic interaction. The indices represent the charges of the groups, respectively.

The strong interaction is described by the $SU(3)_C$ symmetry group, where C indicates the colour charge of QCD. Only particles which carry colour charge participate in the strong interaction. Three different colour states exist, often denoted as red, green, and blue. Gluons are the respective gauge bosons, each of which carries a combination of colour and anti-colour. In terms of $SU(3)_C$ colour symmetry, there are nine possibilities to combine colour and anti-colour triplets to gluons forming a colour octet and a colour singlet ($3 \otimes \bar{3} = 8 \oplus 1$). Since only colour singlet states exist as free particles, a colour singlet massless gluon would give rise to a strong force of infinite range. Since the strong force is of short range, physical gluons are confined. Consequently, there exist eight physical gluons represented by the colour octet.

Electromagnetic and weak interactions are described by the symmetry group of $SU(2)_L \times U(1)_Y$. $SU(2)_L$ describes transformations of left-handed (denoted as L) multiplets of the weak isospin T , and $U(1)_Y$ phase transformations of the weak hypercharge Y . After spontaneous symmetry breaking of $SU(2)_L \times U(1)_Y$ via the Higgs mechanism (section 2.2), it turns out that there is one unbroken symmetry left over, which is a combination of $SU(2)_L \times U(1)_Y$. It is a symmetry with generator

$$Q = T_3 + \frac{1}{2} Y \equiv Q_{em}, \quad (2.1)$$

where \vec{T} and Y are the generators of $SU(2)_L$ and $U(1)_Y$, respectively. Adding a weak hypercharge means that the doublet component with $T_3 = +\frac{1}{2}$ obtains a positive charge, while the other $T_3 = -\frac{1}{2}$ component is neutral. Q generates exactly the symmetry group of electromagnetism $U(1)_{em}$, and the massless gauge boson of the unbroken symmetry is the photon, which acts between electrically charged particles. The electromagnetic interaction is described by QED. Together with the weak interaction, both are unified by the Glashow–Salam–Weinberg theory since they behave similar at high energy scales.

After symmetry breakdown of $SU(2)_L \times U(1)_Y$, the new gauge bosons of the symmetry groups are defined as follows: Denoting the gauge bosons of the $SU(2)_L$ symmetry by W_μ^a ($a = 1, 2, 3$) and the one of $U(1)_Y$ by B_μ , the physical W^\pm bosons are defined as

$$W_\mu^\pm = \sqrt{\frac{1}{2}} (W_\mu^1 \mp iW_\mu^2). \quad (2.2)$$

The physical photon and the Z boson are given by a linear combination of the form

$$A_\mu = B_\mu \cos \theta_W + W_\mu^3 \sin \theta_W, \quad (2.3a)$$

$$Z_\mu = -B_\mu \sin \theta_W + W_\mu^3 \cos \theta_W, \quad (2.3b)$$

where θ_W denotes the Weinberg angle, the mixing angle of electroweak interactions. Latter is defined by the ratio of coupling constants of $SU(2)_L$ and $U(1)_Y$, denoted by g and g' :

$$\tan \theta_W = \frac{g'}{g}. \quad (2.4)$$

In the SM, fermions fall into two main groups: quarks and leptons. Leptons can be further classified by their participation in the different types of interactions. Charged leptons

fermion	generation			electric charge Q	colour	weak isospin	
	1	2	3			left-handed	right-handed
quarks	u	c	t	$+2/3$	r,g,b	$+1/2$	0
	d	s	b	$-1/3$		$-1/2$	0
leptons	ν_e	ν_μ	ν_τ	0	-	$+1/2$	-
	e^-	μ^-	τ^-	-1		$-1/2$	0

Table 2.1: Elementary fermions and their corresponding charges of the SM.

carry an electric charge and weak isospin. They undergo both electromagnetic and weak interaction. Neutrinos carry weak isospin but no electric charge, and participate only in the weak interaction. There are six flavours of quarks, including up (u), down (d), charm (c), strange (s), top (t) and bottom (b). Quarks differ from leptons by carrying colour charge next to electric charge and weak isospin. They can only exist as colourless bound states called hadrons. Hadrons fall into two categories: baryons consisting of three quarks each of which carries a different colour charge, and mesons which are formed by a quark-antiquark pair of opposite colour charges. The elementary fermions and their corresponding charges of the SM are listed in tab. 2.1.

All fermions have an intrinsic and Lorentz-invariant property called chirality. As closely related quantity, helicity is defined by the direction of the particles' spin relative to the direction of its motion. This definition depends on the reference frame of the observer, in which a particle can obtain either positive or negative helicity. For massless particles, which travel with speed of light, chirality and helicity are equal. For massive particles, helicity can change with respect to the chirality eigenstate in different reference frames. Here, a left-chiral fermion can be observed with positive or negative helicity since there is always a Lorentz frame moving faster than the particle. So far, all fermions but neutrinos have been observed in both helicity states. In general, fermions interact differently depending on chirality. It turns out that only left-handed fermions take part in the charged weak interaction. Left-handed fermions are paired up into fundamental representations of $SU(2)_L$ and form doublets of fields which can transform into each other at no cost except for the difference in their mass. Right-handed fermions are trivial under $SU(2)_L$ and form singlet states which do not transform under $SU(2)_L$, i. e. do not participate in weak interactions. Hence, only left-handed ν_L (right-handed $\bar{\nu}_R$) participate in weak interactions. So far, there is no evidence for ν_R ($\bar{\nu}_L$). This can only be consistent within the SM if neutrinos are massless. However, observations prove otherwise (sec. 2.4).

So far, we have not discussed one of the major key building blocks in the SM, the Higgs sector, which is the origin of fermion and gauge boson masses via the mechanism of electroweak symmetry breaking. Since the SM Higgs boson and its properties take the leading role in this thesis they are described in detail in the following.

2.2 Electroweak Symmetry Breaking

An important ingredient of the SM is the spontaneous symmetry breakdown of $SU(2)_L \times U(1)_Y$ to $U(1)_{em}$. In group theory language, three of the four generators of $SU(2) \times U(1)$ are broken. Physically, this means that three of the SM gauge bosons gain masses (W_μ^\pm and Z_μ) and one remains massless (the photon, denoted by A_μ). Spontaneous symmetry breaking is induced by a new scalar field which has to be added to the SM Lagrangian. The interaction of this field with the gauge boson fields must generate the gauge boson masses. This process is called Higgs mechanism [1–3]. The Higgs mechanism represents the simplest choice for achieving spontaneous symmetry breaking.

To understand the principles of spontaneous symmetry breaking, let us illustrate a simple example, following [17, 18]. We consider a real scalar field ϕ with the Lagrange density

$$\mathcal{L} = T - V = \frac{1}{2}(\partial_\mu\phi)^2 - \left(\frac{1}{2}\mu^2\phi^2 + \frac{1}{4}\lambda\phi^4\right), \quad (2.5)$$

which is invariant under the discrete symmetry $\phi \rightarrow -\phi$. Here, $\mu^2, \lambda \in \mathbb{R}$. The first term of eq. 2.5 represents a kinetic term minus an energy potential $V(\phi)$

$$V(\phi) = \frac{1}{2}\mu^2\phi^2 + \frac{1}{4}\lambda\phi^4, \quad (2.6)$$

which is described by the last two terms. Since the ground state (the vacuum) describes the field configuration of minimum energy, $V(\phi)$ must be bounded from below. Therefore, we have $\lambda > 0$. For μ^2 both signs are possible but only in the case $\mu^2 < 0$ the ground state of ϕ is non-vanishing and the minimum occurs at

$$\phi = \pm \sqrt{-\frac{\mu^2}{\lambda}} = \pm v. \quad (2.7)$$

The potentials $V(\phi)$ for $\mu^2 < 0$ and $\mu^2 > 0$ are illustrated in figure 2.1. The ground state value in eq. 2.7 is called vacuum expectation value (VEV), denoted by v . From eq. 2.7 it is obvious that the theory at hand has two possible vacua. The important point is that either choice for v breaks the original reflection symmetry. The symmetry of the Lagrangian in eq. 2.5 is canceled by the arbitrary selection of one particular asymmetrical ground state. We are obliged to work with one of them, which spoils the original reflection symmetry of the system. To investigate the properties of the system after symmetry breakdown, we expand eq. 2.5 around the VEV v in terms of a shifted field η . Thus, we treat the field as fluctuations about the minimum. Such fields must be formulated as deviations from one of the two ground states. We choose $\eta = \phi - v$. The result reads

$$\mathcal{L} = \frac{1}{2}(\partial_\mu\eta)^2 + \mu^2\eta^2 - \lambda v\eta^3 - \frac{1}{4}\lambda\eta^4. \quad (2.8)$$

We observe with the first two terms of the Lagrangian that η describes a particle with physical mass

$$m_\eta = \sqrt{-2\mu^2} = \sqrt{2\lambda v^2}, \quad (2.9)$$

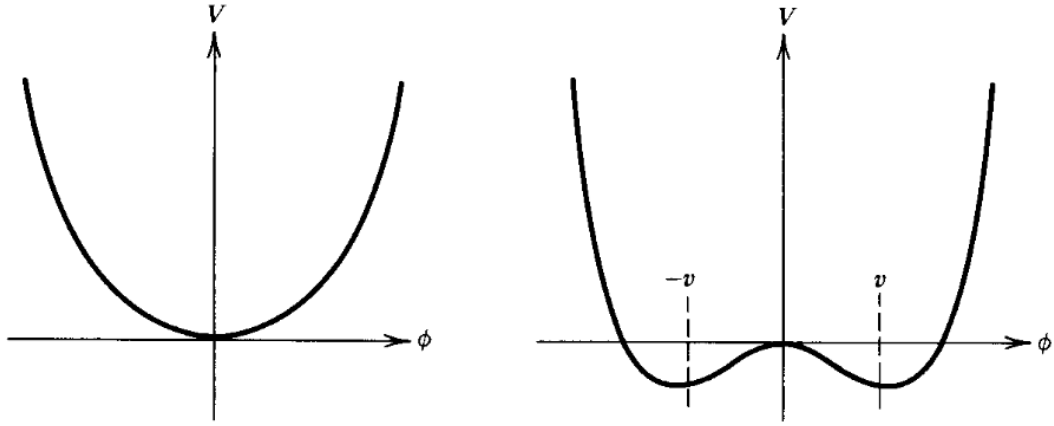


Figure 2.1: Potential $V(\phi) = \frac{1}{2}\mu^2\phi^2 + \frac{1}{4}\lambda\phi^4$ with $\lambda > 0$. Left: for $\mu^2 > 0$ describing a scalar field with mass μ and a ground state corresponding to $\phi = 0$. The reflection symmetry of the Lagrangian is satisfied. Right: for $\mu^2 < 0$, the interesting case having two minima. Figure taken from [17].

which gives the definition of the Higgs mass in the SM. The VEV v reads $v = \sqrt{-\mu^2/\lambda}$ and can be determined from the Fermi constant G_F according to $v = (\sqrt{2}G_F)^{-1/2} \simeq 246$ GeV. The higher order terms in η represent the trilinear and quartic self-interaction of η .

As a next step, let us now look at the spontaneous symmetry breakdown of a $U(1)$ gauge symmetry and the actual Higgs mechanism. From there it is a short way to the case of $SU(2)$ or $SU(2) \times U(1)$. In this case, the scalar field is taken to be complex and it transforms under $U(1)$ as

$$\phi \rightarrow e^{i\alpha(x)}\phi. \quad (2.10)$$

This can be achieved by introducing a massless gauge field A_μ and by replacing the derivative in eq. 2.5 by the covariant derivative $\partial_\mu - ieA_\mu \equiv D_\mu$. The gauging procedure renders a Lagrangian of the form

$$\mathcal{L} = (\partial^\mu + ieA^\mu)\phi^*(\partial_\mu - ieA_\mu)\phi - \mu^2\phi^*\phi - \lambda(\phi^*\phi)^2 - \frac{1}{4}F_{\mu\nu}F^{\mu\nu}. \quad (2.11)$$

Here, $F_{\mu\nu}$ is the usual field strength of the gauge field A_μ . As before, we choose $\mu^2 < 0$ to achieve a ground state that is not invariant under the $U(1)$ symmetry. A naive approach would be to expand eq. 2.11 in terms of the VEV of ϕ and two real scalar fields: $\phi(x) = \sqrt{\frac{1}{2}}(v + \eta(x) + i\xi(x))$. Then, we would observe that η plays the same role as in our previous example. It represents a massive scalar particle. However, ξ remains massless $m_\xi = 0$. It is important to note that it is no coincidence that one of the fields is automatically massless. In fact, this can be generalised by stating Goldstone's theorem [19]: Spontaneous breakdown of a continuous symmetry always implies the existence of a massless, scalar (spin-0) particle, a so-called Goldstone boson.

It appears that our approach of finding a spontaneously broken gauge theory of weak interactions with massive gauge bosons now lets us deal with an unwanted massless scalar

particle. However, it turns out that there is an even more convenient approach that solves this problem: We should note that

$$\phi(x) = \sqrt{\frac{1}{2}}(v + \eta(x) + i\xi(x)) \simeq \sqrt{\frac{1}{2}}(v + \eta)e^{i\xi/v} \quad (2.12)$$

to lowest order in ξ . This suggests that we should substitute another set of real fields h , θ , A_μ as

$$\phi \rightarrow \sqrt{\frac{1}{2}}(v + h(x))e^{i\theta(x)/v}, \quad (2.13)$$

$$A_\mu \rightarrow A_\mu + \sqrt{\frac{1}{ev}}\partial_\mu\theta. \quad (2.14)$$

This is a certain choice of gauge, with $\theta(x)$ chosen so that h is a real scalar field, from now on called Higgs boson. We anticipated that the theory is independent of θ [17]. Inserting the expression into eq. 2.11 we are left with

$$\mathcal{L} = \frac{1}{2}(\partial_\mu h)^2 - \lambda v^2 h^2 - \lambda v h^3 - \frac{1}{4}\lambda h^4 + \frac{1}{2}e^2 v^2 A_\mu^2 + \frac{1}{2}e^2 A_\mu^2 h^2 + ve^2 A_\mu^2 h - \frac{1}{4}F_{\mu\nu}F^{\mu\nu}. \quad (2.15)$$

The second term in eq. 2.15 describes the mass of the Higgs boson. From this we deduce the following facts: The theory now describes two interacting massive particles, the gauge boson A_μ and the Higgs field h . In eq. 2.15, latter is described by $\frac{1}{2}e^2 A_\mu^2 h^2$ and $ve^2 A_\mu^2 h$. In particular, no massless Goldstone boson appears in the Lagrangian due to the particular choice of expression for $\phi(x)$. The Goldstone boson has been “eaten” by the gauge boson to render the latter massive [17] as described by the mass term $\frac{1}{2}e^2 v^2 A_\mu^2$. This is called Higgs mechanism.

One caveat remains: As stated in the beginning of this section, the SM Higgs mechanism also involves an $SU(2)$ gauge symmetry. In the non-Abelian $SU(2)_L \times U(1)_Y$ electroweak theory, one needs to generate masses for the three gauge bosons W^\pm and Z but the photon γ must remain massless. By the correct choice of Higgs fields, one can deduce that after symmetry breakdown of $SU(2)_L \times U(1)_Y$ one obtains mass terms for three of the four gauge bosons. The mathematics in this case is more complicated and the complete calculation can be found in literature [17, 18, 20]. However, for better understanding let us look at the main idea of the computation. Let us start with just an $SU(2)_L$ gauge symmetry. In order to break this symmetry spontaneously, we introduce an $SU(2)_L$ doublet of complex scalar fields

$$\phi = \begin{pmatrix} \phi^+ \\ \phi^0 \end{pmatrix} = \frac{1}{\sqrt{2}} \begin{pmatrix} \phi_1 + i\phi_2 \\ \phi_3 + i\phi_4 \end{pmatrix}, \quad (2.16)$$

which transforms under global $SU(2)_L$ phase transformations as

$$\phi \rightarrow \phi' = e^{i\alpha_a \tau_a / 2} \phi. \quad (2.17)$$

As in our previous example, we introduce the covariant derivative $\partial_\mu + ig\frac{\tau_a}{2}W_\mu^a \equiv D_\mu$ and three gauge fields $W_\mu^a(x)$, where $a = 1, 2, 3$. The latter transform as $W_\mu \rightarrow W_\mu - \frac{1}{g}\partial_\mu\alpha - \alpha \times W_\mu$. Analogously to eq. 2.11, this gauging procedure yields a Lagrangian of the form

$$\mathcal{L} = (\partial^\mu + ig\frac{1}{2}\tau \cdot W^\mu)\phi^*(\partial_\mu + ig\frac{1}{2}\tau \cdot W_\mu)\phi - \mu^2\phi^*\phi - \lambda(\phi^*\phi)^2 - \frac{1}{4}W_{\mu\nu}W^{\mu\nu}. \quad (2.18)$$

Again we choose $\mu^2 < 0$ and $\lambda > 0$ to obtain a minimum in which the symmetry of the system is broken. The minimum reads

$$\phi^* \phi = \frac{1}{2}(\phi_1^2 + \phi_2^2 + \phi_3^2 + \phi_4^2) = -\frac{\mu^2}{2\lambda} \quad \text{with} \quad v^2 = -\frac{\mu^2}{\lambda}. \quad (2.19)$$

We choose $\phi_1 = \phi_2 = \phi_4 = 0$ and $\phi_3^2 = -\frac{\mu^2}{\lambda} \equiv v^2$, and expand $\phi(x)$ about this particular minimum and substitute the expansion

$$\phi(x) = \frac{1}{\sqrt{2}} \begin{pmatrix} 0 \\ v + h(x) \end{pmatrix} \quad (2.20)$$

into our Lagrangian (eq. 2.18). Again, this leaves us with only one scalar neutral field $h(x)$, representing the Higgs field, which determines the masses of three of the four gauge bosons. Our choice of ϕ is the simplest choice to group four fields into one $SU(2)_L$ representation. When ϕ obtains a VEV, the symmetries under which it is charged are spontaneously broken as we have seen in our simple examples. Hence, this theory leads to a system with no massless gauge bosons.

This brings us automatically to the case of $SU(2)_L \times U(1)_Y$. To the previous example, we have to introduce an additional $U(1)$ gauge symmetry by giving the doublet field ϕ a weak hypercharge $Y = +1$. Then, it turns out that there is one unbroken symmetry with the generator given by eq. 2.1, which generates the symmetry group of electromagnetism $U(1)_{em}$. By taking a complex doublet of scalar fields, adding a weak hypercharge Y and choosing this certain form of ϕ_0 has a simple explanation: Any choice of ϕ_0 , which breaks a symmetry, will generate a mass for the corresponding gauge boson. However, if ϕ_0 is still left invariant by some subgroups of gauge transformations, as it is here the case after adding a weak hypercharge of $U(1)_Y$, then the gauge bosons associated with this subgroup will remain massless. Our choice of ϕ_0 breaks both $SU(2)_L$ and $U(1)_Y$ symmetries but since ϕ_0 is electrically neutral, $U(1)_{em}$ with the generator in eq. 2.1 remains unbroken. The new gauge bosons after symmetry breakdown of $SU(2)_L \times U(1)_Y$ were introduced in section 2.1. The W^\pm bosons and the Z boson represent the gauge bosons of the weak interaction. The masses of the physical W^\pm and Z bosons can be expressed in terms of the coupling constants of $SU(2)_L$ and $U(1)_Y$, denoted by g and g' as

$$m_W = \frac{1}{2} g v, \quad \text{and} \quad m_Z = \frac{1}{2} v \sqrt{g^2 + g'^2}. \quad (2.21)$$

Further calculations lead to a relation between the Z - and W -boson masses which reads

$$\frac{M_W}{M_Z} = \frac{g}{\sqrt{g^2 + g'^2}} = \cos \theta_W. \quad (2.22)$$

This relation represents one important prediction of the SM with its simple choice of a single Higgs doublet in the SM electroweak symmetry breaking scenario.

Now that we have described the origin of the SM gauge boson masses, let us turn to the fermions briefly. Up to now, the fermions remain massless in our discussion. To

understand how mass terms for the latter can be generated, let us have a closer look at the quantum numbers of the Higgs field ϕ under $SU(2)_L \times U(1)_Y$. Being a doublet of $SU(2)$, it can combine with an anti-doublet (e.g the left-handed fermionic anti-doublet \bar{L}) to a gauge invariant singlet. We observe that new terms of the form

$$\mathcal{L}_{\text{Yuk}} = -G(\bar{R}\phi^\dagger L + \bar{L}\phi R), \quad (2.23)$$

where $G = \text{const.}$ and R denotes a right-handed $SU(2)$ singlet, are now gauge invariant. Couplings of the form given in eq. 2.23 are called Yukawa couplings. The intriguing feature of these is that fermionic mass terms are generated automatically once ϕ gets a VEV. Then the interaction between left-handed fermion components with ϕ and their right-handed components give non-zero Yukawa couplings. This kind of fermion mass is called Dirac mass. The fermion masses are just parameters of the theory and are not predicted as it is the case for gauge bosons.

We conclude that the Higgs mechanism generates mass terms for gauge bosons of broken symmetries. In addition, the Higgs field is responsible for the fermionic mass terms in the SM via its Yukawa couplings. The minimal choice of a single Higgs doublet is sufficient to generate the gauge boson and fermion masses. The Higgs couplings to fermions, gauge bosons, and to itself are summarised in a Lagrangian as

$$\mathcal{L} = -g_{Hf\bar{f}}Hf\bar{f} + \frac{g_{HHH}}{6}H^3 + \frac{g_{HHHH}}{24}H^4 + \delta_V V_\mu V^\mu \left(g_{HVV}H + \frac{g_{HHVV}}{2}H \right), \quad (2.24)$$

with $V = W^\pm, Z$ and $\delta_W = 1, \delta_Z = 1/2$, and coupling parameters defined as

$$g_{Hf\bar{f}} = \frac{m_f}{v}, \quad g_{HVV} = \frac{2m_V^2}{v}, \quad g_{HHVV} = \frac{2m_V^2}{v^2}, \quad (2.25)$$

$$g_{HHH} = \frac{3m_H^2}{v} = 6\lambda v, \quad g_{HHHH} = \frac{3m_H^2}{v^2} = 6\lambda. \quad (2.26)$$

The couplings of the Higgs boson to the fermions and the gauge bosons are determined as a function of the Higgs mass, which is not predicted by the SM and represents the only free parameter of the SM Higgs sector. Hence, once the Higgs mass is known all other parameters are fixed. The Higgs couplings to the fermions are directly proportional to their masses. More massive fermions will have proportionally stronger couplings to the Higgs. A precise reconstruction of the mass-coupling relation of the Higgs to other particles is crucial to test the electroweak symmetry breaking sector.

A final remark on neutrino masses in the SM should be made: Massless neutrinos can only exist in the SM if there are no right-handed neutrinos ν_R ($\bar{\nu}_L$). Nevertheless, since neutrinos seem to have non-zero masses (section 2.4), a natural explanation can be given by simply adding ν_R ($\bar{\nu}_L$), which results in a usual Dirac mass term [21]. In theory, the existence of ν_R ($\bar{\nu}_L$) is well-motivated since all other known fermions exist with left and right chirality. Additionally, ν_R ($\bar{\nu}_L$) would only participate in Yukawa interactions with ϕ_0 (eq. 2.16) and form a weak isospin singlet which do not transform under $SU(2)_L$ (eq. 2.1).

However, the generation of Dirac neutrino masses via the SM Higgs mechanism does not explain why neutrino masses are so small compared to the other fermions. A way to ensure that even with non-zero neutrino masses weak interactions couple only to ν_L ($\bar{\nu}_R$) is introduced by the Majorana mechanism [22], which generates their masses by requiring that neutrino and antineutrino are the same particle. Here, a massive neutral fermion can be described by a spinor ψ with two independent components by imposing the Majorana condition $\psi = \psi^c$. Following [23] and decomposing this into right-handed and left-handed components, it follows $\psi_R = \psi_L^c$. From the left-handed component ψ_L , the right-handed component ψ_R of the Majorana neutrino field ψ is obtained via charge conjugation. Hence, the Majorana field reads $\psi = \psi_L + \psi_L^c$ and depends only on two components of ψ_L . For more information on massive neutrinos see [24–26] and the references in [27].

2.3 The Standard Model Higgs Boson

2.3.1 Higgs Production in Hadron and e^+e^- Collisions

In order to investigate Higgs properties at particle colliders, we need to know about Higgs production mechanisms and decay modes. The dominant single and double Higgs production mechanisms at hadron and e^-e^+ colliders are discussed in the following.

Higgs Production Mechanisms in Hadron Collisions

At hadron colliders there are four dominant single Higgs production processes, the tree-level Feynman diagrams of which are shown in fig. 2.2. The Higgs production process giving the largest cross section is gluon fusion ($gg \rightarrow H$) [28]. Since the Higgs does not couple to gluons directly and due to the strong coupling to top quarks, the Higgs boson is produced at lowest order by a top-quark loop. The gluon-fusion cross section suffers from high QCD corrections and large uncertainties due to gluon structure functions [29, 30]. Additionally, this signature is overwhelmed by QCD backgrounds in the detector. The second most dominant Higgs production is vector boson fusion ($qq \rightarrow qqH$) [31] in which the Higgs boson is produced in association of a quark pair. For a Higgs mass of 125 GeV its cross section is one order of magnitude lower than the gluon-fusion cross section. Vector boson fusion benefits from two additional jets with high invariant mass in the forward region, which results in a very clear signature in the detector. Additionally, it has a well-known next-to-leading-order cross section and receives only small QCD corrections. There is also vector-boson associated ($q\bar{q} \rightarrow HV$ [$V = W, Z$]) [32] and heavy-quark associated ($gg/qq \rightarrow t\bar{t}H/b\bar{b}H$) [33] production. Both mechanisms have cross sections several orders of magnitude smaller than gluon and vector boson fusion.

There are more Higgs production mechanisms in hadron collisions but of higher perturbative order. Especially interesting for this thesis is double Higgs production, which is

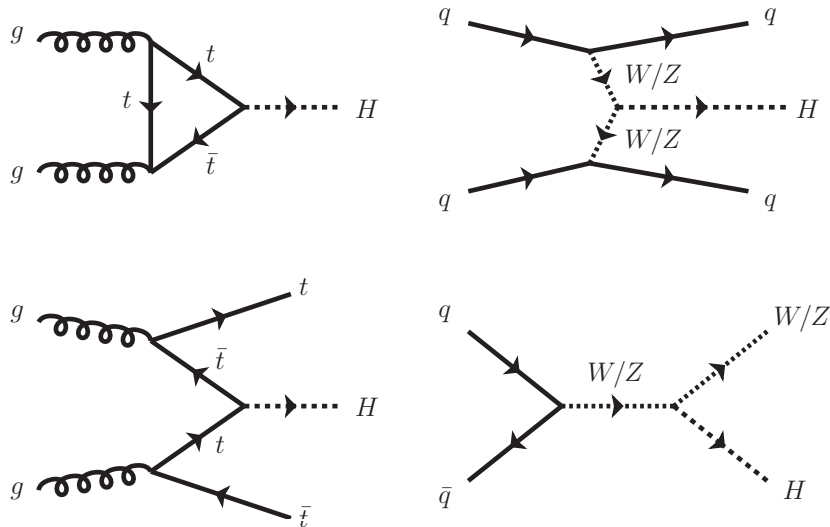


Figure 2.2: Dominant Higgs production in hadron collisions. Top left: gluon fusion, in which the Higgs is produced through a top loop. Top right: vector boson fusion, in which the Higgs is produced together with heavy quarks. Bottom left: heavy-quark associated production with a top pair. Bottom right: vector-boson associated production with W/Z .

sensitive to the Higgs self-coupling λ . At hadron colliders, Higgs pairs are produced through gluon fusion [34] (fig. 2.3), vector boson fusion [35] (fig. 2.4), and double Higgs-strahlung [36] (fig. 2.5). In each production only one diagram contains the Higgs self-coupling vertex, while the other diagrams involve Higgs couplings to fermions or gauge bosons respectively. Gluon fusion is mediated by fermionic triangle and box loops which are dominated by the top quark. However, the triangle and box loops could also be mediated by new-physics particles. Gluon fusion is the dominant process over the entire range of different centre-of-mass energies, also in Higgs-pair production. The other two dominant processes have cross sections of factor 10 to 30 smaller than gluon fusion. Dominant double Higgs production cross sections at next-to-leading order in QCD and their uncertainties as a function of \sqrt{s} are depicted in fig. 2.6. To larger \sqrt{s} the total cross sections of the respective processes increase. However, these cross sections are rather low and large luminosities are needed to confirm double Higgs production.

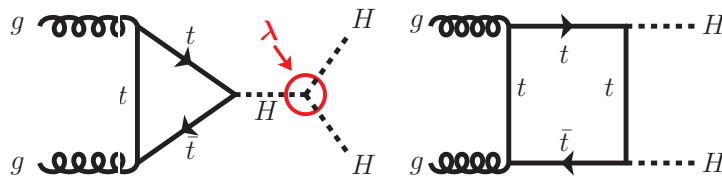


Figure 2.3: Double Higgs production through gluon fusion mediated by heavy-quark loops, mainly top which couples most strongly to the Higgs. The left diagram contains the Higgs self-coupling vertex while the other involves Higgs-fermion couplings.

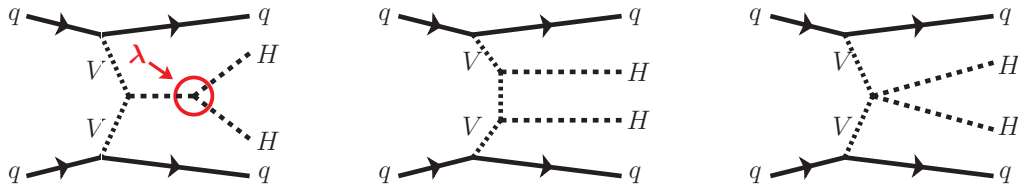


Figure 2.4: Vector boson fusion (with $V = W, Z$) in which the two Higgs are produced in association of two heavy jets. The left diagram involves the Higgs self-coupling diagram and the other diagrams involve couplings to gauge bosons.

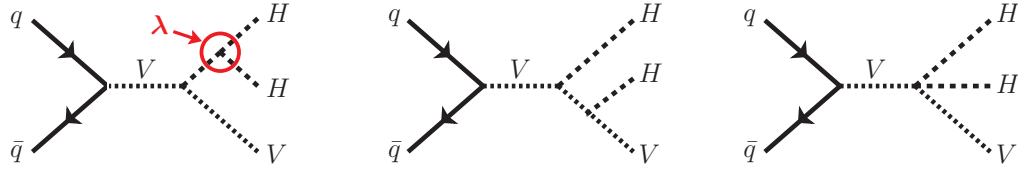


Figure 2.5: Double Higgs-strahlung ($V = W, Z$) in which the two Higgs are produced with either W or Z . The left diagram contains the Higgs self-coupling, while the others involve couplings to gauge bosons.

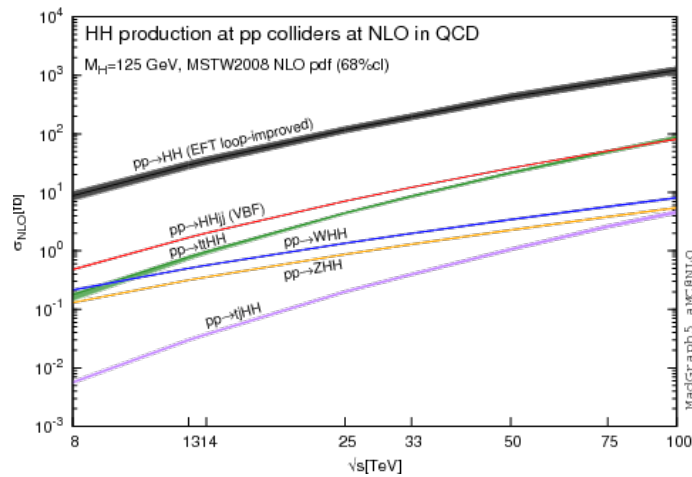


Figure 2.6: Six dominant double Higgs production cross sections at next-to-leading order in QCD at hadron colliders and the uncertainties. Figure taken from [37].

Higgs Production Mechanisms in e^+e^- Collisions

At e^+e^- colliders, the dominant single Higgs production mechanisms are Higgs-strahlung, WW fusion, and ZZ fusion. Due to the ratio of the smaller neutral couplings and the larger charged couplings the production cross section of ZZ fusion is $\sim 16 \cos^4(\theta_W)$ [38] and therefore suppressed by one order of magnitude compared to WW fusion. The respective tree-level diagrams are shown in fig. 2.7. In Higgs-strahlung an on-shell Higgs is emitted from an s -channel Z boson. It is the dominant process at small centre-of-mass energies

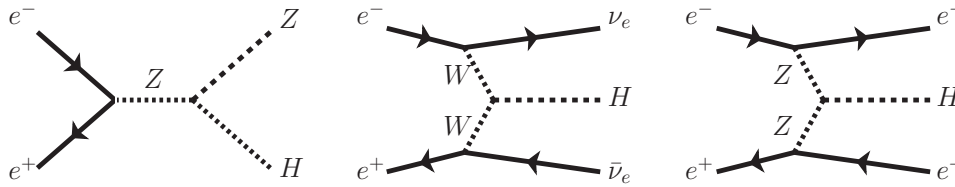


Figure 2.7: Higgs production processes at e^+e^- colliders. From left to right: Higgs-strahlung ($e^+e^- \rightarrow ZH$), WW fusion ($e^+e^- \rightarrow \nu_e\bar{\nu}_eH$), and ZZ fusion ($e^+e^- \rightarrow e^+e^-H$).

around 250 GeV since the cross section scales as s^{-1} and is enhanced at $\sqrt{s} = m_H + m_Z$. The mechanism benefits of the well-known properties of the Z boson. By reconstructing the decay products of the Z boson, Higgs-strahlung allows to search for Higgs signals and determine its properties without any assumptions on the Higgs decay mode. WW and ZZ fusion are formation processes of the Higgs boson in the collision of two quasi-real W or Z bosons, which got radiated off the e^+ and e^- beams. The WW -fusion cross section increases as $\log(s/m_H^2)$. Hence, this process is of similar size as ZH around 350 GeV and becomes dominant at $\sqrt{s} \geq 500$ GeV. The main double Higgs production mechanisms are double Higgs-strahlung [38–40] and WW fusion [41]. The tree-level diagrams including the Higgs self-coupling vertex are depicted in fig. 2.8. Similar to single Higgs production, there is also Higgs-pair production by ZZ fusion which is suppressed by one order of magnitude compared to WW fusion. The Higgs-pair production cross sections have the same scaling behaviour with energy as the single Higgs productions. Double Higgs-strahlung gives an enhanced cross section around the threshold $\sqrt{s} = 2m_H + m_Z + 200$ GeV [42]. Near this threshold the value of the propagator for the intermediate virtual Higgs boson connecting to the two real Higgs bosons through λ is maximal. The WW -fusion cross section increases logarithmically and becomes dominant around $\sqrt{s} = 1$ TeV. The cross sections of ZHH and WW fusion as a function of \sqrt{s} are depicted in fig. 2.9 for $m_H = 125$ GeV and two different beam polarisations. Both Higgs-pair production mechanisms include additional diagrams which do not involve the Higgs self-coupling vertex. The respective tree-level Feynman diagrams are shown in fig. 2.10 for ZHH and fig. 2.11 for WW fusion. The influence of these diagrams and the sensitivity of Higgs-pair production processes to λ are discussed in sec. 2.5.

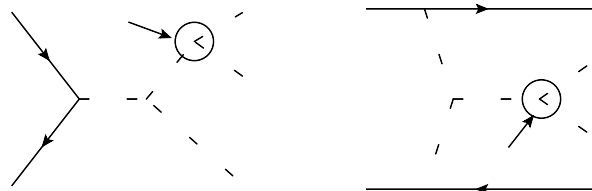


Figure 2.8: Tree-level Feynman diagrams for double Higgs-strahlung ZHH (left) and WW fusion (right). Both diagrams involve the Higgs self-coupling vertex with λ .

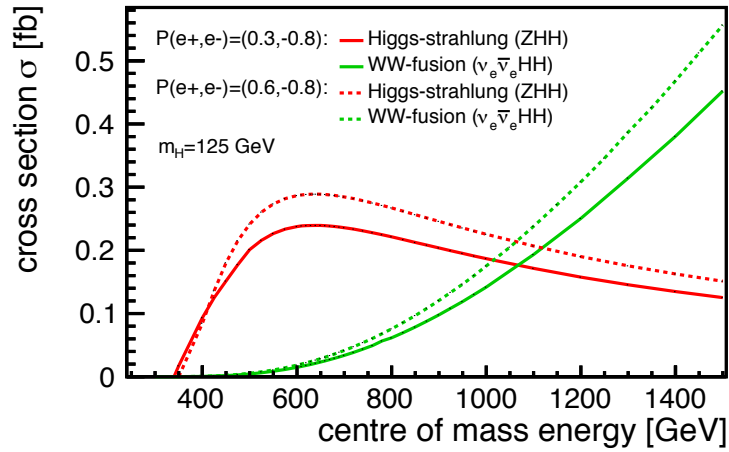


Figure 2.9: Double Higgs production cross sections of WW fusion and ZHH as a function of \sqrt{s} for two different beam polarisations and a Higgs mass of $m_H = 125$ GeV.

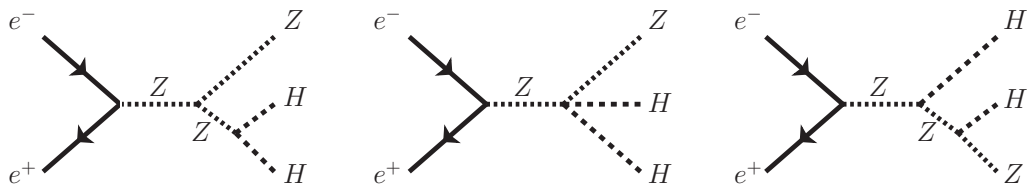


Figure 2.10: Additional amplitudes in double Higgs-strahlung ZHH which do not contain the Higgs self-coupling vertex but only the Higgs couplings to gauge bosons.

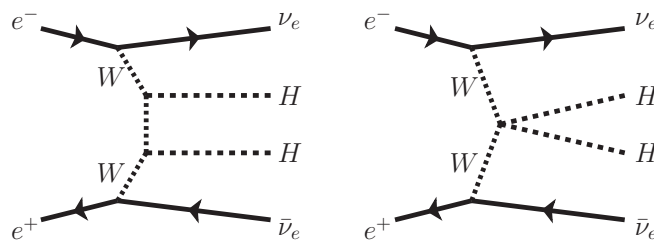


Figure 2.11: Irreducible tree-level diagrams of the WW fusion process, which do not contain the Higgs self-coupling vertex but only the Higgs couplings to gauge bosons.

2.3.2 Higgs Couplings and Decays

The couplings to fermions are proportional to the fermion masses $g_{Hff} \propto m_f$, and the couplings to gauge bosons are proportional to the square of the corresponding boson mass $g_{HVV} \propto m_V^2$ (sec. 2.2). The couplings of the Higgs boson determine its decay modes.

In fig. 2.12, the main branching ratios of the Higgs are depicted as a function of m_H . It is obvious that a Higgs boson with a mass of 125 GeV provides a very favourable situa-

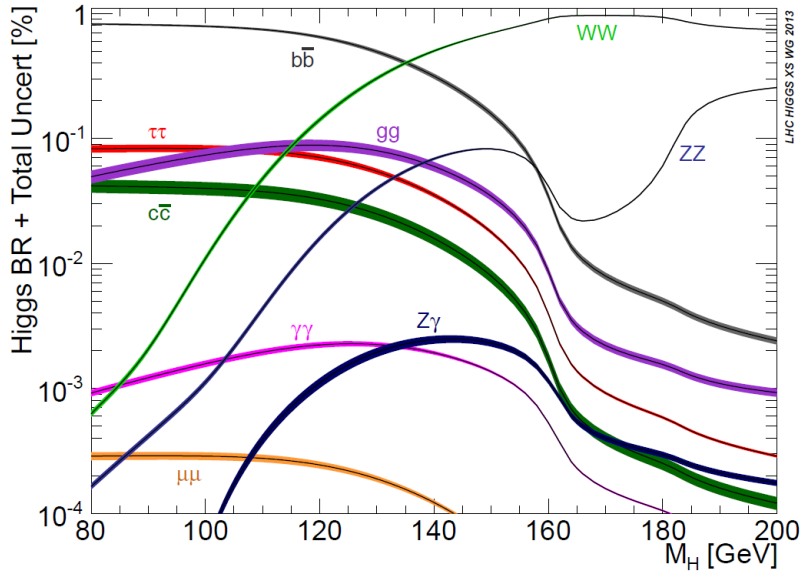


Figure 2.12: Branching ratios for the Higgs boson as a function of the Higgs mass. The solid bands represent the corresponding theoretical uncertainties. Figure taken from [43].

tion in which a large number of decay modes are accessible to experiments that provide large dataset sizes. The Higgs boson can directly decay to fermion pairs (e. g. $b\bar{b}$, $\mu^-\mu^+$, $\tau^-\tau^+$) and gauge boson pairs (WW^* , ZZ^*). The Higgs boson does not couple to γ and g directly, since they are massless and the Higgs does neither carry electric nor colour charge. However, the decay modes $H \rightarrow gg$ and $H \rightarrow \gamma\gamma$ can occur through higher-order loop diagrams as depicted in fig. 2.13. The decay into gluon pairs is possible through virtual top quarks since the top couples most strongly to the Higgs due to its large mass. The decays of $H \rightarrow \gamma\gamma/Z\gamma$ mainly happen through a top-quark loop and a W -boson loop (fig. 2.13). W bosons carry electric charge and thus can emit photons. In $H \rightarrow \gamma\gamma$, the W -loop and top-loop diagrams interfere destructively. At $m_H = 125$ GeV, the most favoured decay mode is $H \rightarrow b\bar{b}$. The second most preferred fermionic decay channel is $H \rightarrow \tau^+\tau^-$. However, in this mass range the branching ratios of the decays to $\tau^+\tau^-$, $c\bar{c}$, and gg together contribute less than $\sim 15\%$. For Higgs masses above 125 GeV, Higgs decays to gauge bosons become dominant. Here, $H \rightarrow WW$ is the dominant decay channel. Once this decay channel opens, the Higgs boson is expected to decay preferably into W -boson pairs due to the larger coupling to gauge bosons compared to the coupling to fermions. Above the threshold $m_H \geq 2m_W$, the branching ratio of $H \rightarrow WW$ is about 100% with an important contribution from $H \rightarrow ZZ$. Below the W^+W^- threshold one of the W bosons is virtual.

A Higgs boson with a mass of 125 GeV gives the opportunity to measure many branching ratios very accurately since all important decay channels can be observed and have large decay rates. These branching ratios can be converted into a precise determination of the Higgs couplings to the corresponding particles. The investigation of the mass-coupling

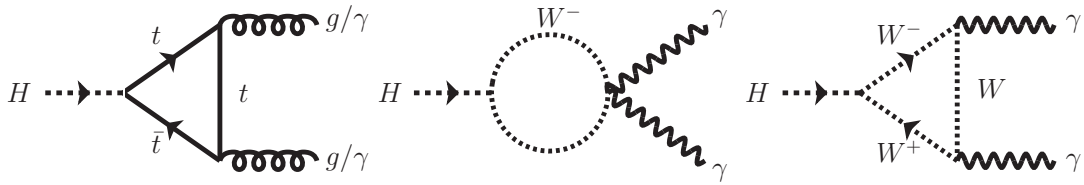


Figure 2.13: Loop diagrams of $H \rightarrow gg$ and $H \rightarrow \gamma\gamma$. The top and W boson are needed in loops, since neither g or γ couple directly to the Higgs. In general these diagrams are interesting for new physics searches, since any new particle could enter the loops.

relation of the Higgs to other particles represents a test of the SM electroweak symmetry breaking sector. Since the coupling strength of the Higgs boson to fermions is proportional to the fermion masses in the SM, measuring the top-Yukawa coupling g_{Ht} represents a test of this SM prediction due to the large top mass compared to other fermion masses.

2.3.3 Higgs Boson Search

Postulated in 1964 and following earlier work on electroweak symmetry breaking, the existence of a neutral scalar particle, the Higgs, was predicted by the Higgs mechanism. There were few theoretical constraints on the Higgs mass at that time. Early searches in the 1970s, focussing on nuclear transitions [44] and neutron-nucleus scattering [45], excluded Higgs mass ranges between $1.03 \text{ MeV} < m_H < 18.3 \text{ MeV}$ and $m_H < 13 \text{ MeV}$, respectively [46]. In the 1980s further limits on the Higgs mass were imposed by experiments studying meson decays, in which a sufficiently light Higgs was expected to decay into a charged lepton pair. Studies of kaon decays at KEK, Brookhaven National Laboratory (BNL), and at CERN Super Proton Synchrotron (SPS) were able to exclude Higgs masses below 3.6 GeV [47–49]. Searches for B -meson decays $B \rightarrow KH$ with Higgs decays to a pair of charged π , μ , or K at CLEO at the Cornell Electron Storage Ring and TASSO Collaboration at PETRA excluded similar ranges of $211 \text{ MeV} < m_H < 3.4 \text{ GeV}$ [50–52].

In the 1990s, the search for a high-mass Higgs boson at particle colliders began at the Large Electron Positron Collider (LEP) at CERN. LEP was operated in two energy phases. During the first phase, the collider started operating at a centre-of-mass energy around 90 GeV close to the Z -boson mass. The energy was subsequently increased to 160 GeV in order to study W -pair production. Direct searches for the Higgs boson were performed by considering Higgs-strahlung $e^+e^- \rightarrow ZH$ production (sec. 2.3.1) using $HZ \rightarrow b\bar{b}Z$ final states since $H \rightarrow b\bar{b}$ is dominant in the Higgs mass range accessible at LEP (fig. 2.12). Moreover, exclusion limits on the Higgs mass range were obtained from high precision measurements of rare electroweak processes [53, 54], the rate of which is affected by loop corrections involving the Higgs boson as depicted in fig. 2.14. Exclusion limits were obtained by fitting all possible Higgs masses to the data. Nevertheless, it was not until the discovery of the top quark [55] in 1995, when the strongest predictions for the SM Higgs

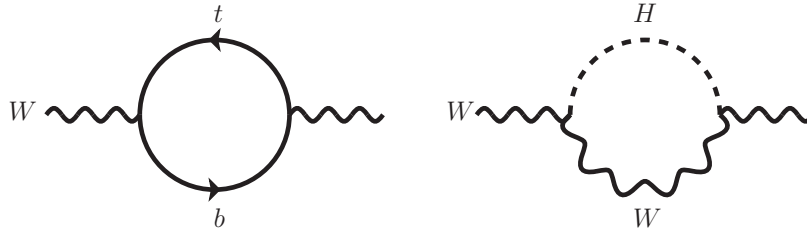


Figure 2.14: Indirect Higgs search in rare electroweak processes the rate of which is effected by loop corrections involving heavy quark and the Higgs boson. The top quark contributes power-like mass corrections $\propto m_t^2$ while the Higgs contributes logarithmic mass corrections $\propto \log(m_H)$. Therefore, it was not until the discovery of the top quark when predictions on the Higgs mass could be obtained in indirect searches.

mass could be obtained from these fits. The observations indicated the exclusion of the Higgs mass below the W -boson mass of 81 GeV. As a result, the centre-of-mass energy was gradually increased. By the year 2000, during the second phase, LEP was operated at a centre-of-mass energy of 209 GeV. However, no significant excess was observed. In 2000, after ten years of operation and the final shutdown of the collider, LEP experiments were able to set a lower limit on the Higgs mass to 114.4 GeV in direct searches [56].

Additional exclusion limits were placed on m_H by the CDF and $D\bar{O}$ experiments located at the Tevatron Collider at Fermilab. Tevatron was a $p\bar{p}$ collider operating at a centre-of-mass energy of $\sqrt{s} = 1.96$ TeV which shut down in 2011. In summer 2012, shortly before the Higgs discovery was announced at LHC, CDF and $D\bar{O}$ updated their results based on the complete data samples corresponding to an integrated luminosity of 10 fb^{-1} . Combining the results of the two collaborations, two regions in the Higgs mass spectrum could be excluded at 95% confidence level [57], namely

$$100 \text{ GeV} \leq m_H \leq 103 \text{ GeV} \quad \text{and} \quad 147 \text{ GeV} \leq m_H \leq 180 \text{ GeV}. \quad (2.27)$$

Moreover, a significant excess in data was observed in the mass range $115 \text{ GeV} \leq m_H \leq 140 \text{ GeV}$, as shown in fig. 2.15. Assuming $m_H = 120 \text{ GeV}$, the corresponding local significance reaches 3.0σ . The global significance for such an excess measures approximately 2.5σ . By investigating separate decay modes, the largest signal-like excess was observed in $H \rightarrow b\bar{b}$. Here, assuming that $m_H = 135 \text{ GeV}$, a local significance of 3.2σ was observed, which yields a global significance of 2.9σ in the complete Higgs mass range.

The Higgs search continued at the LHC at CERN. In 2011, direct searches at the LHC were based on data from proton-proton collisions, corresponding to an accumulated integrated luminosity of 5.1 fb^{-1} at a centre-of-mass energy of 7 TeV. The ATLAS experiment excluded the Higgs mass ranges between

$$111.4 \text{ GeV} \leq m_H \leq 116.6 \text{ GeV}, \quad (2.28)$$

$$119.4 \text{ GeV} \leq m_H \leq 122.1 \text{ GeV}, \quad (2.29)$$

$$129.2 \text{ GeV} \leq m_H \leq 541.0 \text{ GeV}, \quad (2.30)$$

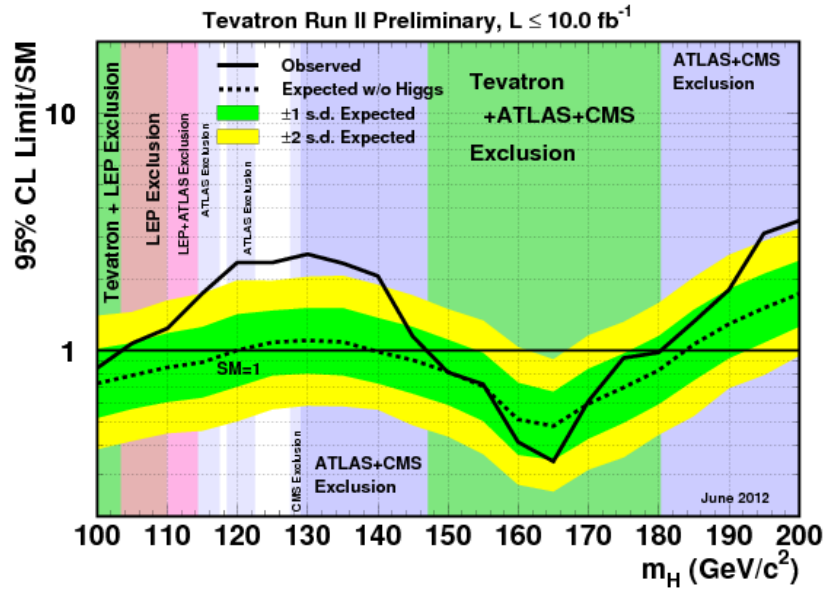


Figure 2.15: Tevatron results on the Higgs search for the combined CDF and $D\bar{0}$ analyses, based on 10 fb^{-1} of data. The observed and expected limits on the signal strength ($\frac{\sigma}{\sigma_{SM}}$) is shown. The green and yellow band around the expected limit correspond to $\pm 1\sigma$ and $\pm 2\sigma$, respectively. Higgs masses with an observed limit below 1 can be excluded. The regions excluded by LEP, ATLAS, and CMS are also indicated. Most of the m_H region between 100 GeV and 200 GeV were excluded by LEP, Tevatron, ATLAS and CMS experiments, except for the region between 115 GeV to 127 GeV. The results were published in summer 2012 shortly before the announcement of the Higgs discovery at LHC in July 2012. Figure taken from [57].

at 95% confidence level [58]. The CMS experiment excluded masses between

$$127 \text{ GeV} \leq m_H \leq 600 \text{ GeV} \quad (2.31)$$

at 95% confidence level [59]. Within the allowed mass region, an excess of events between 2σ and 3σ near a Higgs mass of 125 GeV was reported by both experiments. In 2012, the centre-of-mass energy was increased to 8 TeV and by the end of June an additional integrated luminosity of more than 5.3 fb^{-1} had been collected by each of the two experiments, thereby significantly enhancing the sensitivity of the Higgs search which led to the observation of a new heavy boson with a mass of approximately 125 GeV by the ATLAS and CMS Collaborations. For illustration purpose, figure 2.16 shows the ATLAS results in the dominant decay channel $H \rightarrow \gamma\gamma$. In figure 2.17 the invariant mass distribution of the four-lepton channel observed by CMS is depicted. The high energies and luminosities enabled searches for very clear Higgs decay modes, even for those with very small branching ratios like $H \rightarrow \gamma\gamma$ and $H \rightarrow ZZ \rightarrow l^+l^-l^+l^-$. For the latter the background is very low, while the former can be precisely measured due to the good reconstruction of photon clusters in the electromagnetic calorimeters of the detectors. The two experiments simultaneously published the observation in concise papers [4, 5]. In a combined

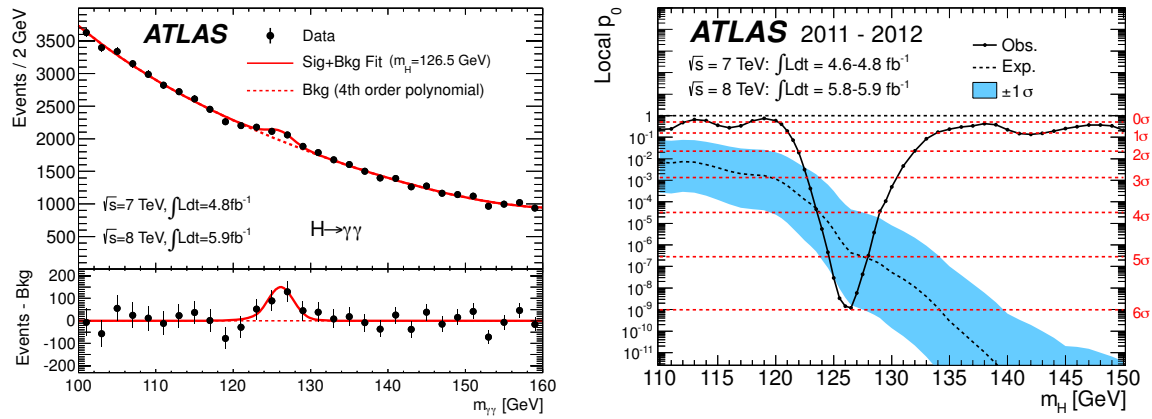


Figure 2.16: *Left: Invariant mass distribution for the two-photon channel using combined $\sqrt{s} = 7$ TeV and $\sqrt{s} = 8$ TeV data samples collected by ATLAS. The new Higgs-like particle appears as an excess around 126.5 GeV. Right: Probability of background to produce a signal-like excess. Figures taken from [60].*

analysis of both experiments using the total available integrated luminosity recorded at $\sqrt{s} = 7$ TeV and $\sqrt{s} = 8$ TeV and by combining different Higgs decay channels, ATLAS and CMS determined the Higgs mass to be [62]

$$m_H = 125.09 \pm 0.21 \text{ (stat.)} \pm 0.11 \text{ (sys.) GeV.} \quad (2.32)$$

Now that a Higgs particle has been discovered, it is crucial to investigate its compatibility with the SM at particle colliders, which is discussed in sec. 2.5. This requires a model-independent reconstruction of the electroweak symmetry breaking sector and the verification of theoretical SM predictions, any deviation of which could indicate new physics beyond the SM (BSM). While precise measurements of the Higgs decays to fermions and gauge bosons can provide sensitivity to BSM physics, the measurement of the Higgs self-coupling λ establishes the Higgs mechanism directly. In various BSM theories, the value of λ differs from the SM prediction. Depending on the deviation, the nature of the Higgs sector can be identified.

2.4 Shortcomings of the Standard Model

Although the SM currently is the best description of the subatomic world, a number of experimental observations and theoretical reasons point to the fact that the SM is incomplete. The SM describes only three of the four fundamental forces, leaving out gravity, since it fails to explain why gravity is so much weaker than electromagnetic or nuclear forces. Another open question is why there are three generations of quarks and leptons with very different mass scales. Moreover, there are experimental observations which directly indicate physics beyond the SM. So far, these are finite neutrino masses, the baryon asymmetry of the universe, and the existence of dark matter and dark energy.

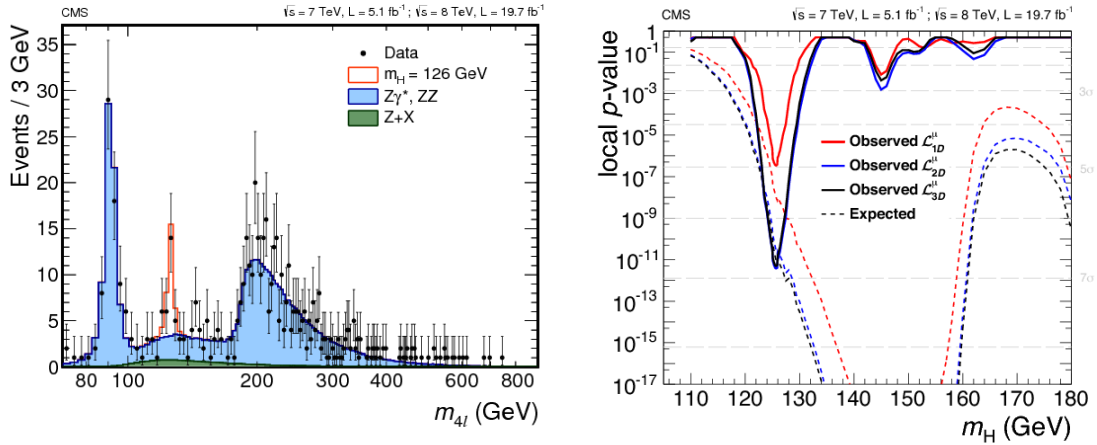


Figure 2.17: Left: Invariant mass distribution for the four-lepton channel of $H \rightarrow ZZ$ using the combined complete $\sqrt{s} = 7$ TeV and $\sqrt{s} = 8$ TeV data sets collected by CMS. Right: Probability of background to produce a signal-like excess. Figures from [61].

In the SM neutrinos are massless. However, experiments have shown that neutrinos can convert from one flavour to another [63]. In order for neutrino oscillations to occur there has to be mixing between neutrino flavour eigenstates and neutrino masses must be unequal, in particular they cannot all be zero [64]. Hence, neutrino oscillations indicate that lepton numbers are not separately conserved and neutrinos appear to have finite masses. Two problems arise from the latter. The first contradiction is related to the missing evidence of neutrinos with right-handed chirality. The couplings to the Higgs field are responsible for fermion masses which include left-handed and right-handed chirality states (section 2.2). In contrast to massive fermions for which both states are present, right-handed neutrinos have not been observed yet, but must exist if neutrinos are massive. The second contradiction is based on the missing explanation of the tiny neutrino masses compared to other fermions. If the neutrino obtained its mass by coupling to the Higgs field, the very small neutrino mass would translate into an extremely small Higgs-neutrino coupling. Therefore, the mass-coupling relation of the Higgs to other particles and the mechanism of mass generation has to be investigated to very high precision to find possible answers to these questions.

Two other issues in the SM arise from cosmology. One refers to the baryon asymmetry in the universe, i. e. in the imbalance of the existing matter and antimatter. Following cosmological data, the baryon asymmetry reads [65]

$$\eta_B = \frac{n_B - n_{\bar{B}}}{n_\gamma} \simeq \frac{n_B}{n_\gamma} \approx 6 \cdot 10^{-10}, \quad (2.33)$$

with n_B , $n_{\bar{B}}$, and n_γ representing baryon, anti-baryon, and photon number densities respectively. Since in standard Big Bang cosmology, baryons and anti-baryons are created in equal numbers, the observed asymmetry must be generated during the evolution of the universe. To explain the generation of the baryon asymmetry, a theory is needed

which satisfies the criteria defined in [66]: (1) baryon number violation, (2) C and CP violation, and (3) a deviation from thermal equilibrium. The SM includes the first two aspects [67, 68] while the last aspect requires a first order electroweak phase transition of the early universe [69, 70]. The theory of electroweak baryogenesis (EWBG) [71–73] gives an explanation of the observed baryon asymmetry in the universe. However, in the SM, electroweak phase transition is of second order and the theory of EWBG is ruled out. Nevertheless, it can still be valid in theories including physics beyond the SM. A detailed discussion of EWBG is given in section 2.5.

The second issue refers to dark energy and dark matter. According to cosmological observations, only 4.9 % of the universe consists of baryonic matter and 95 % of non-interacting dark energy and dark matter [74]. Dark matter manifests itself through gravitational effects in galaxies, galaxy clusters, and the universe as a whole [75–77]. The presence of dark energy relies on measurements of the expansion rate of the universe which indicate that the expansion rate is increasing [78–80]. However, the rate is expected to slow down due to gravitational attraction of galaxies. There are two candidates as source of the acceleration, a cosmological constant giving a constant energy density in space and time, or scalar fields giving rise to a vacuum energy density varying in space and time [81, 82].

There are also theoretical reasons which indicate physics beyond the SM. The discovery of a Higgs boson with $m_H = 125$ GeV engenders several fundamental questions on its properties. There is the hierarchy problem for example, which states that the Higgs field generates the masses of gauge bosons and fermions but its own mass is quadratically sensitive to the mass scale of new physics which couples to it. In contrast to fermion masses, which are protected by chiral symmetries, the masses of elementary scalar fields are quadratically sensitive to the mass scale of new physics. If the SM is valid up to Planck scale ($\Lambda_P \approx 10^{19}$ GeV), the higher-order loop contributions of fermions, gauge bosons, the Higgs itself, or new physics can be orders of magnitude larger than the natural Higgs mass [83]. The natural Higgs mass is defined as

$$m_H^2 = m_{H,bare}^2 + \delta m_H^2 \sim (125 \text{ GeV})^2. \quad (2.34)$$

In the case of a measured Higgs mass of 125 GeV, the difference in size of Λ^2 and m_H reads $\Lambda^2 \approx 10^{34} \times m_H$. This needs to be considered in

$$\delta m_H^2 \propto \frac{1}{16\pi^2} (-6g_t^2 + g_V^2 + \lambda^2) \Lambda^2 - O(\text{new physics}), \quad (2.35)$$

with g_t^2 denoting the top-Yukawa coupling, g_V^2 coupling of gauge bosons to the Higgs ($V = W, Z$), and λ the Higgs self-interaction. To keep the Higgs mass stable, it needs to be renormalised very precisely, cancelling between tree level and the large higher-order corrections. In other words, the SM has to be fine-tuned to a high degree since quantum corrections and the bare mass cancel almost exactly to result in a Higgs mass at the electroweak scale (10^2 GeV). Such a precise fine-tuning indicates that physics beyond the SM should exist, which protects the Higgs mass against large quantum corrections. Since the bare mass does not arise from a natural symmetry, it seems improbable that

nature would choose a finely tuned mass. The accidental amount of fine-tuning is also referred to as fine-tuning problem. The hierarchy problem indicates that not the SM but a new physics model is valid at higher energies. It could be an indication that there is another symmetry in which a light Higgs, such as the discovered one, is required.

The given examples represent some of the open questions of the SM and show that there is still much to be learned about. Next to general searches for new particles, the discovery of the Higgs boson gives the advantage of searching for new physics effects and particles beyond the SM through a precise investigation and reconstruction of the electroweak symmetry breaking sector.

2.5 The Measurement of the Higgs Self-coupling

The Higgs mechanism is the cornerstone in the electroweak sector of the SM. Gauge bosons and fermions acquire their masses through the interaction with a scalar field ϕ . Referring to a simple example given in sec. 2.2, after spontaneous symmetry breaking the energy potential in eq. 2.6 resulted in the Lagrangian given by eq. 2.8. By adding eq. 2.9 the potential reads as

$$V(\eta_H) = \frac{1}{2}m_H^2\eta_H^2 + \lambda v\eta_H^3 + \frac{1}{4}\lambda'\eta_H^4. \quad (2.36)$$

The first term in eq. 2.36 represents the Higgs mass while the trilinear and quartic Higgs self-interaction are described by the second and third term, respectively. These terms are unique in the results of electroweak symmetry breaking (sec. 2.2). Therefore, $V(\eta_H)$ is a characteristic feature in the SM and needs to be measured to establish the Higgs mechanism experimentally. This requires not only a precise measurement of the Higgs mass but also of the Higgs self-coupling λ . In the SM it holds $\lambda = \lambda' = m_H^2/(2v^2)$, which means that λ is directly related to the mass of the Higgs boson. The Higgs mass can be accurately measured at both hadron or lepton colliders. Information on the Higgs self-coupling are experimentally accessible through double Higgs production processes (section 2.3.1) and through triple Higgs production processes. However, the cross section of a triple Higgs production process is reduced by three orders of magnitude compared to double Higgs production processes [42]. The corresponding cross sections are very small, making a measurement at any collider experiment impossible. Consequently, it is crucial to measure the Higgs self-coupling λ very precisely in double Higgs production. Since the Higgs mass is very precisely measured at the LHC and v is known (section 2.2), an SM prediction of λ can be given as

$$\lambda \pm \delta\lambda = \frac{m_H^2}{2v^2} \pm \frac{\delta m_H}{v^2} m_H \sim 0.13 \pm 10^{-3}. \quad (2.37)$$

However, it needs to be investigated at particle colliders whether the then measured value is represented by this SM prediction. The shape of the Higgs potential is highly influenced by λ as shown in fig. 2.18 where the Higgs potential is shown for different values of λ .

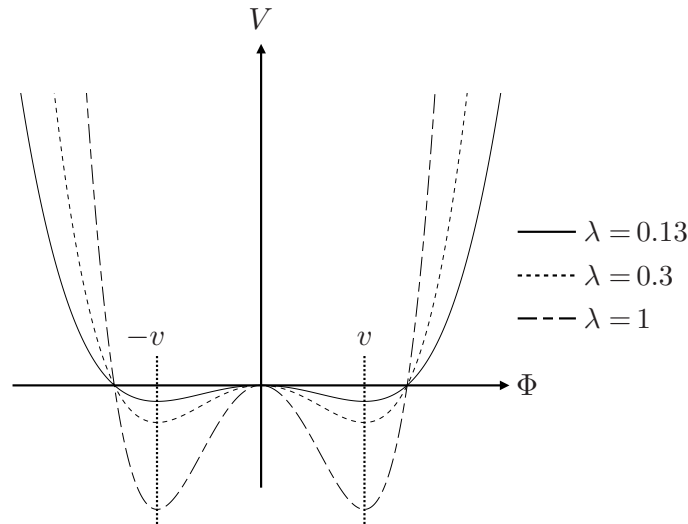


Figure 2.18: Higgs potential for different values of λ . For large values of λ (dashed line) the potential obtains much more pronounced minima. Opposed to this, for smaller values (dotted line) the depth of the minima decreases. Since the intersection with ϕ is always the same the different λ values result also in a broadening or narrowing of the distributions compared to the predicted shape. The solid line represents the SM case for $m_H = 125$ GeV and $v = 246$ GeV. Figure taken from [84].

The Higgs potentials intersect at the same value of ϕ . On the one hand, larger values of λ lead to more distinct minima and to a narrow potential. On the other hand, for smaller λ the minima flatten and the potential obtains a broadened shape.

2.5.1 Special Role of the Top Quark in the SM

The discovery of a Higgs boson with a mass of 125 GeV and so far no sign of BSM physics at collider experiments can indicate that new physics shows up only at high energies at Planck scale ($\Lambda \sim 10^{19}$ GeV). To investigate this scenario the effective Higgs potential $V_{eff}(\phi) = V(\phi) + \delta V(\phi)$ should be known up to very high values of ϕ . In the absence of new physics, it is crucial to investigate whether the Higgs potential can survive up to Planck scale. This is where the top quarks comes in. Being the heaviest known particle in the SM, the top quark couples most strongly to the Higgs field and could offer possible insight into new physics beyond the SM. In the SM, λ receives large quantum corrections as depicted in fig. 2.19. Here, the leading contribution to one-loop corrections to λ comes from the top and is defined by the second term of [85, 86]

$$\lambda \simeq \frac{3m_H^2}{v} \left(1 - \frac{N_c m_t^4}{3\pi^2 v^2 m_H^2} + \dots \right), \quad (2.38)$$

while the first term represents tree level. Since the top quark is a fermion its loop effect on λ is negative. The top-quark loop contributes a quartic term $\mathcal{O}(m_t^4)$ in one-loop corrections to

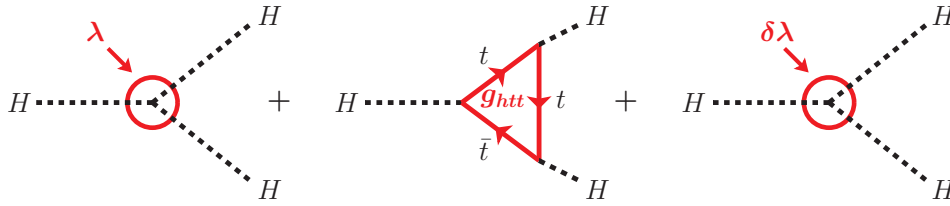


Figure 2.19: Tree-level double Higgs production vertex and quantum corrections to the trilinear Higgs self-coupling. Leading one-loop contributions come from the top, since it couples most strongly to the Higgs. An $O(m_t^4)$ term appears in the renormalised λ . Since λ is sensitive to loop effects of heavy particles new particles with similar properties could also contribute large corrections to the λ_{SM} prediction, denoted as effective change $\delta\lambda$.

the renormalised λ . Depending on the Higgs and top mass, λ has to be large enough at tree level to avoid being driven negative by the one-loop contributions of the top quark. Since λ and m_H are closely related on tree level (eq. 2.9) this leads to a lower bound on λ and m_H called vacuum stability bound. Both Higgs mass and top mass together provide constraints on the stability limit of the SM vacuum. For a Higgs boson with a mass of 125 GeV, the currently measured value of the top mass is too large to ensure absolute stability. Since the Higgs mass can be measured very precisely the leading uncertainty in this evaluation comes from the uncertainty in the top-mass measurement [87, 88]. The current value of the top mass predicts that λ becomes negative at $\sim 10^{11}$ GeV. This indicates that if the SM is valid at energies beyond 10^{11} GeV, the absolute stability of the SM vacuum up to Planck scale would be excluded at 95% C.L. considering $m_H = 125$ GeV. Opposed to this, $m_H = 126$ GeV would allow the stability of the vacuum at the same C.L. [88]. Consequently, precise measurements of the Higgs and top masses are important to test and to understand the fate of the SM. Due to its large impact on the Higgs sector, the top mass is one of the most sought after parameters concerning the evaluation of SM electroweak symmetry breaking. So far, the top quark has never been studied via electron-positron annihilation. However, the high energies available at the ILC offer a great opportunity to study top properties [89].

The quartic one-loop corrections to the trilinear Higgs self-coupling are a unique feature of the top quark. Loop effects of $\approx 10\%$ are expected [85]. On the contrary, the one-loop effective couplings of HVV ($V=W, Z$) obtain only power-like contributions of at most $O(m_t^2)$ from the top quark as [85, 86]

$$g_{HVV} \simeq \frac{2m_V^2}{v} \left(1 - \frac{5N_c m_t^2}{96\pi^2 v^2} + \dots \right). \quad (2.39)$$

In this case, loop effects of only $\approx 1\%$ are expected [85].

2.5.2 Indications of Physics Beyond the Standard Model

In general, new physics can reveal itself not only in direct searches but also in indirect searches represented by precision measurements of observables, which are well predicted by the SM. Similar to the top quark in the SM, new physics can affect the trilinear Higgs self-coupling. Since λ is sensitive to loop effects of heavy particles, new particles with similar non-decoupling properties as the top quark in the SM can also give large corrections to the λ prediction. If the loop particle is heavy it couples strongly to the Higgs and relatively large quantum corrections are expected. Hence, its impact on the Higgs self-coupling can become crucial. Non-decoupling effects of new heavy particles result in power-like contributions of their mass to the measured observable, which leads to large deviations from SM predictions. The decoupling theorem [90] does not hold if new particles receive their masses from the VEV of the Higgs field. In theories with extra heavy scalar fields for example, the Higgs self-coupling λ can receive large non-decoupling effects from loop contributions of extra Higgs bosons if their masses are mainly generated by the mechanism of electroweak symmetry breaking [85, 86, 91]. Large deviations between several 10 % and 100 % can easily appear.

Theory of Electroweak Baryogenesis

Models with extended Higgs sectors in which λ deviates significantly from SM predictions due to non-decoupling effects also exhibit a Higgs sector with strong first-order electroweak phase transition [91–97]. Within the framework of such models the theory of electroweak baryogenesis (EWBG) [71–73] can be valid, giving an explanation to the observed baryon asymmetry in the universe (sec. 2.4). EWBG includes a first-order electroweak phase transition [69, 70], which is required to explain the baryon asymmetry. Following [98], first and second order of electroweak phase transitions can be explained in the context of EWBG. The evolution of the Higgs potential $V(\phi)$ for first and second order phase transitions at different temperatures of the universe is illustrated in fig. 2.20.

Electroweak symmetry was broken down from $SU(2)_L \times U(1)_Y$ to $U(1)$ at high-temperature conditions of the early universe. During cool-down, spontaneous symmetry breaking was accomplished through a phase transition, which may have set the stage for generating the baryon asymmetry of the universe. As the universe cooled down, the vacuum became unstable at a critical temperature T_c and underwent a phase transition from the symmetric to the broken phase, in which the Higgs field received a non-zero VEV v . The latter determines the order of the phase transition. If the phase transition was second order the VEV would change continuously as we go from above to below T_c . ϕ developed a VEV as the temperature dropped below T_c and moved from fluctuating around zero to a non-zero value. During such a phase transition, thermal equilibrium is conserved which generally means that the system loses memory of its initial state. Therefore, no remnants from the unbroken phase are expected at $T < T_c$. In case of a first-order phase transition, the VEV would change discontinuously, which means that there have to be two energetically de-

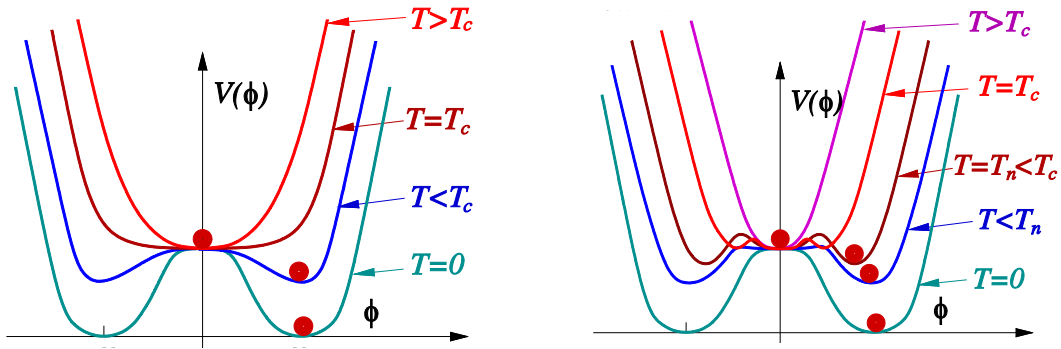


Figure 2.20: The evolution of ϕ for different temperatures of the universe. Left: second order phase transition, which evolves continuously in ϕ . Right: first order phase transition, in which the change in the VEV is discontinuous. Figures taken from [98].

generate phases separated by an energy barrier at T_c . At very high temperatures the global minimum of the effective Higgs potential is at $\phi = 0$. Close to T_c a second local minimum rises at $\phi \neq 0$. At T_c both minima ($\phi = 0, v_c$) become degenerate and result in the coexistence of the two phases. Here, v_c denotes the VEV of the Higgs at the critical temperature T_c . As the temperature drops further, $V(\phi)$ takes smaller values at the non-zero minimum. However, at $\phi = 0$, the field remains trapped at the origin although the second minimum is the energetically favoured state. Below a certain temperature T_n , the potential barrier becomes smaller and the probability for the field to tunnel to the true vacuum becomes larger than the expansion rate of the universe [98]. These so-called Higgs bubble walls separate the symmetric and broken phase. To preserve the generated baryon asymmetry, the condition

$$v_c/T_c \gtrsim 1 \quad (2.40)$$

has to be fulfilled for first-order phase transitions. Therefore, at high temperatures the Higgs potential has to be modified, i. e. by introducing new particles as heavy singlet scalars which strongly couple to the Higgs field. This ensures a strong first-order phase transition since additional quantum corrections of the new heavy particles increase the energy barrier between the broken and symmetric phase, and keep it large enough at the time of the phase transition, making it strongly first order.

The parameter region for EWBG in the SM is experimentally ruled out by the discovered Higgs boson with a mass of 125 GeV. Therefore, electroweak phase transition is of second order in the SM. Nevertheless, it can still be valid in theories which include BSM physics, two examples of which are given in the following.

Two Higgs Doublet Model (2HDM)

The simplest model with an extended Higgs sector in which the trilinear self-coupling of the lightest SM-like Higgs can deviate in the order of $\mathcal{O}(100\%)$ from the SM value is the Two Higgs Doublet Model (2HDM). Typically, in the 2HDM two Higgs doublet fields, H_1 and H_2 , lead to five Higgs bosons: the lightest Higgs boson (h) with mass m_h which is

regarded as the SM-like Higgs boson, two charged heavy (H^\pm) Higgs bosons, one heavy CP-odd (A) and one CP-even (H) Higgs boson. In the 2HDM, two sources give rise to the heavy Higgs boson masses: the VEV of the two Higgs fields $\sqrt{v_1^2 + v_2^2} = v \simeq 246$ GeV and the soft-breaking scale M . The physical masses of the extra scalar bosons read

$$m_{\phi_i}^2 = M^2 + \frac{\lambda_i v^2}{2}, \quad (2.41)$$

where ϕ_i denotes the heavy bosons H , H^\pm or A , and λ_i the coupling to the SM-like Higgs h as $\phi_i^\dagger \phi_i h h$. The origin of the mass determines the decoupling property of the heavy Higgs bosons. The one-loop contribution to the renormalised λ reads [86, 91]

$$\frac{\lambda_{2HDM}}{\lambda_{SM}} \simeq 1 + \frac{1}{12\pi^2 m_h^2 v^2} \left(m_{H^0}^4 \left(1 - \frac{M^2}{m_{H^0}^2} \right)^3 + m_{A^0}^4 \left(1 - \frac{M^2}{m_{A^0}^2} \right)^3 + 2m_{H^\pm}^4 \left(1 - \frac{M^2}{m_{H^\pm}^2} \right)^3 \right). \quad (2.42)$$

If the masses are predominantly generated by v ($M^2 \lesssim \lambda_i v^2$) the loop contribution to λ does not decouple and positive quartic $m_{\phi_i}^4$ contributions to λ are expected as

$$\frac{\lambda_{2HDM}}{\lambda_{SM}} \simeq 1 + \frac{1}{12\pi^2 m_h^2 v^2} \left(m_{H^0}^4 + m_{A^0}^4 + 2m_{H^\pm}^4 \right). \quad (2.43)$$

The non-decoupling effect is maximal at $M = 0$. If the masses of the heavy Higgs bosons are largely given by the gauge invariant mass term $M^2 \gg \lambda_i v^2$, the power-like contributions disappear. Hence, one-loop effects vanish in the large- M limit according to the decoupling theorem as

$$\frac{\lambda_{2HDM}}{\lambda_{SM}} \simeq 1 + \frac{v^2}{96\pi^2 m_h^2} \left(\lambda_{H^0}^3 + \lambda_{A^0}^3 + 2\lambda_{H^\pm}^3 \right) \left(\frac{v^2}{M^2} \right). \quad (2.44)$$

Consequently, if $m_{\phi_i}^2 > m_h^2$ large corrections due to non-decoupling effects of additional heavy bosons are expected.

EWBG is possible within the 2HDM [99–101]. The 2HDM is compatible with $m_H = 125$ GeV for the light SM-like Higgs by making use of loop-effects of the four additional heavy scalar Higgs bosons and exhibits a strong first-order electroweak phase transition. Additionally, it allows for CP-violating phases which are also required for a successful scenario of EWBG (sec. 2.4) [68]. In fig. 2.21, the expected deviations from λ_{SM} for a light SM-like Higgs of $m_h = 120$ GeV in the (M, m_{ϕ_i}) -plane are depicted. The necessary condition for EWBG (eq. 2.40) is indicated. The phase transition is strong enough first order for $m_{\phi_i} \gtrsim 200$ GeV. The deviation of λ is larger than 10% in the parameter region in which EWBG is possible [91]. For larger M even larger m_{ϕ_i} are required for a successful scenario of EWBG. Deviations of λ_{SM} can be $O(100\%)$ in the 2HDM if the masses of the extra scalar Higgs bosons are $m_{\phi_i} \simeq 400$ GeV and $M \simeq 0$. This example corresponds to the maximal non-decoupling effect ($M = 0$).

The given examples indicate that a precise measurement of the trilinear Higgs self-coupling can directly reveal the nature of extended Higgs sectors. The trilinear Higgs self-coupling

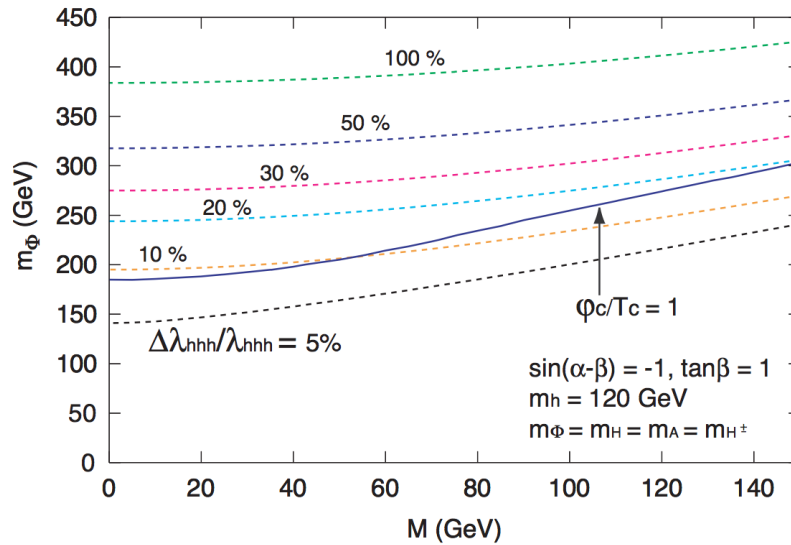


Figure 2.21: Deviation of the trilinear Higgs self-coupling from SM prediction in the 2HDM. For $m_\phi > 200$ GeV EWBG is possible through first-order phase transitions (eq. 2.40). m_ϕ represents the mass of the additional Higgs bosons and M the soft-breaking scale. Depending on m_ϕ and M , large quantum effects of the additional Higgs bosons result in deviations of the trilinear Higgs self-coupling between 10% and 100% from the SM in the parameter region where EWBG is possible. Figure taken from [91].

is one of the most important discriminative quantities to reveal new physics models [106]. First of all, double Higgs production needs to be observed to establish a non-zero trilinear Higgs self-coupling, which can be done at hadron or lepton colliders. It is shown that a precision of at least 20% is required to see deviations from the SM. For example, in the parameter region of the 2HDM in which EWBG is possible, a minimal deviation of 20% from the SM value is expected as shown in fig. 2.22 [7]. In this example, λ could even be twice as high as in the SM. Therefore, we should keep in mind that if we do not live in an SM but a SUSY world we will observe a trilinear Higgs self-coupling larger or smaller than the expected SM value, which results in enhanced or decreased measurement precisions in collider experiments, depending on the sensitivity of double Higgs production processes to λ . A precise measurement of the trilinear Higgs self-coupling at a collider experiment can be an important probe of such a cosmological scenario as EWBG.

Models with fourth-generation fermions

Alternatively, new physics models with a sequential fourth generation of fermions predict large one-loop contributions to the Higgs self-coupling [102]. A fourth generation of fermions in the SM could enhance the theory of EWBG. A fourth fermion generation introduces additional CP-violating phases to the CKM quark mixing matrix, which also favours EWBG. Additionally, it is shown, that SUSY models with four SM fermion generations [103, 104] allow strong first-order phase transitions [105]. Moreover, a fourth-

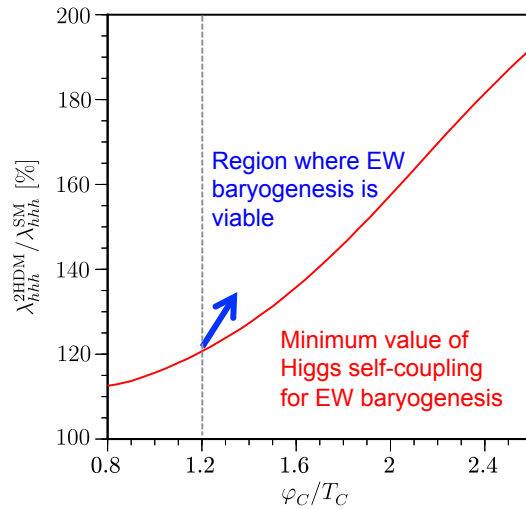


Figure 2.22: In the theory of electroweak baryogenesis in the framework of the 2HDM minimal deviations of 20% from SM predictions are expected. In this example, the Higgs self-coupling could even be twice as high as in the SM. Figure taken from [7].

generation neutrino can contribute to the dark matter density of the universe. Hence, such models can solve various unanswered questions in particle physics (sec. 2.4). In the model with fourth-generation fermions, one-loop corrections to the Higgs self-coupling can result in a deviation from the SM value by more than $O(100\%)$ [106].

2.5.3 Sensitivity of the Higgs Self-coupling

As shown in the foregoing, Higgs-pair production plays a key role not only as production process which is sensitive to λ . By discovering deviations from its SM value, it provides indirect possibilities for probing new physics scenarios and the existence of new heavy particles. Either at lepton or hadron colliders, the SM cross sections for double Higgs production are very small (sec. 2.3.1) and unless new physics produces sizeable enhancements, the measurement of λ is quite challenging. Moreover, not all diagrams in each production process include the Higgs self-coupling vertex (sec. 2.3.1). These additional diagrams degrade the sensitivity of the production cross section to λ .

Sensitivity of λ in the main Production Channels at Hadron Colliders

The sensitivity of SM Higgs-pair production cross sections to the trilinear Higgs self-coupling at hadron colliders is illustrated in fig. 2.23. The left figure shows the total cross section σ as a function of a non-SM λ , which varies in units of λ_{SM} . The right figure illustrates the measurement accuracies on the cross sections which are required to be able to extract λ from double Higgs measurements at the LHC at 14 TeV. In fig. 2.23, it is obvious that σ becomes significantly larger for smaller values of λ . Hence, for theories in which

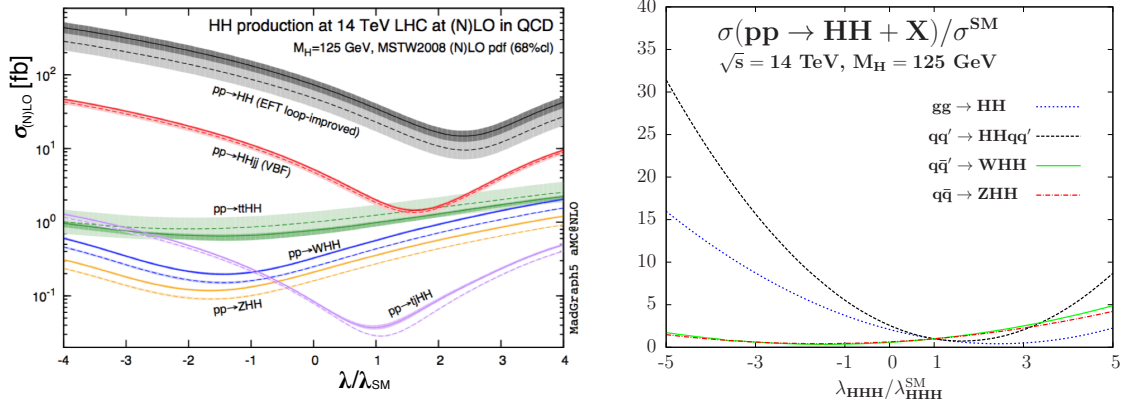


Figure 2.23: Left: total cross sections of the dominant Higgs-pair productions as a function of λ in pp collisions at leading order (LO) and next-to-leading order (NLO) QCD for the LHC at $\sqrt{s} = 14$ TeV. The LO results are illustrated by the dashed and light-coloured bands. The NLO results are represented by the solid dark-coloured bands. The SM cross sections are obtained for $\lambda/\lambda_{SM} = 1$. Figure taken from [37]. Right: the ratios σ/σ_{SM} as a function of λ/λ_{SM} for the dominant Higgs-pair production cross sections are shown for the LHC at 14 TeV. Figure taken from [107].

we expect $\lambda < \lambda_{SM}$ it is possible to observe double Higgs production at hadron colliders and test the Higgs potential. For the case with $\lambda = 0$, the Higgs self-coupling amplitudes vanish. Then, the cross section is enhanced by approximately a factor of 2 compared to the SM case ($\lambda/\lambda_{SM} = 1$). For $\lambda > \lambda_{SM}$ the dominant Higgs-pair production cross sections decrease. Although the cross sections of the three dominant Higgs-pair production mechanisms increase to larger centre-of-mass energies (sec. 2.3.1), the diagrams involving the trilinear Higgs self-coupling are mediated by s -channel propagators, which get suppressed with increasing energy. Despite the increasing SM cross sections the additional diagrams in the respective double Higgs production process become dominant. Therefore, at high centre-of-mass energies as 14 TeV the relative importance of the Higgs self-coupling diagram is suppressed with respect to the other diagrams. At leading order in gluon fusion only one diagram concerns λ . The relative minus sign between those two diagrams results in destructive interference and the total SM cross section is effectively reduced. Studies show [107] that for example the cross section of gluon fusion has to be measured to 50 % precision at $\sqrt{s} = 8$ TeV to be able to extract the Higgs self-coupling with an accuracy of 50 %. To reach the same accuracy on the Higgs self-coupling at $\sqrt{s} = 14$ TeV, the gluon fusion cross section has to be measured to a precision of approximately 40 %. The gluon fusion cross section obtains its minimum at $\lambda \sim 2.5\lambda_{SM}$.

Sensitivity of λ in the main Production Channels in e^+e^- Collisions

At e^+e^- colliders, in both ZHH and WW fusion the additional diagrams degrade the Higgs self-coupling sensitivity. Due to these additional diagrams the cross section σ can be

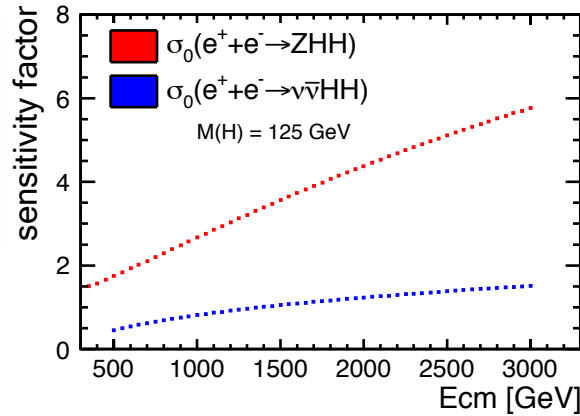


Figure 2.24: Sensitivity factor of the Higgs self-coupling as a function of the centre-of-mass energy for $m_H = 125$ GeV. Figure taken from [110].

expressed as a function of the Higgs self-coupling λ [108]

$$\sigma(\lambda) = a\lambda^2 + b\lambda + c, \quad (2.45)$$

where a denotes a constant originating from the Higgs self-coupling diagram, b from the interference between the additional diagrams and the Higgs self-coupling diagram, and c from the additional diagrams. The precision on λ is related to the measurement accuracy of the double Higgs production cross section σ times a sensitivity factor F and reads

$$\frac{\Delta\lambda}{\lambda} = F \cdot \frac{\Delta\sigma}{\sigma}. \quad (2.46)$$

Without the additional diagrams the sensitivity factor would always be 0.5. In figure 2.24 the sensitivity factor is shown as a function of the centre-of-mass energy \sqrt{s} . It reveals a decreasing coupling sensitivity to larger \sqrt{s} . This is expected as the diagrams involving λ are mediated by s -channel propagators which get suppressed to increasing energy with respect to the remaining other diagrams [109]. Hence, these diagrams become more dominant at higher energies. We have to keep in mind that the ZHH cross section decreases to higher energies (fig. 2.9), which also results in decreasing measurement accuracies of the Higgs-pair production cross section. At $\sqrt{s} = 500$ GeV, the sensitivity factor for $m_H = 125$ GeV for double Higgs-strahlung reads $F = 1.73$ and for WW fusion at $\sqrt{s} = 1$ TeV this factor is $F = 0.8$.

The sensitivity to the trilinear Higgs self-coupling is very large just above the kinematical threshold for Higgs-pair production. Near the threshold the propagator of the intermediate virtual Higgs boson connecting to the two real Higgs bosons through λ is maximal. Therefore, the Higgs self-coupling diagram gives the largest contribution to the total cross section at values of the invariant mass m_{HH} not far from the corresponding energy threshold. By weighting events with respect to m_{HH} the sensitivity factor can be improved to

$$\frac{\Delta\lambda}{\lambda} = 1.62 \cdot \frac{\Delta\sigma}{\sigma}, \quad (2.47)$$

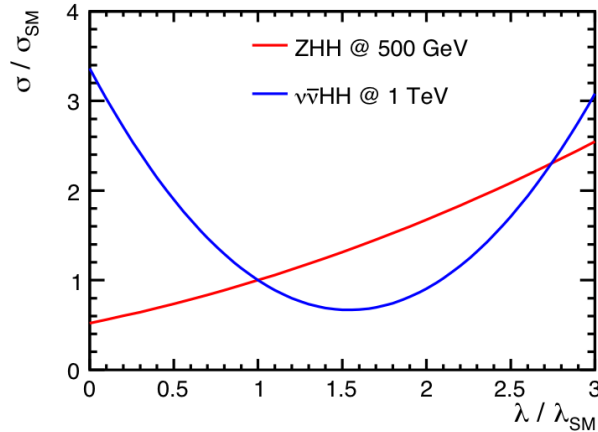


Figure 2.25: Precision of production cross sections for WW fusion and double Higgs-strahlung as function of λ normalised to λ_{SM} . Both, smaller and larger values of λ compared to the SM prediction can be observed at e^+e^- colliders, depending on the available energies at such collider experiments. Figure taken from [111].

for double Higgs-strahlung and to

$$\frac{\Delta\lambda}{\lambda} = 0.73 \cdot \frac{\Delta\sigma}{\sigma}, \quad (2.48)$$

for WW fusion at the respective centre-of-mass energies. Further information on the weighting method based on m_{HH} can be found in [110]. Moreover, both double Higgs production mechanisms are complementary in their sensitivity to new physics due to the sign of interference terms of the additional diagrams. Thus, double Higgs-strahlung and WW fusion behave differently with respect to changes in λ . The precision on the production cross sections as a function of λ normalised to λ_{SM} is depicted in figure 2.25. Higgs self-coupling values of $\lambda < \lambda_{SM}$ can be observed best in WW fusion. Since WW fusion is the dominant process around $\sqrt{s} = 1$ TeV high centre-of-mass energies are required to observe such scenarios. Opposed to this, double Higgs-strahlung events provide measurements of new-physics scenarios with $\lambda > \lambda_{SM}$. In scenarios with EWBG, the expected deviation of the Higgs self-coupling is $\lambda > 1.2\lambda_{SM}$. Scenarios as EWBG in the 2HDM can be observed at e^+e^- colliders with double Higgs-strahlung already at 500 GeV to high precision due to the larger cross sections at the respective λ .

2.5.4 Measurement Prospects of the HL-LHC

The LHC provides high centre-of-mass energies and luminosities which are necessary since large data sets are needed to be sensitive to the measurement. However, as stated in the foregoing, for increasing energies the Higgs self-coupling diagram is suppressed and the cross sections are dominated by additional diagrams. Therefore, it is difficult to

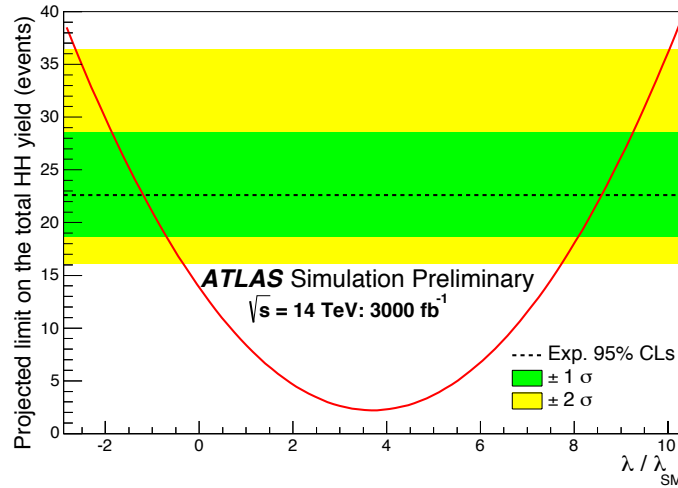


Figure 2.26: ATLAS expected limits on the size of additional contributions added to the expected SM results, overlaid on the number of predicted total Higgs-pair events as a function of λ/λ_{SM} for $\sqrt{s} = 14$ TeV and $\mathcal{L} = 3000 \text{ fb}^{-1}$. The limit on the total number of double Higgs events and $\pm 1\sigma$, 2σ uncertainties are shown. Figure taken from [115].

discover double Higgs production and to observe λ . If $\lambda > \lambda_{SM}$ the sensitivity worsens due to destructive interference of diagrams. For $\lambda < \lambda_{SM}$ the sensitivity increases and there is a chance to observe double Higgs production and extract information on the trilinear Higgs self-coupling. Nevertheless, the small number of signal events needs to be separated from large QCD backgrounds.

Several ATLAS and CMS studies have evaluated the prospects of the high-luminosity (HL) LHC for $\sqrt{s} = 14$ TeV and $\mathcal{L} = 3000 \text{ fb}^{-1}$ for a 125 GeV Higgs boson. Gluon fusion represents the most promising process with an NNLO cross section of $\sigma_{NNLO} = 40.7 \text{ fb}$ at 14 TeV [112]. Theoretical studies [113, 114] generally state larger signal significances, i. e. $\sim 2.3\sigma$ for $HH \rightarrow bb\gamma\gamma$, than most recent evaluations of ATLAS [115, 116] and CMS [117] which find that double Higgs production can be measured with considerably lower significance. The discrepancy arises from the more realistic background estimation, which includes a reliable estimate of fake rates of light jets faking photons or b jets. These investigations include three different search channels $bbWW$, $bb\tau\tau$, and $bb\gamma\gamma$. In all studies the triggers are assumed to be 100% efficient. The analysis of $bbWW$ is based on a fast detector simulation while the $bb\gamma\gamma$ analysis uses MC truth information with four-vector smearing to obtain more realistic results. $bb\tau\tau$ is analysed with a combination of both approaches. Especially $bb\gamma\gamma$ and $bb\tau\tau$ give promising results. For $bb\gamma\gamma$, the expected signal uncertainty is about 67% giving a signal significance of 1.3σ . For $bb\tau\tau$ the signal uncertainty is roughly 105% with 0.9σ signal significance. For ATLAS and CMS, combining $bb\gamma\gamma$ and $bb\tau\tau$ gives a significance for Higgs-pair production of 1.9σ . The expected uncertainty on the signal yield is about 54%. Additionally, exclusion limits on λ/λ_{SM} with regard to BSM models are presented. Therefore, an SM cross section and λ_{SM} are assumed. The 95% C.L. upper limit on the total number of double Higgs events

for $\lambda = \lambda_{SM}$ is compared to the expected number of signal events for different λ . The ATLAS expected limits on the size of additional contributions to the expected SM Higgs-pair events, which are overlaid on the number of total double Higgs events, are depicted in figure 2.26 as a function of λ/λ_{SM} . The projections indicate that at 95% C.L. BSM models with $\lambda/\lambda_{SM} \leq -1.3$ and $\lambda/\lambda_{SM} \geq 8.7$ can be excluded at the HL-LHC.

2.5.5 Linear Collider Studies

At linear e^+e^- colliders Higgs-strahlung and WW fusion provide direct access to λ . Combined with very small signal production cross sections and multi-jet final states, the measurement places many challenges to the detectors and the event reconstruction. At 500 GeV information on the coupling can be extracted from a cross-section measurement of double Higgs-strahlung. An energy upgrade to 1 TeV would offer complementary capabilities for the observation of double Higgs production and the Higgs self-coupling measurement, giving access to WW fusion. Over the last years many studies have been investigating the capabilities of measuring the Higgs self-coupling using ZHH and WW fusion at e^+e^- linear colliders [118–123]. All evaluations are based on a Higgs mass of 120 GeV and apply fast detector simulations, except for [123]. Since this thesis is based on a cross-section measurement of ZHH at $\sqrt{s} = 500$ GeV a brief discussion of studies using the same production process is given in the following.

Limits on the first Fast Monte Carlo (MC) Simulations

The first ZHH analyses [118, 119] were performed with fast MC simulations. Several assumptions were made in the fast simulation which limit the realistic view on the results: (1) all visible particles were perfectly reconstructed and used to form the signal final states; (2) the clustered jets were smeared to simulate a given jet-energy resolution; (3) gluon radiation, which generally is a fundamental component in a multi-jet event, was neglected in the event generation. The probability of a quark to emit a gluon, which causes an additional jet in the event, is about 10%. By neglecting gluon radiation, the events are much less affected by confusion and combinatorics problems in reconstruction. Both studies were performed for $\sqrt{s} = 500$ GeV and $\mathcal{L} = 2 \text{ ab}^{-1}$, assuming a jet-energy resolution of $30\%/\sqrt{E}$. In [118], a precision on σ_{ZHH} of 10% was achieved, which corresponds to a resolution of 18% on λ . In [119], σ_{ZHH} was determined to a precision of 20%, which led to a precision of 35% on λ . Next to different event selections, the results of the analyses rely on the examined ZHH decay modes. While [119] studied only the six-jet final state with $H \rightarrow b\bar{b}$, in [118] the full branching ratio of the Z boson was used. Additionally, the implemented vertex reconstruction was different: a parametrisation in [118] and a realistic reconstruction in [119]. Both aspects explain the different results of the two analyses. Moreover, both studies stressed the importance of achieving good jet-energy resolution for an efficient signal selection. In fig. 2.27 the effect of including gluon radiation in the event generation is illustrated. For a jet-energy resolution of $30\%/\sqrt{E}$, the precision on

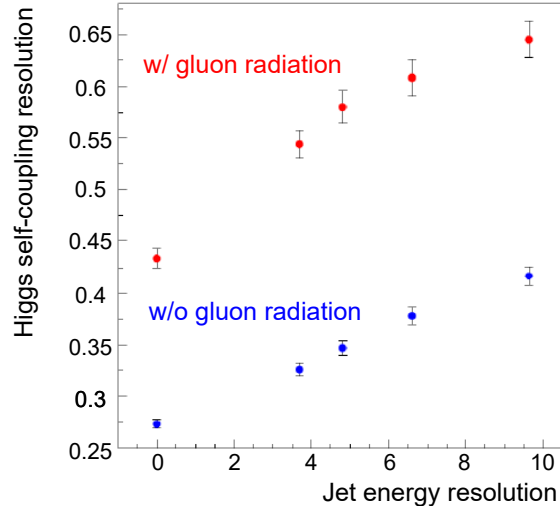


Figure 2.27: Precision on the Higgs self-coupling as a function of the jet-energy resolution without and with gluon radiation considered. The results have been obtained in a fast detector simulation [119]. Figure taken from [124].

the Higgs self-coupling decreases from 32% to 54% [119]. Hence, the resolution on the Higgs self-coupling worsens by a factor of 2 when considering gluon radiation in the event generation. Therefore, this effect cannot be neglected in a realistic simulation.

Limits on the first Full Simulation

The first full simulation was performed in [123] for $\sqrt{s} = 500$ GeV and $\mathcal{L} = 500$ fb⁻¹. The six-jet channel $ZHH \rightarrow qqbbbb$ was studied since it gives the largest contribution to the total ZHH cross section. A precision of 180% on the cross section was achieved. In this analysis, flavour tagging of heavy quarks played a crucial role. It was indicated that by improving the flavour-tag performance, the resolution on the cross section gives potential improvement to roughly 95%. To compare these results with the previous fast simulations, one has to scale the results with respect to the degrading effects due to gluon emission, the different luminosities used in the analyses, and the evaluated Z -boson decay modes. Considering all channels ($Z \rightarrow ll, \nu\nu, qq$) could also enhance the measurement precision. Especially $Z \rightarrow ll$, since it results in a much cleaner environment despite contributing smallest to the total cross section. Taking these effects into account, the resolutions on the cross sections, which were achieved in the fast simulations, read 80% for [119] and 60% for [118] for $\mathcal{L} = 500$ fb⁻¹. These results are much closer to the 95% obtained in the first full simulation, assuming an improved vertex reconstruction. The remaining difference is due to detector simulation models and particle reconstruction. However, to find evidence of double Higgs production an improvement of at least a factor of 3 is required. Several aspects were discussed which could enhance the sensitivity: (1) higher luminosities are

needed. Then, 180% precision on the cross section corresponds to roughly 90% precision for $\mathcal{L} = 2 \text{ ab}^{-1}$. (2) A better reconstruction of jets and vertices. (3) Improvements of the flavour-tag performance. This highly depends on the design of the vertex detector. The flavour-tagging software should be optimised for six-jet final states instead of two-jet final states. (4) A more detailed full detector simulation model is needed.

Most recent Full Detector Simulation for ILC

Based on a full detector simulation with a very detailed ILC detector model and by using new flavour-tagging software, an analysis was performed for all Z decay modes ($ll, \nu\nu, qq$) with $HH \rightarrow bbbb$. The analysis strategy can be found in [108] and serves as guideline for this thesis. The analysis was performed for $m_H = 120 \text{ GeV}$. This latest DBD full simulation could achieve 27% precision on σ_{ZHH} at $\sqrt{s} = 500 \text{ GeV}$, assuming $\mathcal{L} = 2 \text{ ab}^{-1}$, which led to a precision of 44% on λ . Additional analyses of ZHH focus on the signal final state $HH \rightarrow bbWW$ [125]. Combining the different channels a relative improvement of 20% is expected. Several potential areas for improvement were suggested, which offer an expected relative improvement of 20% on the Higgs self-coupling precision: the flavour-tag performance and the isolated lepton selection are crucial to reconstruct the final states of the different decay channels. Both require very high efficiencies and purities. A large degradation is caused by the mis-clustering of particles into jets. Advanced jet-clustering algorithms are required. The mass reconstruction is crucial to improve the signal and background separation. Mis-clustering of jets and wrong jet pairing degrade the mass resolution. Moreover, optimising the analysis for the Higgs self-coupling diagram could reduce the impact of the additional ZHH diagrams.

Motivation for an updated Full Detector Simulation

Evidently, the Higgs self-coupling measurement is very challenging. Regarding the LHC results, a full detector simulation needs to be performed with a more realistic setup for a Higgs boson with a mass of 125 GeV. This includes the investigation of ILC machine backgrounds (sec. 3.4.2), which have not been considered so far. The effects on the analysis need to be studied. Additionally, the various starting points for improvement need to be investigated. One possibility is the application of kinematic fits, which are a tool to improve the jet-energy and invariant mass resolution.

Compared to a Higgs mass of 120 GeV, for $m_H = 125 \text{ GeV}$ the ZHH production cross section is reduced by roughly 15%. The branching ratio $\text{BR}(H \rightarrow b\bar{b})$ also drops by approximately 14% from 65.7% to 57.8%. As a consequence, an even smaller number of signal events is overwhelmed by the same amount of background events. By extrapolating the results in [108] to a Higgs mass of 125 GeV a precision of roughly 33% on the cross-section measurement of double Higgs-strahlung and of roughly 53% on the Higgs self-coupling measurement are expected. The extrapolation includes only the changes in

branching ratio and cross section, and is therefore quite optimistic. The effects of changes in kinematic distributions are not taken into account. They degrade the expected precisions at a centre-of-mass energy of 500 GeV. For a Higgs boson with a mass of 125 GeV the jets are even less boosted and thus have significant overlap. This degrades the performance of analysis techniques, i. e. jet-clustering algorithms or flavour tagging. The extrapolation has to be confirmed by the detailed full simulation.

Chapter 3

The International Linear Collider and Experimental Environment

In this chapter, an introduction to the International Linear Collider (ILC) and its experimental environment is given. In sec. 3.1, the reasons for a linear lepton collider are discussed. Subsequently in sec. 3.2 an overview of the ILC project is given. This is followed by the introduction of the ILC running scenario in sec. 3.3. The experimental environment is discussed in sec. 3.4. Herein, the ILC beam parameters and the resulting backgrounds from beam-beam interactions are introduced, which arise from the strong focussing of the beams at the interaction point. This is followed by an overview on the ILC accelerator design given in sec. 3.5. A detailed description of the accelerator and its subsystems can be found in the different volumes of the Technical Design Report (TDR) [126–130].

3.1 Reasons for an e^+e^- Linear Collider

In the history of particle physics lepton colliders contributed essentially to the verification of the SM, e. g. the gluon discovery at PETRA [131, 132] or precise measurements of the Z boson at LEP and SLC [133]. A valuable interplay between lepton and hadron colliders was present, e. g. in the top discovery and exclusion limits in the Higgs search (sec. 2.3.3). The top mass was predicted by LEP experiments from quantum corrections in electroweak processes and was finally discovered in the predicted energy range at Tevatron. In turn the top discovery allowed constraints on the Higgs mass from electroweak measurements at LEP (sec. 2.3.3). Now after the Higgs discovery a lepton collider with sufficient energy would give a perfect complement to the LHC to perform precision measurements.

3.1.1 Experimental Features of Lepton Colliders

Four advantages of e^+e^- colliders make them ideal for precision measurements and offer discovery potential for signatures which are not detectable at hadron colliders [127]:

Detail Due to the collision of two elementary particles, e^+e^- colliders have a well-defined centre-of-mass energy $\sqrt{s} = 2E_{beam}$. The problem of not knowing the initial kinematic configuration is not relevant and allows the use of full kinematic information from the events in the reconstruction, e. g. the application of kinematic fits. Opposed to this, at pp colliders the exact kinematic configuration of each collision is unknown since two composite particles collide. The centre-of-mass energy is not equally distributed among quarks and gluons. Moreover, the e^+e^- beams can be highly polarised which offers a promising approach for spin measurements.

Cleanliness The multiplicity of processes produced in e^+e^- annihilation are much lower compared to hadron collisions. The machine background is dominated by $\gamma\gamma$ collisions having a cross section six orders of magnitude smaller than backgrounds at the LHC. This leads to controllable backgrounds even for the high luminosities. This cleaner environment simplifies event reconstruction.

Calculability In e^+e^- collisions all processes proceed via weak interactions. First order corrections to cross sections can be easily calculated and are expected to be in the order of a few %. This improves the theoretical uncertainty on the predicted cross sections. The enhanced theoretical and experimental precisions make e^+e^- colliders sensitive even to only small quantum corrections to cross sections. This allows to observe new physics even if it is out of the direct kinematic reach.

Democracy At e^+e^- colliders the couplings of the Z boson and photon to all other particles are of the same size and the production rates are only limited by the phase space of the reaction. Despite the generally small cross sections, there is no large hierarchy between SM and BSM physics. Therefore, no triggers are needed and a continuous readout can be used. Moreover, all final states of decaying particles can be used for physics analyses, which gives the opportunity to measure absolute branching ratios and total widths and allows to identify hadronic W and Z decays.

3.1.2 Advantages of Linear Colliders

In contrast to the circulating massive protons, using electrons and positrons as beam particles in a circular collider leads to the problem of significant energy loss due to synchrotron radiation. Synchrotron radiation occurs when relativistic particles move through a magnetic field which forces them on a circular trajectory. At high energies, leptons are highly relativistic due to their small masses and the radiated photons represent a considerable energy loss [27]. In a circular collider the energy loss rises as

$$\Delta E \propto \frac{E_{beam}^4}{rm^4}, \quad (3.1)$$

where E_{beam} denotes the beam energy, r the bending radius, and m the mass of the circulating particles. There are two options to compensate the energy loss: either the bending

radius is increased as indicated in eq. 3.1, or additional acceleration modules are installed. Both possibilities lead to an increase in costs. For circular colliders cost optimisations show a quadratic growth in costs with beam energy [134]. Applying eq. 3.1 to a linear collider with $r \rightarrow \infty$ we obtain $\Delta E \rightarrow 0$. Hardly any synchrotron radiation is present. However, at linear colliders many acceleration modules have to be installed to achieve high beam energies since the beams pass through the acceleration only once. The number of acceleration modules to achieve the desired beam energies, and therefore the costs, are linearly proportional to the length of the accelerator [134]. Beyond beam energies of 200 GeV linear colliders are more budget-friendly than circular machines [134].

On the whole, the advantages of lepton colliders without the drawback of radiation losses, which can be solved by guiding the beam particles along straight lines, are brought together in the concept of a linear lepton collider. Since it provides high precisions and exactly known initial-state conditions, it is able to precisely measure particle properties and new physics effects and therefore, is a logical complement to the LHC.

3.2 The International Linear Collider Project

Nowadays, the ILC is the only high-energy accelerator for the post-LHC era which moved to the engineering stage. The ILC is one of the largest next generation collider projects. It is planned as a complement to the LHC to perform precision measurements of known and possibly new particles. Japan shows great interest in hosting the ILC and started reviews on the project. In geological evaluations the Kitakami mountain region in the north of the Japanese main island was selected as candidate site. In 2014, the Japanese Ministry for Education, Culture, Sports, Science and Technology (MEXT) initiated an expert committee which investigates various issues regarding the ILC raised by the Science Council of Japan. The ILC expert committee is divided in three subcommittees. The first subcommittee for particle and nuclear physics investigates the ILC physics case. The second subcommittee evaluates costs and technical feasibility, as it is described in the TDR. The TDR was published in 2012 and consists of five volumes containing a realistic technical design and implementation plan, including physics studies, accelerator technologies, detector concepts, and engineering studies [126–130]. The third subcommittee focusses on human resources. The outcome of this process is extremely important since it guides the Japanese government to the decision whether or not it will officially bid to host the ILC.

3.3 ILC Operating Scenario

In its first stage the ILC can be operated at centre-of-mass energies up to 500 GeV. Several running scenarios have been studied and evaluated by their impact on the physics programme, especially the evolution of the physics output with time. These investigations are based on extrapolations of the physics results published in [127]. At the ILC, the

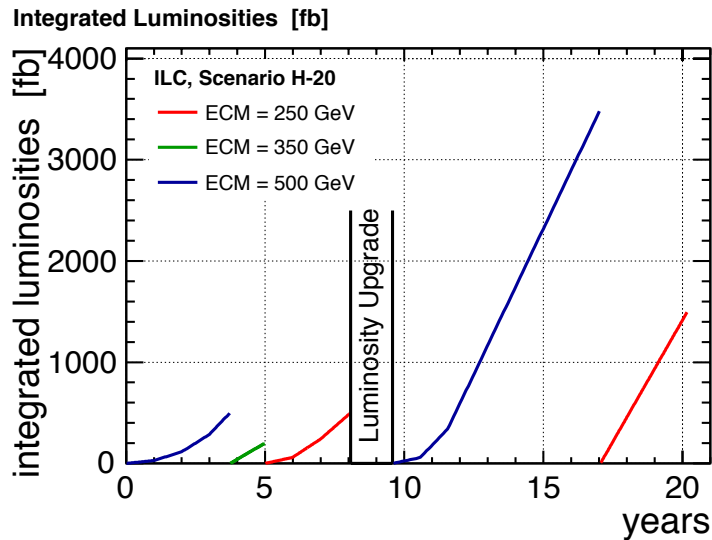


Figure 3.1: Timeline of the preferred ILC operation scenario, which was evaluated using extrapolations of the physics results in [127]. The integrated luminosity is illustrated as a function of ILC calendar years for each running energy, respectively. An ILC calendar year includes eight months of running at an efficiency of 75%. Figure taken from [136].

most important role in the physics programme take direct and model-independent precision measurements of Higgs boson properties, the top quark, as well as direct searches for BSM physics. The complete ILC physics programme and detailed analyses descriptions can be found in the TDR physics volume [127].

Different scenarios were studied for 20 years of operation, after which a potential upgrade to 1 TeV or other running energies is considered. It should be noted that the actual detailed running scenario and the best combination of dataset sizes will follow physics results from the LHC or even from the early operating ILC. The recommended running scenario based on current knowledge is illustrated in fig. 3.1. The corresponding information are listed in tab. 3.1. The updated physics results corresponding to the recommended operation scenario of the ILC PARAMETERS JOINT WORKING GROUP can be found in [135]. More details and alternative scenarios can be found in the respective document [136].

In the initial phase, starting at the full energy of 500 GeV the ILC would accumulate 500 fb^{-1} of data, before collecting 200 fb^{-1} at 350 GeV and 500 fb^{-1} at 250 GeV. Running at $\sqrt{s} = 500 \text{ GeV}$ is beneficial for early Higgs precision measurements since the precisions on most of the Higgs couplings are limited by the coupling g_{HWW} , which becomes accessible at $\sqrt{s} \geq 350 \text{ GeV}$. An energy threshold scan at $\sqrt{s} = 350 \text{ GeV}$ provides a measurement of the top-quark mass. Here, 200 fb^{-1} are sufficient to improve theoretical uncertainties and to run at different polarisations. At 250 GeV Higgs-strahlung is the dominant Higgs production and benefits from the well-known properties of the Z boson. These allow searching and reconstructing Higgs events completely model-independent by measuring the recoil mass from the Z-decay products [137]. Since no Higgs recon-

Stage	ILC500			ILC500 LumiUP		
\sqrt{s} [GeV]	500	350	250	500	350	250
\mathcal{L} [fb^{-1}]	500	200	500	3500	-	1500
time [a]	3.7	1.3	3.1	7.5	-	3.1

Table 3.1: Energy stages of the preferred running scenario, the final integrated luminosities and real time of each energy stage. Table taken from [136].

		(-,+)	(+,-)	(-,-)	(+,+)
250 GeV	fraction [%]	67.5	22.5	5	5
	\mathcal{L} [fb^{-1}]	1350	450	100	100
350 GeV	fraction [%]	67.5	22.5	5	5
	\mathcal{L} [fb^{-1}]	135	45	10	10
500 GeV	fraction [%]	40	40	10	10
	\mathcal{L} [fb^{-1}]	1600	1600	400	400

Table 3.2: Helicity configurations $\text{sgn}(P(e^-); P(e^+))$ for each centre-of-mass energy, and the collected integrated luminosity per beam helicity configuration [136].

struction is required the recoil mass technique is the key to a fully model-independent reconstruction of the Higgs sector and provides high precision measurements of g_{HZZ} and σ_{HZ} . The initial programme requires approximately 8 years of running and is followed by a luminosity upgrade. The respective shut down takes 18 months. Additional 3500 fb^{-1} would be collected at 500 GeV, before returning to 250 GeV with additional 1500 fb^{-1} of data after the upgrade. The additional luminosity taken at 500 GeV concerns enhanced measurement precisions of the top-Yukawa coupling and the Higgs self-coupling measurement. The complete running scenario takes 20 years. In total, an integrated luminosity of 4000 fb^{-1} at 500 GeV, 200 fb^{-1} at 350 GeV, and 2000 fb^{-1} at 250 GeV is foreseen.

Additionally, the advantage of using polarised e^+e^- beams affects the potential reach of measurement precisions. At the various \sqrt{s} data taking is proposed to be shared between different helicity configurations of the foreseen beam polarisations of $|P(e^-)| = 80\%$ and $|P(e^+)| = 30\%$. The relative sharing between different helicity configurations for each energy stage and the correspondingly collected integrated luminosities are listed in tab. 3.2. At smaller \sqrt{s} the physics programme covers mainly SM processes. Therefore, helicity configurations of opposite signs are favoured. Since BSM physics searches are sensitive to like-sign helicity configurations these dataset sizes are larger for $\sqrt{s} = 500 \text{ GeV}$.

3.4 Experimental Environment

The goal of precision measurements requires high demands on the accelerator and the beam structure. To perform precision measurements one needs to collect large datasets in a clean environment. The properties of particle collisions not only depend on the available centre-of-mass energies and luminosities but also on various ILC beam parameters. Additionally, the ILC environment deals with its own background issues which need to be mastered to perform precision measurements. The rate of hard e^+e^- interactions at design luminosity is expected to be in the order of 0.1 per bunch train and therefore, contributes less than 1% to the recorded data [130]. To achieve the optimal performance, the machine backgrounds need to be understood and taken into account.

3.4.1 Beam Parameters

The cross section and the luminosity define the event rate $N_{evt} = \sigma \times \mathcal{L}$ of a certain physics process. To collect large numbers of events in a certain amount of time, large luminosities are necessary. Both centre-of-mass energy and luminosity depend on various other parameters defining the properties of particle collisions. These parameters mainly concern the ILC particle bunch structure [128, 129]:

- the number of particles per bunch N ,
- the number of bunches per bunch train n_b ,
- the time spacing between bunch trains Δt_b ,
- the bunch size at the interaction point σ_x^* , σ_y^* , and σ_z .

At a collider with Gaussian beam shapes, the luminosity is related to these parameters as

$$\mathcal{L} = \frac{n_b N^2 f_{rep}}{4\pi\sigma_x^* \sigma_y^*} H_D, \quad (3.2)$$

where f_{rep} is the plus repetition frequency and H_D a so-called beam enhancement factor, which is described in context of energy loss in this section. The ILC baseline design foresees a repetition rate of $f_{rep} = 5$ Hz at which so-called bunch trains are accelerated. A bunch train is formed by $n_b = 1312$ bunch crossings, each of which consists of $N = 2 \cdot 10^{10}$ particles. Inside of a bunch train, the bunch crossings are separated by $\Delta t_b = 554$ ns. The baseline beam parameters of the ILC are listed in table 3.3. A luminosity upgrade can be achieved by increasing the repetition rate from baseline $f_{rep} = 5$ Hz to $f_{rep} = 10$ Hz and doubling the number of bunches per pulse from $n_b = 1312$ to $n_b = 2625$. This results in a doubling of the average beam power and hence, the luminosity. The beam power P_{beam} reads as

$$P_{beam} = n_b N f_{rep} \sqrt{s} \propto \eta_{RF} P_{RF}, \quad (3.3)$$

Centre-of-mass energy	\sqrt{s}	GeV	250	350	500
Luminosity pulse repetition rate	f_{rep}	Hz	5	5	5
Bunch population	N	$\times 10^{10}$	2	2	2
Number of bunches	n_b		1312	1312	1312
Bunch separation	Δt_b	ns	554	554	554
RMS bunch length	σ_z	μm	300	300	300
RMS horizontal beam size at IP	σ_x^*	nm	729	684	474
RMS vertical beam size at IP	σ_y^*	nm	7.7	5.9	5.9
Luminosity	\mathcal{L}	$\times 10^{34} \text{ cm}^{-2}\text{s}^{-1}$	0.75	1.0	1.8
Fractional RMS energy loss	δ_{BS}	%	0.97	1.9	4.5

Table 3.3: Summary table of the ILC baseline parameters for the energies 250 GeV, 350 GeV, and 500 GeV [129].

which is directly related to eq. 3.2 and proportional to the provided RF power P_{RF} . η_{RF} represents the conversion efficiency from the power of the accelerating radio frequency cavities to the beam and usually is in the order of 20% – 65% [138]. Consequently, to reach high luminosities high RF power and large conversion efficiencies are needed.

High luminosities are achieved by strongly focussing the bunch size of the e^+e^- beams at the interaction point (eq. 3.2). To reach the ILC luminosity goals, nanometer size beams with $\sigma_x^* = 474 \text{ nm}$ and $\sigma_y^* = 5.9 \text{ nm}$ are required. However, the strong focussing of the beams at the interaction point gives rise to large electromagnetic fields. The field of one bunch attracts the particles of the colliding bunch. As a result particles are accelerated towards the centre of the oncoming bunches. The so-called pinch effect is illustrated in fig. 3.2. The effect causes additional focussing due to the electromagnetic field of the oppositely charged bunches, which increases the luminosity. In eq. 3.2, the beam enhancement factor H_D accounts for the pinch effect and typically is in the order of two [139], i. e. the luminosity is almost doubled by the effect. However, the electromagnetic fields force the particles to radiate photons. These so-called beamstrahlung photons represent significant energy loss. The average energy loss δ_{BS} of a particle in the colliding bunches is proportional to [138]

$$\delta_{BS} \propto \frac{\sqrt{s}N^2}{\sigma_z(\sigma_x^* + \sigma_y^*)^2}. \quad (3.4)$$

It is important to find a balance between high luminosities and small energy loss. To achieve high luminosities $\sigma_x^*\sigma_y^*$ has to be small (eq. 3.2). However, for small energy loss $(\sigma_x^* + \sigma_y^*)$ has to be large. This is achieved with flat beams $\sigma_x^* \gg \sigma_y^*$ [140]. σ_x^* defines the level of energy loss and σ_y^* the possible reach of high luminosities. The radiated photons represent the dominant machine background, as discussed in the following.

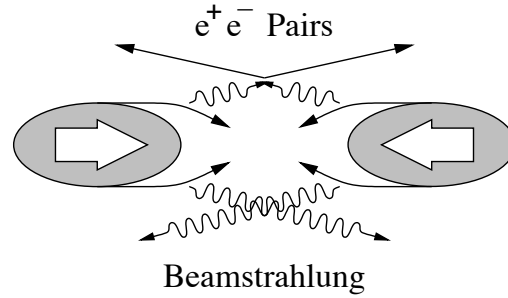


Figure 3.2: Illustration of the pinch effect. Beamstrahlung photons are created in high electric fields of the particle bunches. These photons can produce e^+e^- pairs. Beamstrahlung results in an energy loss and thus, reduces the available centre-of-mass energy for hard e^+e^- interactions. Figure taken from [141].

3.4.2 Backgrounds

As discussed in the foregoing, the ILC has to cope with energy loss due to beamstrahlung as a consequence of the strong focussing of the e^+e^- beams at the interaction point.

Beamstrahlung (sec. 3.4.1) is created by the interaction of the electric fields of the colliding particle bunches at the interaction point (fig. 3.2). The pinch effect results in the emission of photons in the forward direction. It forms the main source of background from beam-beam interactions. The energy loss δ_{BS} entails a reduction of the effective energy which is available for hard e^+e^- interactions. At 500 GeV, an average energy loss of $\delta_{BS} = 4.5\%$ is expected at the ILC [129]. The corresponding distribution is highly non-Gaussian. Hence, the large tails towards high energy losses are the reason for the large average loss.

In this section, backgrounds from beam-beam interactions and their scattering products are discussed. Descriptions of additional machine backgrounds, which arise from the operation of the accelerator, can be found in [130].

Due to the large number of photons at the interaction point, three different $\gamma\gamma$ interactions occur: between two real beamstrahlung photons, between a beamstrahlung and a virtual photon emitted by an e^+ or e^- in the particle bunch, and between two virtual photons, all of which result in large backgrounds.

e^+e^- pairs are produced in two-photon collisions at the interaction point and represent a large source of background. The e^+e^- pairs have low transverse momenta and result in high occupancies predominantly in the vertex detector and in the forward detectors. This is challenging for the pattern recognition algorithms. However, the background can be reduced by time stamping in the tracking system [130]. As a consequence, e^+e^- -pair production is neglected in the event simulation, except for the BeamCal.

Low- p_T $\gamma\gamma \rightarrow$ hadrons receives contributions from virtual photons which got radiated off the primary beam electrons, and real photons due to bremsstrahlung and synchrotron radiation. This background gives rise to much lower occupancies. Its cross section becomes extremely large and highly depends on the ILC centre-of-mass energies. On average $\langle N \rangle = 1.2$ events per bunch crossing are expected for the instantaneous luminosity foreseen for the ILC500 [142]. The resulting hadrons have low transverse momenta and appear as jet-like objects parallel to beam direction. These events act as a pileup to any other hard process and have to be taken into account. Since the events result in real tracks and clusters, simulated events are overlaid statistically before the reconstruction. We refer to this background as $\gamma\gamma$ overlay throughout this thesis. For all DBD benchmark analyses the $\gamma\gamma$ overlay does not have large impact on the measurement results. The effect of this background on the Higgs self-coupling analysis is investigated in this thesis. This study gives a significant hint on whether more sophisticated tools are needed to deal with this background, including a precise modelling of the $\gamma\gamma$ overlay.

Despite of not arising from beam-beam interactions, another effect – next to beamstrahlung – responsible for a reduction of the effective centre-of-mass energy in e^+e^- collisions is discussed in the following.

Initial-state radiation (ISR) The initial e^+e^- system can emit real photons just before the collision. The initial-state-radiation photons are emitted from the highly relativistic incoming electrons and positrons and carry away a certain amount of energy, reducing the effective centre-of-mass energy \sqrt{s} to $\sqrt{s'}$

$$\sqrt{s'} = \sum_{i=1} (E_i, \vec{P}_i) = (\sqrt{s} - E_\gamma^{ISR}, -\vec{P}_\gamma^{ISR}) . \quad (3.5)$$

ISR can alter the available centre-of-mass energy differently for each event. The ISR photons escape detection since they are predominantly emitted parallel to the incoming beam. Hence, their directions are very forward and backward and the events obtain large $|\cos(\theta_{miss})|$.

Beamstrahlung and ISR photons take a leading role in the evaluation of kinematic fits in the context of the Higgs self-coupling analysis in this thesis. In the following parts of this thesis, both effects are referred to as ISR if not stated otherwise.

3.5 Overview of the Accelerator

The ILC is designed to satisfy the anticipated energy and luminosity goals and therefore, the beam parameters discussed in section 3.4.1. The baseline design of the ILC accelerator is depicted in figure 3.3. A detailed description of the complete accelerator and its subsystems can be found in the respective TDR volumes [126–130].

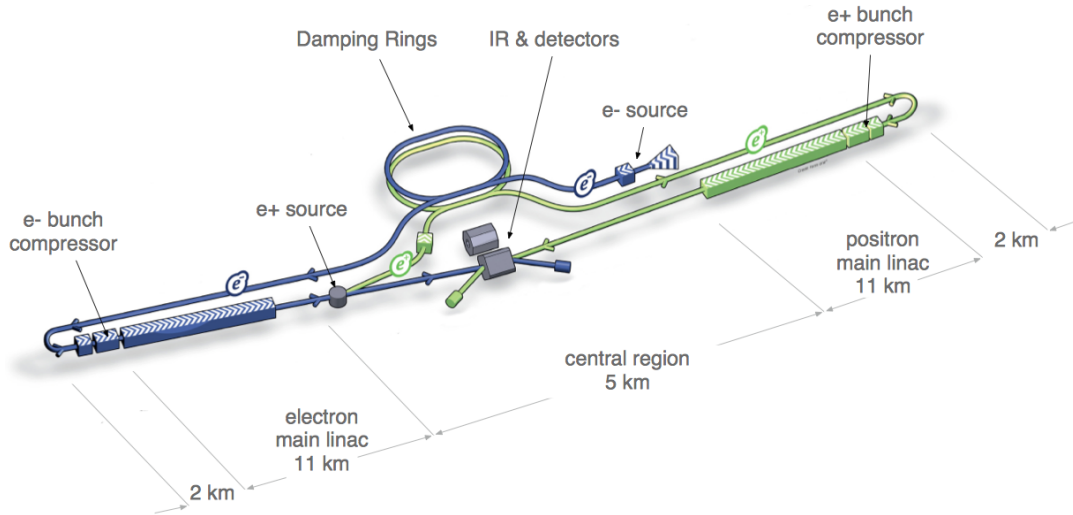


Figure 3.3: The baseline design of the ILC. Figure taken from [126].

The baseline design foresees an accelerator length of 31 km for $\sqrt{s} = 500$ GeV. In case of a 1 TeV energy upgrade, the accelerator length is increased to 50 km. The acceleration process starts with the production of polarised electrons. The electron source consists of a laser which illuminates a strained photocathode in a direct current (DC) electron gun located in the central region accelerator. The chosen material for the photocathode is gallium-arsenide. This setup allows to achieve an electron polarisation of $\sim 85\%$. At this stage, the emittance of the electron beam is very large and needs to be reduced. This is important since a large beam density is required to reach the design luminosity of the ILC. The damping rings play an essential role since their key function is the reduction of the transverse and longitudinal emittance of the beams. There is a separate damping ring for the electron and the positron beam, respectively. Each damping ring has a circumference of 3.2 km. For the damping so-called wigglers are installed. By passing the wigglers, the electrons are forced to emit synchrotron radiation. As a result, the particle bunch becomes more and more parallel in motion which leads to a significant reduction of the transverse and longitudinal beam emittance. The damped electron bunches are then transported in a 15 km long transport line to the main linac. Before feeding the electrons into the main linac, the bunch length is compressed from 6 mm to 0.3 mm and the beam is accelerated from 5 GeV to 15 GeV. In the main linac the electrons are accelerated to the final beam energy used for collision.

The beam positrons are created from the electron beam after final acceleration in the main linac. The electron beam is extracted from the main linac and passes a 147 m long helical undulator in which the electrons generate circular polarised photons. These photons are guided onto a titanium-alloy target creating longitudinally polarised e^+e^- pairs. A magnetic chicane helps to separate these positrons from the electrons and photons which get dumped. The positrons are accelerated to 5 GeV before they enter the positron damping ring. From there on they follow a path which is identical to the one described for the

electrons. The electron and positron beams are planned to be polarised to $|P(e^-)| = 80\%$ and $|P(e^+)| > 30\%$, respectively. The latter can be increased up to 60% with an additional collimator.

The final part of the accelerator is the Beam Delivery System (BDS) with a length of 3.5 km. The BDS transports the particles from the exit of the main linac to the interaction point while focussing them to nanometer sizes required to achieve the high ILC luminosity goals (sec. 3.4.1). At the interaction point, final focussing magnets demagnify the beams to the required size and bring the electron and positron beams to collision under a crossing angle of 14 mrad. The beam properties are measured inside the BDS. This includes emittance measurements, polarimetry, and energy diagnostics [143]. A laser beam setup in horizontal and vertical direction foresees a measurement of the beam size to 1 μm accuracy [129]. This is planned to be followed by a Compton polarimeter measuring the beam polarisation P to a precision of $\Delta P/P \sim 0.25\%$ [144]. An energy measurement is planned to be performed with an upstream energy spectrometer before collision and a downstream energy spectrometer after collision [145]. This setup allows to take into account collision effects. To achieve the ILC design goals, the beam energy has to be determined to a precision of $\Delta E/E \sim 10^{-4}$ [129]. After collision the beams are transported to the main dumps with an extraction line, which contains additional energy and polarisation diagnostics.

In order to be able to carry out more than one experiment at the ILC, the interaction point is planned to be shared alternately by two independent moveable detectors in a so-called push-pull detector operation. Two independent detectors can be moved on and off the beam line on short time scales. The detectors of ILC will be discussed in chapter 4.

Chapter 4

The International Large Detector Concept

The wide range of high precision measurements in the ILC physics programme sets new standards on detector technologies and their physics performance. In sec. 4.1 the performance goals of ILC detectors are discussed. To meet the full programme of high precision measurements, the ILC detector concepts target the best possible particle detection and reconstruction of events with multi-jet final states. The ILC detector designs are optimised for the particle flow approach, which is introduced in sec. 4.2. To face the physics challenges, the ILC detectors combine precise tracking with a small material budget, and high granularity calorimeters. Therefore, in sec. 4.3, the International Large Detector (ILD) is described. This includes a discussion of the sub-detector systems driving the physics performance that is crucial for this study. Additionally, the ILD detector performance is discussed, which is driven by physics optimisation studies in full detector simulations. In order to get information on the particles produced in e^+e^- collisions in the ILD, four major steps have to be performed. The events have to be generated, simulated, reconstructed, and finally stored in a convenient data structure. The software used for each task is introduced shortly in sec. 4.4 and 4.5. The content of this chapter follows [130].

4.1 Detector Design Challenges

To meet the full programme of high precision measurements the ILC detector concepts target the best possible particle detection and reconstruction of events. The interesting physics processes include heavy boson decays to multi-jet final states accompanied by charged leptons or missing energy. Figure 4.1 illustrates a double Higgs-strahlung event $e^+e^- \rightarrow ZHH \rightarrow b\bar{b}HH$ at 500 GeV. ZHH events are not suited for detector optimisation studies due to the very small production cross section. Nevertheless, the observation of double Higgs-strahlung gives access to the Higgs self-coupling measurement, which represents one of the most essential physics goals at the ILC and highly depends on the

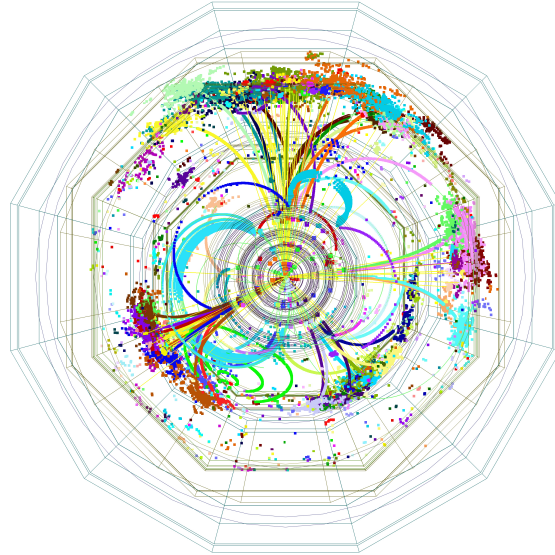


Figure 4.1: Event display of $ZHH \rightarrow b\bar{b}HH$ at $\sqrt{s} = 500$ GeV at the ILD. This process has a very small production cross section and requires an excellent detector performance.

detector performance. The observation of double Higgs-strahlung is very important for the physics reach of the ILC project and has to be reconstructed as precisely as possible. ZHH gives four-jet or six-jet final states depending on the decay mode of the Z boson. At a Higgs mass of 125 GeV, the Higgs boson predominantly decays into a pair of b quarks, which results in complex signatures in the detector. At 500 GeV these events are produced near the kinematic threshold and thus, the jets have significant overlap with each other. High flavour-tagging efficiencies are required being robust against mis-clustering of particles into jets. Leptonic decays of the Z boson need high track momentum resolutions which can help in the event reconstruction, i. e. in the application of kinematic fits. A high track momentum resolution favours the reconstruction of the Z -boson mass and sets precise constraints on the reconstruction of the hadronic jets from the two Higgs bosons. All mentioned aspects are directly linked to the performance requirements of ILC detectors to fulfil the large range of physics programme and reach the desired measurement precisions. The performance requirements are discussed in the following.

4.1.1 Jet-Energy Resolution

A precise event reconstruction and identification of heavy boson decays to multi-jet final states relies on an accurate reconstruction of invariant di-jet masses. The invariant mass of a di-jet system is given by

$$M^2 = m_1^2 + m_2^2 + 2E_1E_2(1 - \cos \theta_{12}), \quad (4.1)$$

where $E_{1,2}$ represents the energy of each jet respectively, and θ_{12} denotes the angle between the two jets. The masses $m_{1,2}$ of the jets are assumed to be small compared to the jet

energies. Thus, the invariant mass determination depends on a precise reconstruction of the jets in the detector. Due to the small ZHH production cross section it is essential to reconstruct the small number of signal events very precisely. In the reconstruction the boson mass distributions play an essential role. The jets representing the primary quarks have to be reconstructed and paired to form the signal bosons. In reality, the precise reconstruction of the primary quarks by measuring the jet properties is limited by

- errors in jet fragmentation and hadronisation,
- limited detector resolutions,
- particles which escape detection by travelling through ineffective regions of the detector,
- particles which stay undetected as neutrinos,
- hard gluon radiation,
- and mis-clustering of particles into jets.

At LEP, the application of kinematic fits allowed the precise reconstruction of di-jet masses by imposing energy and momentum conservation requirements on the events [146]. This determination was almost independent of the jet-energy resolution, which was dominated by the intrinsic resolution of the Hadronic Calorimeter (HCAL). The HCAL has the worst energy resolution of all detector sub-systems of $> 55\% / \sqrt{E(\text{GeV})}$ [146]. This sets limits to the achievable measurement precisions. At the ILC the impact of ISR and beamstrahlung (section 3.4) degrades the benefits of kinematic fits. Therefore, the invariant mass reconstruction driving the overall physics performance at the ILC relies on an excellent jet-energy resolution. However, processes with very high jet multiplicities, as ZHH , suffer from jet-finding ambiguities which dominate the mass resolution. Therefore, these processes are less affected by the jet-energy resolution.

The performance goal is driven by benchmark studies of hadronic W and Z decays, the masses of which differ only by 10 GeV. An invariant mass resolution comparable to the natural widths of the bosons, i. e. ~ 2 GeV, gives 3σ separation of the W and Z boson mass peaks. Considering eq. 4.1 and neglecting angular uncertainties, the jet-energy resolution transforms into a di-jet mass resolution $\sigma_M/M = \alpha / \sqrt{E_{ij}(\text{GeV})}$, with E_{ij} denoting the energy of the di-jet system. The ILC design goal envisages a jet-energy resolution for hadronic W and Z decays comparable to their natural widths of

$$\sigma_E/E = 3\% - 4\%. \quad (4.2)$$

In terms of classic calorimetry this is equivalent to $\sigma_E/E = 30\% / \sqrt{E(\text{GeV})}$ for 100 GeV jets. At $\sqrt{s} = 500$ GeV the relevant physics processes cover four-jet to six-jet final states with typical jet energies between 50 GeV and 125 GeV. Since in classic calorimetry the jet-energy resolution is limited by the HCAL the particle flow approach was developed to fulfil this performance goal as introduced in sec. 4.2.

4.1.2 Track Momentum Resolution

The overall tracking system presents a key element of an ILC detector. The high-precision measurements, in particular in the Higgs sector, require advanced event-reconstruction techniques with very high tracking efficiencies down to low momenta, and excellent two-particle separation. Therefore, the goal for precision measurements places high demands on the momentum resolution of charged tracks of

$$\sigma_{1/p_T} \approx 2 \times 10^{-5} \text{ GeV}^{-1} \oplus \frac{1 \times 10^{-3}}{p_T \sin \theta}. \quad (4.3)$$

This performance goal is mainly driven by benchmark analyses of the Higgs recoil mass using Higgs-strahlung events with leptonic $Z \rightarrow \mu^- \mu^+$ decays. In the measurement, the momentum resolution is closely related to the achievable precision on the Higgs mass. The required level of performance ensures that this measurement is dominated by the beam-energy spread rather than the detector resolution [130]. In case of ZHH events, leptonic decays of the Z boson need high track momentum resolutions which can help in the event reconstruction, i. e. in the application of kinematic fits. A high track momentum resolution favours the reconstruction of the Z -boson mass and sets precise constraints on the reconstruction of the hadronic jets from the two Higgs bosons.

4.1.3 Impact Parameter Resolution

The reconstruction of hadronic multi-jet events from heavy-flavoured quarks from Z , W , or Higgs boson decays is one of the key features in most physics analyses. Consequently, the precise identification of hadronic jets originating from heavy quarks is an important performance goal at the ILC. At a Higgs mass of 125 GeV, the Higgs boson predominantly decays into a pair of b quarks. In case of double Higgs-strahlung, we expect four b jets coming from the two Higgs bosons. At 500 GeV these events are produced near the kinematic threshold and thus, have significant overlap with each other. Therefore, high flavour-tagging efficiencies are required which are robust against mis-clustering of particles into jets. This is achieved by a precise measurement of the track parameters of the charged decay products within short distance of the interaction point. Compared to jets from light-flavoured quarks, heavy quarks have special characteristics which can be used for flavour tagging, such as the long lifetime of b hadrons and its large mass which results in large decay multiplicities and large jet invariant masses. The decay length L of a b hadron is large enough to be observed as a displaced vertex in the vertex detector, as indicated in fig. 4.2. The decay products do not point back to the primary vertex. The impact parameter defines the minimal transverse distance between the track and the expected interaction point, which is inconsistent with the primary vertex hypothesis of the heavy-quark decay. Therefore, the performance of the vertex detector can be expressed by the resolution of the impact parameter of charged particles. It is related to the single point resolutions, the overall occupancy in the detector, and the location of the first mea-

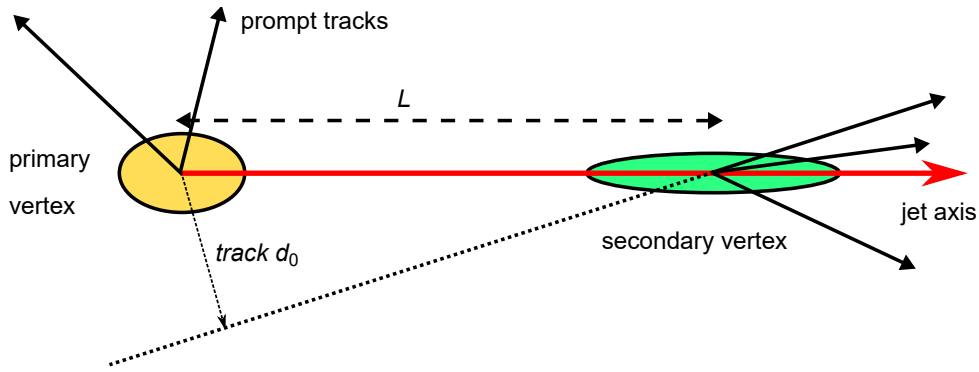


Figure 4.2: Schematic illustration of a long-lived particle decay, which can be detected as a secondary vertex. The impact parameter of the tracks of the decay products are different from the primary vertex position. Figure taken from [147].

surement. To satisfy the desired flavour-tagging performance the main design goal of the ILC vertexing system is a track impact parameter resolution of

$$\sigma_{r\phi} = 5 \mu\text{m} \oplus \frac{10}{p(\text{GeV}) \sin^{2/3} \theta} \mu\text{m}. \quad (4.4)$$

4.1.4 Precise Knowledge of Machine Backgrounds

In addition, the ILC deals with different types of background, which must be overcome by new detector technologies. These backgrounds result in high occupancies in the detector sub-systems, especially in the forward region. The large number of $\gamma\gamma$ collisions results in a large number of hit densities predominantly in the vertex detector. The different background sources can give additional tracks and clusters, which require proper handling and precise knowledge of the background event properties since they degrade the measurement precisions. This is extremely important for measurements with very small production cross sections, as it is the case for double Higgs production.

4.2 Particle Flow Concept

The ILC detector designs are optimised specifically for the particle flow concept, which is described in detail in [148, 149]. Particle flow is based on a precise reconstruction of the four-vectors of charged particles in an event. The energy of each particle is measured with the sub-detector giving the best energy estimation for the respective particle type. Charged particle momenta are measured in the tracking system, photons and neutral hadrons in the calorimeters. This demands an excellent interplay between tracking and calorimetry. The reconstructed jet energy is the sum of the energies from the individual particles.

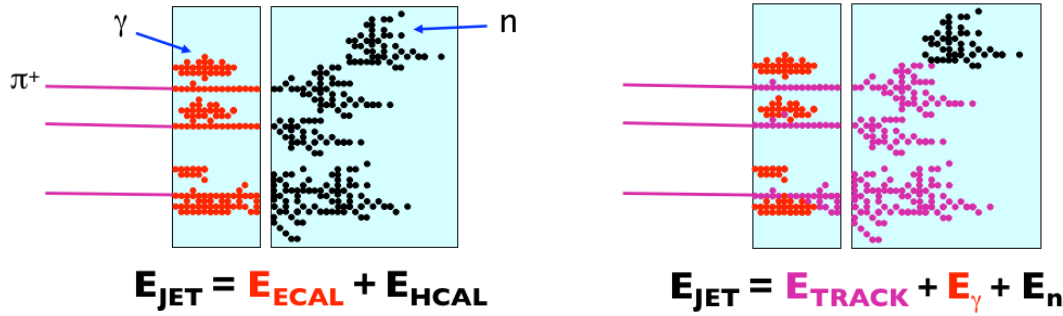


Figure 4.3: The transition from the traditional calorimetric approach (left) to particle flow calorimetry (right). Both the calorimeter and tracking system enter into the particle flow performance. Figures taken from [148].

The composition of jets is known from LEP experiments in which the fragmentation and hadronisation of jets were investigated [150]. Subdividing the jet energy, typically 62% is carried by charged particles, 27% by photons, 10% by long-lived neutral hadrons, and 1.5% by neutrinos. Traditional calorimetry determines jet energies by combining energy measurements from the electromagnetic calorimeter (ECAL) and the HCAL. With regard to the components of a jet, this indicates that 72% of the jet energy are measured in the HCAL which has the worst energy resolution of all detector subsystems. The ILC jet-energy resolution goal (eq. 4.2) cannot be achieved with traditional calorimetry.

The transition from traditional calorimetry to particle flow is illustrated in fig. 4.3. The momenta of all charged particles are measured in the tracking detectors and translated into the corresponding particle energies. The corresponding energy deposits are then removed from the calorimeters. This is advantageous since the tracking system provides very good resolution compared to the calorimeters (table 4.1). Additionally, the momentum resolution of the tracking system is crucial for particle flow since 62% of the jet energy is carried by charged particles. Large tracking efficiencies are needed even for particles with small transverse momenta. At the same time, the particle flow approach poses challenges to the calorimeters since they need to be able to identify and separate shower profiles of single particles. ECAL and HCAL require very high granularity in longitudinal and transverse direction to deal with multi-jet events. The tracking systems need to have an overall small material budget to minimise interactions before the calorimeters, while thick calorimeters are required to absorb the particle showers.

In the particle flow approach, only photon and neutral hadron energies are measured in the calorimeters. Consequently, only 10% of the jet energy is measured in the HCAL and therefore affected by its poor energy resolution. Ideally, this would lead to an overall energy resolution of $\sim 20\% / \sqrt{E(\text{GeV})}$ [149]. However, this demands a perfect assignment of calorimeter energy deposits to the correct particle tracks, and a perfect separation of nearby showers. In practice, this cannot be fully achieved:

Energy loss We suffer from energy loss if close-by neutral and charged particle clusters are combined. Since the energy of the charged particle is reconstructed in the track-

Component	Detector	Energy fraction	Intrinsic resolution
Charged particle X^\pm	Tracker	$\sim 0.6E_{jet}$	$10^{-4}E_{X^\pm}^2$
Photon γ	ECAL	$\sim 0.3E_{jet}$	$0.15\sqrt{E_\gamma}$
Neutral hadrons h^0	HCAL	$\sim 0.1E_{jet}$	$0.55\sqrt{E_{h^0}}$

Table 4.1: Contributions from different particle types to the jet-energy resolution. The jet energy fraction carried by these particle types, as well as the energy resolutions of charged particles, photons and neutral hadrons are listed. Table taken from [149].

ing detector, the charged cluster is removed from the calorimeters and thus also the energy of the neutral cluster.

Double counting If clusters and tracks are wrongly associated some energy can be misidentified as neutral hadron and double counted.

These effects contribute to the so-called confusion term. The overall jet-energy resolution can be written as

$$\sigma_{jet} = f_{X^\pm} \cdot \sigma_{X^\pm} \oplus f_\gamma \cdot \sigma_\gamma \oplus f_{h^0} \cdot \sigma_{h^0} \oplus \sigma_{confusion} \quad (4.5)$$

$$= f_{X^\pm} \cdot \sigma_{tracking} \oplus f_\gamma \cdot \sigma_{ECAL} \oplus f_{h^0} \cdot \sigma_{HCAL} \oplus \sigma_{PFA}. \quad (4.6)$$

Here, f denotes the jet energy fraction carried by charged particles X^\pm , photons γ , and neutral hadrons h^0 , respectively. The confusion term limits the overall performance at higher energies. The resolution of the HCAL is the limiting factor at small energies. To reduce the confusion term highly granular calorimeters are required.

4.3 The International Large Detector

At the ILC, physics measurements are planned to be performed with two different experiments, which share the interaction point alternately. The ILC detector concepts are the International Large Detector (ILD) [151] and the Silicon Detector (SiD) [152]. Both detector concepts are designed to fulfil the performance requirements (section 4.1) and are based on the particle flow approach (section 4.2). The main difference between the two concepts is the central tracking detector. SiD foresees five layers of silicon trackers and the ILD employs a Time Projection Chamber (TPC). Since this thesis is based on an ILD full detector simulation, the ILD detector concept is described briefly. Further information and detailed descriptions of the ILD and SiD detector concepts can be found in [130]. A schematic sketch of ILD is shown in figure 4.4. For this analysis, the performances of the vertex detector, the tracking system and the calorimeters are most important, all of which are introduced in the following. The detector is enclosed by a return yoke, which is instrumented to recover energy leakage from the calorimeters, and for muon identification purposes. A surrounding superconducting coil provides a magnetic field of 3.5 T.

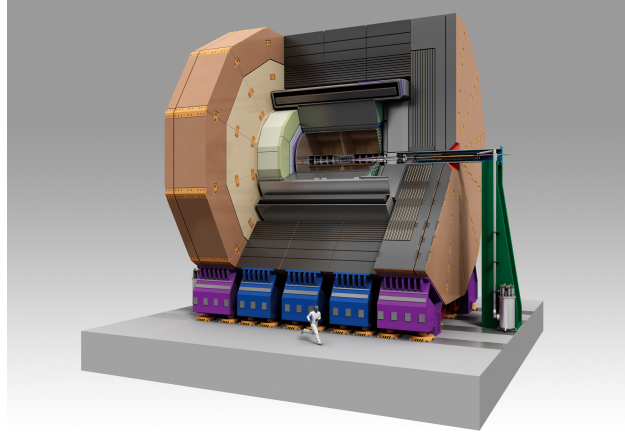


Figure 4.4: Schematic illustration of the ILD detector concept. Figure taken from [153].

4.3.1 Vertex Detector and Flavour Tagging Performance

The interaction point (IP) is surrounded by a multilayer vertex detector, consisting of several layers of silicon pixel sensors. The vertex detector design and the impact parameter resolution (eq. 4.4) are crucial for achieving the goal of precise flavour tagging of heavy particles. The first layer of the pixel vertex detector is located at 1.6 cm from the IP, which allows measurements of displaced vertices very close to the IP. A spatial resolution better than 3 μm near the IP, a pixel occupancy below a few percent, and a material budget below 0.15% of a radiation length per layer satisfy the performance goal. Another important aspect for the vertex detector is the timing resolution, which is crucial to reduce the machine backgrounds which create high occupancies in the vertex detector. High occupancies degrade the tracking performance and thus reduce the flavour-tagging capabilities.

Two vertex designs are currently studied: the baseline design foresees a vertex detector consisting of three double ladders, each of which has pixel sensors on both sides, giving six measurement points. The second design foresees five equally spaced single-sided layers giving five space points per track. In comparison, the first technology has a slightly worse resolution, but so-called mini vectors can be combined with the hits of a double layer which helps to improve pattern recognition capabilities [154]. Three pixel sensor technologies are investigated for ILD: CMOS Pixel Sensors (CPS) [155], Fine Pixel CCD (FPCCD) sensors [156], and DEPLETED Field Effect Transistor (DEPFET) sensors [157]. Since each technology does not fully satisfy all the detector requirements a combined use is discussed. This allows to benefit from the respective advantages of each technology.

The vertex detector performance is illustrated in fig. 4.5. The left figure shows the impact parameter resolution of single muon events as a function of the transverse track momentum for different polar angles. The design goal (eq. 4.4) is indicated by the solid lines. The achieved impact parameter resolution outperforms the targeted performance down to a track momentum of 1 GeV. In the right figure, the purity as a function of the b and c tagging efficiency is shown for $ZZZ \rightarrow q\bar{q}q\bar{q}q\bar{q}$ events at $\sqrt{s} = 500$ GeV and $\sqrt{s} = 1$ TeV,

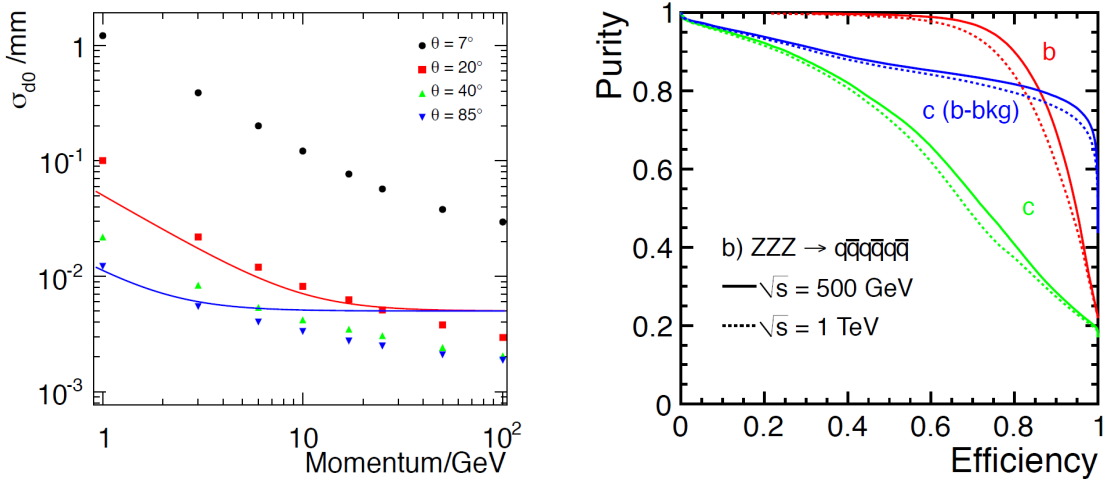


Figure 4.5: Flavour-tagging performance at the ILD, estimated from a detailed GEANT4-based full ILD detector simulation. Left: impact parameter resolution as a function of the transverse momentum for different polar angles. The solid lines depict the design goal for different angles of the track with respect to the beam axis. Right: purity as a function of the efficiency for b - and c -tagged jets for $Z \rightarrow q\bar{q}q\bar{q}q\bar{q}$ at $\sqrt{s} = 500$ GeV and $\sqrt{s} = 1$ TeV. Figures taken from [130].

respectively. In the events, the Z bosons decay into the same quark flavour. The colours indicate the separation of b -tagged jets from $udsc$ jets (red), c -tagged jets from $udsb$ jets (green), and c -tagged jets when considering only b quarks as background (blue). The results degrade to high energies. This is also observed for increasing numbers of jets in an event due to the busy environment which degrades the reconstruction performance. However, the excellent performance of the entire tracking system leads to outstanding abilities in flavour tagging. The presented results do not include the effects of $\gamma\gamma$ overlay. Currently, this is under study. First results show a degraded performance [154, 158].

4.3.2 Tracking System and Performance

The vertex detector is surrounded by the tracking system, the central detector of which is the TPC. The TPC provides a measurement of particle momenta via their specific energy loss dE per track length dx depending on the distinctive particle masses. This gives a powerful tool for particle identification. Since the tracking detectors have to deal with multi-jet events with high track multiplicities, they have to provide very high tracking efficiencies and precision while staying robust against machine backgrounds. The TPC records up to 224 three-dimensional space points per particle track and therefore provides huge pattern recognition capabilities. The large number of measurement points results in a momentum resolution of $\delta(1/p_T) \approx 10^{-4}$ c/GeV. This corresponds to a transverse point resolution better than 100 μm for the complete drift and a double hit resolution of < 2 mm. As required by particle flow, the TPC is designed with minimum material budget, which helps to reduce effects of machine backgrounds per bunch crossing.

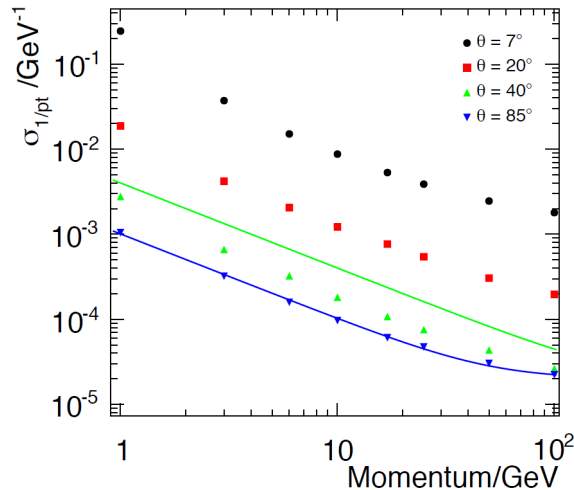


Figure 4.6: Achievable transverse momentum resolution for different polar angles for single muon events. The solid lines illustrate the design goal for different angles: $\theta = 30^\circ$ (green) and $\theta = 85^\circ$ (blue). Figure taken from [130].

The silicon part of the tracking system consists of the Silicon Inner Tracker (SIT) and the Silicon External Tracker (SET), both of which link the TPC to the vertex detector and the calorimeter system. They provide additional space points before and after the TPC, which contribute to an improved momentum resolution. The large number of measurement points in the overall tracking system yields the targeted momentum resolution (eq. 4.3). The SIT especially improves the reconstruction of low- p_T tracks and therefore plays an important role in the identification of the low- p_T background from the $\gamma\gamma$ overlay (section 3.4.2). Next to high spatial precision, silicon detectors have a good timing resolution relative to the time separation of ~ 300 ns of ILC bunch crossings. This allows time stamping of tracks and the identification of the corresponding bunch crossing within a bunch train to a precision of 2 ns. The end cap component behind the TPC endplate (ETD) and the forward tracker (FTD) complete the silicon tracking system providing low angle tracking coverage.

The tracking performance is illustrated in figure 4.6 and figure 4.7, respectively. Figure 4.6 depicts the transverse momentum resolution of the entire tracking system as a function of the track momenta for single muon events. The solid lines indicate the performance goal (eq. 4.3). For $\theta = 85^\circ$, the momentum resolution goal is reached over the entire momentum range from 1 GeV up to 200 GeV. For $\theta = 30^\circ$ the achieved performance degrades but is still compatible to the detector design goal. The tracking efficiencies are studied using six-jet events from $t\bar{t}$ decays at 500 GeV and 1 TeV, respectively. The studies have been performed with a detailed GEANT4-based [159] full detector simulation of ILD. Effects of pair background and $\gamma\gamma$ overlay are taken into account. The tracking efficiency as a function of the track momentum and of the polar angle are shown in figure 4.7, respectively. Tracks with a momentum larger than 1 GeV obtain a reconstruction efficiency of almost 100%. For the entire range of polar angles an average efficiency of 99.7 %

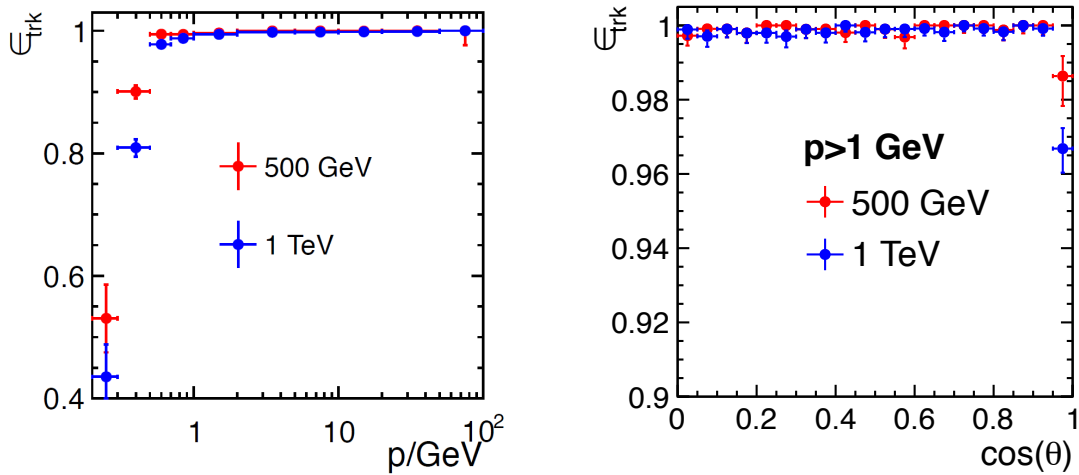


Figure 4.7: Tracking efficiency at ILD as a function of the momentum (left) and as a function of the polar angle (right), studied for 6-jet events of $t\bar{t}$ decays in the presence of pair background for $\sqrt{s} = 500$ GeV and $\sqrt{s} = 1$ TeV. Figures taken from [130].

can be achieved. The very large efficiencies for large $|\cos(\theta)|$ verify an excellent forward tracking performance of ILD. A slightly worse performance can be observed for tracks with low transverse momentum. New approaches to increase the tracking performance for low-momentum tracks are under investigation [154, 160, 161]. The increasing number of $\gamma\gamma$ -overlay events to higher centre-of-mass energies results in a degradation of the efficiency for low-momentum tracks at $\sqrt{s} = 1$ TeV. Nevertheless, the results verify that the tracking design goals are fulfilled.

4.3.3 Calorimeter System

The tracking system is surrounded by highly granular calorimeters. The calorimeter system consists of an ECAL, which is enclosed by the HCAL. Both are highly segmented sampling calorimeters. To minimise the material budget in front of the calorimeter, they are placed inside a magnetic coil. Being the main cost driver, the latter stipulates a compact ECAL. Additionally, the particle flow approach demands high granularity in transverse and longitudinal direction to identify the shower profiles of individual particles. In the ECAL, this can be achieved by using tungsten as absorber material. Tungsten fulfils the requirements of

- a small Molière radius ($R_M = 9$ mm) favouring a separation of close-by showers,
- a large ratio between interaction length ($\lambda_I = 99$ mm) and radiation length ($X_0 = 3.5$ mm). In the ECAL this induces early photon and electron showers, and late hadronic showers.

In general, the energy resolution of a calorimeter is defined as

$$\frac{\sigma_E}{E} = \frac{a}{\sqrt{E}} \oplus \frac{b}{E} \oplus c = \sqrt{\frac{a^2}{E} + \frac{b^2}{E^2} + c^2}. \quad (4.7)$$

Here, a/\sqrt{E} describes a stochastic term, b/E noise and background fluctuations, and c a constant associated to calibration errors. For high energies, σ_E/E is limited by c . For smaller energies σ_E/E is limited by noise and statistics. To ensure the best energy resolution the ECAL is segmented into 30 layers. The HCAL offers energy measurements of neutral hadrons, which need to be separated from charged hadron showers. Therefore, also the HCAL is highly segmented. Stainless steel is used as absorber material. It provides an interaction length of $\lambda_I = 17$ cm and a radiation length of $X_0 = 1.8$ cm, and can be used as supporting structure. A BeamCal and LumiCal are positioned in the very forward region of the detector. The LumiCal provides luminosity measurements via Bhabha scattering events to a precision of $\Delta\mathcal{L}/\mathcal{L} \sim 10^{-3}$ [129].

4.3.4 Particle Flow Performance

At the ILC the interesting processes consist of four- to six-jet final states with typical jet energies between 80 GeV and 250 GeV at $\sqrt{s} = 500$ GeV and $\sqrt{s} = 1$ TeV. At 250 GeV four-jet final states with jet energies of approximately 60 GeV are studied. The jet-energy resolution goal (eq. 4.2) requires an excellent interplay between tracking and calorimeters. In figure 4.8 the ILD particle flow performance is illustrated as a function of the jet energy. The figure is based on $Z \rightarrow q\bar{q}$ events with $q = u, d, s$. The particle flow performance varies with energy. The energy resolution from traditional calorimetry (blue) shows an increase to higher jet energies. This is due to energy leakage of high-energetic jets out of the HCAL. An assumed typical stochastic constant term (red) performs better at higher jet energies. The particle flow approach (solid black) performs best and is mainly limited by confusion towards higher energies. At higher energies, the reconstruction of the individual particles in a jet is more difficult since the jets are more collimated. For small jet energies the performance is driven by the jet-energy resolution which is dominated by the neutral hadron reconstruction. Nevertheless, the overall design goal is achieved.

However, the respective study applies several assumptions to prevent effects which degrade the particle flow performance, and thus the jet-energy resolution [149]:

- Z decays into light quarks (u, d, s) are investigated. Light jets do not suffer from missing energy from semi-leptonic decays as it is the case for heavy quarks, e. g. $b \rightarrow c\ell\nu$. Missing energy degrades the jet-energy resolution.
- ISR and beamstrahlung cause missing energy and are not included in the analysis.
- To avoid mis-clustering of jets in the jet-finding procedure the total energy for $Z \rightarrow q\bar{q}$ is divided by two. Jet mis-clustering degrades the event-reconstruction performance and energy resolution. At the ILC, this is crucial due to the measurement of generally four-jet to six-jet final states. At higher energies, jets are strongly collimated, which results in a small energy resolution. At small energies, in reality jets are less collimated and the jet mis-clustering has a large influence.

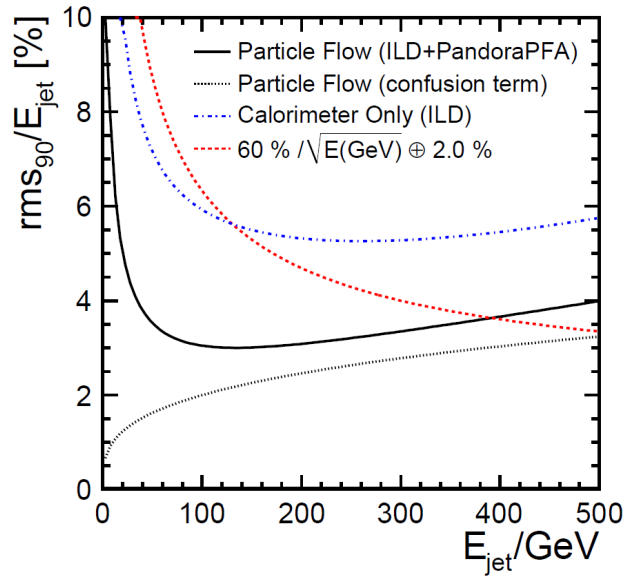


Figure 4.8: Particle flow performance of ILD. Simulated jet-energy resolution of $Z \rightarrow uds$ events with particle flow algorithm. Figure taken from [149].

- Due to confusion the observed jet-energy resolution is not described by $\sigma_E/E = \alpha/\sqrt{E(\text{GeV})}$. The energy resolution is determined using RMS_{90} . The RMS_{90} is defined as the RMS in the smallest region of reconstructed energy that contains 90% of the events. It is introduced to reduce the sensitivity to tails since the effects of confusion lead to an inherently non-Gaussian energy distribution.
- There are significant beam related backgrounds. The increasing number of low- p_T $\gamma\gamma \rightarrow$ hadrons events per bunch crossing for higher centre-of-mass energies is not included in this study. However, it needs to be considered in particle flow reconstruction. Calorimeter clusters may contain hits from more than one particle particularly in the forward region of the detector. In presence of such background events, it is important to identify and remove the corresponding events as precisely as possible.

Some limitations in the reconstruction of primary quarks (section 4.1.1) are not covered by the ILD definition of the jet-energy resolution, which highly depends on the particle flow performance (figure 4.8). Jet fragmentation and hadronisation as well as limited resolutions of the detector are taken into account. It does not cover missing energy from semi-leptonic decays and mis-clustering of jets. At the ILC, invariant mass reconstruction relies on an excellent jet-energy resolution due to the impact of large beamstrahlung (section 3.4) which do not allow the application of kinematic fits. However, by including these particle flow degrading effects in the kinematic fit the combined use of particle flow and kinematic fitting could help to improve the reconstruction of particle four-vectors and offer improvements to the measurement performances at the ILC.

The ILD performance has been studied in terms of technical performance criteria and optimisation studies of selected physics processes. Testbeam campaigns with prototype setups allow to investigate single detector components. However, to study the complete detector setup a detailed full detector simulation is crucial. A realistic reconstruction with detailed knowledge on mechanical aspects provides a realistic picture of the overall detector performance. The optimisation of the detector concept in terms of particle flow requires a high level of detail in the simulation. The presented performance studies are based on a full GEANT4 [159] detector simulation and the analysis framework ILCSofT [162]. The software chain is introduced in the following.

4.4 Event Generation

Events are generated using the Monte Carlo (MC) event generator WHIZARD 1.95 [163]. WHIZARD is ideal for the event generation of physics processes at the ILC since it allows to include parameters as ISR and beamstrahlung, and user-defined beam polarisations. In the generation procedure, WHIZARD calls two elements internally:

- the tree-level matrix element generator O'Mega [164, 165]. O'Mega computes helicity amplitudes for any physics process. It supports SM processes and a large number of BSM models. The O'Mega output is used as input in WHIZARD.
- for fragmentation and hadronisation of the generated events PYTHIA [166] is used since WHIZARD only generates hard interactions. Hereby, the hadonisation tune to LEP data is used, as provided by OPAL, which is essential for particle flow [167]. The PYTHIA library is called from inside WHIZARD and no external interface is needed.

The generated events can be written to files of various standard formats. Here, the standard output StdHep is used. After event generation, the passage of the events through the detector material is simulated. ILCSofT [162] provides a framework for the simulation and reconstruction of the generated events.

4.5 Software Framework

ILCSofT [162] includes various software packages which are developed by the linear collider community. ILCSofT provides a persistency framework for linear collider studies, and an event data model given by LCIO (Linear Collider I/O) [168]. The LCIO event data model provides classes for the generated and reconstructed objects as well as relations between different object classes. This allows to reproduce entire physics processes, e. g. decay chains from generator level to reconstruction level. As created by the event genera-

tor, the MC truth particles are contained within the `MCParticle` class. During simulation, the simulated particles are added to the existing list of `MCParticles`.

At reconstruction level, there exist four main classes. The `ReconstructedParticle` class serves as foundation for most physics analyses storing every reconstructed particle. New subset collections of `ReconstructedParticle` can be created, e. g. holding single particles as identified isolated leptons, or compound objects like jets consisting of many reconstructed particles. The central `ReconstructedParticle` class, however, always contains a list of tracks, clusters and reconstructed particles, which are included in additional collections. This allows to retain any required information. LCIO can be easily extended for user-specific purposes, i. e. if one needs to store additional information for a respective analysis.

4.5.1 Detector Simulation

The interactions of the generated particles in the detector are simulated with `Mokka` [169]. `Mokka` is a `GEANT4`-based [159] simulation tool. `GEANT4` provides a tool for simulating the passage of particles through the detector material. Physics lists steer the underlying physics processes to achieve a good agreement between simulation and testbeam campaigns. It allows to impose various factors on the particles, e. g. the size of magnetic fields or the rate of energy loss of the particles in the sub-detector systems.

`Mokka` requires as input the event samples generated by `WHIZARD` and a detailed and realistic model of the full detector, including dead material, labelling, support structures, or gaps. Currently, there are various ILD detector models available for simulation studies, only differing in calorimeter technologies. In this thesis, the ILD detector model `ILD_o1_v05` is used which includes a silicon-tungsten ECAL and an analogue HCAL. The simulated events are written into an LCIO output file, which is the standard output for ILC related studies. The LCIO data files contain lists of MC particles and particle hits in the sub-detector systems.

4.5.2 Beam-Background Overlay

Due to the large cross section of the low- p_T $\gamma\gamma \rightarrow$ hadrons background (section 3.4.2) several interactions per bunch crossing are expected. The interaction rate depends on the centre-of-mass energy at the ILC. On average $\langle N \rangle = 1.2$ (2.7) events per bunch crossing are expected at $\sqrt{s} = 500$ GeV (1 TeV) [142]. Giving additional real tracks and clusters in the detector, these events have to be taken into account properly in the reconstruction. Based on the cross section model in [170], the events are generated with `PYTHIA` and simulated with `Mokka`. Arising from different vertices than events from hard interactions, in the simulation their z position from the interaction point is smeared with a spread of $300 \mu\text{m}$ ($225 \mu\text{m}$) for $\sqrt{s} = 500$ GeV (1 TeV), representing the Gaussian beam profile [130]. To simulate their effects, the background events are statistically laid

over the events from hard interactions before the reconstruction. At the time of the MC mass production for the TDR an overestimated number of $\langle N \rangle = 1.7$ (4.1) events was mistakenly overlaid for the $\sqrt{s} = 500$ GeV (1 TeV) event samples [130]. This results in overall pessimistic results of the Higgs self-coupling analysis with $\gamma\gamma$ overlay.

4.5.3 Standard Event Reconstruction

Using the LCIO data format, the reconstruction of the events is performed with `Marlin` (Modular Analysis and Reconstruction for the LInear Collider) [171]. The analysis modules are structured into so-called processors, which contain specific reconstruction algorithms and perform the actual computing task. The processors analyse data in an `LCEvent` and create a new defined output collection, which is added to the events or directly written to the initial collection. Such an output collection can be re-used as input for one of the subsequently executed processors. A steering mechanism reads the LCIO files and processes them on an event-by-event basis. The executing order of a set of processors is chosen by an editable XML steering file. The XML file allows to modify global parameters and processor parameters, e. g. input files, the number of processed events, or processor input collections.

The standard event reconstruction starts with pattern recognition in the tracking detectors using the packages `Clupatra` and `FwdTracking`. The `KalTest` and `FullLDCTracking` packages perform a global track fit and the combination of different track segments from various sub-detectors, respectively. The list of tracks serves as input to the particle flow algorithm (PFA), which is embedded in the software package `PandoraPFANew` [148]. So-called particle flow objects (PFOs) are given as output, which represent charged and neutral reconstructed particles in the detector. The PFOs serve as foundation for physics analyses and further reconstruction tools. Also part of the standard reconstruction is `LCFIVertex` and `LCFIPlus` [172]. Both packages provide vertex finding, jet clustering, and flavour tagging. Only vertex finding is run by default in the standard reconstruction.

Various analysis tools are included in `MarlinReco` [173]. Depending on user-specific needs various processors are provided, e. g. for lepton finding, jet clustering, or kinematic fitting. Existing processors can be easily extended by users and new processors can be build independently and included to an analysis specific XML steering file. Additionally, `Marlin` goes hand in hand with `ROOT` [174, 175]. `ROOT` provides an object-orientated framework for data analyses in high energy physics. `Marlin` allows to create analysis processors which create simple `ROOT` Trees with a column-wise `Ntuple` structure from LCIO collections after executing the desired reconstruction steps. This way, user-defined information can be stored in an `Ntuple` data structure and analysed using `ROOT`.

Chapter 5

Event Reconstruction and Analysis Strategy

The Higgs self-coupling analysis is based on a full GEANT4 [159] detector simulation. The analysis strategy in this thesis follows the DBD Higgs self-coupling study for a Higgs mass of 120 GeV in [108]. To study the Higgs self-coupling for a Higgs boson with a mass of 125 GeV and considering the $\gamma\gamma$ overlay, the signal and background processes used in the analysis are generated, simulated and reconstructed, following the MC mass production chain as discussed in the foregoing chapter and as provided by ILCSoft [162]. The signal and background processes used in the analysis are introduced in section 5.1. Hereafter, the analysis strategy is described in section 5.2, which includes a discussion of the main analysis steps. Finally, an overview on the standard reconstruction tools used in this study is given in section 5.3.

5.1 Signal and Background Processes

To study the Higgs self-coupling for a Higgs boson with a mass of 125 GeV the same background processes and the corresponding data samples are used as in [108]. The background samples were created in a private production equivalent to the official MC mass production [130] (sec. 4.4 and sec. 4.5). The signal and background processes, which include a Higgs boson, are produced for a Higgs boson with a mass of 125 GeV. Following the standard procedure, event samples were created for the polarisation states $P(e^-e^+) = (+1, -1)$ and $P(e^-e^+) = (-1, +1)$. These allow to weight all events with respect to the desired beam polarisation. To study the effect of the $\gamma\gamma$ overlay all samples are simulated with and without the $\gamma\gamma$ overlay, respectively. To be consistent with the TDR mass production an overestimated number of $\langle N \rangle = 1.7$ events are overlaid. This gives overall pessimistic results. In the future, the analysis should be re-run with data samples including the correct number of overlaid events.

$P(e^-e^+)$	(0.0, 0.0)	(-0.8, 0.0)	(-0.8, 0.3)	(-0.8, 0.6)
w_{pol}^{LL}	0.25	0.45	0.315	0.18
w_{pol}^{LR}	0.25	0.45	0.585	0.72
w_{pol}^{RL}	0.25	0.05	0.035	0.02
w_{pol}^{RR}	0.25	0.05	0.065	0.08

Table 5.1: Event weights for different beam polarisations determined with eq. 5.1. The weights for the opposite-sign polarisation can be obtained by exchanging R and L .

Generally, the cross section of a certain process can be expressed with respect to a desired beam polarisation as

$$\sigma_{P(e^-e^+)} = \left(\frac{1 - P_{e^-}}{2}\right)\left(\frac{1 + P_{e^+}}{2}\right)\sigma_{LR} + \left(\frac{1 + P_{e^-}}{2}\right)\left(\frac{1 - P_{e^+}}{2}\right)\sigma_{RL}, \quad (5.1)$$

where σ_{LR} denotes the cross section at $P(e^-e^+) = (-1, +1)$ and σ_{RL} the cross section at $P(e^-e^+) = (+1, -1)$. Similar terms exist for σ_{LL} and σ_{RR} which are not listed in eq. 5.1 since in the Higgs self-coupling analysis the considered SM processes are only sensitive to $P(e^-e^+) = (-1, +1)$ and $P(e^-e^+) = (+1, -1)$. For the ILC baseline polarisation $P(e^-e^+) = (-0.8, 0.3)$, the polarisation weights read

$$\sigma_{(-0.8, 0.3)} = 0.585 \cdot \sigma_{LR} + 0.035 \cdot \sigma_{RL}. \quad (5.2)$$

The resulting weights for all four helicity states for various polarisations are listed in tab. 5.1. Additionally, the number of events used in the event selection need to be weighted corresponding to the integrated luminosity (here $\mathcal{L} = 2 \text{ ab}^{-1}$). Combined with the polarisation weighting this leads to an overall weighting factor of

$$w_{tot} = \frac{\sigma \cdot \mathcal{L}}{N_{gen}} \cdot w_{pol}, \quad (5.3)$$

where N_{gen} denotes the number of generated events of a certain process and helicity state, and w_{pol} the polarisation weighting factor.

5.1.1 Signal Process

The analysis is based on a full GEANT4 detector simulation, considering $\sqrt{s} = 500 \text{ GeV}$ and $\mathcal{L} = 2 \text{ ab}^{-1}$, and the ILC baseline beam polarisation of $P(e^-e^+) = (-0.8, 0.3)$. At these conditions, the ZHH cross section is $\sigma(ZHH) \sim 0.2 \text{ fb}$ for $m_H = 125 \text{ GeV}$. This corresponds to approximately 395 events.

The Higgs self-coupling analysis is performed by dividing ZHH into three channels with respect to the Z -decay mode ($Z \rightarrow ll, \nu\nu, qq$) as sketched in fig. 5.1. This assumption can be made if the three channels are statistically independent. In $llHH$, an isolated lepton pair

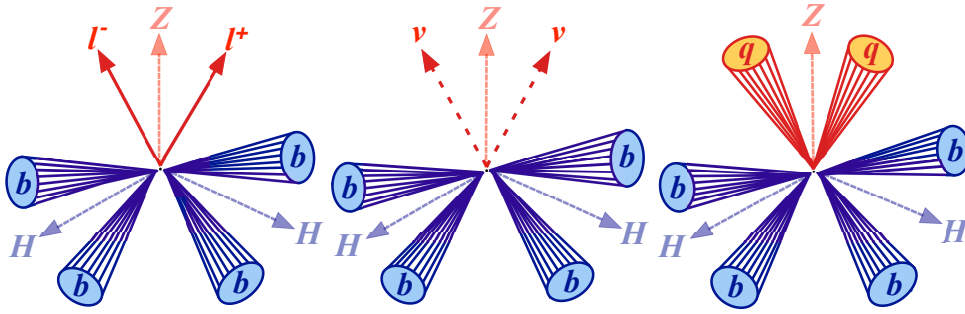


Figure 5.1: Signal channels categorised by the decay mode of the Z boson. The lepton channel $Z \rightarrow ll$ (left), the neutrino channel $Z \rightarrow \nu\bar{\nu}$ (middle), and the hadron channel $Z \rightarrow qq$ (right). The final state with $HH \rightarrow bbbb$ is investigated in this thesis.

requirement rejects all full-hadronic events. Therefore, $llHH$ is statistically independent of $qqHH$. The missing energy in $\nu\nu HH$ is not satisfied in both $llHH$ and $qqHH$. Thus, $\nu\nu HH$ is statistically independent of the other two channels.

Separate samples are produced for each channel as listed in tab. 5.2. During event generation the Z decay has been restricted to one of the respective decay channels. The data samples include all Higgs decay modes. The largest fraction of events in the samples are expected to be Higgs boson decays into a pair of b quarks with $BR(H \rightarrow bb) \approx 57.7\%$ [27]. This channel represents the desired signal final state in this thesis. Contributions of ZZ fusion and WW fusion are not considered since they are negligible at $\sqrt{s} = 500$ GeV.

Lepton Channel

From the overall 395 ZHH events, only 10% correspond to $llHH$, which is equivalent to ~ 40.5 events. Considering $HH \rightarrow bbbb$ leaves 14.2 events. Although $llHH$ gives the smallest contribution to ZHH , it offers the cleanest final state with four b jets from the two Higgs bosons and two isolated leptons originating from the Z boson. To avoid complications of τ decays we focus on $l = e, \mu$ in the event selection of $ZHH \rightarrow llbbbb$.

In this channel backgrounds contribute with only small missing four-momentum in the final state. Processes with more than two neutrinos in the final state can be easily rejected by missing transverse momentum (p_T) requirements. Backgrounds with at least one isolated lepton in the final state are taken into account, due to possible inefficiencies in isolated lepton finding. Full-hadronic backgrounds are also considered which result in four-jet and six-jet final states. However, the events can be suppressed by efficient isolated lepton identification.

Neutrino Channel

Roughly 20% of the ZHH events correspond to $\nu\nu HH$, which is equivalent to 80.1 events. Only 28.5 events correspond to $\nu\nu bbbb$. The final state consists of four b jets and missing

signal	σ [fb]	N_{exp} [evts]	fraction	N_{gen} [evts]
$llHH$ ($llbbbb$)	0.02 (0.007)	40.5 (14.3)	10% (3.6%)	$3.45 \cdot 10^5$
$\nu\nu HH$ ($\nu\nu bbbb$)	0.04 (0.014)	80.1 (28.5)	20% (7.2%)	$3.91 \cdot 10^5$
$qqHH$ ($qqbbbb$)	0.14 (0.049)	273.1 (99.5)	70% (25.0%)	$1.13 \cdot 10^6$

Table 5.2: Summary of signal channels for a Higgs mass of 125 GeV. The given numbers correspond to the ILC baseline polarisation $P(e^-e^+) = (-0.8, 0.3)$ and $\mathcal{L} = 2 \text{ ab}^{-1}$.

energy equivalent to the Z-boson mass. In the event generation no discrimination is made between the different neutrino flavours.

In contrast to the lepton channel, backgrounds with missing four-momentum are evaluated in context of this channel. This includes backgrounds with two neutrinos in the final state. Due to inefficiencies in the isolated lepton identification semi-leptonic backgrounds are also considered. Moreover, since ISR can carry a certain amount of energy which stays undetected, four-jet and six-jet full-hadronic backgrounds can pass a missing energy requirement and need to be considered. ISR does not carry p_T since these photons are very forward and backward. Backgrounds with more than one isolated lepton in the final state can be easily suppressed and are not evaluated in this channel.

Hadron Channel

The largest contribution of $\sim 70\%$ to the total number of ZHH events is given by $qqHH$. This is equivalent to 273 events, 99.5 events of which correspond to $qqbbbb$. This channel results in a challenging environment in the detector. Providing a six-jet final state with at least four b jets, which generally have larger multiplicities compared to light jets, the hadron channel poses high demands on the reconstruction software and detector technologies (section 4.1).

As discussed in the neutrino channel, semi-leptonic backgrounds are taken into account. Additionally, next to six-jet full-hadronic backgrounds, four-jet full-hadronic backgrounds are considered due to possible mis-identification caused by mis-clustering and gluon radiation. Six-jet full-hadronic backgrounds are taken into account which include at least two b jets in the final state. Events with large missing four-momentum can be suppressed by missing p_T requirements. Moreover, backgrounds giving up to eight-jet final states, i. e. ttg , ttZ , are taken into account in this channel.

The entire backgrounds used in this analysis are discussed in the following.

5.1.2 Background Processes

The small signal production rate is overwhelmed by a large number of different SM background processes. Since large efficiencies in flavour tagging at the ILC (sec. 4.3.1) allow

the identification of b jets, all SM backgrounds with two or more b quarks in the final state are considered in the analysis. Two-fermion background can be easily suppressed by flavour tagging and is not taken into account. The various background processes are summarised in tab. 5.3.

The most challenging background is represented by ZZH and ZZZ . The former process has a rather small production cross section of $\sigma = 0.898$ fb compared to ZZZ with $\sigma = 12.18$ fb. Feynman diagrams for both background processes are shown in fig. 5.2 in case of $Z \rightarrow ll$. Both backgrounds can give the same final state as the signal. Therefore, it is crucial to reconstruct these backgrounds very precisely to be able to discriminate the events from signal events. In order to suppress such backgrounds, the most essential discriminative variables in the event selection are boson mass distributions which take a leading role this thesis. ZZH samples with the final states of $llqqH$, $\nu\nu qqH$, and $qqqqH$ are generated by restricting one Z to the desired decay mode and the other to $Z \rightarrow qq$. The samples for the ZZZ background correspond to the final states of $llbbqq$, $\nu\nu bbqq$, and

background	σ [fb]	N_{exp} [evts]	N_{gen} [evts]
ZZH (total)	0.63	1259.4	$8.76 \cdot 10^5$
$\rightarrow llqqH$	0.08	150.9	$1.91 \cdot 10^5$
$\rightarrow \nu\nu qqH$	0.22	447.0	$2.96 \cdot 10^5$
$\rightarrow qqqqH$	0.33	662.6	$3.89 \cdot 10^5$
ZZZ (total)	12.18	$2.4 \cdot 10^4$	$4.16 \cdot 10^5$
$\rightarrow llbbbb$	0.03	69.5	$1.49 \cdot 10^5$
$\rightarrow \nu\nu bbbb$	0.05	96.8	$1.08 \cdot 10^5$
$\rightarrow qqbbbb$	0.07	140.5	$1.59 \cdot 10^5$
$tt \rightarrow lvbbqq$ (total)	370.05	$7.40 \cdot 10^5$	$5.84 \cdot 10^6$
$\rightarrow ev_e bbqq$	124.23	$2.48 \cdot 10^5$	$2.46 \cdot 10^6$
$\rightarrow \mu\nu_\mu bbqq$	122.97	$2.46 \cdot 10^5$	$2.01 \cdot 10^6$
$\rightarrow \tau\nu_\tau bbqq$	122.85	$2.46 \cdot 10^5$	$1.37 \cdot 10^6$
$tt/WWZ \rightarrow bbqqqq$ (total)	312.03	$6.24 \cdot 10^5$	$3.88 \cdot 10^6$
$\rightarrow bbcssc$	77.95	$1.56 \cdot 10^5$	$1.31 \cdot 10^6$
$\rightarrow bbuddu$	78.07	$1.56 \cdot 10^5$	$1.03 \cdot 10^6$
$\rightarrow bbc sdu$	156.01	$3.12 \cdot 10^5$	$1.54 \cdot 10^6$
ttZ/H	1.09	$2.20 \cdot 10^3$	$8.49 \cdot 10^4$
ttg ($g \rightarrow bb$)	1.05	$2.11 \cdot 10^3$	$8.25 \cdot 10^4$
$bbbb$	20.12	$4.02 \cdot 10^4$	$1.02 \cdot 10^6$
$llbb$	166.07	$3.32 \cdot 10^5$	$6.53 \cdot 10^6$
$\nu\nu bb$	136.40	$2.73 \cdot 10^5$	$4.79 \cdot 10^5$

Table 5.3: Summary of background processes used in the analysis. Here, $l = e, \mu, \tau$. The listed numbers correspond to $\mathcal{L} = 2 \text{ ab}^{-1}$ and $P(e^-e^+) = (-0.8, 0.3)$. The $tt/WWZ \rightarrow bbqqqq$ background only includes final states with two b quarks. In ZZZ and ZZH at least two b jets are present.

$qqbbqq$. Here, qq represents a quark pair of the same flavour, i. e. $u\bar{u}$, $c\bar{c}$. However, final states with at least two light jets can be well-suppressed using flavour-tag information. The challenging contribution of ZZZ and ZZH is given by final states with four b jets.

The second most challenging background is given by full-hadronic final states $bbqqqq$ ($q = u, d, c, s$), i. e. $b\bar{b}c\bar{c}d\bar{d}u$, $b\bar{b}u\bar{d}d\bar{u}$, and $b\bar{b}c\bar{c}s\bar{s}c$. Example Feynman diagrams which contribute to this background type are shown in fig. 5.3. These events come from WWZ and $t\bar{t}$. In this case, the most challenging background in the event selection is $b\bar{b}c\bar{c}s\bar{s}c$, which requires large flavour-tagging efficiencies of b jets combined with a small fake rate for c jets. c tagging is less effective in the event selection, since the short life times of c and the secondary vertices result in less effective c tagging compared to b tagging. Also originating from $t\bar{t}$ and WWZ are semi-leptonic backgrounds $lvbbqq$, i. e. $lvbbcs$, $lvbbdu$ ($l = e, \mu, \tau$). Example Feynman diagrams are shown in fig. 5.3. These backgrounds include one isolated lepton and a neutrino causing missing four-momentum. Moreover, hadronically decaying τ can make b tagging less effective. Semi-leptonic background can be suppressed by either selecting an isolated lepton pair or rejecting events with isolated leptons. Moreover, $t\bar{t}Z/H$ and $t\bar{t}g$ events are taken into account. Gluon radiation and $Z/H \rightarrow qq$ can result in up to eight-jet final states. However, the cross sections of these processes are comparably small.

Also considered in the analysis are backgrounds which come from ZZ , $Z\gamma$, bbZ , $\nu\nu Z$ and llZ . These backgrounds give $llbb$, $\nu\nu bb$ and full hadronic final states. For the latter, $bbbb$ is dominant, since backgrounds as $bbqq$ ($q = u, d, c, s$) are well-suppressed by flavour-tagging requirements. Example Feynman diagrams are shown in fig. 5.4.

5.2 Analysis Strategy

The analysis is based on the strategy used in [108]. The analysis is performed for a Higgs boson with a mass of 125 GeV. So far the low- p_T $\gamma\gamma \rightarrow$ hadrons background has not been considered in previous analyses yet and is investigated in this study. Therefore, the analysis is performed for the case with and without overlay to get an estimate of its effects. In the following, the main steps of the event selection are outlined and explained. To compare changes in the event selection strategy refer to [108]. The crucial steps in the preselection and final selection are investigated in this thesis.

5.2.1 Preselection

The preselection is very similar for the three channels. It already offers many starting points for possible improvements in the analysis, which can be investigated and optimised.

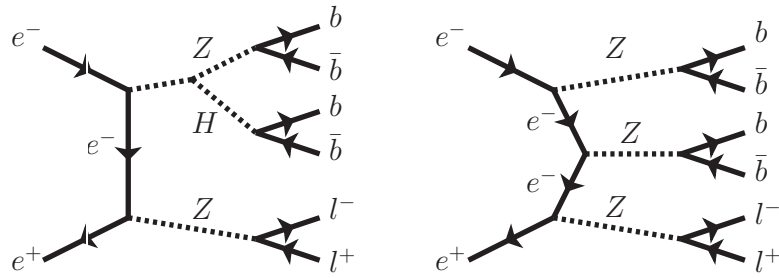


Figure 5.2: Example ZZH and ZZZ background diagrams for the same final state as the signal. The example diagrams correspond to the channel with $Z \rightarrow ll$.

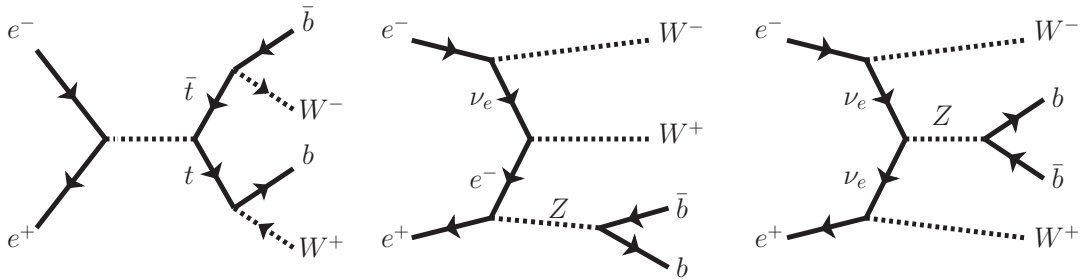


Figure 5.3: Example diagrams contributing to the semi-leptonic and fully hadronic backgrounds. Backgrounds in which either one W boson decays leptonically or both W bosons decay hadronically are taken into account in the analysis. The backgrounds come from $t\bar{t}$ and WWZ decays.

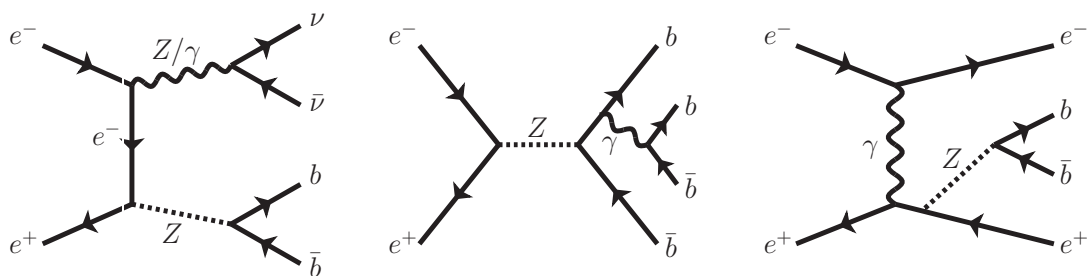


Figure 5.4: Example Feynman diagrams for backgrounds with two jets, or four-jet fully hadronic backgrounds.

Isolated Lepton Tagging

Depending on the evaluated signal channel, it is important to select or reject events with isolated leptons. In both the $\nu\nu HH$ and $qqHH$ channel no isolated lepton is present in the final state. Leptons can only occur as part of a jet. The isolated lepton selection can be used as veto against semi-leptonic backgrounds. In the $llHH$ channel, the final state includes two isolated leptons. Selecting events with two isolated leptons helps to suppress full hadronic backgrounds and semi-leptonic background processes. In $llHH$ the mass of the lepton pair has to be consistent with the Z -boson mass within $|M_{ll} - M_Z| < 40$ GeV. The isolated lepton selection is the first step of the analysis, in which large background contributions can be rejected. Thus, high efficiencies and purities are needed.

Overlay Removal

In the analysis with $\gamma\gamma$ overlay, the overlaid events need to be identified and removed from the reconstructed particle list to recover the original events. Then, it is possible to investigate the impact of the overlay on the Higgs self-coupling measurement. So far, the $\gamma\gamma$ overlay has not been considered in previous Higgs self-coupling analyses. Therefore, this study gives a significant hint on whether more advanced removal strategies and more sophisticated tools are needed which include a precise modelling of low- p_T $\gamma\gamma \rightarrow$ hadrons background and exploit the full power of high granularity detectors. To investigate the effects of the $\gamma\gamma$ overlay on the analysis the standard DBD overlay removal strategy needs to be evaluated and optimised.

Jet Clustering and Flavour Tagging

All other PFOs are then clustered into either four or six jets, depending on the investigated signal channel, and flavour-tag information are obtained. Mis-clustering of jets can degrade the mass reconstruction. Therefore, advanced clustering algorithms are required. Flavour-tag information are crucial, since the Higgs decays predominantly into a pair of b quarks. Moreover, flavour tagging plays a crucial role also in the jet pairing of the six-jet final state of $qqHH$, as discussed in the following.

Jet Pairing

Double Higgs-strahlung events result in four- and six-jet final states. Due to the small ZHH production cross section it is essential to reconstruct the small number of signal events very precisely and suppress the large background contributions. Since boson masses play an essential role in the event selection the jets representing the primary quarks have to be reconstructed and finally paired to form the signal bosons. The clustered jets are paired to form the bosons of the signal final state by choosing the jet pair combination

with the smallest χ^2

$$\chi^2 = \frac{(M(j_i j_j) - M(H))^2}{\sigma_H^2} + \frac{(M(j_k j_l) - M(H))^2}{\sigma_H^2} + \frac{(M(j_m j_n) - M(Z))^2}{\sigma_Z^2}, \quad (5.4)$$

in which $\sigma_H = 7.2$ GeV represents the Higgs mass resolution, and $\sigma_Z = 6.0$ GeV the Z-mass resolution. Taking different values for σ_H does not affect the jet pairing. The natural width of the Higgs boson is very narrow for the investigated Higgs mass ($\Gamma_H < 10$ MeV), and thus the detector resolution on the Higgs mass is significantly larger than the natural width of the Higgs boson [127]. $M(H)$ and $M(Z)$ denote the nominal Higgs and Z mass, respectively. Eq. 5.4 can be modified for various final-state hypotheses. In the lepton and neutrino channel jets are combined to the two Higgs bosons by using a light constraint on the Higgs masses as $|M_{jj} - 125 \text{ GeV}| < 80 \text{ GeV}$. In the hadron channel flavour-tag information are necessary to find the correct jet pairs.

5.2.2 Challenges in Higgs Mass Reconstruction

Compared to neutrinos and leptons, the precise reconstruction of the primary quarks by measuring jet four-momenta is limited. The primary quarks fragment into quark-antiquark pairs and gluons. These fragments share the initial four-momentum of the quarks. This process is called parton showering. The fragments tend to move collinear to the direction of the initial quark. Shower fragments following a particular direction are known as jet. Due to the colour confining nature of QCD, the fragments form colour singlet hadrons. This is known as hadronisation. The average number of hadrons in a jet increases logarithmically with the energy of the initial quark. Moreover, quarks can emit gluons. Gluons produce additional jets which have different characteristics compared to the jets initiated by a quark. At higher energies, a gluon-initiated jet is broader than a quark-initiated jet. Additionally, gluon jets contain hadrons with higher multiplicity than that of quark-induced jets. Aspects limiting the reconstruction of quarks were listed in sec. 4.1.1. Mis-clustering and the wrong jet pairings are two aspects degrading the mass resolution. Possible semi-leptonic decays of b and cascade c quarks also lead to wrongly reconstructed jet four-momenta. Moreover, since the ZHH events are produced close to energy threshold at 500 GeV, the jets are less collimated and a significant overlap is present. While in both the lepton and neutrino channel only four jets need to be combined to form the two Higgs bosons, the hadron channel $ZHH \rightarrow qqbbbb$ is very challenging with its six-jet environment. There are 45 possible combinations to form the signal final state of ZHH . It is challenging to find the correct pairing, since many jet-pair combinations obtain small χ^2 . In this channel, jet pairing is prone to errors due to combinatorics. The mis-identification of the correct jet permutation is rather high for two permutations with very small differences in their χ^2 value. Therefore, in the hadron channel a b -tag requirement is used to support the jet pairing by choosing the permutation with smallest χ^2 (eq. 5.4). A detailed discussion is given in chapter 8.

5.2.3 Final Selection

The number of background events is significantly reduced in the preselection. However, the background in each channel is still three orders of magnitude larger than the signal. The main idea of the final selection is the usage of multivariate analysis techniques (MVA) as implemented in TMVA [176]. MVAs take into account the correlations between variables used for the event selection which is also the main advantage over cut-based strategies. Various classifiers are available. Detailed information can be found in [176]. The best MVA classifier is evaluated by testing different algorithms. The training algorithm creates a mapping function which is used to calculate whether an event is signal-like or background-like. Statistically independent event samples of known processes are required for training and testing in order to prevent overtraining. Overtraining indicates that the output classifier is sensitive to statistical fluctuations of the training sample. This is often the case for limited statistics. The statistical fluctuations can lead to an overestimation of the discriminative power between signal and backgrounds. The best classification techniques are boosted decision trees (BDT) [177, 178] and artificial neural networks (MLP) [176]. However, in TMVA the training time of BDTs is an order of magnitude shorter than for neural nets. Decision trees with gradient boosts (BDTG) are also less sensitive to overtraining. Moreover, compared to neural nets, decision trees are insensitive to the amount of input variables and poorly discriminating variables. While neural nets have difficulties to deal with such variables, BDTs ignore non-discriminating variables [176].

In the analysis, several MVAs are trained for the dominant backgrounds after preselection. Also considering the limited statistics, training just one MVA for the entire background in each signal channel would degrade the performance of the MVA classifier, since the strongest impact during training would be given by the largest background process. Consequently, since the various background types have very different event topologies and different weights, separate MVAs are trained to suppress the dominant backgrounds. The MVAs are trained sequentially, which means that the foregoing cuts of the event selection are considered in training. This also includes cuts on previous MVA outputs. In [108] MLPs are used. However, in this thesis various MVA techniques have been evaluated and optimised to see if the background suppression can be improved. The use of BDTGs instead of MLPs results in a relative improvement of the signal significance by 10% in the lepton channel and by 5% in the neutrino channel. In the hadron channel both classifiers give similar results. The input variables for MVA training are optimised in this thesis. A detailed discussion is given in chapter 8. Before MVA training, precuts on specific signal channel properties are applied to reduce the backgrounds and be more sensitive to the signal. The cuts on the BDTG outputs are optimised with respect to the maximum signal significance $\sigma = \frac{s}{\sqrt{s+b}}$ in the final selection. Since each BDTG is trained for one background type respectively, optimising the optimal cut values suggested in training could suppress other background types. For BDTG training additional statistically independent data samples for signal and backgrounds are used. The weights for the different processes are normalised to the corresponding cross sections and beam polarisation.

Lepton Channel

After preselection the dominant backgrounds are: (1) $ZZ \rightarrow llbb$, (2) semi-leptonic backgrounds $lvbbqq$, and (3) the background processes ZZH and ZZZ . For each of the three background types an MVA is trained. In the event selection, the events are divided into electron-type and muon-type events. The MVAs are trained by using kinematic variables. However, due to the limited statistics combined MVAs are trained since the used input variables are of similar shapes for both lepton-type events, since final-state radiation (FSR) is recovered in the events. Nevertheless, training three MVAs for the electron-type and muon-type events respectively, could improve the event selection. More statistics would be needed. Additional precuts on the boson masses and missing transverse momentum are applied in [108] before training to be more sensitive to the signal. At the end of the event selection, the application of flavour-tag information is evaluated to select $ZHH \rightarrow llbbbb$ events after the background suppression via MVA. A detailed discussion is given in chapter 8.

Neutrino Channel

In the neutrino channel, missing energy consistent with the Z mass is carried away by neutrinos. Missing energy and missing transverse momentum requirements are applied, which especially concern fully-hadronic backgrounds after the preselection. In the signal missing transverse momentum can occur from semi-leptonic decays in the jets and $Z \rightarrow \nu\nu$, while missing energy is also carried away by ISR. Backgrounds with only two b jets are suppressed with additional cuts on the Higgs masses and the invariant mass of all PFOs, which should be equal to the mass of the two Higgs bosons in case of the signal. After these precuts, the dominant backgrounds are given by $bbbb$, $lvqqbb$ and $\nu vbbbb$. For the three background categories separate MVAs are trained. Flavour-tag information are used at the end of the event selection of select the desired $\nu vbbbb$ final states.

Hadron Channel

After preselection in the hadron channel, which includes an isolated lepton veto and flavour-tag requirement in the jet pairing, additional precuts are applied to reduce the large number of background events before MVA training. MVAs are trained for $bbbb$, and for the full-hadronic backgrounds $bbqqqq$ ($q \neq b$) and $qqbbbb$. In the final selection, all events are separated into two categories, called “ $bbHH$ dominant” and “light $qqHH$ dominant”, according to the flavour tag of the two jets from the Z -boson decay. The sum of b likeliness of the two jets assigned to the Z is illustrated in fig. 5.5. The b likeliness is shown for true $bbHH$ and $qqHH$ events, as well as true $HH \rightarrow bbbb$ events. At large b -tag values the events are well-reproduced. At small b -tag values, the true $bbHH$ and $bbbbbb$ events show different distributions. This is due to the jet-pairing requirement and will be discussed in chapter 8. We have investigated that by optimising and performing the event

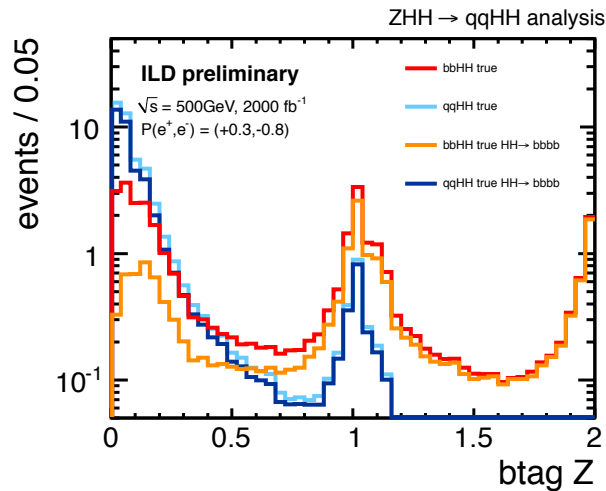


Figure 5.5: The combined flavour tag $btagZ$ of the two jets which are assigned to the Z -boson decay in the $qqHH$ channel. The $\gamma\gamma$ overlay is not included.

selection without such a separation of $qqHH$ into two categories, the signal significance is degraded by 10% compared to the evaluation of the two separate categories. Therefore, this strategy [108] is also adapted in this study using the threshold $btagZ > 0.54$ for “ $bbHH$ dominant” and $btagZ < 0.54$ for “light $qqHH$ dominant”. This threshold reproduces the events most precisely.

Similar to the lepton channel, the kinematic distributions look similar for both categories. Due to limited statistics, combined MVAs are trained. While the selection cut on the first MVA output ($bbbb$) should not differ for both categories, the cuts on the second ($bbqqqq$) and third ($qqbbbb$) MVA output are slightly adjusted and optimised for the different categories. Training separate MVAs could enhance the signal selection. However, larger statistics would be needed (chapter 8). Since this channel gives the largest contribution to the overall ZHH events, optimising this mode is very important.

The event selection and MVA training for the three channels is discussed in chapter 8. After the event selection the combined ZHH significance is determined, indicating whether double Higgs production can be observed at the ILC at $\sqrt{s} = 500$ GeV using ZHH events. Additionally, the ZHH cross section is extracted, which gives information on the achievable precision of the Higgs self-coupling measurement.

5.3 Standard Analysis Tools

Most of the analyses of multi-jet final states apply jet-clustering algorithms and flavour-tagging tools as it is the case for double Higgs-strahlung events. As indicated in the foregoing, the resulting information are necessary to reconstruct the final states. Various analysis tools are included in MarlinReco [173], e. g. processors for lepton finding, jet

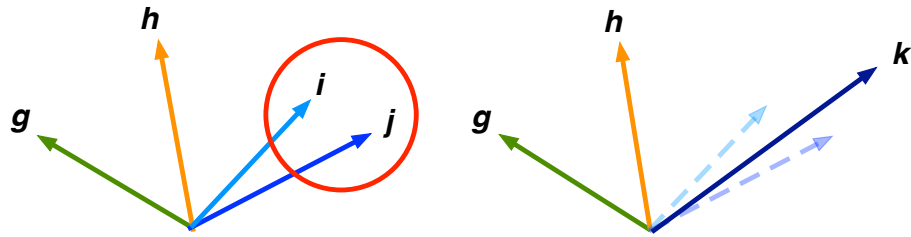


Figure 5.6: Schematic sketch of the Durham jet-clustering algorithm. Two (pseudo) particles i and j having the smallest angular distance θ_{ij} and energy $\min(E_i^2, E_j^2)$ are clustered into a new pseudo particle k .

clustering, or kinematic fitting. Such processors can be easily extended and new processors can be build independently and included to the analysis. The standard analysis tools, which are basically used in ILC physics studies and in the Higgs self-coupling analysis, are described in the following. This includes the standard jet-clustering and $\gamma\gamma$ overlay removal algorithm, and the flavour-tagging procedure.

5.3.1 Jet Clustering

In the event selection, reconstructed particles are clustered into jets using the Durham algorithm [179, 180], the description of which is based on [180]. Next to the Durham algorithm, there are various jet-clustering algorithms available for physics analyses. Durham is the most frequently used algorithm. In this analysis non-standard algorithms for e^+e^- studies play a role in context of the $\gamma\gamma$ -overlay removal (sec. 6.2) and will be described in the next section. The Durham algorithm is based on the relative distance measure y_{ij} between two particles i and j and reads

$$y_{ij} = 2\min(E_i^2, E_j^2) \frac{(1 - \cos \theta_{ij})}{E_{CM}^2}. \quad (5.5)$$

Here, θ_{ij} denotes the angle between the particles i and j , $E_{i,j}$ the energy of the respective particle, and E_{CM} the centre-of-mass energy of the event. The Durham algorithm evaluates y_{ij} for every pair of reconstructed particles. A schematic sketch is shown in fig. 5.6. The two particles with smallest relative distance y_{ij} are clustered to a pseudo particle k by combining their four-momenta $p_k^\mu = p_i^\mu + p_j^\mu$. This recombination is called E scheme. The Durham algorithm is an iterative process which terminates when the number of merged pseudo particles matches the number of requested jets. Compared to the exclusive k_t jet-clustering algorithm (sec. 5.3.2) in which certain particles are clustered into beam jets and removed from the particle list, Durham involves all particles in the clustering of the requested number of jets. Additionally, the algorithm provides two output parameters $y_{m,m+1}$ and $y_{m-1,m}$. m denotes the number of requested jets. These parameters can be explained as follows: Starting with n particles, the iterative clustering procedure gives $n-1, n-2, n-3, \dots, m$ clustered objects until the predefined number of jets m is reached.

For instance, after iteration $(n - 1)$ the resulting pseudo particle k is further away from a third and now closest particle h than was the nearest of the two original particles i and j before clustering: $y_{kh} > \min(y_{ih}, y_{jh})$. Hence, the pseudo particle k which was clustered from particles i and j , has a larger smallest distance to the now nearest particle in the next iteration: $y_{n-1,n} > y_n$. Until m is reached and the jet-clustering algorithm is terminated, the smallest distances after every iteration follow

$$y_{n-1,n} < y_{n-2,n-1} < \dots < y_{m-1,m}. \quad (5.6)$$

Consequently, $y_{m-1,m}$ represents the smallest distance between the two closest jets in an m -jet configuration. This parameter is an important measure to separate events with m -jet topologies from events with $(m - 1)$ -jet and $(m - 2)$ -jet final states. $y_{m-1,m}$ is expected to be large if the event is consistent with the predefined m -jet configuration. The second output parameter $y_{m,m+1}$ describes the relative distance between an object and its nearest neighbour before merging in the last iteration step. If the event is consistent with the predefined m -jet configuration, $y_{m,m+1}$ is expected to be small. This parameter can be used to separate m -jet final states from events with $(m + 1)$ -jet or $(m + 2)$ -jet topologies.

5.3.2 Standard Overlay Removal

Similar to the beam remnants in pp collisions, the overlaid $\gamma\gamma$ events (sec. 3.4.2) have small transverse momenta. They are detected in the forward region of the detector and resemble jets which move along beam line. These characteristics allow to apply an overlay-removal strategy based on the exclusive k_t jet-clustering algorithms, originally developed for hadron-collider analyses (sec. 5.3) [181, 182].

The general technique is based on exclusive jet-clustering algorithms, in which not all reconstructed particles in an event are assigned to hard final-state jets but also to two additional very forward jets. The particles in these so-called beam jets get removed from the reconstructed particle collection. The exclusive k_t jet-clustering algorithm, which is included in FastJet [183] in ILCSoft, is applied to unselect the overlaid particles. The exclusive k_t algorithm is based on two distance measures [184]

1. the distance d_{ij} between each pair of particles i and j defined as

$$d_{ij} = d_{ji} = \min(p_{ii}^2, p_{ij}^2) \cdot \frac{\Delta R_{ij}^2}{R^2}, \quad (5.7)$$

with $p_{ii,tj}$ denoting the transverse momentum of particle i and j with respect to beam direction, and R representing the jet radius parameter defined as $\Delta R_{ij}^2 = (y_i - y_j)^2 + (\phi_i - \phi_j)^2$. Here, y_i and ϕ_i denote pseudo-rapidity and azimuth angle of particle i , respectively.

2. the distance d_{iB} between every particle and the beam, which reads

$$d_{iB} = p_{ii}^2. \quad (5.8)$$

In the exclusive k_t algorithm the values of d_{iB} and d_{ij} for every particle i and every pair ij are evaluated. Among both distances the smallest value is determined. If $d_{ij} < d_{iB}$, particle i and j are paired to a so-called pseudo jet by combining their four-vectors $p_i + p_j$. If $d_{iB} < d_{ij}$, particle i is assigned to the forward beam jets and removed from the particle list. This procedure is iterated until the number of jet candidates is equal to the number of requested jets N_{jets} . Thus, N_{jets} serves as termination threshold for the exclusive k_t algorithm. After the jet-clustering procedure we are left with two beam jets and the requested number of hard jets. By considering only particles included in the hard jets and by discarding the two beam jets, the bare events without overlay can be recovered. The hard jets are decomposed back into single PFOs which are then used in the analysis. Since in this clustering procedure we are only interested in the overlay removal, the requested number of jets N_{jets} can differ from the original event topology. Requesting more jets has no impact on the reconstruction of the final-state processes later in the analysis and can be interpreted as improving the resolution of the algorithm.

5.3.3 Vertex Finding and Flavour Tagging

Vertex finding and flavour tagging is performed using LCFIPlus [172] which is embedded in ILCSofT and described in the following. The description is based on [172]. LCFIPlus includes algorithms for vertex finding to reconstruct primary and secondary vertices, for jet finding optimised for heavy-flavour jets, and for flavour tagging based on multivariate analyses implemented in TMVA [176]. In LCFIPlus vertex finding is performed before jet clustering and flavour tagging to prevent effects from jet-finding ambiguities, i. e. wrongly grouped secondary vertices.

Vertex finding is part of the standard event reconstruction. However, during the overlay removal particles are removed from the event collection, which can alter the results of the vertex finder. As a result, vertex finding needs to be re-run. The vertex finder is implemented as a χ^2 minimiser and split into primary and secondary vertex finding. In primary vertex finding all reconstructed particles are fitted and a global χ^2 is determined for all the tracks in the event. If a track contributes the largest to the global value and its χ^2 is larger than a predefined threshold, it is removed. The procedure is iterated until only tracks with a χ^2 below the threshold are left over. Secondary vertex finding concerns tracks which do not arise from primary vertices. Those tracks are paired, while certain criteria need to be fulfilled [172], e. g. neutral particles, so-called V^0 particles, which decay or convert into a pair of charged tracks are rejected. V^0 particles leave signatures which resemble b and c quarks. Filters are applied which reconstruct and remove V^0 particles, as K_s^0 , Λ^0 or photon-pair conversion, from the list of particles. The identification is based on kinematic variables of the track pairs. To identify vertices with more than two decay products all tracks are tested if they are compatible with the vertex candidates. In such a case the tracks are attached to the track pairs. This is repeated until no more

tracks can be combined according to the selection criteria. To avoid using tracks in more than one vertex the vertices are sorted with respect to the number of tracks and their χ^2 value. The first vertex is selected and the related tracks are removed from other vertices. This procedure is iterated until no more vertex candidates remain.

Jet clustering is applied after vertex finding in LCFIPlus. This way the vertex information are preserved in the jet-clustering stage since jet-clustering algorithms could cluster particles from the same vertex into different jets, which would degrade the flavour-tagging performance. The vertices are identified first and combined if the opening angle between them is ≥ 0.2 rad. The particles of these vertices are used as seed jets for jet clustering. The basic jet-clustering algorithm relies on the Durham algorithm (section 5.3.1). The reconstructed jets contain all vertex information. Hence, the design of LCFIPlus is optimised for efficient flavour tagging of jets. A detailed description of the LCFIPlus jet finder can be found in [172].

Flavour tagging is based on a neural net approach implemented in TMVA [176], and combines track and vertex information to distinguish b , c , and light jets. According to the number of reconstructed vertices, the jets are grouped into different sets. For each set a multivariate classifier, a so-called Boosted Decision Tree (BDT), is trained for three flavour hypotheses: b , c , and uds . The set of input variables is listed in [172]. The input variables are normalised with respect to the jet energy to remove the jet energy dependence. The latter cannot be avoided due to acceptance cuts and detector effects, which are not invariant as a function of the jet energy. Therefore, various classifier weighting samples are provided, covering a wide range of centre-of-mass energies. Event samples with six-jet final states are employed for 500 GeV. For each jet the routine returns a flavour-tag value between 0 and 1, corresponding to the flavour likeliness of the jet. For b jets we expect a peak at 1, and a peak at 0 for jets of the other flavours. As a result flavour-tag information can be used in the event selection of physics studies.

Chapter 6

Reconstruction Improvements

In this analysis, the three different signal final states need to be reconstructed with high efficiencies. As discussed in the previous chapter, the analysis strategy provides several starting points for improvements. In the context of this thesis, three crucial analysis steps are investigated and optimised:

1. The selection of isolated leptons requires high efficiencies and purities to suppress large background contributions and keep as much signal events as possible. Depending on the signal channel, events with isolated leptons are selected or rejected. A neural net based strategy is developed and discussed in sec. 6.1.
2. The $\gamma\gamma$ overlay (sec. 3.4.2) needs to be identified and removed from the reconstructed particle list to recover the bare events. So far the $\gamma\gamma$ overlay has not been included in previous Higgs self-coupling analyses. In sec. 6.2 the standard DBD removal is studied and optimised to investigate the impact on the analysis.
3. Jets are paired to form the bosons of signal and background processes. Misclustering and wrong jet pairings degrade the mass resolution. Tools to improve invariant mass resolutions are kinematic fits which take a leading role in this thesis. The concept of kinematic fits is introduced in sec. 6.3. Analysis applications are studied using default settings of MarlinKinfit [185] and are discussed in sec. 6.4 and 6.5.

6.1 Isolated Lepton Tagging

In the following, the isolated lepton selection is described in context of $llHH$. In this channel events are selected which contain an isolated lepton pair consistent with M_Z .

DBD Isolated Lepton Selection

The isolated lepton identification used in [108] is a cut-based method which is mainly based on the energy distributions in the calorimeters. Electrons deposit almost their entire

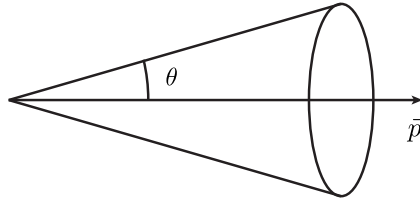


Figure 6.1: Schematic sketch of a defined cone around the direction of a reconstructed particle with momentum \vec{P} . The cone angle is denoted by θ .

energy in the ECAL, whereas muons deposit just a small fraction of their energy in the ECAL and HCAL. Opposed to this, charged hadrons shower in the HCAL.

There are four main contaminations [108]: (1) Semi-leptonic decays from b and c quarks, i. e. $b \rightarrow cl\nu$ and $c \rightarrow sl\nu$. (2) Semi-leptonic W decays in case of $H \rightarrow WW$. (3) Charged pions π^\pm which interact in the ECAL and produce $\pi^0 \rightarrow \gamma\gamma$. They shower in the ECAL and resemble electrons. (4) High-energetic π^\pm which do not shower in the HCAL and reach the yoke. These pions can be mis-identified as muons.

Compared to isolated prompt leptons, mis-identified particles in (1) - (3) have generally smaller momenta and more particles around them from parton showering and fragmentation. To reduce mis-identification, information on the impact parameters $d0$ and $z0$ are used to constrain leptons to the primary vertex. Additionally, a so-called cone energy is defined. A cone with an angle θ is defined around the momentum of each particle and the energies of the particles inside the cone are summed up (fig. 6.1). Here, $\cos(\theta) = 0.98$. Further discrimination is achieved by using the total momentum P and the yoke energy. The applied cuts for the isolated electron and muon selection can be found in [108].

Optimised Isolated Lepton Selection

A new strategy is developed which is based on neural net training of a multivariate classifier (MVA). The so-called `IsolatedLeptonTagger` was initially developed for the Higgs self-coupling analysis (`ZHH114JLeptonSelectionProcessor`), but can be modified to either reject events with isolated leptons or select events with one or more isolated leptons. Using samples with two isolated leptons in the final state, i. e. e^+e^-HH and $\mu^+\mu^-HH$, neural nets were trained against full hadronic $bbbb$ background samples. For the selection of one isolated lepton, $lvbbqq$ samples are used and trained against $bbbb$ events. The samples were generated for $\sqrt{s} = 500$ GeV and include the $\gamma\gamma$ overlay. Neural nets were trained separately for electron-type and muon-type events. The respective weight files are available for analysis processors. The input variables are shown in fig. 6.2 for electron and in fig. 6.3 for muon classification. Both MVAs share following input variables:

- **Cone energy:** if charged (neutral) PFOs are considered, it is called charged (neutral) cone energy. It is expected to be large for mis-identified PFOs as isolated e^\pm/μ^\pm .

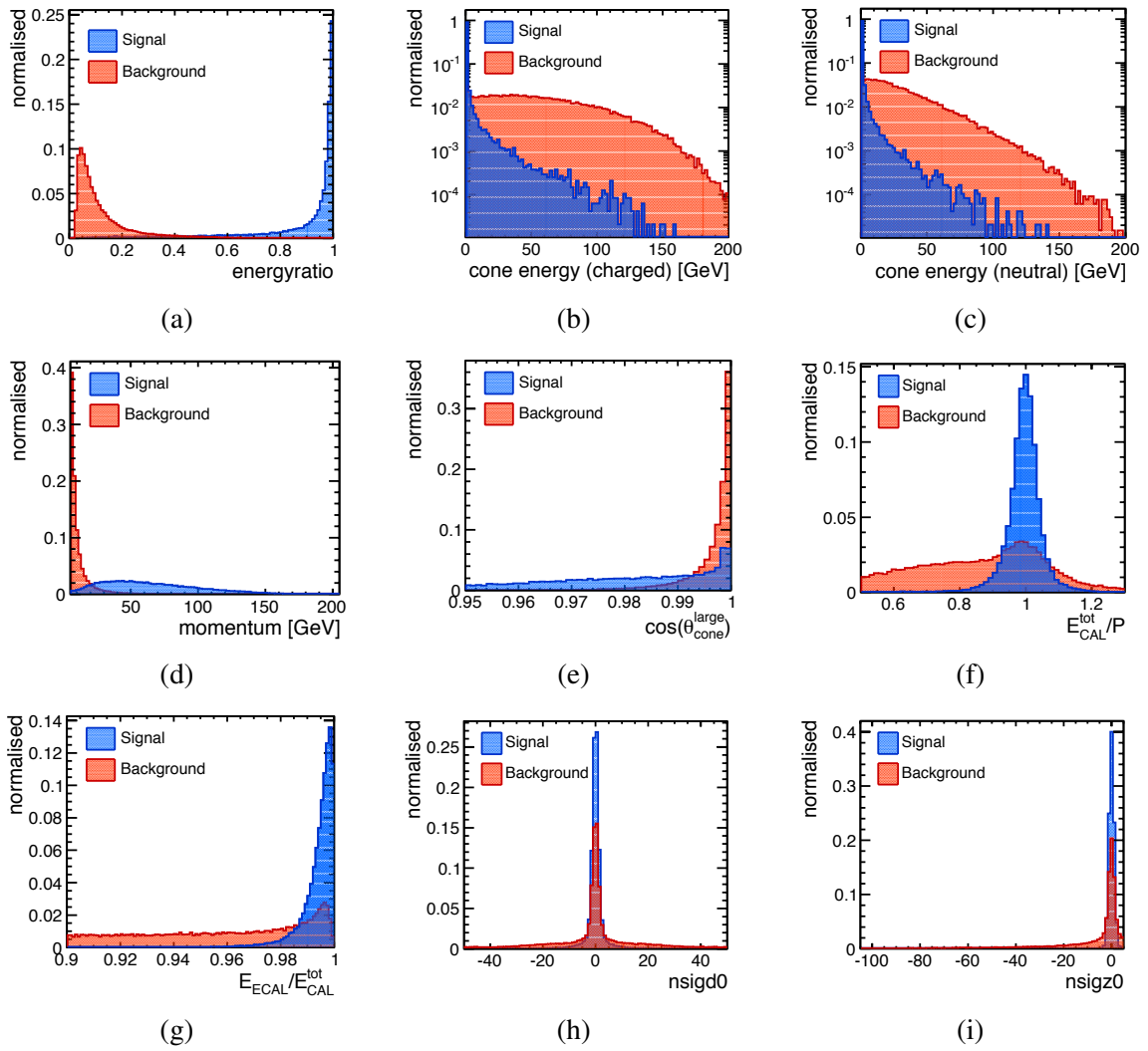


Figure 6.2: Input variables for electron-type events. Description can be found in the text.

- **Energy ratio $E/(E + E_{cone})$:** a cone around the direction of a reconstructed particle is defined and the energies are summed up. Since isolated leptons have a small cone energy, the energy ratio is close to 1.
- **Total momentum:** mis-identified leptons generally have smaller momenta compared to isolated prompt leptons. Therefore, the total momentum is taken into account.
- **Impact parameters $d0$ and $z0$:** the isolated leptons from the Z boson are expected to originate from a primary vertex.
- **Cone angle $\cos(\theta_{cone}^{large})$:** in this case, the cone angle is defined as $\cos(\theta_{cone}^{large}) = 0.95$, to take into account the size of the jets. The $\cos(\theta_{cone}^{large})$ of every PFO is evaluated. Since mis-identified leptons can be part of jets, their cosine of the larger cone angle is expected to be larger compared to isolated leptons.

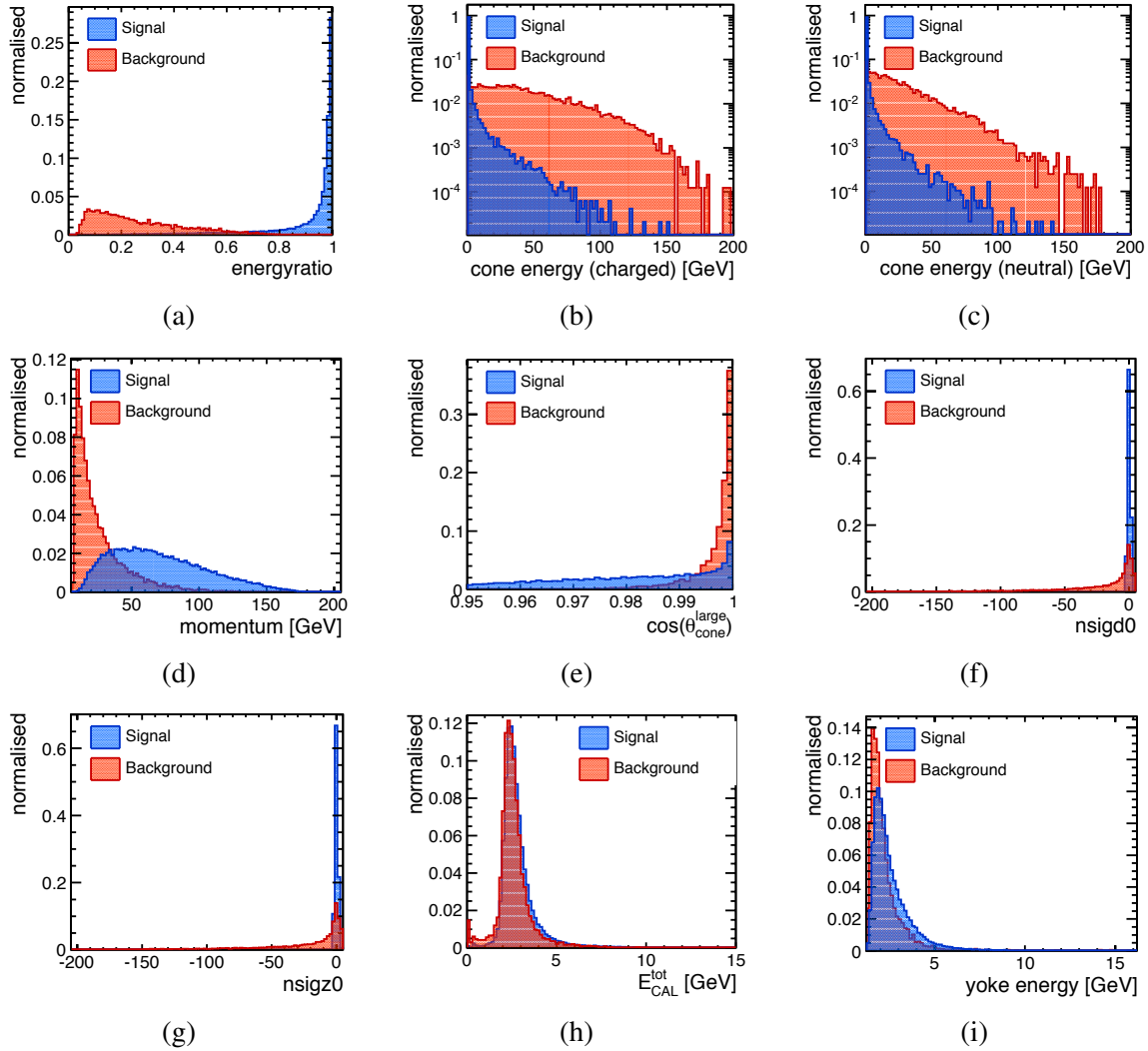


Figure 6.3: Input variables for muon-type events. Description can be found in the text..

The only difference in input variables for electron-type and muon-type events are the following:

- **For electrons:** the ratio of the energy in the ECAL and the total calorimeter energy E_{ECAL}/E_{CAL}^{tot} , and the ratio between the total calorimeter energy and the momentum E_{CAL}^{tot}/P . Both distributions are expected to give larger values for isolated leptons.
- **For muons:** the total calorimeter energy $E_{CAL}^{tot} = E_{ECAL} + E_{HCAL}$, and the yoke energy. The latter is expected to be larger for isolated muons.

The neural nets are trained – and tested in the analysis – for charged PFOs which fulfil similar requirements as the DBD selection strategy. The neural net is trained for electrons which satisfy $0.5 < E_{CAL}^{tot}/P < 1.3$, $P > 5$ GeV, $E_{ECAL}/E_{CAL}^{tot} > 0.9$, and which are constrained to the primary vertex by using information on $d0$ and $z0$. Muons are selected if they satisfy $E_{CAL}^{tot}/P < 0.3$, $P > 5$ GeV, $E_{yoke} > 1.2$ GeV, and if they originate from the

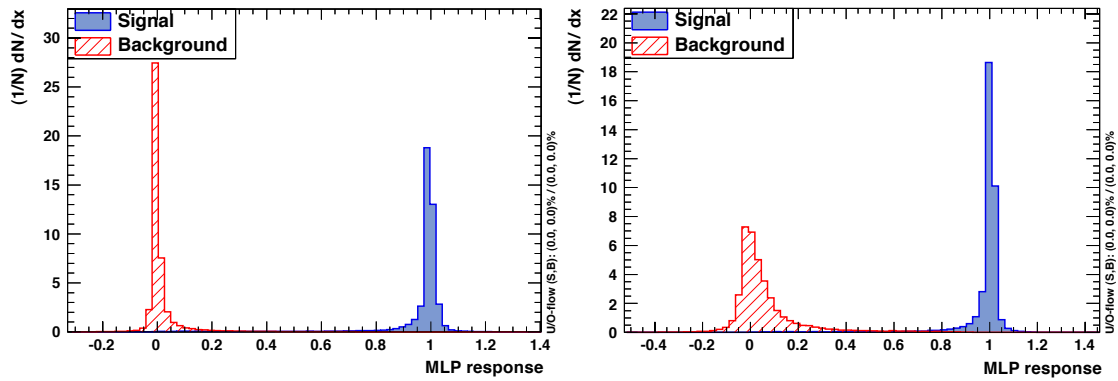


Figure 6.4: Neural net output for the electron-type (left) and the muon-type (right). Particles are selected as isolated electrons if they fulfil $MVA > 0.5$ and as isolated muons if they satisfy $MVA > 0.7$. The neural net output can be written into a particle collection. The distribution can be read out in the analysis and optimised in the final selection.

primary vertex, also using $d0$ and $z0$. The classifier output is used for the isolated lepton selection. Additionally, the neural net output can be written into a particle collection and used for particle selection.

Only charged reconstructed particles, which pass the previously listed selection cuts, are tested with the corresponding weights. These lepton candidates receive an MVA classifier value. Particles are selected as isolated lepton if they pass a selection cut on the MVA classifier output as shown in fig. 6.4. Isolated electrons with $MVA > 0.5$ and isolated muons with $MVA > 0.7$ are selected.

The selection efficiencies of the cut-based DBD strategy [108] and the optimised neural-net based strategy are listed in tab. 6.1. Compared to the DBD strategy the optimised strategy achieves an improved isolated lepton selection. The signal selection efficiency is slightly increased and the suppression of the hadronic and the semi-leptonic backgrounds is significantly improved. For the same signal efficiency, the background suppression is enhanced by a factor of 10.

In the $l\bar{l}HH$ channel, events are selected with an isolated lepton pair of opposite charge, which is consistent with the Z mass. The MVA outputs of the two selected leptons are sorted by size. This results in a larger and smaller MVA value. The signal is expected to

efficiency (%)	$eeHH$	$\mu\mu HH$	$bbbb$	$evbbqq$	$\mu vbbqq$
DBD selection	85.7	88.4	$2.8 \cdot 10^{-2}$	1.44	0.10
optimised strategy	87.0	89.1	$1.7 \cdot 10^{-3}$	0.32	0.02

Table 6.1: Efficiencies of the isolated lepton selection strategy in [108] and the optimised neural net based strategy. The background suppression is improved by a factor of 10 for the same signal efficiency.

have two isolated leptons and thus two large MVA values, while background processes as $lvbbqq$, which survive the isolated lepton selection, are expected to have one large and one small MVA value. These MVA outputs are written as parameters to a lepton collection. Since $mvalarge$ and $mvasmall$ are useful for the background suppression, they can be read out in the analysis and optimised in the final selection.

6.2 Optimised Overlay Removal

The effects of the $\gamma\gamma$ overlay (sec. 3.4.2) have not been considered in previous Higgs self-coupling studies. However, the effect of this background on the analysis is investigated in this thesis. The overlaid $\gamma\gamma \rightarrow \text{low-}p_T$ hadrons events need to be identified and removed from the reconstructed particle list to recover the original events. Then, it is possible to investigate the impact of the overlay on the Higgs self-coupling measurement. Additionally, this study gives a significant hint on whether more advanced removal strategies and more sophisticated tools are needed which include a precise modelling of low- p_T $\gamma\gamma \rightarrow$ hadrons background and exploit the full power of high granularity detectors.

Removal Strategy

The exclusive k_t clustering algorithm (sec. 5.3) is included in FastJet [183] in ILCSOFT. It allows to request a fixed number of jets N_{jets} and R parameters of $R \leq \pi/2$. N_{jets} can differ from the original event topology since hard gluon radiation can cause additional jets. To achieve an optimised overlay removal, the most efficient combination of both parameters is evaluated. This is done by comparing Higgs mass distributions after the overlay removal to the ideal case without $\gamma\gamma$ overlay. Generally, to compare the distributions after overlay removal to the ideal Higgs mass, MC truth information are used to remove the overlaid particles from the events. In figure 6.5 the Higgs mass distributions of $ZHH \rightarrow ll\bar{b}b\bar{b}b$ events for different R parameters are shown for $N_{jets} = 4$ (left) and $N_{jets} = 6$ (right), respectively. These two N_{jets} configurations are chosen since $N_{jets} = 4$ represents the $llHH$ final state hypothesis and larger N_{jets} can be interpreted as improving the resolution of the algorithm. The figures already indicate that better results can be achieved with $N_{jets} = 6$.

Removal Performance

Fig. 6.5 indicates that better results can be achieved by requesting a larger number of jets N_{jets} . This is verified by investigating the overlay removal performance for different N_{jets} and R parameter combinations in an evaluation of

1. the reconstructed energy efficiency E_{fj}/E_{noovl} after overlay removal, which is defined by the total energy E_{fj} of the four Durham jets after overlay removal divided

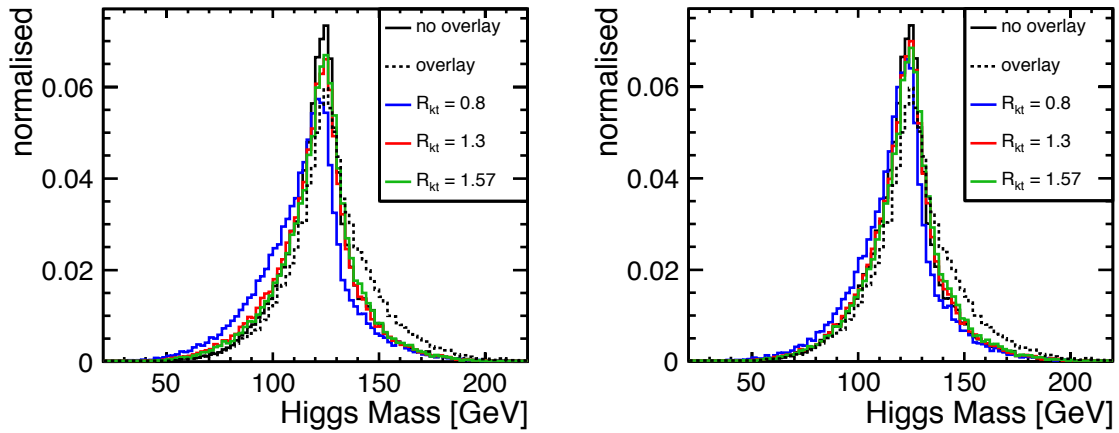


Figure 6.5: Exemplary Higgs mass distributions for different R parameters for $N_{jets} = 4$ (left) and $N_{jets} = 6$ (right) for $ZHH \rightarrow llbbbb$. The overlay removal has to be optimised to recover the bare events most precisely.

by the total energy E_{noovl} of the four Durham jets without overlay.

2. a shape comparison of the Higgs mass distributions after overlay removal to the result without overlay. Therefore, a χ^2 test is performed.

The corresponding performance plots are illustrated in fig. 6.6 for $N_{jets} = 4$ and $N_{jets} = 6$, respectively. The respective results of both performance tests are listed in tab. 6.2. It is evident, that the choice of N_{jets} influences the performance of the overlay removal. The increase of efficiency slows down to larger R parameters in both cases. R parameters < 1.0 can be excluded. For $N_{jets} = 6$ larger efficiencies and smaller uncertainties are obtained over the entire range of R parameters compared to $N_{jets} = 4$.

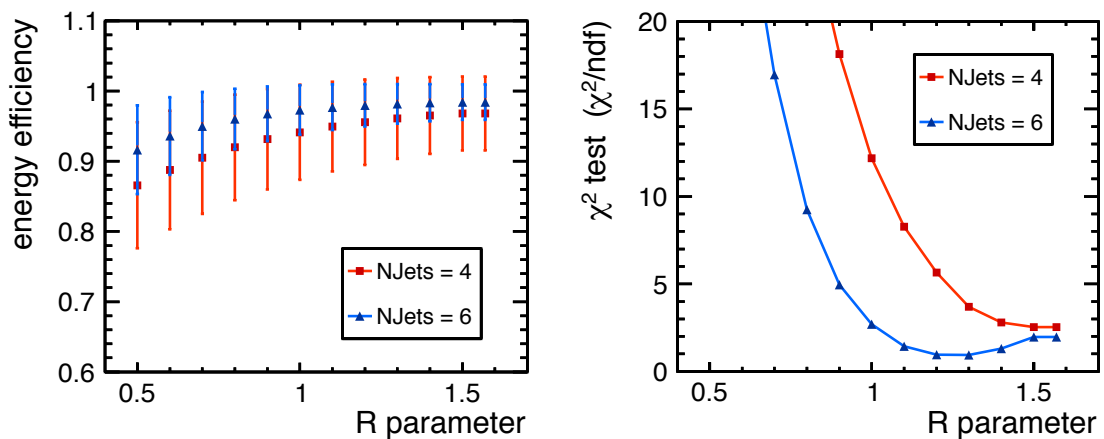


Figure 6.6: Performance plots of the overlay removal using exclusive k_t jet clustering. Left: reconstructed energy efficiency for different R parameters. Right: χ^2 for different R parameters. The corresponding results are listed in table 6.2.

energy efficiency			χ^2/ndf		
R	$N_{jets} = 6$	$N_{jets} = 4$	R	$N_{jets} = 6$	$N_{jets} = 4$
0.8	0.960 ± 0.043	0.920 ± 0.075	0.8	9.255	26.064
0.9	0.968 ± 0.039	0.931 ± 0.072	0.9	4.958	18.147
1.0	0.973 ± 0.035	0.941 ± 0.072	1.0	2.699	12.188
1.1	0.977 ± 0.033	0.949 ± 0.061	1.1	1.432	8.267
1.2	0.979 ± 0.030	0.956 ± 0.061	1.2	0.953	5.654
1.3	0.982 ± 0.028	0.961 ± 0.058	1.3	0.943	3.697
1.4	0.983 ± 0.027	0.965 ± 0.055	1.4	1.309	2.797
1.57	0.984 ± 0.026	0.968 ± 0.053	1.57	1.972	2.539

Table 6.2: Performance tests for $N_{jets} = 4$ and $N_{jets} = 6$. Left: reconstructed energy efficiency for different R parameters. Right: χ^2 of the χ^2 test for different R parameters.

To evaluate an optimised R parameter, a χ^2 test is performed. For $N_{jets} = 6$ overall better χ^2 values can be achieved over the entire range of R parameters. Focussing on $R \geq 1.0$, the smallest χ^2 is obtained at $R = 1.3$. Taking into account the results of the energy efficiency test, at the respective R parameter the efficiency reads 98.2% for $N_{jets} = 6$. Consequently, an optimised overlay removal is achieved most efficiently for $N_{jets} = 6$ with $R = 1.3$. This is consistent with the evaluated channel $\nu\nu HH$. The R parameter reads $R = 1.3$ for all three channels. Since $qqHH$ is a six-jet final state, $N_{jets} = 8$ is requested. The effect of the $\gamma\gamma$ overlay on the analysis is discussed in chapter 9.

6.3 Kinematic Fitting

6.3.1 Motivation

Double Higgs-strahlung events result in four- and six-jet final states. Due to the small ZHH production cross section it is essential to reconstruct the small number of signal events very precisely and suppress the large SM backgrounds. Since boson mass distributions play an essential role in the event selection, the jets representing the primary quarks have to be reconstructed and finally paired to form the signal bosons. As discussed in sec. 5.2.2, the precise reconstruction of the primary quarks by measuring jet properties is limited due to the complicated processes of fragmentation and hadronisation. All limiting aspects are listed in sec. 4.1.1. By exploiting the known measurement resolutions and by imposing well-known demands on specific properties, the reconstruction of particle four-momenta can be improved and the compatibility of an event with a specific hypothesis can be tested. A useful tool to improve the invariant mass resolutions and enhance the

jet-energy resolution are so-called kinematic fits. The applications of kinematic fits to the Higgs self-coupling analysis play a central role in this thesis, since they offer several areas of potential improvement by

- optimising the event selection of the current analysis strategy (sec. 5.2) by improving boson mass resolutions of the signal and background processes. In the current analysis strategy mass distributions are used as input variables for neural net training. Especially in the suppression of backgrounds with the same final state particles as the signal, the discriminative power of the neural net outputs is very important. Such background processes are given by ZZH/Z .
- changing the analysis strategy by introducing new variables obtained from the kinematic fit as input to neural nets or as simple cut. Different fit hypotheses are evaluated with respect to their discriminative power between signal and background.
- improving the jet-boson assignment which influences the correct jet pairing. This was investigated in [84]. It was shown that by combining two fit hypotheses, or the fitted four-momenta with the jet pairing used in the current analysis strategy (eq. 5.4), boson mass distributions can be improved. The results in [84] are used in the investigation of kinematic fits in this analysis.

Kinematic fits take into account measurement resolutions and so-called constraints, which generally represent known properties of the event. These are formed by conservation of energy, momentum, and the masses of the initial particles. A complete set of imposed constraints is called fit hypothesis. In general, the measured parameters are subject to measurement errors, and therefore do not fulfil all constraints exactly. The kinematic fit varies the measured quantities under the condition that the imposed constraints are fulfilled, taking into account the allowed uncertainties. How much a measured parameter is allowed to vary depends on the measurement errors. Per definition, the results of the fit satisfy all applied constraints, e. g. by requiring energy conservation the energy balance after kinematic fitting is exactly 0. These constraints are ineffective as selection variable in an event selection.

At the ILC, the mass reconstruction relies on the realisation of the particle flow concept and the achievable jet-energy resolution, as discussed in chapter 4. However, particle flow does not consider effects from mis-clustering of jets, ISR and beamstrahlung, or missing energy from semi-leptonic decays. However, these effects can be implemented into kinematic fits. The combined use of particle flow and kinematic fitting can help to improve the reconstruction of particle four-vectors at the ILC. In this study `MarlinKinfit` [185] is used for kinematic fitting, which is available within `Marlin` [171] in `ILCSoft`. The general concepts of kinematic fitting and methods of evaluating the fit performance are described following the detailed description in [185]. Hereafter, the applications of kinematic fits to the analysis are discussed.

6.3.2 General Concept and Working Principle

The kinematic fitting procedure is an iterative process, which is based on the Principle of the Least-Squares and the method of Lagrange Multipliers [186], minimising the variable χ_T^2 with respect to the applied constraints and measurement resolutions. χ_T^2 reads

$$\chi_T^2 = \chi^2(\boldsymbol{\eta}, \mathbf{a}) + \sum_{k=1}^K \lambda_k \cdot f_k(\boldsymbol{\eta}, \boldsymbol{\xi}) + \sum_{l=1}^L \chi_l^2(\boldsymbol{\eta}, \boldsymbol{\xi}). \quad (6.1)$$

The first term represent the usual χ^2 , which describes the deviation between the measured and fitted quantities as

$$\chi^2(\boldsymbol{\eta}, \mathbf{a}) = (\boldsymbol{\eta} - \mathbf{a})^T C(\boldsymbol{\eta})^{-1} (\boldsymbol{\eta} - \mathbf{a}), \quad (6.2)$$

with $\boldsymbol{\eta}$ representing the vector of measured observables, e. g. containing the energy E and the angles θ and ϕ of the detected objects. \mathbf{a} denotes the vector of the fitted quantities, which is the initial guess in the iteration procedure. The energy E , the transverse momentum p_T , and the angles θ and ϕ of jets and leptons can be measured with finite resolution. As required by the fit, the corresponding errors are described by Gaussian functions. Therefore, these variables represent candidates for specific parameterisations of measured objects. In equation 6.2, $C(\boldsymbol{\eta})^{-1}$ represents the covariance matrix which contains the estimated measurement errors and possible correlations.

The constraints are described by the second and third term of equation 6.1, allowing the consideration of unmeasured parameters, like neutrinos. λ_k represents Lagrange multipliers and $f_k(\boldsymbol{\eta}, \boldsymbol{\xi})$ k functions of hard constraints, which impose an exact requirement on the reconstructed events, i. e. energy conservation. Here, $\boldsymbol{\xi}$ gives a set of J unmeasured quantities, i. e. (p_x, p_y, p_z) of a neutrino. Each unmeasured variable consumes one degree of freedom ν . Since a neutrino for example stays undetected, a number of parameters remain unmeasured and must be calculated from the measured parameters by using some of the constraints. The unmeasured momentum of the neutrino follows from three-momentum conservation. The number of degrees of freedom ν of the fit is defined as

$$\nu = N_m - N_f + n, \quad (6.3)$$

where N_m is the number of measured parameters and N_f the number of fitted parameters. Here, n is defined as $n = K - J$, with K representing the total number of applied constraints. Depending on K and J the fit is called nC fit, e. g. a fit with energy and three-momentum conservation is a so-called $4C$ fit.

A mass constraint taking into account the natural width of a particle represents a so-called soft constraint. These soft constraints do not impose a precise requirement on the reconstructed event and are described by $\chi_l^2(\boldsymbol{\eta}, \boldsymbol{\xi})$. This term vanishes if the soft constraints are fulfilled. The χ^2 minimisation with respect to the parameter sets yields the best estimates for the parameters when

$$\frac{\partial \chi_T^2}{\partial \boldsymbol{\eta}_i, \boldsymbol{\xi}_j} = 0, \quad (6.4)$$

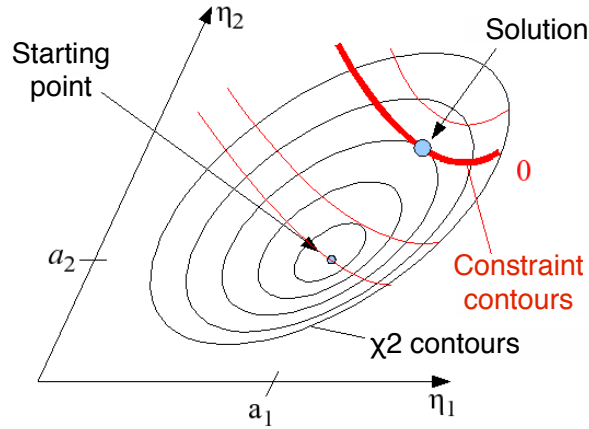


Figure 6.7: Working principle of the fit engine. The fit varies the measured parameters iteratively, approaching a solution for the smallest χ^2 . The latter is reached at the intersection point of the constraint and χ^2 contours. Figure taken from [187].

which at the same time satisfy the equation of constraints as

$$\frac{\partial \chi_T^2}{\partial \lambda_k} = f_k(\boldsymbol{\eta}, \boldsymbol{\xi}) = 0. \quad (6.5)$$

The difference between the measured and fitted values is expected to be small if an event fulfils the applied fit hypothesis. In this case, χ^2 is in the order of ν . A soft constraint adds $0.5C$ to the fit.

In terms of software, in the fitting procedure the system of equations is solved by a so-called fit engine. In MarlinKinfit, three fitting algorithms are available in different fit engines: OpalFitter, NewFitter and NewtonFitter. The latter is used in the analysis. Details can be found in [185]. The general working principle of the fit engine is illustrated in fig. 6.7. This example includes one hard constraint and two parameters. The fitting procedure starts with the measured values a_1 and a_2 at the starting point $\chi^2 = 0$. In each iteration the parameters are varied, slowly approaching the solution with the smallest χ^2 . At the intersection point of the χ^2 contour and the constraint contour the fit obtains a solution. As input, the fit engine uses information about the so-called fit objects and the applied constraints. Neutrinos, jets, or leptons are treated as fit objects, which contain information about measured parameters and their parametrisation before and after the fit, including the respective covariance matrices. According to the explanations in the foregoing, the fit objects are parametrised by a specific set of quantities. The fit objects are described in the following and are summarised in table 6.3.

Lepton Fit Object Leptons are treated as one measured object and are parametrised by $(1/p_T, \theta, \phi)$. The transverse momentum p_T can be measured very precisely by the tracking system. The ILD detector provides excellent tracking systems which are designed to reach the asymptotic momentum resolution $\sigma_{1/p_T} = 2 \times 10^{-5} \text{ GeV}^{-1}$

fit object	parameters	mass	property
hadronic jets	(E, θ, ϕ)	m	3× measured
leptons	$(1/p_T, \theta, \phi)$	m	3× measured
neutrinos	(p_x, p_y, p_z)	0	3× unmeasured
Zinvisible	(p_x, p_y, p_z)	91.18 GeV	3× unmeasured
ISR photon	p_z	0	1× pseudo-measured

Table 6.3: Parametrisation for different fit objects. The mass of hadronic jets is non-vanishing and chosen as constant. For the purpose of this analysis, the Zinvisible fit object was developed. It allows to treat $Z \rightarrow \nu\bar{\nu}$ decays in final states.

(sec. 4.1) [130]. In contrast to muons, electrons can also be parametrised by the energy measured in the calorimeter instead of using $1/p_T$, since electrons and photons from final-state radiation and bremsstrahlung are both measured in the calorimeter and combined with the measured momentum in the tracking system.

Jet Fit Object Hadronic jets are parametrised by (E, θ, ϕ) and with non-vanishing mass m . Here, θ and ϕ represent the polar and azimuth angle, respectively. Invariant mass resolutions are dominated by the jet energies rather than the jet angles. Therefore, in this analysis we take the angular resolutions as constant in the fit. For a successful fit performance the jet-energy resolution σ_E is crucial, since σ_E enters the fit in the covariance matrix C^{-1} . At the ILC, considering a superb particle flow performance, the ideal resolution reads $30\%/\sqrt{E}$ for 100 GeV jets (sec. 4.1) [130]. However, in reality several aspects degrade the particle flow performance which have not been included in the evaluation of the energy resolution goal (sec. 4.3.4). It does not account for mis-clustering of jets, or missing energy from semi-leptonic decays. Neutrinos from semi-leptonic decays of b quarks and to a lesser degree c quarks can carry away a certain amount of energy which adds to the measurement uncertainties of the reconstructed b jets. Consequently, for such events momentum and energy conservation is not automatically fulfilled. In [84] a detailed study of jet energy uncertainties of $ZHH \rightarrow llbbbb$ events was performed in context of kinematic fits. The result is used in this study and the energy resolution reads

$$\frac{\sigma_E}{E} = \frac{(56.8 \pm 0.4)\%[\sqrt{GeV}]}{\sqrt{E}} \oplus \frac{(330 \pm 1)\%[GeV]}{E}. \quad (6.6)$$

ZHH events are produced close to kinematic threshold at $\sqrt{s} = 500$ GeV. The jets are less boosted, which results in some overlap. Combined with high jet multiplicities, the invariant mass resolution is dominated by jet-finding ambiguities rather than the jet-energy resolution. Therefore, at smaller energies the resulting jet-energy resolution worsens quickly. This is taken into account by the second term in eq. 6.6.

Neutrino Fit Object Neutrinos stay undetected and their properties remain unmeasured. The neutrino fit object adds three unmeasured parameters to the fit (p_x, p_y, p_z) , each of which consumes one constraint. In case of one neutrino in the parton-level final state, its three-momentum can be derived from three-momentum conservation.

Zinvisible Fit Object The neutrino channel includes missing energy from $Z \rightarrow \nu\bar{\nu}$. Apparently, introducing two neutrino fit objects to the fit, which are constrained to the Z -boson mass, seems to be the most simple way to treat missing energy from Z -boson decays in the fit. However, two neutrino fit objects introduce six unmeasured parameters, which have to be compensated by at least seven constraints to ensure that the fit is not trivial. To solve this issue and to be able to use kinematic fits in every ZHH mode, the *Zinvisible* fit object is developed, describing $Z \rightarrow \nu\bar{\nu}$. The *Zinvisible* fit object works similar as the neutrino fit object. Its three momentum follows from three-momentum conservation in an event, introducing only three unmeasured parameters to the fit. These can be easily compensated by requiring energy and momentum conservation, and by imposing mass constraints. While the neutrino fit object is considered massless, the *Zinvisible* fit object automatically imposes one mass constraint of $M_{\nu\nu} = M_Z$ to the fit.

ISR Photon Fit Object An ISR photon fit object provides treatment of ISR and beamstrahlung photons (sec. 3.4) in the kinematic fit [187]. In this thesis, both are simply referred to as ISR in the context of kinematic fits. The ISR photon fit object allows to take into account a single photon which is emitted parallel to the beam along z direction. Since these photons are very forward and backward in the detector, their transverse momentum is fixed to $p_x = p_y = 0$ and they only affect energy conservation and longitudinal momentum conservation p_z . It is parametrised by the total missing p_z of an event, which is then converted to $E_\gamma^{ISR} = |-p_z|$. It helps to satisfy energy and momentum conservation since small angle ISR escape through the beam pipe. The ISR photon fit object was developed and tested successfully using u and d jets in WW processes [187]. The parametrisation is performed in a way that events without, with small, and with large missing energy from ISR are reconstructed correctly. After the fit, the same mass resolution was achieved for events with and without significant ISR [187]. In this analysis, ISR recognition can be much more challenging due to additional missing four-momentum from semi-leptonic decays of the b quarks from the Higgs bosons. It needs to be tested whether it still works properly. Additionally, the application of the ISR photon fit object in combination with the *Zinvisible* fit object has to be evaluated, since it compensates the presence of the neutrinos from the Z decay.

6.3.3 Fit Performance Measures

Goodness of Fit χ^2 and Fit Probability $P(\chi^2)$

The goodness of fit is given by χ^2 , which implies that the result of the minimisation gives a quantitative measure of the overall agreement between fitted and measured objects. The probability density function of χ^2 for ν degrees of freedom is given by [188]

$$f(\chi^2; \nu) = \frac{2^{-\frac{\nu}{2}}}{\Gamma(\frac{\nu}{2})} (\chi^2)^{(\frac{\nu}{2}-1)} \exp(-\frac{\chi^2}{2}). \quad (6.7)$$

If all measurement errors are estimated properly and no systematic errors are present we expect a mean χ^2 equal to ν , which concludes that the events are well described by the chosen uncertainties and constraints. ν has large impact on the shape of the χ^2 distribution. For small ν , the χ^2 distribution is highly skewed. The χ^2 distribution becomes more symmetric for increasing ν , before finally approaching a Gaussian shape for large ν . If the events do not fulfil the requirements imposed by the fit, the χ^2 distribution deviates from these expectations and obtains a peak at higher or lower values. χ^2 can be converted into the so-called fit probability $P(\chi^2)$ as follows [188]

$$P(\chi^2) = \int_{\chi^2}^{\infty} f(\chi'^2; \nu) d\chi'^2 = 1 - F(\chi^2; \nu), \quad (6.8)$$

where $F(\chi^2; \nu)$ denotes the cumulative χ^2 distribution for a certain ν . $P(\chi^2)$ represents the probability for obtaining a χ'^2 which is larger than χ^2 in a new minimisation with similar measurements and the same model. Eq. 6.8 indicates that $P(\chi^2)$ is distributed between 0 and 1. Large values of χ^2 correspond to small $P(\chi^2)$, while small χ^2 correspond to large $P(\chi^2)$. Any deviation of $P(\chi^2)$ from a uniform distribution indicates that either the measurements or the fit hypothesis are incorrect.

Moreover, $P(\chi^2)$ gives information on whether the estimation of the measurement errors is correct. A correct error estimation is important since the measurement resolutions enter the fit in the covariance matrix C^{-1} . In the fit, the definition of χ^2 always assumes that the measured parameters and the corresponding errors are Gaussian distributed. However, this does not automatically indicate that they are well described. Figure 6.8 illustrates the importance of precisely estimated uncertainties for the fit performance. A schematic sketch of the behaviour of various χ^2 and the corresponding $P(\chi^2)$ distributions for three different types of events is shown. Here, the sketch corresponds to a fit with $\nu = 5$. Events which are Gaussian distributed and well described obtain a χ^2 distribution as indicated in green. The corresponding $P(\chi^2)$ is normal distributed between 0 and 1. Compared to events which satisfy a fit hypothesis, the χ^2 distribution peaks at larger or smaller χ^2 for events which do not fulfil the fit hypothesis. This is indicated in red and blue, respectively. The red distribution describes the case in which the errors are underestimated, resulting in overall smaller $P(\chi^2)$. Due to an underestimation of errors also those events receive small

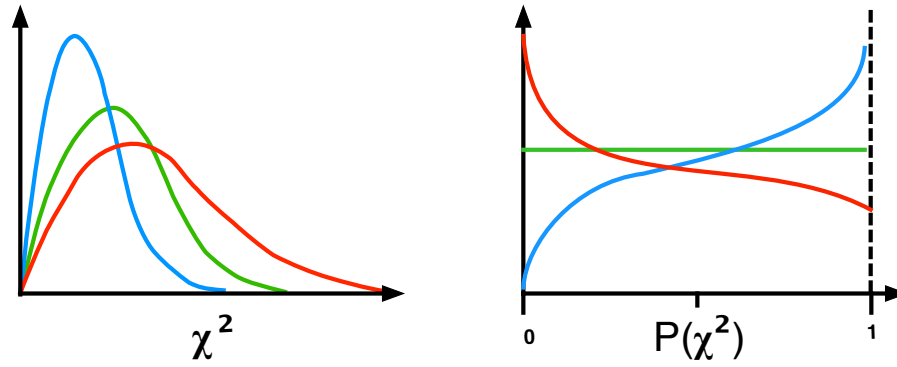


Figure 6.8: Example distributions for χ^2 (left) and the corresponding $P(\chi^2)$ (right) for a fit with $\nu = 5$. The green lines correspond to a fit with well-estimated errors. The blue line corresponds to a fit in which the errors are overestimated. The red line illustrates a fit with underestimated uncertainties. $P(\chi^2)$ for the fit with correct errors is uniformly distributed, whereas the other two fits obtain peaks at large or small $P(\chi^2)$, respectively.

fit probabilities which generally fulfil the applied fit hypothesis. If $P(\chi^2)$ was used as selection variable applying a simple cut would then reject signal events. Hence, we would lose signal events due to an underestimation of the errors in the fit. The blue distributions correspond to the case in which the errors are overestimated. The overall smaller χ^2 results in a peak at larger $P(\chi^2)$. An overestimation of the errors would affect events which do not fulfil the fit hypothesis since these events obtain an overall larger $P(\chi^2)$. Then, background events would survive a cut on $P(\chi^2)$, degrading the signal selection efficiency. In reality there is often a peak at low $P(\chi^2)$, which corresponds either to events that are not well described by the fit hypothesis, or to the presence of systematic errors. We strive to minimise these cases by improving the fit hypothesis description.

Pull Distributions

Although events can be well described by the applied fit hypothesis, an incorrect error parametrisation of the measured quantities can result in biased $P(\chi^2)$ distributions to either smaller or larger $P(\chi^2)$. A way to guard against this is given by pull distributions [189]. Pull distributions give a useful measure to test the reliability of the assumed uncertainties on the measured parameters. In the kinematic fit pull distributions describe the deviation of the fitted from the measured values normalised to the errors on the measured and fitted quantities. In constrained fits the pull of the measured parameter x is defined as [189]

$$pull(x) = \frac{x_m - x_f}{\sqrt{\sigma_m^2 - \sigma_f^2}}. \quad (6.9)$$

$x_m \pm \sigma_m$ denotes the measured value and its resolution before fitting, and $x_f \pm \sigma_f$ the value and corresponding error after fitting. The determination of σ_f is highly non-trivial and was implemented in context of this thesis. A detailed calculation can be found in [190].

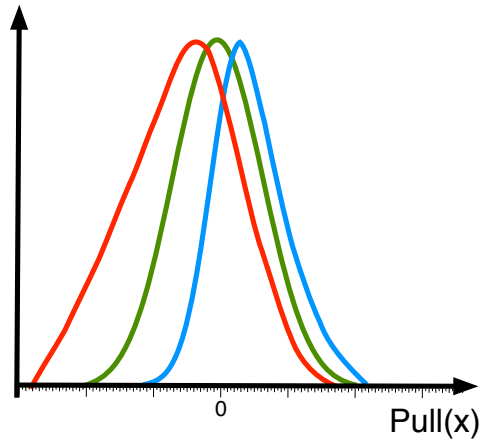


Figure 6.9: Schematic illustration of pull distributions of the variable x . The green distribution corresponds to the fit with well-estimated errors. The blue pull corresponds to a fit with overestimated errors, whereas the red pull illustrates a fit with underestimated uncertainties. Both are shifted from 0 and are of non-Gaussian shape.

The investigation of pulls gives an indication on whether the used input resolutions are correct or not. A schematic sketch of pull distributions is shown in figure 6.9. If the measurement values and uncertainties are determined precisely and no systematic errors existed, the deviation between measured and fitted values should form a normal distribution which is centred at 0 with a standard deviation σ of 1 (green). In this case, the kinematic fit is just as probable to increase a specific value as to decrease it taking into account the used fit hypothesis. A non-Gaussian shape indicates that the measurement errors are not normal distributed or the fit hypothesis is wrong. A shift from 0 to either positive or negative values indicates a bias in the measured parameters, the reason of which can be systematic errors. Likewise, a deviation of σ from 1 indicates that the uncertainties on the measurements are either overestimated (blue) or underestimated (red). Hence, σ contains information about the size of the input errors. In case of overestimated measurement uncertainties σ_m the pull is too narrow, whereas an underestimation of σ_m results in a too broad distribution.

6.3.4 Building of Fit Hypotheses

Next to the fit objects, the fit engine uses information on the applied constraints. The fit objects describe the final state particles, while a set of constraints form a fit hypothesis. The various possibilities of implementing kinematic fits in the analysis require different fit hypotheses for each application (sec. 6.3.1). The final state and the event properties need to be well-described by fit objects and fit hypotheses. Therefore, several fit hypotheses are evaluated for different purposes in their application to the analysis. The lepton channel $ZHH \rightarrow llbbbb$ is used as benchmark. The lepton mode can be described by four jet

fit objects and two lepton fit objects. Since this mode does not have missing energy in its initial state, it is ideal as benchmark process to study the full potential of kinematic fits with regard to the Higgs self-coupling analysis. Later, the results are applied to all three signal channels and evaluated individually. The different constraints which can be combined to a fit hypothesis are described in the following, before the fit hypotheses are discussed which are used in the analysis.

Energy and Momentum Conservation Energy and momentum conservation represent hard constraints imposing an exact requirement on the reconstructed events as

$$\sum_i E_i = 500 \text{ GeV}, \quad (6.10)$$

$$\sum_i \vec{P}_i = 0. \quad (6.11)$$

Soft Mass Constraints If the natural width of a particle can be resolved by the detector, it needs to be considered in the fit. This is done by a soft mass constraint. A soft Z -mass constraint can be imposed on $Z \rightarrow l^-l^+$. The invariant mass of the two leptons has to be equal to M_Z taking into account the decay width Γ_Z as

$$M_{ll} = M_Z \pm \Gamma_Z = (91.18 \pm 2.49) \text{ GeV}. \quad (6.12)$$

In this case, the lepton resolutions are much better than the natural width of the Z boson. Hence, a slight deviation from the nominal Z -boson mass would not be due to measurement resolutions but to the natural width of the Z boson. The contribution of the soft constraint to the total χ_T^2 (eq. 6.1) vanishes if the constraint is fulfilled. The fit assumes a Gaussian shape for the invariant mass of a particle. However, the Z -boson mass is described by a Breit-Wigner function [186]. Consequently, in the fit the Gaussian σ needs to be expressed in terms of Γ_Z : the Breit-Wigner function drops very slowly compared to a Gaussian. Hence, it adds only small values to the total χ_T^2 and does not contribute significantly to $P(\chi^2)$ for events with large differences between fitted and generated Z mass, here denoted as Δm . A Gaussian distribution contributes large values to the total χ_T^2 for events with large Δm , thus influencing $P(\chi^2)$ more effectively. By expressing σ in terms of Γ_Z , the Gaussian describes a Breit-Wigner shape at least for events with small Δm as

$$\sigma = \frac{k^2 \Gamma_Z^2}{2 \ln(4k^2 + 1)}, \quad \text{here: } k = 1.0, \quad (6.13)$$

where k represents the value of Δm until which the Gaussian describes the Breit-Wigner shape and both intersect. More details can be found in [191]. As a result, events with small Δm obtain only small contributions to χ_T^2 from the soft mass constraint. For events with large Δm , χ_T^2 is highly influenced by the soft constraint due to the steep rising of the Gaussian approximation. This leads to small $P(\chi^2)$ for events in the tails of the Breit-Wigner distribution.

Hard Mass Constraints Hard constraints can be enforced on the masses of di-jet systems. Di-jet masses are then fixed to a certain value. Applying hard mass constraints to ZHH gives delta peaks at 125 GeV for both Higgs masses after the fit. In this case, imposing a soft mass constraint would give the same result as the hard mass constraint since the total width of the Higgs boson is too narrow to be resolved by the detector.

Equal-Mass Constraint The equal-mass constraint represents a hard mass constraint which is useful for the investigation of fitted mass distributions. The fit assumes an averaged invariant mass for two di-jet systems. Jets are paired and fitted so that the di-jet pairs obtain equal masses

$$M_{ij} = M^{kl} . \quad (6.14)$$

Wrong estimated jet-energy resolutions, missing energy due to ISR or semi-leptonic decays, or mis-clustering of jets degrade the fit performance. Fit hypotheses with equal-mass constraints are easily affected by these limitations, e.g. in processes with different bosons as ZZH . In this case, the equal-mass constraint usually leads to fitted masses between the nominal Higgs and Z mass. The b quarks from the Higgs decay can decay semi-leptonically, causing missing energy and momentum in the jets. This, as well as detector inefficiencies can cause a mis-reconstruction of the Higgs as a Z boson by the fit, giving a mass close to M_Z . Due to this constraint, ZZH is then reconstructed as ZZZ .

In the current analysis strategy, mass distributions play a central role since they are used for the signal and background separation as input variables for neural net training. Especially the separation of backgrounds with the same final state particles as the signal require large discriminative power of the neural net outputs. Such background processes are represented by ZZH and ZZZ . Large contributions are also given by $t\bar{t}$ backgrounds, but not considered for the investigation of kinematic fits. More details can be found in chapter 8. A large variety of fit hypotheses for the signal ZHH and dominant backgrounds ZZH and ZZZ are studied. The most promising results, which are used throughout the entire analysis are described in the following. Commonly used in all fit hypotheses are energy and momentum conservation. Additionally, a soft Z -mass constraint on the two isolated leptons is imposed. Before the fit, final-state radiation and bremsstrahlung photons are recovered to ensure an accurate Z -mass reconstruction. The main difference in the various hypotheses relies on the treatment of the masses of the hadronically decaying bosons.

Equal-Mass Hypothesis The main application of kinematic fits is the improvement of mass resolutions used in the event selection. Therefore, an equal-mass constraint is imposed on the two di-jet pairs from the bosons. The fit hypothesis represents a $5.5C$ fit in the lepton and hadron channel, and a $2.5C$ fit in the neutrino channel. The fit hypothesis is denoted as equal-mass fit (eqm).

Signal Hypothesis The second application is the evaluation of variables from the fit, which can improve the event selection. Therefore, hard Higgs mass constraints to 125 GeV are imposed on the two di-jet pairs. The fit hypothesis represents a 6.5C fit in the lepton and hadron channel, and a 3.5C fit in the neutrino channel. The signal hypothesis is denoted as *ZHH* fit.

Background Hypotheses There are two fit hypotheses each of which describes one of the dominant background processes:

- For the *ZZH* background process a soft *Z*-mass constraint is enforced on one of the di-jet pairs and a hard Higgs mass constraint on the other one. The fit hypothesis represents a 6C fit in the lepton and hadron channel, and a 3C fit in the neutrino channel. The background hypothesis is denoted as *ZZH* fit.
- For the *ZZZ* background, a soft *Z*-mass constraint and a hard *Z*-mass constraint are imposed on the jet pairs. The fit hypothesis represents a 6C fit in the lepton and hadron channel, and a 3C fit in the neutrino channel. The background hypothesis is denoted as *ZZZ* fit. The fit hypothesis helps to separate the two background processes, since *ZZH* fulfils the hard *Z*-mass constraint and only one of the soft *Z*-mass constraints. The second soft constraint adds large contributions to the overall χ^2 , which results in smaller $P(\chi^2)$ for *ZZH* events.

6.4 Fit Performance of Default Setup

The investigated signal final states, in which both Higgs bosons decay into a pair of *b* quarks, can suffer from missing four-momentum from ISR and semi-leptonic decays of the *b* quarks. The fit performance on *ZHH* \rightarrow *llbbbb* events is investigated. Therefore, the fit is applied to the events using the default settings of MarlinKinfit [185], which do not automatically include ISR photon treatment. This allows to get a first impression of the fit performance.

The quality of the fit is visible in the distribution of $P(\chi^2)$, which is an important measure to evaluate performance issues. $P(\chi^2)$ obtains a uniform distribution if the errors of the measured parameters are Gaussian distributed and the events fulfil the fit hypothesis. A peak at smaller or larger $P(\chi^2)$ results from events which are not well-described by neither the fit hypothesis nor the measurement resolutions. Fig. 6.10 shows $P(\chi^2)$ of the equal-mass fit as a function of the total missing energy before fitting ($\sum E_{vis} - 500$ GeV). There is a large event population at small $P(\chi^2)$. These events have large missing energy, the source of which can be semi-leptonic decays as well as ISR. The dominance of the energy constraint is visible by the sharp edge on the left side of the distribution towards larger missing energies, which is also impacted by the jet energy uncertainties allowed in the fit. Since the equal-mass fit favours *ZHH* events, this observation indicates that the large population at smaller $P(\chi^2)$ is not caused by the wrong fit hypothesis but missing energy in the events. Hence, missing energy degrades $P(\chi^2)$ and thus the fit performance.

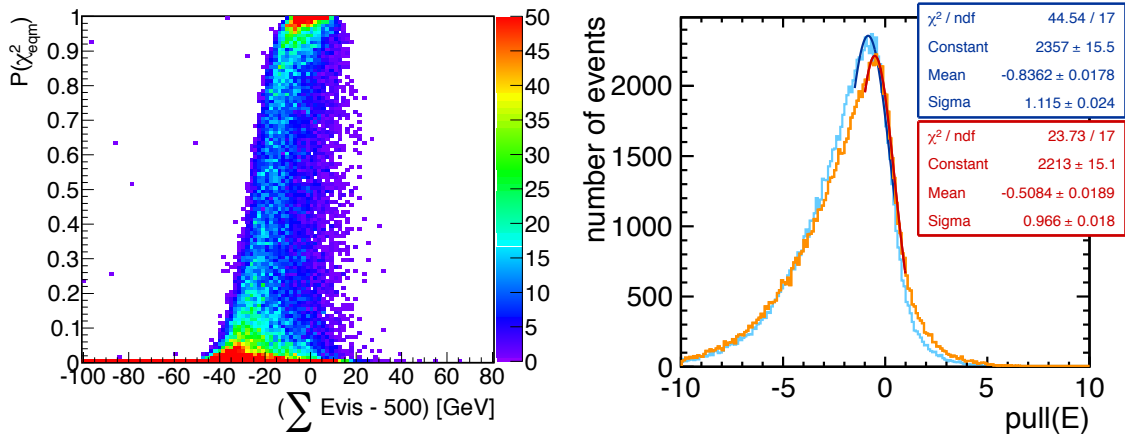


Figure 6.10: Left: $P(\chi^2_{eqm})$ as a function of the total missing energy before fitting. Missing energy comes from ISR and semi-leptonic decays and degrades the fit performance. Left: Jet energy pulls of the ZHH fit (orange) and the equal-mass fit (blue).

Another measure to evaluate the fit quality regarding measurement errors of fitted parameters are pull distributions. Since missing energy degrades the performance of $P(\chi^2)$ we focus on the energy pulls out of all measured quantities which parametrise the jets in the kinematic fit. For ZHH events two pull distributions are shown in fig. 6.10, which correspond to the equal-mass fit (blue) and the ZHH fit (orange), respectively. The energy pulls of the four jets are added to one histogram. For both fits, the pulls are of non-Gaussian shape, which is biased to smaller values. The broad distributions indicate that some events are shifted stronger than others to fulfil the fit hypotheses. The shifted peak indicates that the fitted value is generally larger than the measured value. This is due to the energy conservation constraint. Energy conservation is not fulfilled for events with missing energy. If an event suffers from large missing energy, the shift in the pull is more pronounced. Moreover, it becomes visible that the impact of different mass constraints is small. The widths of the pulls are not a reliable measure, since the fitted Gaussians do not describe the distributions properly and are just applied to get an estimate of the mean.

6.5 Application of Fits to the Analysis Concepts

The applications of kinematic fits to the analysis (sec. 6.3.1) are investigated using the default settings of MarlinKinFit. ISR treatment is available but not enabled by default. The applications of kinematic fits to the analysis concepts are introduced in the following.

6.5.1 Hypothesis Testing

One aspect of using kinematic fits in the Higgs self-coupling analysis is improving the event selection strategy by including variables obtained from the fit, i. e. χ^2 or $P(\chi^2)$.

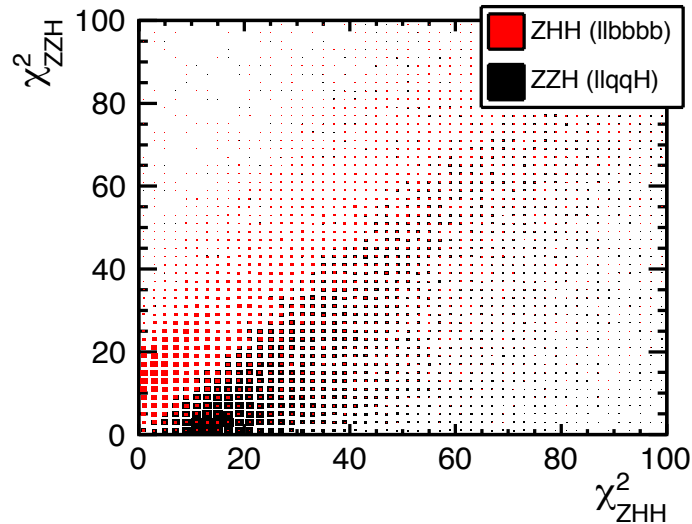


Figure 6.11: χ^2_{ZZH} vs. χ^2_{ZHH} scatter plot obtained from kinematic fitting. ISR is not treated in the fit. A promising separation of signal and background events can be observed. This distribution represents a valuable variable for the event selection as input for neural net training. First investigations indicate a relative improvement of 20% in $l\bar{l}H$.

Promising results are achieved with the ZHH fit and the ZZH fit. The ZHH fit hypothesis has discriminating power between signal and backgrounds. Since the hard Higgs mass constraints need to be fulfilled exactly by the events, ZZH and ZZZ events do not satisfy the fit hypothesis. The ZZH fit hypothesis offers a good separation between signal and backgrounds to large $P(\chi^2)$. The ZHH events fulfil the hard Higgs mass constraint, but not the soft Z -mass constraint on the second jet pair. Therefore, ZHH events receive large contributions to χ^2 from the soft mass constraint which leads to small $P(\chi^2)$. In figure 6.11, a scatter plot of the corresponding χ^2 distributions of both fit hypotheses is shown. A very clear separation of signal and backgrounds can be achieved. Signal events obtain smaller χ^2 values and thus larger $P(\chi^2)$ for the ZHH fit hypothesis. For the ZZH fit, the χ^2 values of the signal are larger and thus indicating smaller $P(\chi^2)$. As expected, ZZH events show the opposite behaviour for the respective fit hypotheses. This results in the very clear separation of the events. First investigations show that by adding this distribution as input variable to the respective neural net (sec. 5.2) a relative improvement in the lepton channel of 20% can be obtained compared to the current analysis strategy. The impact on the event selection in the Higgs self-coupling analysis is discussed in detail in chapter 8. In both cases $\gamma\gamma$ overlay is not included (sec. 5.2).

6.5.2 Mass Reconstruction

The mass distribution of the most energetic Higgs boson before and after the equal-mass fit is shown in figure 6.12 for signal and backgrounds, respectively. The signal mass resolution is improved. Both sides of the distribution are shifted to larger masses after the

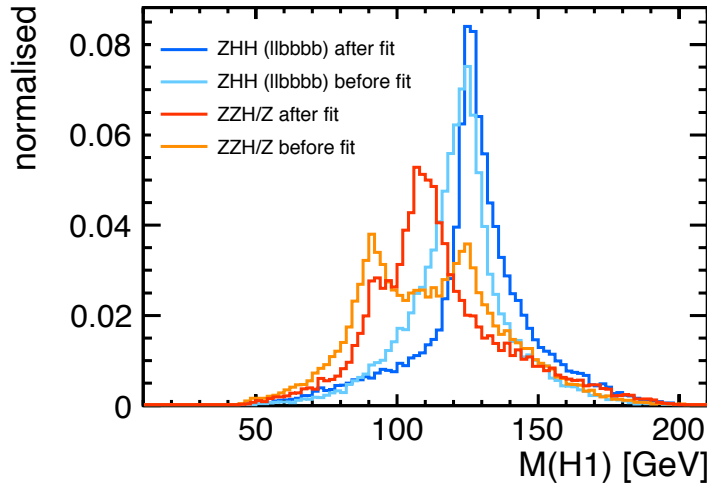


Figure 6.12: Higgs mass for signal and backgrounds before and after the equal-mass fit, respectively. So far ISR is not considered in the fit.

fit. This is very pronounced for the left side of the mass distribution and the conspicuous tail to larger masses. The shape of the background distribution is less affected by ZZZ events, due to the much smaller cross section compared to ZZH after the preselection. Before fitting the Higgs boson mass is obtained by using the jet pairing of eq. 5.4. The background distribution obtains peaks at around 125 GeV and 91 GeV. As expected by the equal-mass constraint, the fit chooses a mass value between the nominal Higgs and Z mass, represented by the peak at around 110 GeV after the fit. However, a second peak at around 90 GeV is present. Seemingly, next to the small contribution of ZZZ events, ZZH events have been mis-reconstructed by the fit. Plausible reasoning can be missing energy and momentum in the events.

In conclusion, missing four-momentum degrades the fit performance and has large impact on the mass reconstruction. ISR and beamstrahlung can be present in the events, but are not yet considered in the fit. Additionally, the impact of missing four-momentum from semi-leptonic decays of b jets on the fit performance and the ISR treatment needs to be studied. The impact of missing four-momentum from ISR and semi-leptonic decays are studied in the following chapter. Strategies to include both effects in kinematic fits are evaluated, solving performance issues in processes with heavy-flavoured jets.

Chapter 7

Considering ISR and Semi-leptonic Decays in Kinematic Fits

In the investigation of kinematic fits, we cannot simply consider energy and momentum conservation due to the presence of ISR. Additionally, the investigated processes contain b jets. Compared to light quarks, b quarks can decay semi-leptonically, i. e. $b \rightarrow cl\nu$, with a branching fraction of $BR(b \rightarrow \text{semi-leptonic}) \sim 10.7\%$ [27]. The neutrinos in such decays carry a certain amount of four-momentum. Both effects cause missing four-momentum. The results of the previous chapter indicate that missing four-momentum degrades the fit performance. Since ISR reduces the effective centre-of-mass energy it has to be taken into account. However, it needs to be studied whether an automatic ISR recognition, as generally provided by the ISR photon fit object, is still possible for events with additional missing four-momentum from semi-leptonic decays of b and cascade c quarks. In sec. 7.1, the effects of treating ISR in kinematic fits are discussed. Subsequently in sec. 7.2, the fit performance is evaluated. Hereafter, different approaches are discussed which provide an ISR treatment in processes including b jets. In sec. 7.3, a strategy is presented in which ISR is treated on an event-by-event basis using ISR properties. The developed strategy yields an optimised mass resolution. Hereafter, a more sophisticated approach is investigated in which semi-leptonic decays are considered. The impact of semi-leptonic decays on kinematic fitting and therefrom arising issues are discussed in sec. 7.4. A strategy of correcting missing energy in the jets is introduced in sec. 7.5. Since the investigation is based on MC truth information, an outlook on particle identification tools on reconstruction level is given in sec. 7.6. By correcting the jet energies, potential improvements in the fitting procedure are investigated with regard to the fit performance, effects on the ISR recognition, and mass resolution as discussed in sec. 7.7. In the following, the investigations are illustrated using $ZHH \rightarrow llbbbb$ as benchmark process. To investigate the full potential of kinematic fits the $\gamma\gamma$ overlay is not included. Unless noted otherwise, the shown figures correspond to the equal-mass fit.

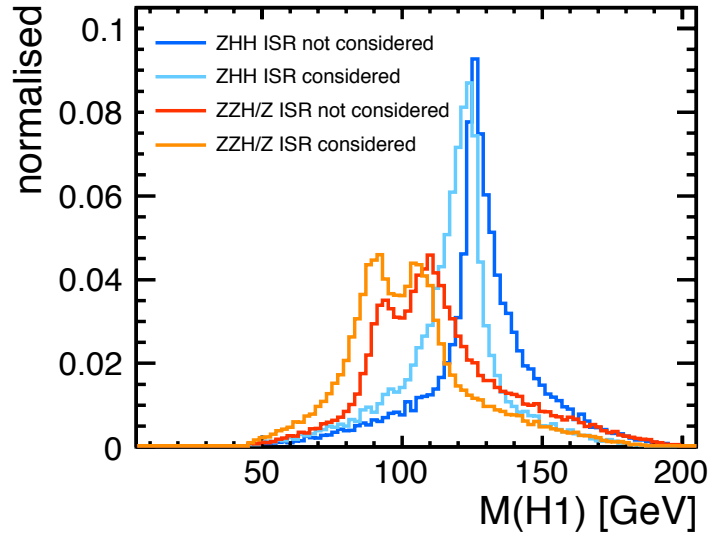


Figure 7.1: Fitted mass distribution of the most energetic Higgs boson for ZHH obtained from the equal-mass fit without (dark blue) and with ISR considered (light blue). The fitted mass distribution for the background processes ZZH and ZZZ are also shown without (red) and with (orange) ISR in the fit.

7.1 Considering ISR in the Fit

ISR can be treated with an additional ISR photon fit object which helps to satisfy energy and momentum conservation constraints (sec. 6.3.2). Since more than one ISR photon can be present in an event, the ISR photon fit object takes into account the most energetic ISR photon, which is emitted along z direction [187]. It is parametrised by the total missing p_z of an event, which is converted into ISR energy. So far, the ISR feature has not been tested in processes with heavy jets. Compared to light jets, four-momentum conservation of reconstructed b jets is not necessarily satisfied, since b and cascade c quarks can decay semi-leptonically, i. e. $b \rightarrow cl\nu$ and $c \rightarrow sl\nu$. In a first attempt the ISR photon fit object is included in the fit for all events as in [187]. The resulting mass distribution of signal and backgrounds is shown in fig. 7.1. For better comparison, the fit result without considering ISR is also shown. Generally, considering ISR should lead to a correct reconstruction of events independently of the amount of ISR energy [187]. However, following issues arise:

- Not including ISR in the fit affects events with ISR. In this case, to satisfy energy and momentum conservation missing four-momentum is compensated by assigning all energy and momentum to the jets. This results in an overestimation of the jet four-momenta and leads to a bias to larger masses.
- Considering ISR in the fit is expected to work well for events with ISR. The longitudinal component of missing p_z in such events is assigned to the ISR photon fit object as $E_\gamma^{ISR} = |-p_z|$ and the jet four-momenta should be reconstructed correctly.

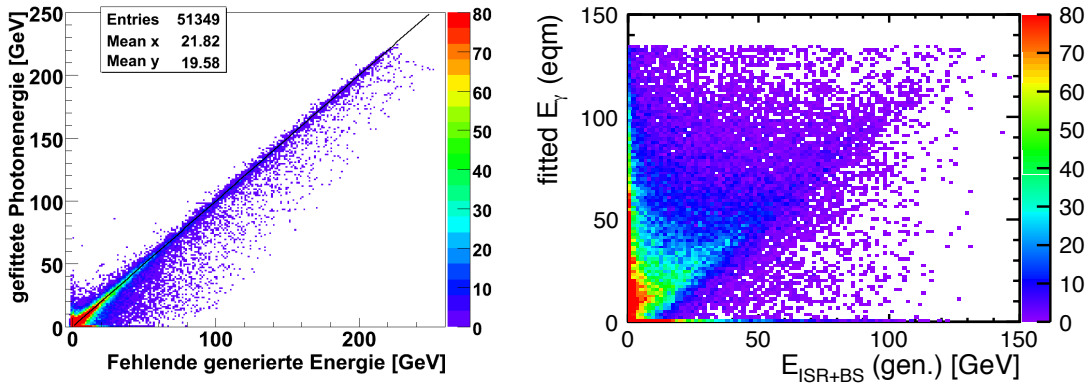


Figure 7.2: Fitted photon energy as a function of the generated ISR and beamstrahlung energy (both denoted as ISR throughout this thesis). Left: for $e^+e^- \rightarrow WW$. Figure taken from [187]. Right: for the equal-mass fit of $ZHH \rightarrow llbbbb$ events.

Opposed to this, the fit assigns “fake” ISR to events without ISR. This fraction of four-momentum is then missing to the jets and results in an underestimation of the fitted jet four-momenta. In the reconstruction of boson masses, this leads to a biased mass distribution to smaller values.

7.2 Fit Performance with ISR

The kinematic fit compensates four-momentum conservation by increasing or decreasing the four-momenta of the fit objects. This leads to biased boson mass distributions to either smaller or larger values depending on the ISR treatment. Therefore, the fit performance is evaluated by using three measures:

1. the fitted ISR energy compared to the generated ISR energy,
2. the jet energy pulls, since including ISR in the fit should improve the pulls compared to the fit without ISR,
3. and the fit probability as a function of the total missing energy before fitting which gives an indication of the fit performance for events suffering from missing energy.

In fig. 7.2 the fitted photon energy is shown as a function of the generated photon energy for light jets in $e^+e^- \rightarrow WW$ [187], and the equal-mass fit using $ZHH \rightarrow llbbbb$ events. Compared to light-flavoured jets, in which the photon energy is well reconstructed by the fit, for events with heavy jets the fitted photon energy is overestimated for many events. Especially, this concerns events with small generated photon energies. Requiring $P(\chi^2) > 0.0001$ gives better results. The respective photon energy correlation of the equal-mass (left) and the ZHH fit (right) are shown in figure 7.3. The hard constraints on the two Higgs masses in the ZHH fit lead to a better correlation. However, even then the fitted and generated photon energies are not as well correlated as for light jets. In the

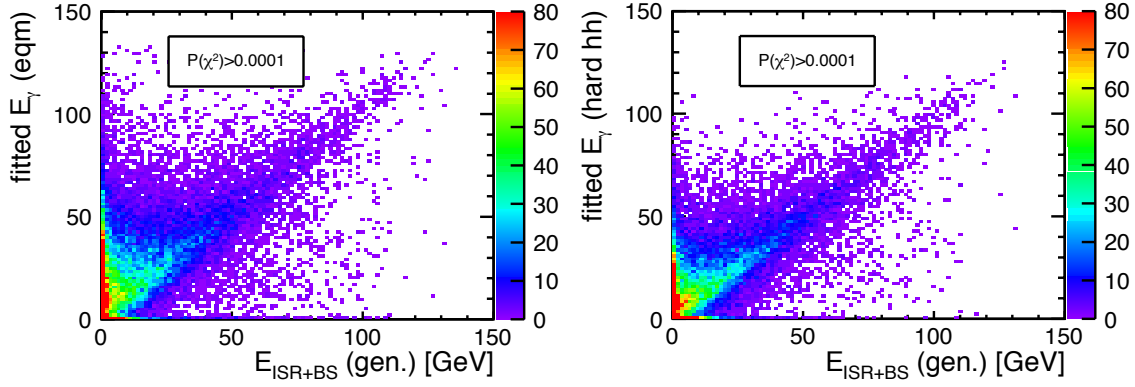


Figure 7.3: Fitted photon energy as a function of the generated photon energy after applying a cut of $P(\chi^2) > 0.0001$. Left: for the equal-mass fit. Right: for the ZHH fit.

events additional missing four-momentum from semi-leptonic decays could falsify the photon reconstruction. This becomes even more obvious when looking at $P(\chi^2)$ of the equal-mass fit with ISR considered as a function of the total missing energy before fitting ($\sum E_{vis} - 500$ GeV) as illustrated in figure 7.4. Compared to the fit without ISR considered (left), similar results for events with approximately $(\sum E_{vis} - 500$ GeV) $\gtrsim -20$ GeV can be observed. Events with larger missing energy obtain larger fit probabilities when considering ISR in the fit. However, a large event population is still present at small $P(\chi^2)$ over the entire range of $(\sum E_{vis} - 500$ GeV). Events with small $P(\chi^2)$ have additional missing four-momentum which leads to wrong results. Since ISR is considered in the fit, the source of additional missing four-momentum are semi-leptonic b and cascade c decays. The fit does not distinguish between different types of missing four-momentum. ISR reduces the effective centre-of-mass energy, while semi-leptonic decays cause missing energy and momentum in the fragmentation and hadronisation of jets.

The energy pulls for fits without and with considering ISR are shown in figure 7.5. The energy pulls of the four b jets in the signal final state are added to one histogram. The

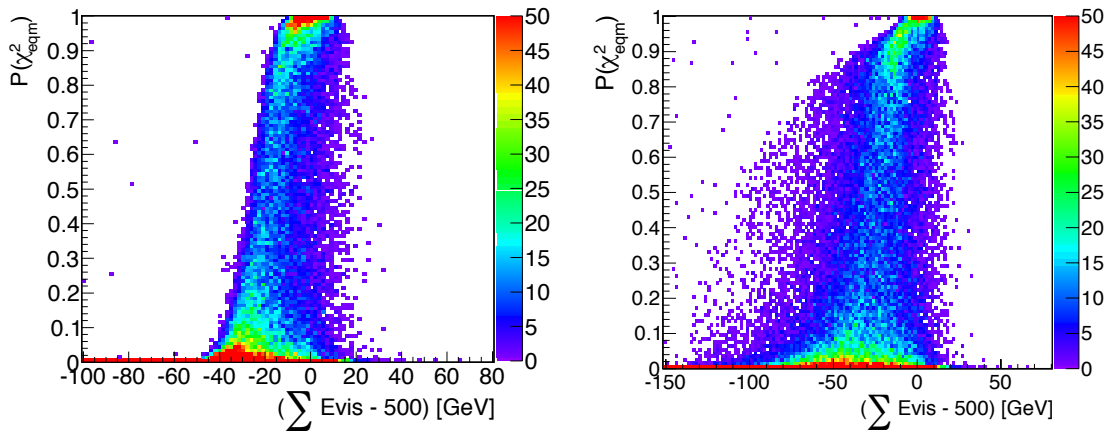


Figure 7.4: $P(\chi^2)$ as a function of the total missing energy before fitting. Left: without ISR treated in the equal-mass fit (sec. 6.4). Right: with ISR treated in the equal-mass fit.

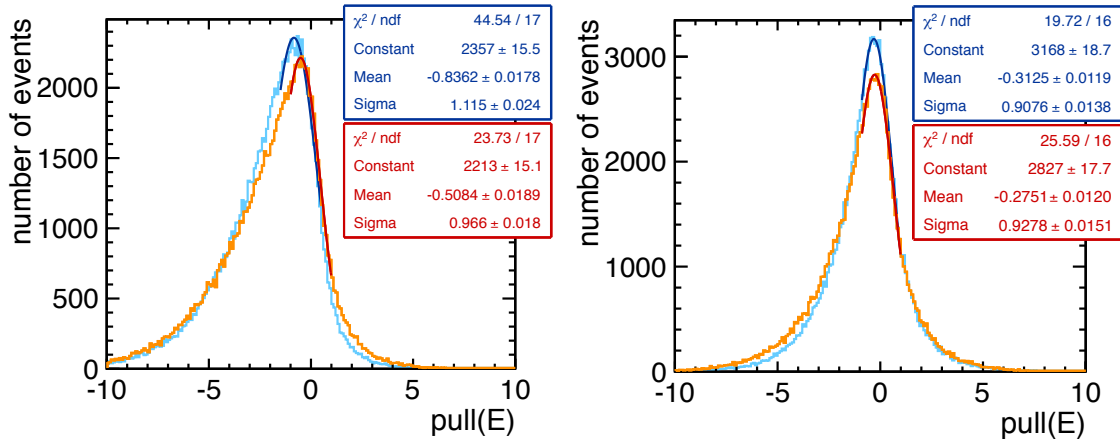


Figure 7.5: Jet energy pulls for $ZHH \rightarrow llbbbb$ events of the ZHH fit (orange) and equal-mass fit (blue). Left: without ISR considered (sec. 6.4). Right: with ISR considered. In direct comparison, a large improvement can be seen in both fits when considering ISR.

widths of the pulls are not a reliable measure, since the Gaussian does not describe the distributions properly. Compared to the fit without ISR, a tremendous improvement can be seen for both fit hypotheses when considering ISR. In particular the distributions are much more symmetric indicating an improved event reconstruction in the fit including ISR. Considering ISR helps to fulfil four-momentum conservation. Therefore, the shift to smaller values is less dominant and the large tail to negative values is improved. The tail indicated that some events were shifted much stronger by the fit without ISR to satisfy the constraints. The pulls are still of non-Gaussian shape and the peak is shifted from 0. The shifted peak indicates that the fitted value is generally larger than the measured value before fitting and the errors fulfil $\Delta E_{fit} < \Delta E_{meas.}$. This is still caused by the energy conservation constraint. Despite of having treated ISR in the fit, energy conservation is not fulfilled for b jets in which the b and cascade c quarks decay semi-leptonically. Therefore, two different approaches of solving the issues with ISR recognition and additional missing four-momentum are investigated in this thesis:

1. A strategy on an event-by-event basis is developed to identify events with and without ISR by using ISR characteristics as missing energy and large $|\cos(\theta_{miss})|$ values since low angle ISR escape detection through the beam pipe. This does not provide an automatic ISR recognition in the fit as for light jets, but is a simple approach to decide whether to include the ISR photon fit object in the fit for certain events.
2. Semi-leptonic decays of b and c quarks cause a mis-reconstruction of jet momenta in the fit since the additional missing four-momentum is mis-identified as ISR. Missing four-momenta from semi-leptonic decays do not allow an automatic ISR recognition. A strategy is developed in which missing energy from such decays is corrected in the jets. The impact on the fit performance is studied.

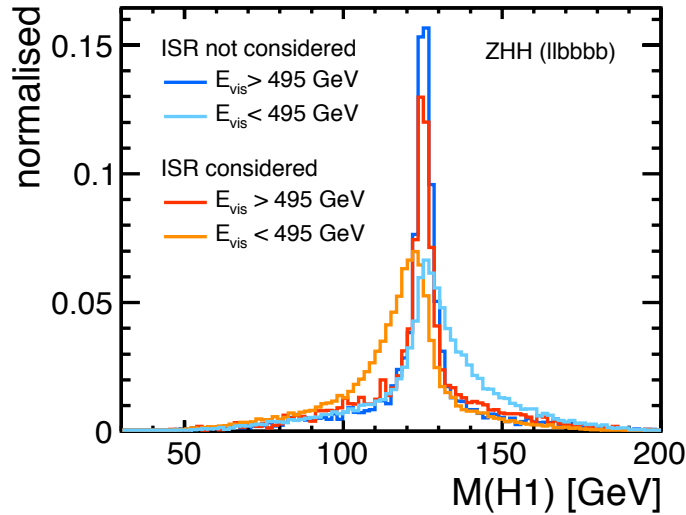


Figure 7.6: Higgs mass after the equal-mass fit without and with considering ISR. Events are separated with respect to E_{vis} . Events with small missing energy are independent of the ISR treatment. Events with large missing energy depend on the ISR consideration.

7.3 Strategy for an Event-specific ISR Treatment

The first approach allows working around the issue with automatic ISR recognition in the fit. In this strategy all events are categorised into “without” and “with” ISR by using ISR characteristics as missing energy and $|\cos(\theta_{miss})|$. This allows for an event-specific ISR treatment, which yields an optimised Higgs mass resolution.

7.3.1 Event Identification using ISR Properties

Events with significant ISR at small angles miss a certain amount of energy. The fitted Higgs mass without and with ISR treated in the fit is shown in fig. 7.6. The events are separated with respect to E_{vis} . Events without significant missing energy obtain similar mass distributions regardless of the ISR consideration in the fit. These events are populated around 125 GeV. Opposed to this, events with significant missing energy depend on the ISR consideration. These events obtain different mass distributions, biased to either smaller or larger masses. This indicates that a mere requirement on missing energy is not effective in the event categorisation. This is supported by the relation of visible energy and χ^2 , as depicted in fig. 7.7. In the fit without ISR considered, events with $E_{vis} \lesssim 490$ GeV are shifted to larger χ^2 and thus smaller $P(\chi^2)$. Opposed to this, including ISR in the fit moves the events to smaller χ^2 and thus larger $P(\chi^2)$. Events with $E_{vis} \gtrsim 490$ GeV are hardly affected by the ISR treatment. Therefore, especially events with $E_{vis} \lesssim 490$ GeV depend on the ISR consideration and need additional differentiation using $|\cos(\theta_{miss})|$. Since ISR photons are emitted at small angles in the beam pipe, events with ISR tend to have large $|\cos(\theta_{miss})|$ values next to missing energy. In the foregoing it seemed that

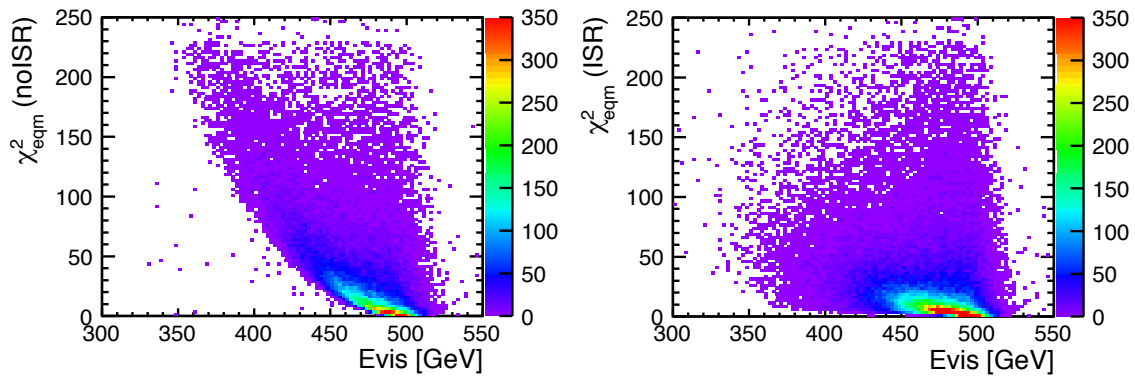


Figure 7.7: χ^2 of the fit without (left) and with ISR (right) as function of E_{vis} for $ZHH \rightarrow llbbbb$. Considering ISR results in improved χ^2 for events with large missing energy.

events with small missing energy are independent of the ISR consideration. Something different can be observed when looking at $|\cos(\theta_{miss})|$ as a function of the fitted Higgs mass for fits without and with ISR as depicted in fig. 7.8. Fitting without considering ISR results in a bias to larger masses for events with large $|\cos(\theta_{miss})|$. This is anticipated since the jet four-momenta are overestimated by the fit when compensating ISR to ensure four-momentum conservation. Additionally, the same fit shows a rather unbiased mass distribution around 125 GeV at small $|\cos(\theta_{miss})|$. However, considering ISR results in a bias to smaller masses over the entire range of $|\cos(\theta_{miss})|$. For events with small $|\cos(\theta_{miss})|$ the fit underestimates the jet four-momenta by assigning some four-momentum to “fake” ISR. However, a shift to smaller masses for events with large $|\cos(\theta_{miss})|$ is not expected. These events are expected to have ISR and thus indicate an issue with the automatic ISR recognition in the fit. This issue can be caused by the presence of missing energy and momentum from semi-leptonic b and cascade c decays. In this case, the fit mis-identifies additional missing four-momenta as ISR which results in a wrong event reconstruction. In general, events with large $|\cos(\theta_{miss})|$ are better represented by the fit with ISR, as shown in fig. 7.9. The observations indicate, that information on both $|\cos(\theta_{miss})|$ and E_{vis} need to be combined to categorise the events with respect to their ISR content.

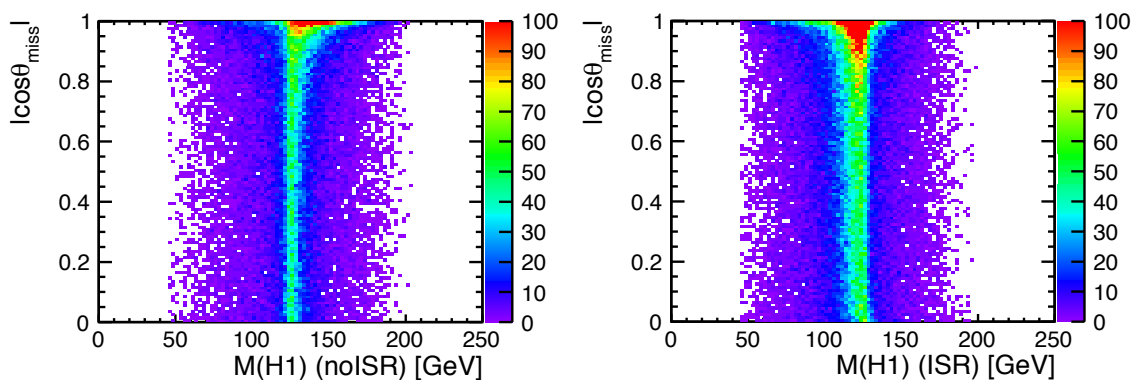


Figure 7.8: $|\cos(\theta_{miss})|$ as a function of the fitted Higgs mass $M(H1)$ for $ZHH \rightarrow llbbbb$ events without ISR (left) and with ISR (right) considered in the equal-mass fit.

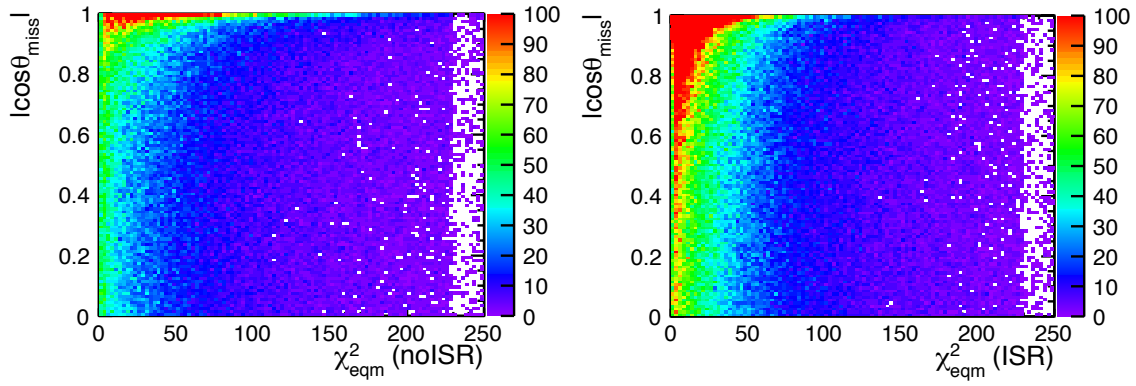


Figure 7.9: $|\cos(\theta_{miss})|$ as a function of χ^2 for $ZHH \rightarrow llbbbb$ events without ISR (left) and with ISR (right) in the equal-mass fit.

7.3.2 Optimised Event Categorisation

The separation strategy of events with and without significant ISR is depicted in fig. 7.10. Missing energy is present over the entire $|\cos(\theta_{miss})|$ range, which again indicates that energy alone does not give valuable information for the event separation. Most of the events are placed in the region of large $|\cos(\theta_{miss})|$ in which events with large ISR are expected. Events with small $|\cos(\theta_{miss})|$ and only small missing energy correspond to events without significant ISR. Therefore, the events are categorised as

$$\text{no ISR: } E_{vis} \geq X \text{ GeV} \quad \text{or} \quad |\cos(\theta_{miss})| \leq Y, \quad (7.1)$$

$$\text{ISR: } E_{vis} < X \text{ GeV} \quad \text{and} \quad |\cos(\theta_{miss})| > Y, \quad (7.2)$$

and treated differently in the fit. The strategy yields an optimised Higgs mass distribution. Combining all events after having treated them differently in the fit should give an unbi-

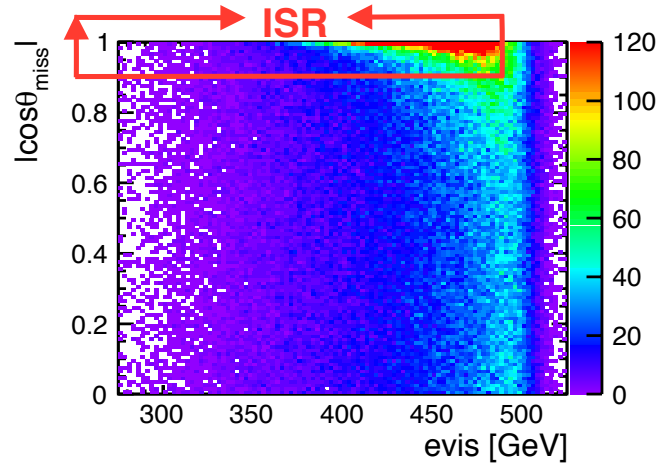


Figure 7.10: $|\cos(\theta_{miss})|$ as a function of E_{vis} for $ZHH \rightarrow llbbbb$ events. Missing energy is present over the entire range of $|\cos(\theta_{miss})|$. The red box indicates the area in which the events should be treated with ISR in the kinematic fit.

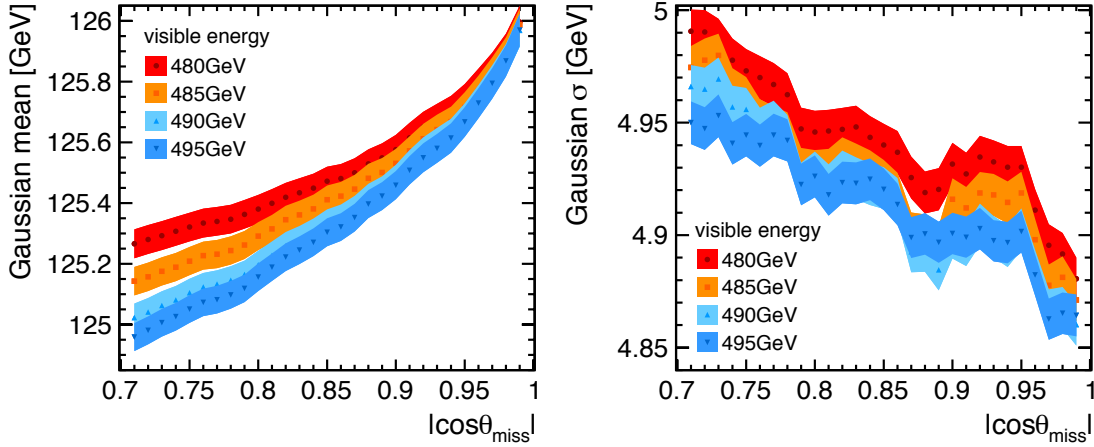


Figure 7.11: Gaussian mean (left) and σ (right) of the combined Higgs mass distribution as a function of $|\cos(\theta_{miss})|$ for different visible energies for $ZHH \rightarrow llbbbb$ events.

ased combined mass distribution. Referring back to the Higgs mass distributions shown in fig. 7.1, the combined Higgs mass should ideally be represented by the left side of the signal mass distribution without ISR considered (dark blue) and the right slope of the signal mass distribution with ISR considered in the fit (light blue). Since the biased sides of these distributions are caused by events which do not satisfy the imposed ISR treatment in the respective fits, selection thresholds X and Y for E_{vis} and $|\cos(\theta_{miss})|$ are determined, giving an optimised unbiased combined mass resolution. Therefore, various combinations of $|\cos(\theta_{miss})|$ and E_{vis} are evaluated in terms of the combined Higgs mass. The thresholds of E_{vis} and $|\cos(\theta_{miss})|$ have to be evaluated for each signal channel individually due to the close relation to an optimised mass resolution.

The ISR treatment with the ISR photon fit object works well for photon energies larger than the detector resolution [187]. Therefore, four energies around 490 GeV are evaluated for $|\cos(\theta_{miss})|$ values between 0.70 and 1.00. To decide which combination of $|\cos(\theta_{miss})|$ and E_{vis} gives the best mass resolution a Gaussian is fitted to the combined mass around the centre of the peak. Fig. 7.11 shows the Gaussian mean and standard deviation σ resulting from the Gaussian fits as a function of $|\cos(\theta_{miss})|$. Ideally, the mass distribution with the smallest σ and with a mean close to 125 GeV should give the optimised result. However, we observe a conflict of goals. While the mean values are close to the nominal Higgs mass at small $|\cos(\theta_{miss})|$, the standard deviations improve to large $|\cos(\theta_{miss})|$. Therefore, either a broader distribution close to the nominal Higgs mass is chosen, or a slightly shifted distribution to larger masses but with better resolution. The latter is chosen since this strategy yields an optimised mass resolution. Overall smaller mean values are obtained for larger energies over the entire $|\cos(\theta_{miss})|$ range and σ obtains a minimum for $E_{vis} = 490$ GeV. The thresholds are selected as

$$E_{vis} = 490 \text{ GeV}, \quad |\cos(\theta_{miss})| = 0.89. \quad (7.3)$$

There is no large difference in the mass resolution if a slightly different $|\cos(\theta_{miss})|$ and E_{vis} is chosen, since the Gaussian is fitted around the centre of the peak. However, the distributions are less symmetric. Selecting smaller or larger $|\cos(\theta_{miss})|$ values results in larger tails to smaller or larger masses, respectively. Then, more events are mistakenly treated with ISR in the fit. This is also the case for E_{vis} . By choosing smaller E_{vis} some events are mis-reconstructed by the fit, since missing energy does not solely originate from ISR but also from possible semi-leptonic decays of b and c quarks. The selected combination gives the best resolution with small and symmetric tails to both sides. The optimised combined result for $ZHH \rightarrow llbbbb$ is shown in fig. 7.12 and discussed in the following.

7.3.3 Results of the Mass Reconstruction

Fig. 7.12 illustrates the combined Higgs mass for $ZHH \rightarrow llbbbb$ events compared to the results of the equal-mass fit without and with ISR considered, respectively. Due to the developed strategy the combined mass distribution successfully approaches the left side of $M(H1)$ without ISR consideration (dark blue) and the right slope of $M(H1)$ with ISR considered in the fit (light blue). Additionally, the Higgs mass before fitting is shown (green). Despite the conflict of goals in the developed strategy, using kinematic fits and applying the event-specific ISR treatment results in an optimised mass resolution. In fig. 7.13 the mass distribution for the ZZH/Z backgrounds before fitting, without and with ISR in the fit, and the combined results are depicted. The separation of these backgrounds and the signal is very important for the Higgs self-coupling analysis, since these processes have the same final state particles. The mass distribution is not much influenced by ZZZ due to its small cross section compared to ZZH after preselection. Generally, the equal-mass fit shifts the Higgs and Z -boson masses to a central value, represented by the peak around 110 GeV. A second peak around 90 GeV is present which does not correspond solely to ZZZ events, but also originates from ZZH events with additional missing four-momentum from semi-leptonic b and c decays. This is discussed in the following section.

To compare the discriminating power of the Higgs mass for the signal and the discussed background processes before and after fitting, a simple selection cut can be applied to the lower mass distribution since ZZH/Z events need to be suppressed. For example, by selecting events with $m_H > 115$ GeV the signal selection efficiency improves by more than 15% from 62% to 71%. The corresponding significances $N_S / \sqrt{N_S + N_B}$ before and after fitting are illustrated in fig. 7.14. A significant improvement can be achieved by applying kinematic fits and the developed strategy. The separating power for signal events and the discussed background processes is improved. The impact on the analysis needs to be studied, since the generally large number of background events from different processes overwhelm the signal events.

To summarise, the developed strategy allows ISR treatment on an event-by-event basis. The combined mass distributions obtain an optimised mass resolution and result in an

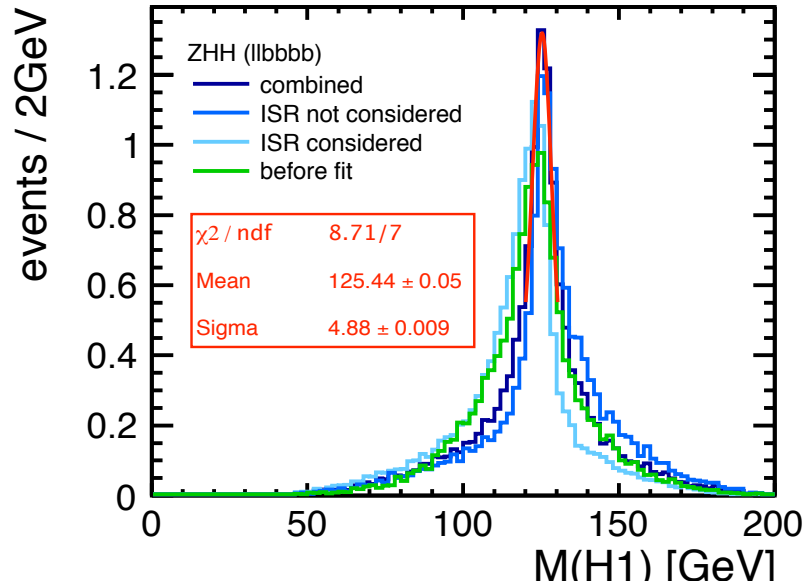


Figure 7.12: $M(H1)$ before and after fitting of ZHH events. The combined optimised mass distribution is shown, as well as the results of the equal-mass fits with and without ISR. The choice of E_{vis} and $|\cos(\theta_{miss})|$ results in a distribution which successfully approaches the sides of the masses without and with ISR in the fit. The errors of the fit correspond to the full MC statistics.

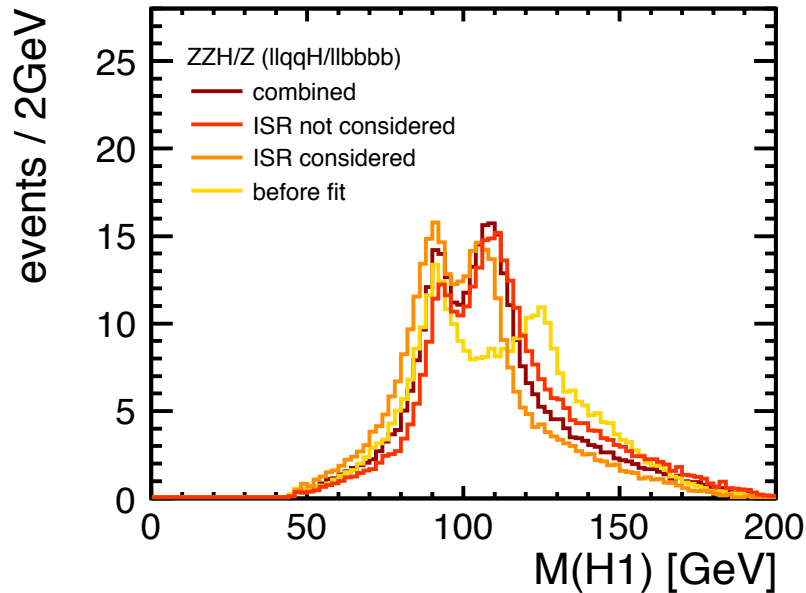


Figure 7.13: $M(H1)$ before and after fitting for ZZH/Z backgrounds. The combined distribution is shown, as well as the results of the equal-mass fits without and with ISR considered.

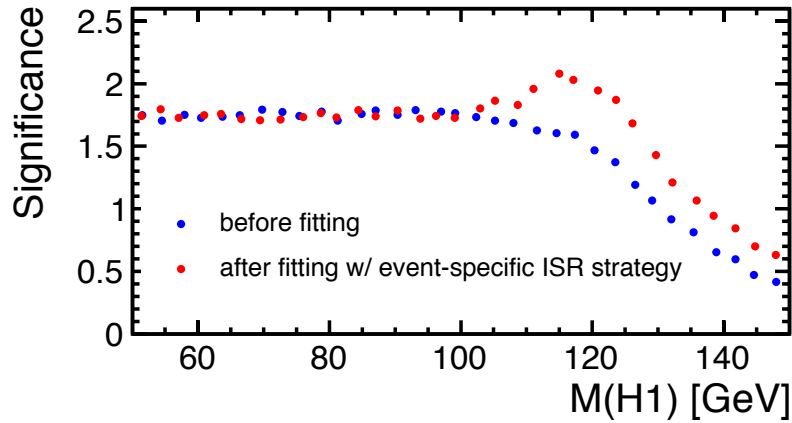


Figure 7.14: Significance $N_S / \sqrt{N_S + N_B}$ after applying a lower mass cut on ZHH and ZZH/Z events. The separation of these processes is crucial in the analysis. The significance before fitting (blue) and after fitting using the event-specific ISR treatment (red) is shown. A significant improvement can be observed after applying the event-specific strategy.

enhanced separation of signal and background events. However, the conflict of goals in this strategy points to the need of a more sophisticated approach to solve the issues with the automatic ISR recognition in the fit. Events with additional missing four-momentum from semi-leptonic decays are not treated correctly by the kinematic fit with the ISR photon parametrisation, and thus degrade the fit performance. The observations indicate that by considering missing energy from semi-leptonic decays in the jets, the fit performance could be improved and the issues with the automatic ISR recognition could be solved. Therefore, the possibility of considering semi-leptonic decays in the kinematic fit and the impact of such an advanced approach on the fit performance is studied in the following.

7.4 Impact of Semi-leptonic Decays

7.4.1 Effect on ISR Consideration and Mass Reconstruction

The most obvious issue of missing four-momentum from semi-leptonic decays in b jets regards the ISR recognition in the kinematic fit. The generated ISR energy is not well reconstructed by the fit. Additional missing four-momentum from semi-leptonic decays leads to biased boson mass distributions to either smaller or larger values depending on whether ISR is considered in the fit. The respective effects are obvious by looking at the ZZH/Z background mass distributions in fig. 7.13. The various background distributions show a peak at around 90 GeV which is more pronounced for the fit with ISR compared to the fit without ISR. This peak can be explained in terms of additional missing four-momentum from semi-leptonic decays: In case of the equal-mass fit with ISR considered, the fit does not discriminate between different sources of missing four-momentum. Addi-

tional missing four-momentum is assigned to ISR which results in a wrong reconstruction of boson masses to smaller values. Since the equal-mass constraint yields an averaged boson mass, and due to the missing four-momenta from semi-leptonic decays, the ZZH events then resemble ZZZ and are mis-reconstructed by the fit since they do not naturally satisfy the equal-mass constraint. Events without missing energy are reconstructed correctly. Such a mis-reconstruction can also be present in the fit without considering ISR, which results in an overestimation of the jet four-momenta. In case of ZZH events, the total missing four-momentum results in smaller fitted masses but the overestimation of the jet momenta shifts more events closer to 110 GeV. Consequently, the second peak at around 90 GeV is not as dominant as for the fit with ISR.

Despite of having improved the mass resolution by applying the event-specific ISR treatment, especially the background mass distributions indicate that missing four-momenta from semi-leptonic decays lead to a mis-reconstruction of boson masses. This can be improved by correcting missing energy from semi-leptonic decays in the jets. Since the ISR treatment in the kinematic fit works well for u and d quarks [187], correcting missing energy from semi-leptonic decays in heavy jets could enable an automatic ISR recognition and improve the event reconstruction in the fit.

7.4.2 Effect on Energy Error Parametrisation

The success of kinematic fits strongly depends on a correct error parametrisation of the measured quantities of the various fit objects. Recently, the error parametrisation of jet energies for $ZHH \rightarrow llbbbb$ events was studied in detail in [84]. In this study, the uncertainties on the jet energies are obtained by using MC truth information. ΔE_{jet} is determined by comparing the initial quark energies to the reconstructed jet energies. Each jet is associated to the corresponding initial quark by choosing the combination in which the MC quark has the smallest angular distance to the measured jet. The difference between

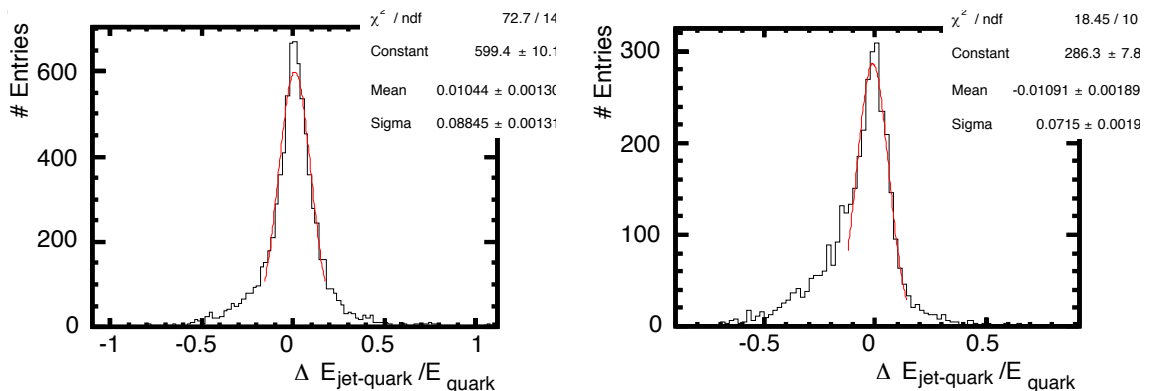


Figure 7.15: Deviation of reconstructed jet energy from the corresponding MC quark. Left: energy deviation of u and d quarks in WW processes. Right: energy deviation of b jets in ZHH processes. Figures are taken from [84].

the energy of the measured jets and the associated MC truth quarks are filled into histograms each of which covers 10 GeV of the quark-energy range. Examples are shown in fig. 7.15 for light and heavy quarks, respectively. Such distributions are used to determine the jet-energy resolution σ_E , which enters the kinematic fit in the covariance matrix C^{-1} as

$$\Delta E_{jet} = E_{jet} \cdot \sigma_E . \quad (7.4)$$

For light quarks the distributions are Gaussian shaped without significant tails. Compared to light jets, these non-Gaussian tails are dominant for b jets. They originate from missing energy caused by semi-leptonic decays. Semi-leptonic decays represent an important source of error on σ_E , since they are not included in the definition of the MC truth quark. σ_E is determined by fitting Gaussians in the range of $\pm 0.75 \cdot RMS$ to the core of the distributions. Hence, the tails are excluded and the estimate of σ_E (eq. 6.6) is rather optimistic. As a consequence, ΔE_{jet} is underestimated especially for events with large missing energy. If the energy deviations between reconstructed jets and initial quarks are not included in the fit, they degrade the fit performance. Considering the non-Gaussian tails in the jet-energy resolution could enhance the fit performance, since ΔE_{jet} for events with additional missing energy becomes large enough so that the kinematic fit is more likely to be successful. The impact of the non-Gaussian tails is visible in the mean of the distributions. For b jets the mean is shifted to small values. The shift of the mean can be improved by correcting missing energy from semi-leptonic decays.

7.5 Strategy of Jet Energy Correction

This strategy takes advantage of the fact that every neutrino from semi-leptonic decays is accompanied by a charged lepton, the energy of which can be measured to very high precision. The strategy to correct for missing energy from semi-leptonic decays in jets is

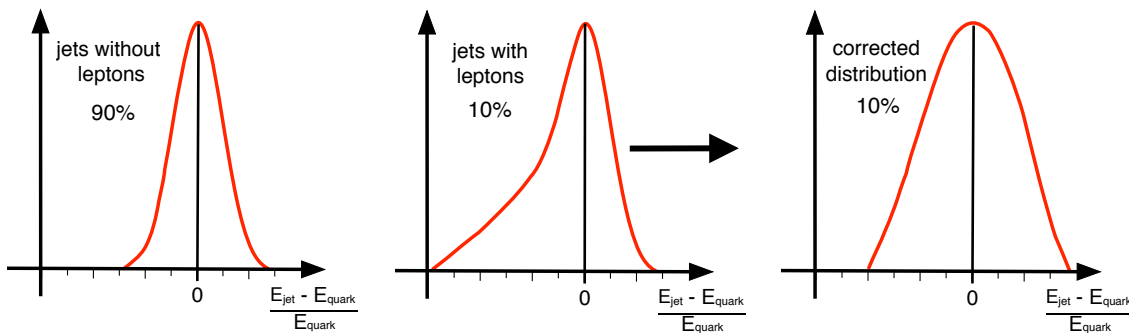


Figure 7.16: Schematic sketch of the idea for correcting jet energies. Left: in 90% of the jets no semi-leptonic decays of b or c quarks are expected. Middle: 10% of the jets contain semi-leptonic decays, which result in non-Gaussian tails to smaller jet energy fractions. Right: missing energy from semi-leptonic decays is corrected for in these 10% of the jets. Considering the tails leads to a broader distribution $\sigma_{nolep} < \sigma_{lep}$.

schematically illustrated in fig. 7.16. The branching ratio of semi-leptonic b decays reads $\text{BR}(b \rightarrow \text{semi-leptonic}) \sim 10.7\%$ [27]. Therefore, roughly 90% of the jets do not suffer from missing energy from semi-leptonic b decays and do not require a correction of their energy. In this case, the energy deviation of the reconstructed jet from the respective initial quark is Gaussian distributed without significant tails. In roughly 10% of the jets, missing energy from semi-leptonic b decays is expected. Since cascade c quarks can also decay semi-leptonically, missing energy from c and b decays is considered in this investigation. In this case non-Gaussian tails are visible in the energy deviation distributions and need to be considered in σ_E to include proper uncertainties in the fit. Therefore, missing energy in these jets is corrected by adding a fraction of the energy carried by the charged lepton which accompanies the neutrino in such decays. The energy correction broadens the distribution of the energy deviation, so that $\sigma_{\text{nolep}} < \sigma_{\text{lep}}$, but at the same time the non-Gaussian tails are taken into account.

All jets are divided into jets “without leptons” and “with leptons”. Jets without leptons do not need any correction of their energy. The errors on the jet energies are given by (eq. 6.6)

$$\Delta E_{\text{jet}} = \sqrt{(0.568)^2 E_{\text{jet}} + (3.301)^2}. \quad (7.5)$$

Jets are assigned to the second category if they contain at least one lepton. In this case, the neutrino energy E_ν is corrected for by taking advantage of the precisely measured lepton energy E_{lep} . E_ν can be described as fraction x of the corresponding E_{lep} as

$$E_{\text{jet}}^{\text{corr}} = E_{\text{jet}} + E_\nu = E_{\text{jet}} + x \cdot E_{\text{lep}}. \quad (7.6)$$

Here, x can be determined through the lepton-energy fraction as

$$x = \frac{E_{\text{lep}}}{(E_{\text{lep}} + E_\nu)} \Leftrightarrow E_\nu = \left(\frac{1}{x} - 1\right) E_{\text{lep}}. \quad (7.7)$$

Figure 7.17 illustrates the lepton energy from semi-leptonic decays divided by the total energy of the lepton-neutrino pair. For semi-leptonic b and cascade c decays the distribution shows a correlation to which a Gaussian is fitted. The mean and σ of the Gaussian give an estimate of x and Δx . The energies of leptons and neutrinos which do not originate from semi-leptonic b and c decays are uncorrelated. These distributions are based on MC truth information and derived from approximately 1000 events. For now, to investigate the full potential of the jet-energy correction in kinematic fitting, this requirement is sufficient. In sec. 7.6, the quality of this approximation is discussed by giving an outlook on particle identification tools on reconstruction level.

Combining eq. 7.6 and eq. 7.7, the corrected jet energy reads

$$E_{\text{jet}}^{\text{corr}} = E_{\text{jet}} + \left(\frac{1}{\langle x \rangle} - 1\right) E_{\text{lep}}, \quad (7.8)$$

where $\langle x \rangle$ denotes the mean. The errors on the corrected jet energies read

$$\Delta E_{\text{jet,corr}}^2 = \Delta E_{\text{jet}}^2 + \left(\frac{\Delta \langle x \rangle}{\langle x \rangle^2}\right)^2 E_{\text{lep}}^2 + \left(\frac{1}{\langle x \rangle} - 1\right) \Delta E_{\text{lep}}^2. \quad (7.9)$$

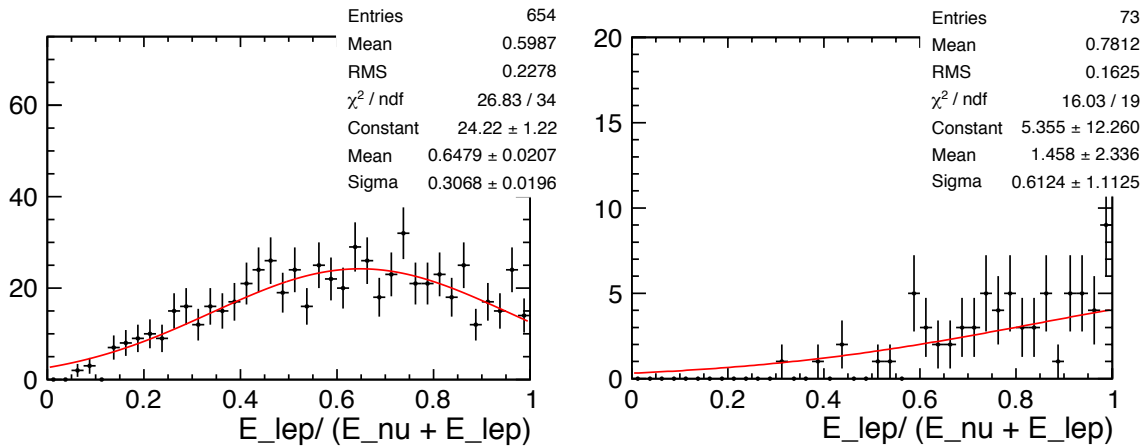


Figure 7.17: Left: lepton energy fraction from semi-leptonic b and c decays in the jets based on generator level. The correlation gives a rough estimation of the missing energy which needs to be corrected in the jets. Right: lepton energy fraction from other decays.

The last term includes the error on the lepton energy ΔE_{lep} , which is given by the track momentum resolution of the ILD tracking system (sec. 4.1). For high momenta a track momentum resolution of $\sigma_{1/p_T} = 2 \times 10^{-5} \text{ GeV}^{-1}$ is achieved [130]. Therefore, ΔE_{lep} can be neglected. Using the fit results of fig. 7.17, E_{jet}^{corr} and $\Delta E_{jet,corr}^2$ can be written as

$$\langle x \rangle = 0.65 \rightarrow E_{jet}^{corr} = E_{jet} + 0.54 \cdot E_{lep}, \quad (7.10)$$

$$\Delta \langle x \rangle = 0.31 \rightarrow \Delta E_{jet,corr}^2 = \Delta E_{jet}^2 + (0.73 \cdot E_{lep})^2. \quad (7.11)$$

The corrected jet energy enters the kinematic fit as described by eq. 7.10. ΔE_{jet}^{corr} enters the fit as

$$\Delta E_{jet}^{corr} = \sqrt{(0.568)^2 E_{jet} + (3.301)^2 + (0.73 \cdot E_{lep})^2}. \quad (7.12)$$

The introduced jet-energy correction procedure is added to the kinematic fit. In the analysis, after searching for leptons from semi-leptonic b and c decays in the jets, the sum of the lepton energies in each jet is used for the energy correction procedure. Jets without leptons from semi-leptonic decays obtain a total lepton energy of $E_{lep} = 0.0 \text{ GeV}$ and thus keep their original energy and the corresponding error (eq. 7.12 becomes eq. 7.5). The impact of the jet-energy correction on the ISR recognition and on the fit performance is investigated in the following.

7.6 Lepton Identification

In this investigation, leptons in the jets are identified using MC truth information. To get an estimate of the potential improvement in kinematic fitting by correcting semi-leptonic decays, the study is based on particle identification (PID) of cheated e^\pm and μ^\pm with a total momentum larger than 3 GeV. This choice of threshold is based on fig. 7.18, which

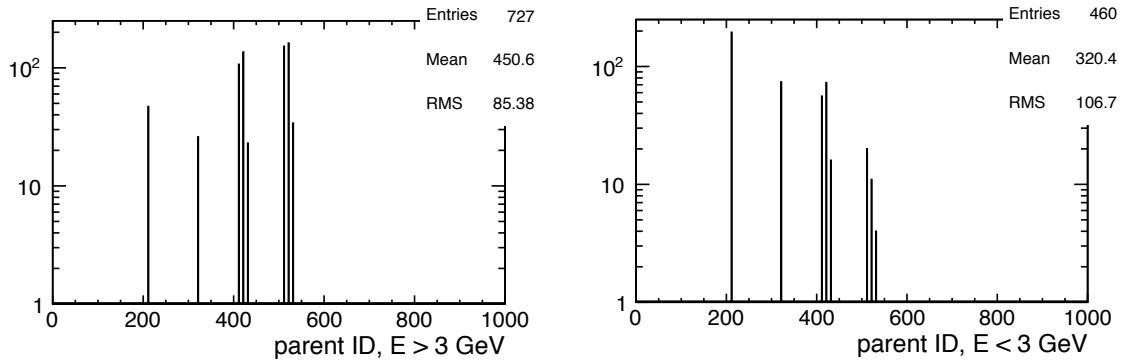


Figure 7.18: Parent ID of leptons which are found in the jets. Left: parent ID of leptons with a total momentum larger than 3 GeV. These leptons originate predominantly from semi-leptonic b and c decays. Right: parent ID of leptons with a total momentum smaller than 3 GeV. These leptons are mainly identified as from light mesons.

shows the parent IDs of leptons in the jets above and below the threshold of 3 GeV, respectively. Leptons with $P > 3$ GeV predominantly come from semi-leptonic b and c decays, which have particle identification numbers between 400 and 600 [27]. Leptons with a total momentum below this threshold mainly originate from light mesons. The latter have particle ID numbers between 200 and 400 [27].

As cross check, the presented study was also performed by requiring a mother particle with a PID number corresponding to c and b mesons, instead of using a momentum cut. Compared to the actually used cheated lepton selection, requiring a mother particle excludes any misidentification. Both cases of cheated lepton identification can be compared by looking at $|\cos(\theta_{miss})|$ as a function of the fitted Higgs mass after jet-energy correction, as shown in figure 7.19. The Higgs masses do not show significant differences after fitting. Consequently, the identification of semi-leptonic b and c decays is not an issue if leptons can be found, even without information on impact parameter or secondary vertices. Hence, for now it is sufficient to perform the study by identifying cheated leptons with $P > 3$ GeV, since it gives a realistic estimate of particle identification.

The analysis is based on data samples, which are reconstructed using the standard DBD reconstruction (sec. 4.5). However, there have been many efforts in software development, including improvements in PID tools [192–194]. At the time of this thesis, this large variety of PID tools was not included in the standard DBD reconstruction and is now implemented to a new reconstruction. Re-reconstructing the data samples can clearly benefit from the new PID tools in the new reconstruction. Therefore, this should be performed in the future. The new reconstruction includes the following PID tools:

- BasicPID uses traditional variables for particle identification which include information on impact parameters and on calorimetric energy deposits, i. e. $E_{ecal}/(E_{ecal} + E_{hcal})$ and E_{tot}/P_{tot} .
- dE/dx uses information of each track in the tracking system. It is based on the well-known energy loss dE of a particle per length dx in the TPC, depending on the mass

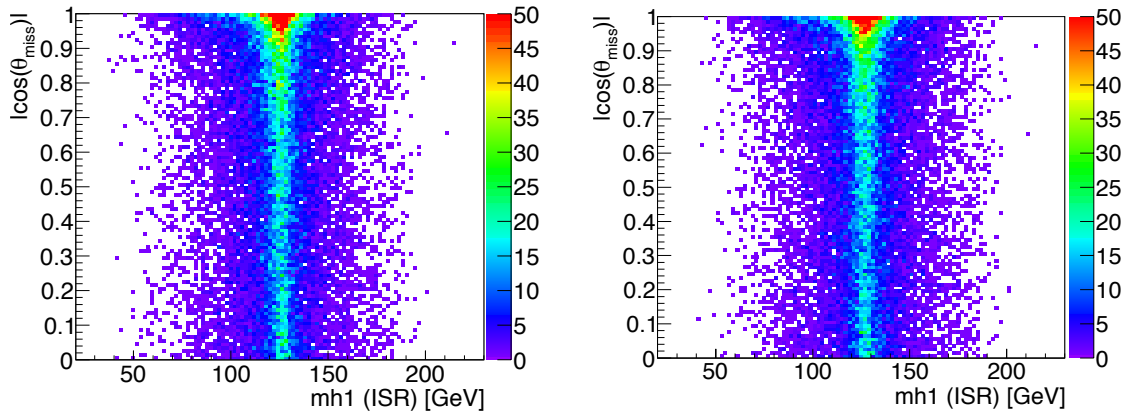


Figure 7.19: $|\cos(\theta_{miss})|$ as a function of $M(H1)$ obtained from the equal-mass fit with ISR considered and jet-energy correction applied. Left: cheated leptons are identified by requiring a mother particle with a PID corresponding to b and c mesons. Right: cheated leptons are identified with a total momentum of $P > 3$ GeV, since b and c decays are most dominant in this region.

of the respective particle. Consequently, dE/dx is a useful tool for the identification of particles with different masses, i. e. μ and π . This PID tool is not well suited for electrons, which are highly relativistic due to the very small mass.

- ShowerPID is based on cluster shapes of well-known particle showers (hadrons, e , μ , γ) in the calorimeters. The characteristics of clusters are used to distinguish tracks. This is useful to separate π and μ . Muons are detected as minimum ionising particles (MIP) in the calorimeters, while π is measured as hadronic shower.
- LikelihoodPID is based on output classifiers of multivariate techniques, which use various parameters as input. The parameters concern energy deposits in the calorimeters, cluster shape variables, and parameters based on dE/dx in the tracker. Consequently, LikelihoodPID combines information of the first three PID approaches.

The quality of the PID tools on reconstruction level with respect to 3 GeV leptons are shown in fig. 7.20 and 7.21. The identification efficiency and fake rates for electrons and muons for the available PID tools are illustrated.

Except for dE/dx , particle identification looks reasonably well for electrons. The electron identification is extremely pure with $> 90\%$. The best performance is given by the LikelihoodPID approach. The muon identification is more challenging. LikelihoodPID gives a muon identification efficiency of almost 90%. However, the misidentification rate as pions is roughly 10%. dE/dx gives a muon identification efficiency of roughly 75% with a large fake rate as π . Muon identification obtained with ShowerPID is less promising, due to the challenging separation of low-energetic muons and pions. Depending on the energy, low-energetic μ can already deposit their energy in the ECAL or the HCAL. Low-energetic π can also start showering in the ECAL. In this case it is very challenging to identify both particle types. Muons are identified best by the BasicPID reconstruction tool.

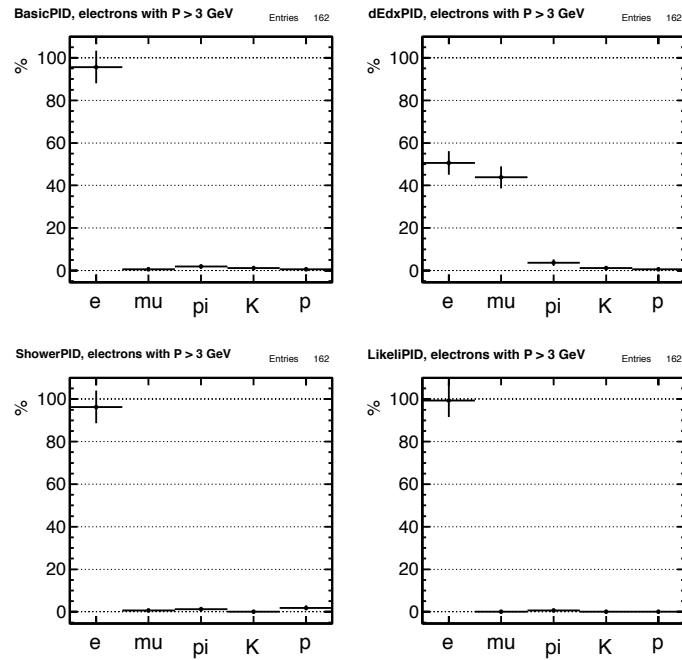


Figure 7.20: Tools for particle identification. Electrons with a total momentum larger than 3 GeV can be well identified using the BasicPID or LikelihoodPID tools in the new reconstruction software. The fake rates are small.

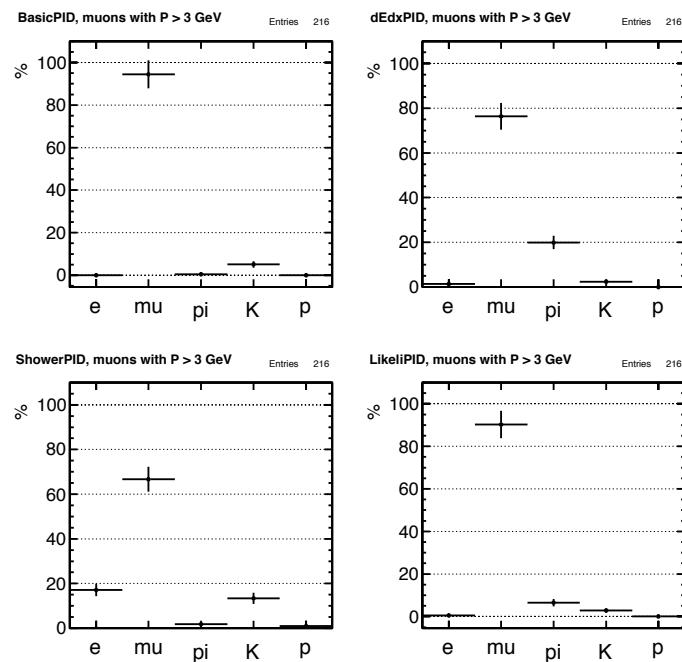


Figure 7.21: Tools for particle identification. Muons with a total momentum larger than 3 GeV can be identified using BasicPID or LikelihoodPID in the new reconstruction software. The fake rate is larger than for electrons, but in a reasonable range.

With regard to these information, the identification of semi-leptonic b and c decays should not be an issue. The new PID tools result in large identification efficiencies for electrons and muons. The identification of leptons in jets with a total momentum of 3 GeV is not an issue on reconstruction level. For now it is sufficient to perform this study by identifying cheated leptons with a threshold of $P > 3$ GeV, since it gives a realistic estimate of particle identification on reconstruction level.

7.7 Improvements due to the Energy Correction

The correction of missing energy from semi-leptonic decays in the jets results in improvements regarding the jet energy uncertainties, the fit performance, and the automatic ISR recognition in the fit. All aspects are discussed in the following.

7.7.1 Jet Energy Uncertainties

The energy correction procedure is expected to broaden the distribution of the jet energy deviations for jets with missing energy from semi-leptonic decays while improving the non-Gaussian tails. The effect is visible in the mean of the energy deviation histograms as discussed in section 7.4. The effect of the jet-energy correction on the mean and the errors of the mean of $\Delta E_{jet-quark}/E_{quark}$ is shown in figure 7.22 for the case without and with energy correction, respectively. For better comparison reason, the red lines are visual indications of the interesting region. The data points correspond to 25 of the energy-deviation histograms (e. g. fig. 7.15) each of which corresponds to 10 GeV of the quark energy range. The shift of the means to lower energy deviations is improved. The mean is shifted closer to the centre around 0 of $\Delta E_{jet-quark}/E_{quark}$. However, mis-identified leptons and light mesons, i. e. kaons and pions, can cause an overestimation of the jet energies.

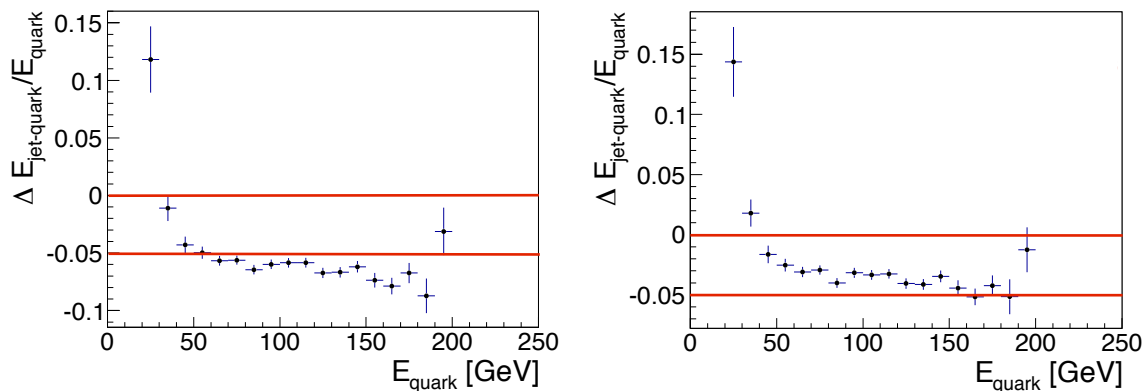


Figure 7.22: Energy deviation between initial quarks and reconstructed jets as a function of the quark energy before (left) and after (right) jet-energy correction. The means and errors of 25 energy deviation histograms are shown, each of which corresponds to 10 GeV of quark energy. The red lines are visual indications for better comparison.

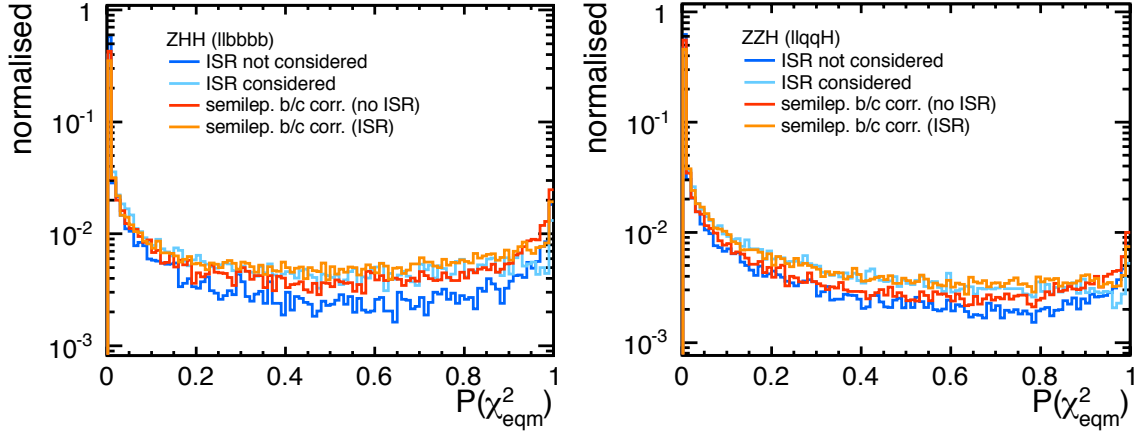


Figure 7.23: Fit probabilities $P(\chi^2_{eqm})$ of the equal-mass fit for $ZHH \rightarrow llbbbb$ events (left) and $ZZH \rightarrow llqqH$ events (right).

7.7.2 Fit Performance

The jet-energy correction becomes visible in $P(\chi^2)$. The kinematic fit varies the measured parameters with respect to their allowed measurement resolutions and under the condition that the applied constraints are fulfilled. If errors are wrongly estimated events obtain small $P(\chi^2)$ or the fit fails completely. If all errors on the measured parameters are Gaussian distributed, $P(\chi^2)$ obtains a uniform distribution. Peaks at 0 and 1 indicate a wrong estimation of the uncertainties or fit hypothesis. The fit probability of the equal-mass fit for ZHH events and ZZH events is shown in fig. 7.23, respectively. Since ZZH events do not naturally satisfy the equal-mass constraint, the fit probability decreases to larger values. For ZHH events a very flat distribution is achieved by correcting the jet energies. The distributions after energy correction receive a slightly larger peak at 1, indicating overestimated measurement uncertainties. Additionally, smaller peaks at 0 are obtained. Among different aspects, peaks at 0 are influenced by an underestimation of measurement errors (sec. 6.3.3). This is expected, since 90 % of the b jets do not receive an energy correction and keep the original uncertainties (eq. 7.5), in which the non-Gaussian tails were excluded [84]. It was stated that the results are rather optimistic and the jet energy uncertainties are underestimated [84]. The overestimation of jet energies can arise from the simple estimation of lepton energies used in this strategy and from misidentified light mesons. However, the new strategy results in a significant improvement in the fit performance for ZHH events.

The effect of the energy correction is also visible in fig. 7.24. $P(\chi^2)$ as a function of the total missing energy before fitting ($\sum E_{vis} - 500 \text{ GeV}$) is shown with and without treating ISR, respectively. Both distributions include the energy correction. For better comparison reason and to see the effect of the energy correction on the fit performance, the “original” E_{vis} is used in both plots although fractions of lepton energies have been added to E_{vis} during the correction procedure. In both cases, events with missing energy obtain improved $P(\chi^2)$ after correcting missing energy from semi-leptonic decays.

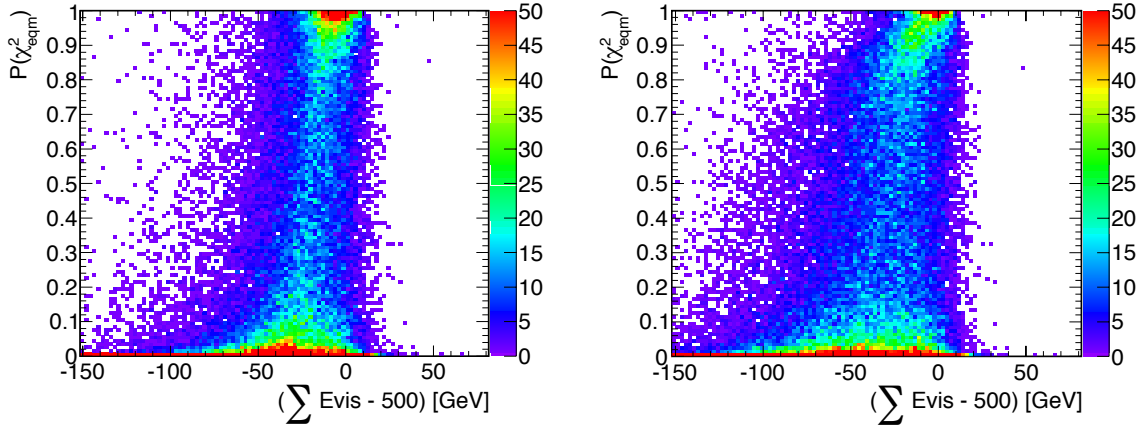


Figure 7.24: $P(\chi_{eqm}^2)$ after energy correction for $ZHH \rightarrow llbbbb$ as a function of the total missing energy before fitting. Left: without ISR in the fit. Right: with ISR in the fit.

Both plots can be compared to fig. 7.4 without energy correction. Without ISR consideration, correcting missing energy gives overall better results for events with approximately $(\sum E_{vis} - 500 \text{ GeV}) \gtrsim -60 \text{ GeV}$. Events without ISR but missing energy from semi-leptonic decays obtain improved $P(\chi^2)$, since energy conservation is now fulfilled. For events with large missing energy from semi-leptonic decays, the fit includes larger errors on the jet energy and is more successful. The recent error parametrisation is sufficient and therefore not affected for events without missing energy. Considering ISR in the fit also gives better results after correcting the jet energies. Without the latter, $P(\chi^2)$ started already decreasing for events with roughly $(\sum E_{vis} - 500 \text{ GeV}) \lesssim -10 \text{ GeV}$ (fig. 7.4). This is significantly improved by correcting the jet energies. Especially, enhanced $P(\chi^2)$ can be achieved for events with $(\sum E_{vis} - 500 \text{ GeV}) \gtrsim -50 \text{ GeV}$. Also events with larger missing energy receive much better $P(\chi^2)$.

The energy pulls of the b jets after jet-energy correction are shown in fig. 7.25 for the fits without and with ISR considered. The pulls correspond to the equal-mass fit (blue) and the ZHH fit (orange). Compared to the pulls without energy correction (fig. 7.5), a tremendous improvement can be achieved by using the energy correction. Especially in the fit without considering ISR, the large tail to smaller values is removed which indicated that some events were shifted much stronger by the fit to satisfy four-momentum conservation. The pulls of the fits without ISR considered are still slightly shifted towards smaller values, which reflects that the energy correction is not completely eliminating the bias towards smaller jet energies. This is expected since ISR is not considered. In the fits with ISR considered, the energy correction results in a symmetric pull distribution. The pulls of both fit hypotheses are slightly shifted to larger values. This is expected since 90% of the jets keep the originally determined jet energy resolution (eq. 7.5). Excluding non-Gaussian tails in the determination of σ_E gives optimistic results and underestimated jet energy uncertainties [84]. Therefore, the results are consistent with the expectations. With regard to these results, the large impact of semi-leptonic decays is now evident. The correction of the jet energies results in a substantial improvement of the fit performance.

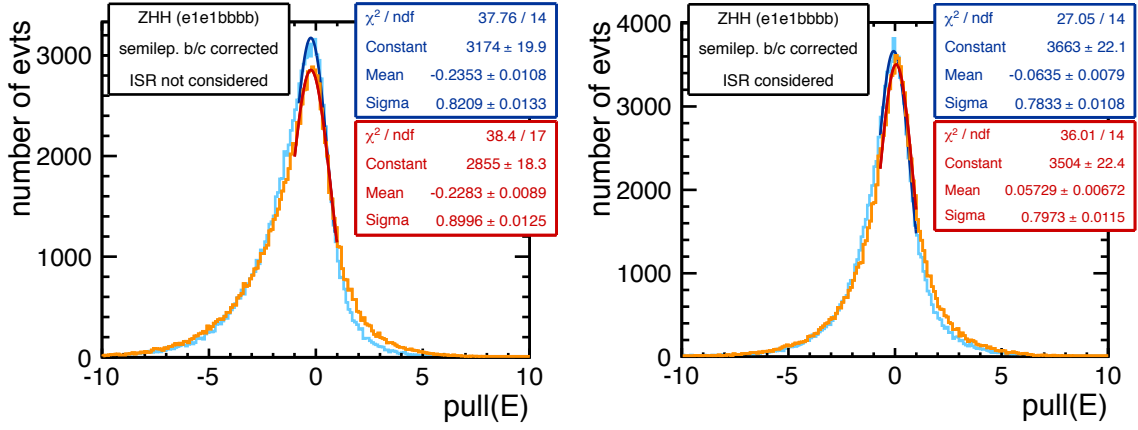


Figure 7.25: Energy pull distributions of $ZHH \rightarrow llbbbb$ for the equal-mass fit (blue) and the ZHH fit (orange) after correcting for missing energy from semi-leptonic decays in the jets. Left: without considering ISR in the fit. Right: considering ISR in the fit.

7.7.3 Automatic ISR Recognition

The second aspect of correcting semi-leptonic b and c decays in the jets is the investigation on whether it allows an automatic ISR recognition as for light jets [187]. Since the ISR photon fit object is parametrised by missing p_z (sec. 6.3.2), the additional missing energy and momentum in b jets results in performance issues. This is obvious when looking at the correlation between the fitted ISR energy and the generated photon energy. Without energy correction, the energies are not well correlated as for light jets (fig. 7.2).

The correlation of the photon energies after jet-energy correction are shown in fig. 7.26 for the equal-mass fit. After correcting missing energy in the jets, less missing energy is present in the events which can be assigned to ISR. An improved correlation can be observed. The region above the diagonal is less populated which contains events with overestimated fitted photon energies. Especially events without generated photon energies obtain improved results. In these events, missing energy from semi-leptonic decays was

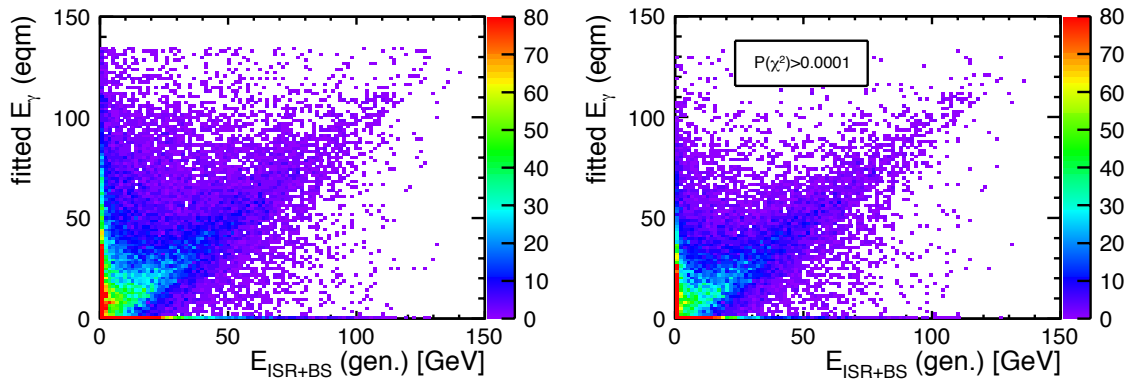


Figure 7.26: Fitted ISR energy as function of the generated photon energy after energy correction in the equal-mass fit: without cut (left), cut on $P(\chi^2_{eqm}) > 0.0001$ (right).

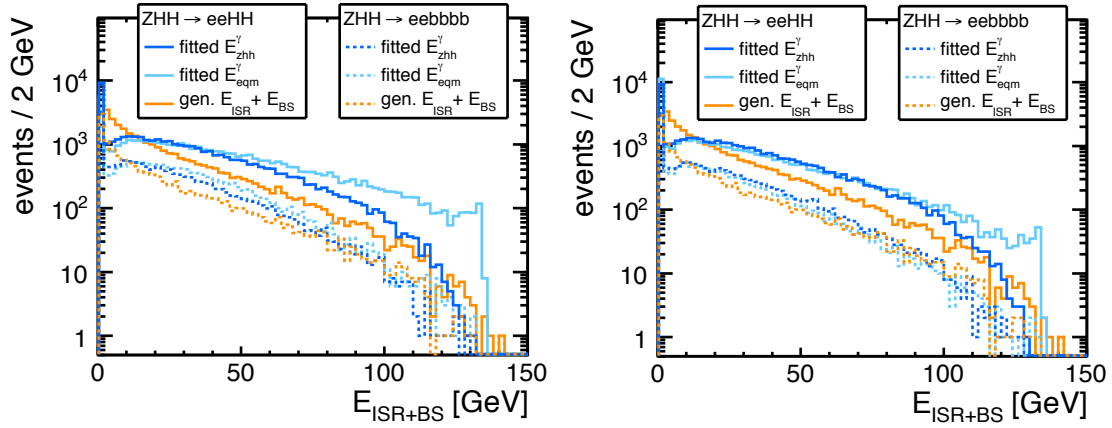


Figure 7.27: Generated photon energies compared to fitted photon energies for $ZHH \rightarrow eeHH$ (solid lines) and $ZHH \rightarrow eebbbb$ (dotted lines) events. Left: without jet-energy correction. Right: with jet-energy correction. The jet-energy correction strategy allows a more precise reconstruction of ISR energies by the fit.

mis-identified as ISR. This can also be observed in the various ISR energy distributions as shown in fig. 7.27. The ISR energies of the equal-mass fit and ZHH fit are compared to the generated photon energies for ZHH events, once without energy correction (left) and with energy correction (right). The dotted lines show the results for the desired signal final state $ZHH \rightarrow eebbbb$. The new strategy leads to a much more precise reconstruction of ISR energies. Over the entire range of ISR energies, the fit hypotheses give similar results. The drop at ISR energies below ~ 10 GeV results from the parametrisation of the ISR photon fit object, which works well for photon energies larger than the detector resolution [187]. The photon reconstruction at such ISR energies is arbitrary since the fit either overestimates ISR energies or assumes no ISR at all.

7.7.4 Mass Reconstruction

The improvements in the fitting procedure with regard to a better ISR reconstruction also affects the fitted mass distributions. Generally, ISR events are very forward and backward and occur at large $|\cos(\theta_{miss})|$. Previously, when considering ISR in the fit, those events were reconstructed with a bias to lower masses due to additional missing energy in the jets (sec. 7.3.1). Events at small $|\cos(\theta_{miss})|$ values, which do not contain ISR, also received a bias to smaller masses. Ideally, the ISR parametrisation should give unbiased resolutions for all events [187]. Correcting missing energy in the jets solves this issue. $|\cos(\theta_{miss})|$ as a function of the improved mass distribution is shown in fig. 7.28. For better comparison reason, the plot without energy correction, as presented in sec. 7.3.1, is repeatedly shown here. After the jet-energy correction the bias in the mass distribution is vanished over the entire range of $|\cos(\theta_{miss})|$. Events with and without ISR are well reconstructed by the fit. The fitted Higgs mass distributions before and after jet-energy correction in the fits with and without considering ISR, are compared in figure 7.29 and figure 7.30 for signal and

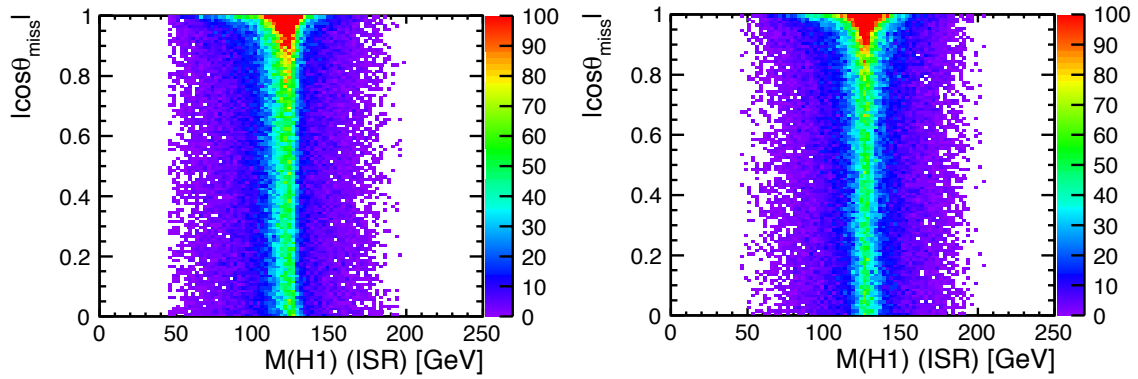


Figure 7.28: $|\cos(\theta_{miss})|$ as a function of $M(H1)$ with ISR considered in the equal-mass fit of $ZHH \rightarrow llbbbb$ events. Left: without jet-energy correction. Right: with jet-energy correction. Due to the jet-energy correction, the bias to smaller masses vanished.

backgrounds, respectively. The mass distributions without energy correction (light and dark blue) have already been discussed in section 7.3.3. The orange and red distributions correspond to the fit after jet-energy correction with and without ISR treatment.

Fit without ISR After applying the semi-leptonic energy correction the remaining missing energy in the events should be due to ISR. In such events missing energy is compensated by increasing the jet four-momenta, since four-momentum conservation needs to be satisfied. This leads to a biased Higgs mass to larger values. In case of the ZZH and ZZZ backgrounds the peak at around 90 GeV vanished due to the overestimation of jet four-momenta in the events. However, a small contribution of ZZZ events should be visible in such a peak. The overestimation of jet four-momenta moves ZZZ events to larger masses.

Fit with ISR The signal distribution results in a symmetric shape. The shift to smaller masses vanished completely after having applied the jet-energy correction. Except for very small masses a slight shift is vaguely perceptible. The background distribution shows the expected peak at around 110 GeV and the anticipated small peak at 90 GeV corresponding to ZZZ events.

The correction of missing energy in the jets results in improved mass distributions at generally larger masses compared to the fits without energy correction. Therefore, the fit with ISR and energy correction (orange) and the fit without ISR (dark blue) obtain similar shapes. The correction of missing energy from semi-leptonic decays results in a tremendous improvement of the fit performance and enables an automatic ISR recognition for b jets as for light jets. Additionally, boson masses are well reconstructed corresponding to the initial boson hypothesis of a process. To compare the discriminative power to the event-specific ISR treatment and the mass distributions without fitting, one can apply an example cut on the lower edge of the distribution to suppress ZZH/Z background events. For example a cut of $m_H \geq 115$ GeV results in a signal selection efficiency of 69%.

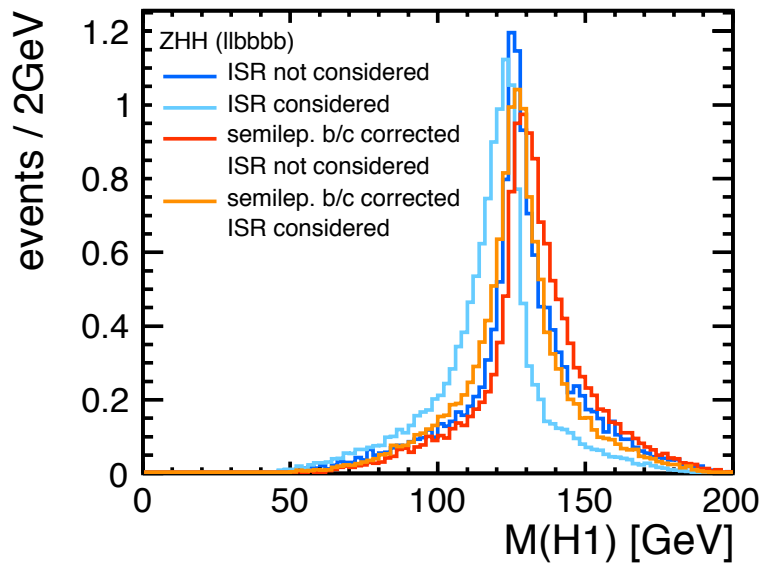


Figure 7.29: Comparison of various $M(H1)$ distributions after the equal-mass fit of $ZHH \rightarrow llbbbb$ events. Illustrated are the results without and with jet-energy correction for the equal-mass fit with and without ISR considered, respectively.

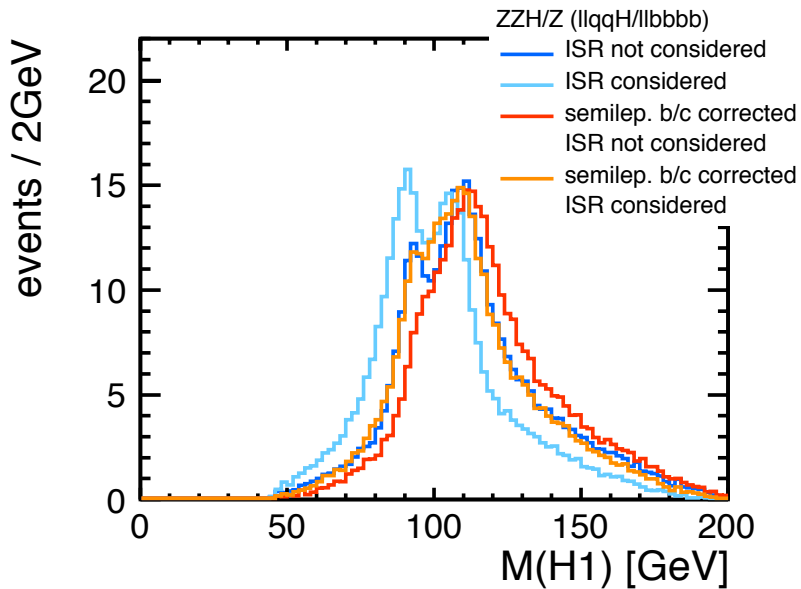


Figure 7.30: Comparison of various $M(H1)$ distributions after the equal-mass fit of ZZH/Z events. Illustrated are the results without and with jet-energy correction for the equal-mass fit with and without ISR considered, respectively.

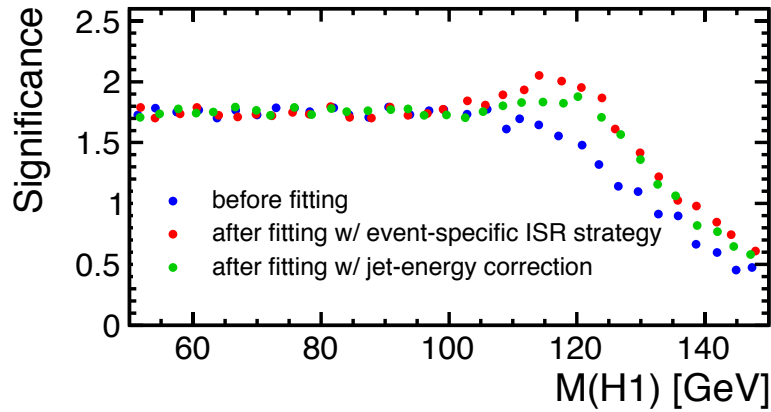


Figure 7.31: Significance $N_S / \sqrt{N_S + N_B}$ after applying a mass cut to the lower edge of the distribution of ZHH and ZZH/Z events since ZZH/Z events need to be suppressed. The significance before fitting (blue) and after fitting using the event-specific ISR treatment (red) and the jet-energy correction strategy (green) is shown.

The selection significance $N_S / \sqrt{N_S + N_B}$ for a lower cut on the Higgs mass for the two discussed strategies and before fitting is shown in fig. 7.31. Despite of being slightly less effective in the selection compared to the event-specific approach, the energy correction strategy is used in the following parts of this thesis since it solves issues with the fit performance and ISR parametrisation. Nevertheless, its effect on the analysis and neural net training has to be investigated in the following.

The strategy for correcting missing energy from semi-leptonic decays can be applied to events independent of kinematic fits. Correcting semi-leptonic decays in the jets can also enhance the standard jet pairing procedure (eq. 5.4) to find the di-jet pairs corresponding to the desired boson hypothesis.

7.8 Hypothesis testing in both Strategies

The scatter plot of the χ^2 distributions for the ZHH and ZZH fit after applying the event-specific ISR treatment and jet-energy correction are shown in fig. 7.32. Compared to the default settings (fig. 6.11), events without significant ISR should give the same result. Events with significant ISR should obtain larger $P(\chi^2)$ (smaller χ^2) since they are treated with ISR in the event-specific approach. This is evident in the less populated region close to the diagonal at larger χ^2 for both fit hypotheses. After the event-specific ISR treatment the events are mainly concentrated at smaller χ^2 . Nevertheless, a very clean separation of signal and backgrounds can be obtained. Signal events obtain smaller χ^2 and thus larger $P(\chi^2)$ in the ZHH fit, and larger χ^2 and smaller $P(\chi^2)$ in the ZZH fit. ZZH events show the opposite behaviour for the respective fit hypotheses. Also shown is the result after jet-energy correction. The events show similar behaviours and result in a clear separation of signal and backgrounds. Nevertheless, it is hard to see a difference with re-

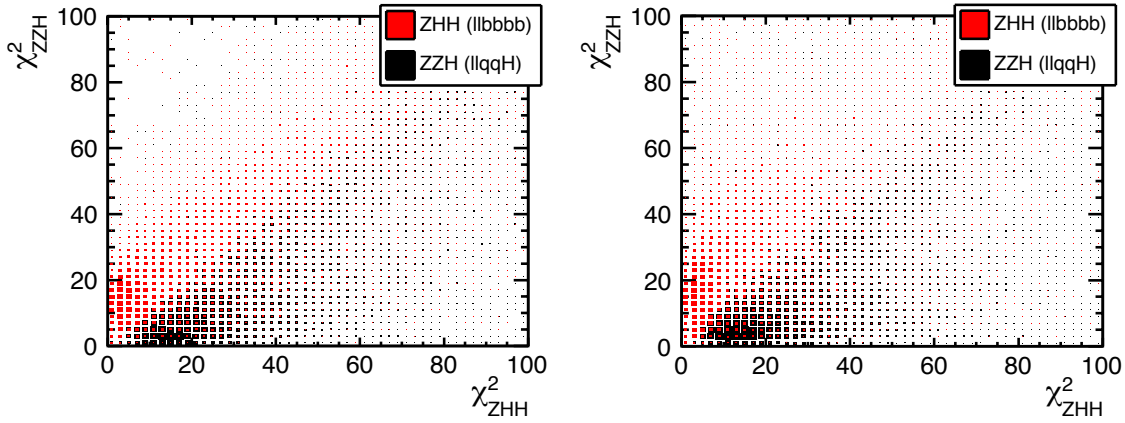


Figure 7.32: χ_{zzh}^2 vs. χ_{zhh}^2 scatter plot for the event-specific ISR treatment (left) and the jet-energy correction strategy (right). Both χ^2 distributions show a promising event separation. First investigations lead to a relative improvement of 20% by adding these distributions to the neural nets in the Higgs self-coupling analysis.

spect to the discriminating power between signal and backgrounds. By applying a cut on the distributions, the signal efficiency reads 75% for the first strategy for the optimal cut $\chi_{ZZH}^2/\chi_{ZHH}^2 > 0.75$ giving a signal significance of 2.1σ and 82% for the energy correction, in which $\chi_{ZZH}^2/\chi_{ZHH}^2 > 0.5$ represents the optimal threshold with a significance of 1.9σ . In the latter the background suppression is less effective. The corresponding significances $N_S/\sqrt{N_S + N_B}$ are shown in fig. 7.33. Both strategies give similar results. First investigations using the default kinematic fit settings indicated a relative improvement of 20% by adding this distribution to the neural net training. This needs to be confirmed for the jet-energy correction strategy. The energy correction strategy represents the more advanced and clean approach to deal with heavy-flavoured jets and ISR in kinematic fits, and is used in the Higgs self-coupling analysis.

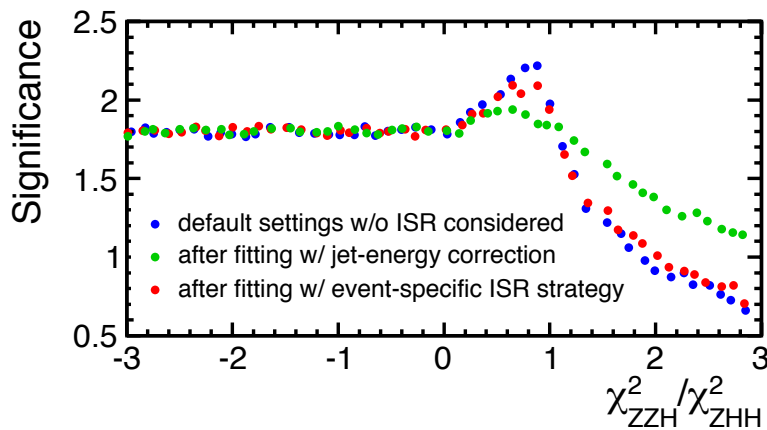


Figure 7.33: Significance $N_S/\sqrt{N_S + N_B}$ after applying a cut on $\chi_{ZZH}^2/\chi_{ZHH}^2$ for ZHH and ZZH/Z events. The significance for the default settings (blue), after the event-specific ISR treatment (red) and the jet-energy correction strategy (green) is shown.

Chapter 8

Event Selection

In this chapter, the event selection of the three signal channels is described, following the strategy introduced in sec. 5.2. The investigated improvements in analysis techniques and the developed semi-leptonic jet-energy correction are included in the selection of ZHH events. As first step of the analysis a preselection is performed to improve the signal-to-background ratio before separate MVAs are trained for the dominant backgrounds in each signal channel. The background is five orders of magnitude larger than the signal. The suppression of background events before MVA training allows to achieve an optimal selection performance. The separate MVAs are trained sequentially. Hence, all foregoing selection cuts are considered. At the end of the signal selection flavour-tag information are used. The signal modes are discussed individually. In sec. 8.1, the selection of the lepton channel is introduced and described in detail. Since the neutrino and hadron modes follow the same strategy, the important aspects of the selection are outlined. This includes a brief discussion of the kinematic fit results. The event selection of the neutrino and hadron channel are illustrated in sec. 8.2 and sec. 8.3, respectively. Hereafter, the results of the event selection are summarised and discussed in sec. 8.4. The outlined results do not take into account the $\gamma\gamma$ overlay. The effect of the overlay is discussed later in this thesis. The respective results are listed in the appendix A. The semi-leptonic correction (sec. 7.5) is applied to all jets in which a lepton is present.

8.1 Lepton Channel

8.1.1 Preselection

As discussed in sec. 5.2, by using the optimised isolated lepton strategy (sec. 6.1) events are selected which include a pair of isolated leptons, the mass of which is consistent with the Z-boson mass within $|M_{ll} - 91 \text{ GeV}| < 40 \text{ GeV}$. This requirement suppresses semi-leptonic and full-hadronic events from tt , WWZ , and ZZ . Misidentified leptons in these events must be part of a jet. Hence, their momentum is relatively small and the cone

energy large. These variables are used in MVA training of the isolated lepton selection strategy (sec. 6.1) and thus allow a good background suppression. However, the isolated lepton strategy is not optimised for τ events to avoid complications of the non-trivial τ decays. Hence, at this stage of the analysis only electron and muon signal events survive the preselection and the number of signal events is reduced by one third. The preselection results are listed in tab. 8.1. In total, 25.5 events of $llHH$ pass the isolated lepton selection. From originally 13.5 $eeHH$ events and the same amount of $\mu\mu HH$ events, 12.5 events of each category survive the selection, while 0.5 events correspond to $\tau\tau HH$. Optimising the lepton selection strategy also for τ can be useful to include $\tau\tau HH$ signal events. If the selection of $\tau\tau HH$ gave similar results as the $eeHH$ and $\mu\mu HH$ channels, including this mode could improve the precision of the ZHH cross-section measurement by relative 8%. Moreover, less than 10% of τ decay leptonically and a dedicated algorithm to identify hadronic τ decays could improve the background suppression.

After the isolated lepton finding, all other reconstructed particles are clustered into jets, which are then paired to form the signal bosons by using eq. 5.4 (sec. 5.2). During jet-pairing, the di-jet pairs have to fulfil $|M_{ij} - 125 \text{ GeV}| < 80 \text{ GeV}$. Even this loose requirement on the Higgs masses rejects tt and ZZ backgrounds. The preselection reduces the total background by three orders of magnitude, while keeping $\sim 55\%$ of the signal. As mentioned before, this is due to the missing isolated τ selection.

The preselection results are listed in tab. 8.1. Since the generated MC statistics are limited, the MC statistical errors on the expected number of events for each process after every selection cut are listed. The expected number of events N after each cut can be calculated with $N = N_{exp} N_{MC}^a / N_{MC}^b$, using the generated number of MC events before selection N_{MC}^b , the number of MC events after the respective selection cut N_{MC}^a , and the expected number of events weighted to the corresponding cross section and luminosity $N_{exp} = \sigma \cdot \mathcal{L}$. For the latter, no systematical error is considered. The relative error on the number of events $1 / \sqrt{N_{exp}^a}$ after a selection cut decreases one over the square root of the selected MC sample size N_{MC}^a . For example, to obtain a relative error of 10% for $N_{exp} = 5$ events the generated MC data sample size should be 20 times larger than the expected number of events. After preselection, there already is a lack of statistics in the full-hadronic backgrounds. At this stage, the relative error on the number of six-jet full-hadronic background events reads roughly 20% and the relative error on the number four-jet full-hadronic background events is roughly 25%. Although these backgrounds do not play an important role in the lepton channel more statistics could be useful.

Before MVA training, cuts are applied to reduce background events and make the MVA training procedure more sensitive to the signal. Hence, cuts are applied on variables which reconstruct the signal properties (fig. 8.1). The cuts are chosen such that the signal efficiency is as large as possible, but at least 80%. Backgrounds which do not satisfy the requirements are excluded. If needed, these cuts can be tightened later in the selection. The first choice of variables are the two Higgs masses $M(H1)$ and $M(H2)$. First, a cut on the first Higgs boson mass of $60 \text{ GeV} < M(H1) < 180 \text{ GeV}$ is applied to the events

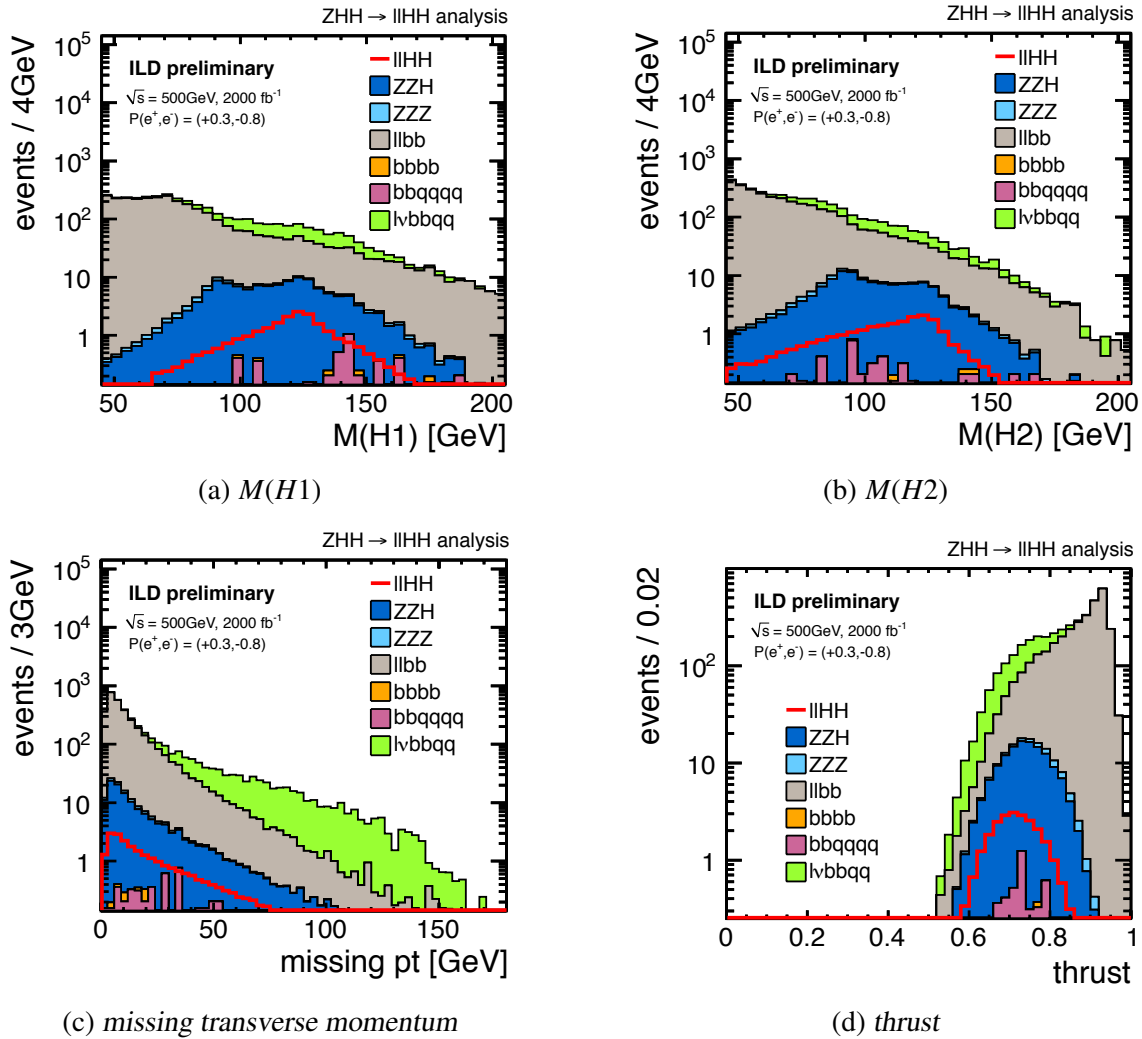


Figure 8.1: Preselection variables after having applied all foregoing cuts.

(fig. 8.1a). Then, the same thresholds are imposed to $M(H2)$ (fig. 8.1b). These cuts mainly reduce $ZZ \rightarrow llbb$ events. The second choice of variable is the missing transverse momentum. The $llHH$ mode does not include large missing p_T . Missing p_T can only occur from semi-leptonic decays of b and cascade c quarks, the missing energy of which is corrected for in the jets on a statistical basis (sec. 7.5). ISR does not affect the transverse momentum. The events need to satisfy $m_{pt} < 70$ GeV (fig. 8.1c). By applying this cut, the $lvbbqq$ background is again suppressed by almost 30%. The third choice of selection variable is the thrust, which reflects the anisotropy of an event. It indicates whether there is a special direction favoured by the events. Perfectly spherical events obtain values close to $1/2$, while back-to-back two-body decays receive values close to 1. Since ZZ is a two-body s -channel process those particles are very forward and backward and the thrust is close to 1. The signal obtains smaller values, since it is a three-body decay. Therefore, the events have to fulfil $thrust < 0.9$ (fig. 8.1d). This requirement rejects roughly 35% of $llbb$. After preselection, the background is still three orders of magnitude larger than the signal.

	$e\bar{e}b\bar{b}$	$\mu\bar{\mu}b\bar{b}$	$e\nu b\bar{b}q\bar{q}$	$\mu\nu b\bar{b}q\bar{q}$	$\tau\nu b\bar{b}q\bar{q}$	$b\bar{b}q\bar{q}q\bar{q}$	$b\bar{b}b\bar{b}$	$l\bar{l}b\bar{b}b\bar{b}$	$l\bar{l}q\bar{q}H$	Background	$l\bar{l}H\bar{H}(l\bar{l}b\bar{b}b\bar{b})$
σ [fb]	142.1	24.8	124.2	123.0	123.0	312.0	20.1	0.03	0.08	869.1	0.02
expected events	$2.84 \cdot 10^5$	$4.95 \cdot 10^4$	$2.48 \cdot 10^5$	$2.46 \cdot 10^5$	$2.46 \cdot 10^5$	$6.24 \cdot 10^5$	$4.02 \cdot 10^4$	69.51	150.87	$1.73 \cdot 10^6$	$40.51 (14.3)$

Preselection Cuts

$N_{isollep} \geq 2$	$6.4 \cdot 10^4 \pm 78$	$2.1 \cdot 10^4 \pm 37$	1911 ± 22	226 ± 7	195 ± 5.9	25.5 ± 2.0	2.4 ± 0.3	21.8 ± 0.1	135 ± 0.5	$8.8 \cdot 10^4 \pm 89$	$25.2 \pm 0.07 (7.9)$
$ M_{H^*} - M(Z) < 40$ GeV	$2.6 \cdot 10^4 \pm 50$	$1.6 \cdot 10^4 \pm 32$	558 ± 12	77 ± 4	33 ± 2.4	4.5 ± 0.9	0.4 ± 0.1	15.3 ± 0.1	132 ± 0.5	$4.3 \cdot 10^4 \pm 63$	$24.0 \pm 0.07 (7.9)$
$ M_{H^*} - M_H < 80$ GeV	2183 ± 14	901 ± 8	544 ± 12	73 ± 4	29 ± 2.3	4.2 ± 0.8	0.4 ± 0.1	12.5 ± 0.1	130 ± 0.5	3877 ± 21	$22.5 \pm 0.06 (7.9)$

Additional Precuts

60 GeV < M_{H^*} < 180 GeV	1530 ± 12	632 ± 6	529 ± 11	66 ± 4	27 ± 2.2	3.8 ± 0.8	0.3 ± 0.1	12.2 ± 0.1	127 ± 0.5	2928 ± 18	$22.5 \pm 0.06 (7.8)$
60 GeV < M_{H^*} < 180 GeV	956 ± 10	398 ± 5	481 ± 11	59 ± 4	25 ± 2.1	3.7 ± 0.8	0.3 ± 0.1	11.6 ± 0.1	123 ± 0.4	2057 ± 16	$22.4 \pm 0.06 (7.7)$
missing $p_T < 70$ GeV	948 ± 10	397 ± 5	343 ± 9	46 ± 3	12 ± 1.5	3.7 ± 0.8	0.3 ± 0.1	11.6 ± 0.1	119 ± 0.4	1880 ± 15	$21.4 \pm 0.06 (7.7)$
thrust < 0.9	603 ± 8	288 ± 4	341 ± 9	46 ± 3	12 ± 1.5	3.7 ± 0.8	0.2 ± 0.1	11.5 ± 0.1	119 ± 0.4	1424 ± 13	$21.4 \pm 0.06 (7.7)$

Table 8.1: Preselection results for the lepton channel, corresponding to a beam polarisation of $P(e^+e^-) = (0.3, -0.8)$ and an integrated luminosity of $\mathcal{L} = 2 \text{ ab}^{-1}$. If not stated otherwise, $l = e, \mu, \tau$. Also listed are the MC statistical errors on the number of events after every cut. The isolated lepton selection is not optimised for τ events. Only isolated e and μ pairs are selected. Hence, the isolated lepton selection reduces the signal events by one third. From originally 13.5 $e\bar{e}H\bar{H}$ events and the same amount of $\mu\bar{\mu}H\bar{H}$ events, 12.5 events of each category survive the selection, while 0.5 events correspond to $\tau\bar{\tau}H\bar{H}$. Optimising the lepton selection strategy also for τ could be useful to include $\tau\bar{\tau}H\bar{H}$ signal events in this study. This can improve the precision of the ZHH cross-section measurement by relative 8% if similar results for $\tau\bar{\tau}H\bar{H}$ are achieved as in $e\bar{e}H\bar{H}$ and $\mu\bar{\mu}H\bar{H}$.

8.1.2 MVA Training and Final Selection

The main idea of the final selection is the application of multivariate analysis techniques (MVA), as described in sec. 5.2. Separate MVAs are trained for the three dominant background processes using the package of TMVA [176] (sec. 5.2). Separate MVAs are trained since the various background types have very different event topologies and different weights. In the analysis the MVAs are trained sequentially, which means that all foregoing cuts of the preselection and final selection are considered in training. This also includes selection cuts on previous MVA outputs. The dominant backgrounds are: (1) $ZZ \rightarrow llbb$, (2) semi-leptonic backgrounds $lvbbqq$, and (3) ZZH and ZZZ which have the same final state as the signal. For each of these background types a boosted decision tree (BDTG) is trained. Statistically independent data samples are used. The weights for the different processes are normalised to the corresponding cross sections and beam polarisation.

Although in the $llHH$ channel, the events are categorised into electron-type and muon-type events in the event selection, combined BDTGs are trained due to the limited statistics. The BDTGs are trained using kinematic variables. The input variables are of similar shape for both lepton-type events, since in $eeHH$ final-state radiation photons (FSR) are recovered. Training separate BDTGs for both categories could improve the event selection. In this case, more statistics would be needed. In the following, the input variables for the three different BDTGs are introduced.

First BDTG: $llbb$ vs. $llHH$ ($llbbbb$)

The most dominant background after the preselection consists of two leptons and two b jets in the final state. It originates from ZZ , ZZ^* , bbZ , and llZ processes. Due to possible gluon radiation and cascade decays to b quarks, mis-clustering of jets can lead to a wrong reconstruction of such events as four-jet final states, which then survive the preselection. The optimised input variables for BDTG training are described in the following. The corresponding distributions are shown in fig. 8.2.

- **$M(Z)$** : Since some background events originate from a t -channel process, the two charged leptons in the final state are not from a Z decay. In such events the reconstructed Z mass does not peak at the nominal Z mass, which is indicated by the flat distribution at the tails (fig. 8.2a).
- **$thrust$** : The thrust indicates whether there is a special direction favoured by the events. Since $ZZ \rightarrow llbb$ is a two-body decay those particles are very forward and backward and the thrust is close to 1. The signal obtains smaller values, since it is a three-body decay (fig. 8.2b).
- **$costhrust$** : Since most of the backgrounds are two-body decays, they are very forward-peaked. Hence, they are much closer to beam direction compared to the signal. This is visible in the polar angle of the thrust axis (fig. 8.2c).

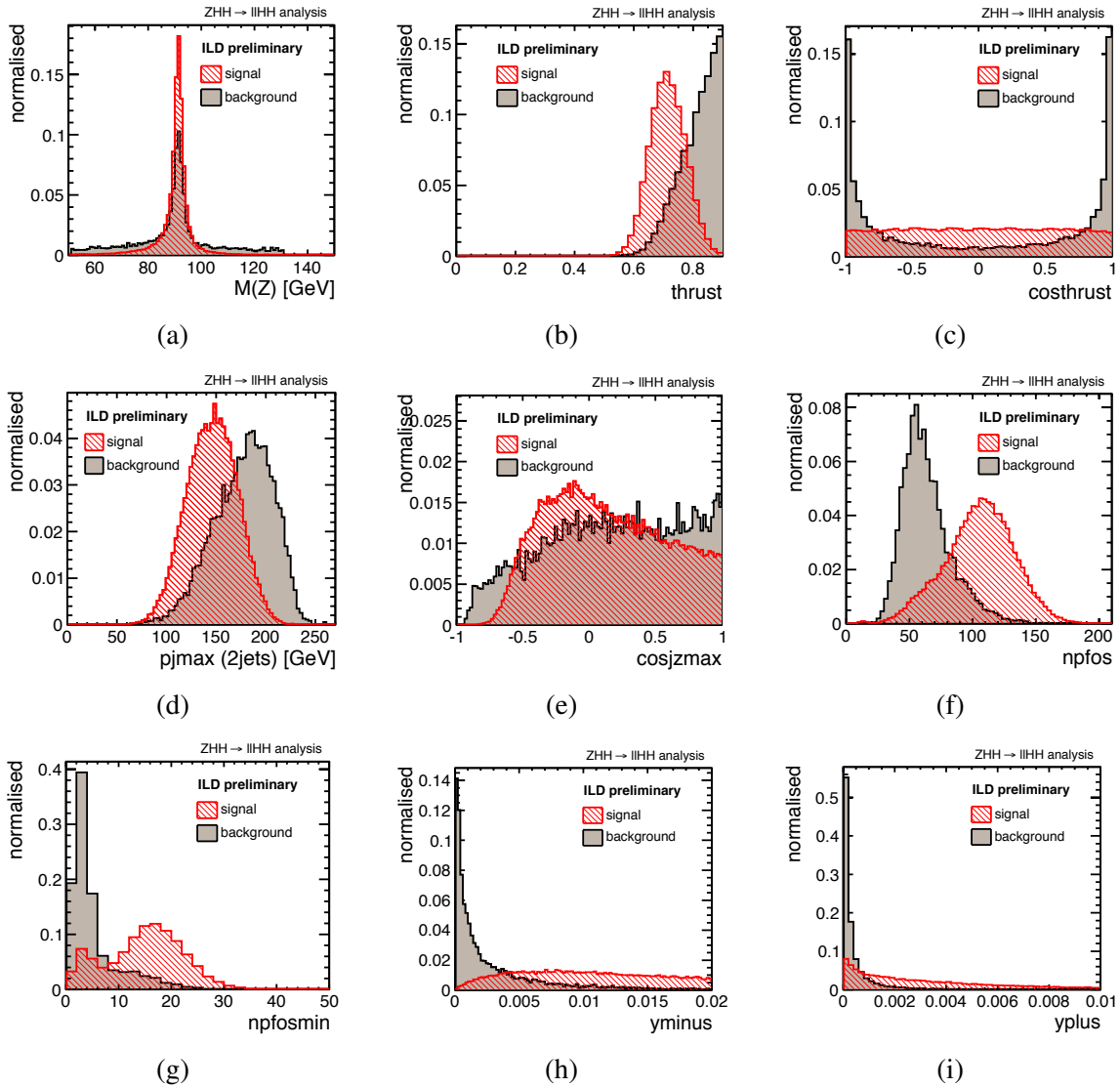


Figure 8.2: Inputs for $bdtg(llbb)$ training. The descriptions can be found in the text.

- **p_{jmax} (2jets)**: As a test, the events are reconstructed as two-jet final states. Then, the jet momenta of background events are relatively large compared to the signal. The largest jet momentum offers discriminative power (fig. 8.2d).
- **$cosjzmax$** : The largest angle between the reconstructed Z and the other two jets of a four-jet event helps to reduce backgrounds from bbZ , where Z is radiated from one of the b quarks. In this case the Z is very close to one of the two b jets, since the events are very boosted (fig. 8.2e).
- **$npfos$ and $npfosmin$** : The total number of PFOs helps to discriminate between two b -jet background and four b -jet signal events. Signal events contain much more PFOs compared to the background, since they include four b jets. Moreover, the smallest number of PFOs in a jet is used (fig. 8.2f, fig. 8.2g).

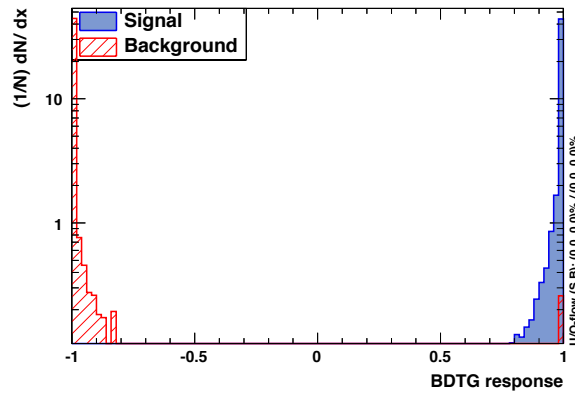


Figure 8.3: Classifier response of the first BDTG: $llbb$ vs. ZHH ($llbbb$).

- ***yminus***: The Durham parameters given by the Durham jet clustering algorithm (sec. 5.3.1) allow to discriminate events with different numbers of jets in the final state. Events are clustered into four-jets. In this case *yminus* indicates the likeliness to be a four-jet event instead of a three-jet event. Thus, this variable is useful to discriminate backgrounds with less jets compared to the signal (fig. 8.2h).
- ***yplus***: In case of clustering particles into two jets, *yplus* denotes the likeliness with which events are misidentified as three-jet events instead of two-jet events. Hence, the signal tends to receive larger values compared to the background (fig. 8.2i).

The classifier response of the BDTG is shown in fig. 8.3. A clear signal and background separation can be achieved. The resulting classifier weights are applied to the analysis. The optimal cut on the output is suggested to be 0.78. Since combined BDTGs are trained for electron-type and muon-type events due to finite MC statistics, this cut is included in the training procedure of the second BDTG. However, it is optimised in the final selection for both lepton-type categories separately according to the maximum signal significance $\sigma = \frac{s}{\sqrt{s+b}}$. This way other background types than $llbb$ can be suppressed. To train separate BDTGs for each category, twice the statistics is needed.

The $bdtg(llbb)$ distributions for the electron-type and the muon-type events are shown in fig. 8.4 after preselection. The entire cutflow of the final selection is listed in tab. 8.2. The errors on the expected number of events are also listed. The optimised cut on the first BDTG reads $bdtg(llbb) > 0.87$ for electron-type events (fig. 8.4a) and $bdtg(llbb) > 0.28$ for muon-type events (fig. 8.4b). The cut on $bdtg(llbb)$ is much more strict for the electron-type compared to the muon-type events due to the large contribution of $eebb$. Moreover, a much larger contribution of $evbbqq$ events survives the preselection compared to $\mu vbbqq$ and $\tau vbbqq$. Also the full-hadronic six-jet background is part of the background contribution to the electron-type category. As mentioned before the relative error on the number of $bbqqqq$ events is 21%. Therefore, this result has to be taken with care. More

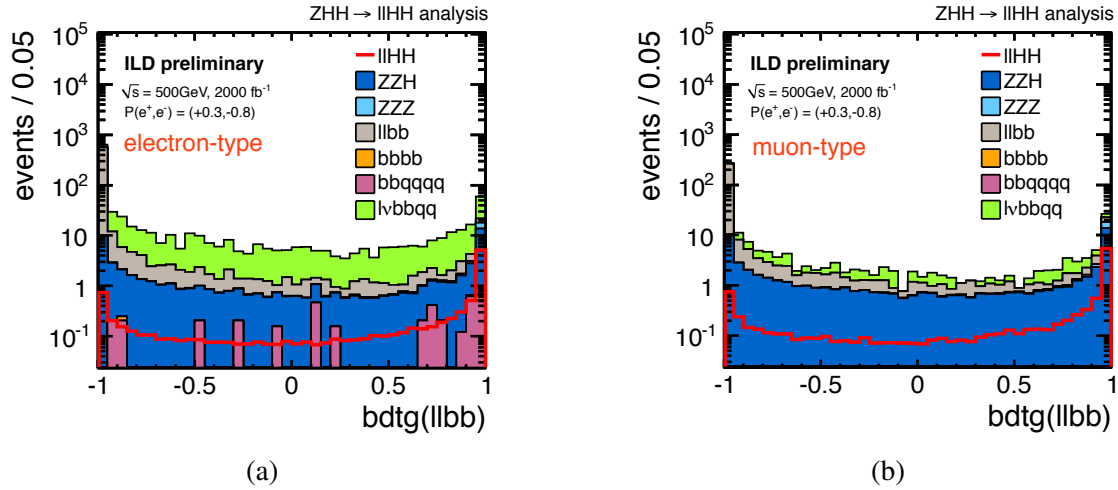


Figure 8.4: a) A cut of $bdtg(llbb) > 0.87$ is applied to electron-type events. b) A cut of $bdtg(llbb) > 0.28$ is applied to muon-type events.

statistics could be useful to get a clearer picture of the suppression of $bbqqqq$ events. To obtain a relative error of at least 10% on the number of events, the MC sample size should be almost 30 times larger than the expected number of events.

Second BDTG: $lvbbqq$ vs. lHH ($llbbbb$)

Even though $lvbbqq$ is largely suppressed by the preselection, it still gives the second largest contribution to the background. The semi-leptonic background consists of $evbbcs$ and $evbbud$ events and the corresponding μ and τ modes. It originates from tt and WWZ processes. After the foregoing selection cuts, there is a relative error of 10% on the number of $evbbqq$ events. A relative error of almost 20% and 35% is present for $\mu vbbqq$ and $\tau vbbqq$, respectively. In this case, even more statistics is needed for the training of one combined BDTG. For example, to obtain a relative error of 5% on the respective number of events at this stage of the analysis, 8 times larger MC sample sizes are needed for $evbbqq$, 30 times larger for $\mu vbbqq$ and 180 times larger for $\tau vbbqq$, respectively. The input variables for BDTG training are discussed in the following.

- **visible energy:** The total visible energy for signal events is larger than for background events, which contain one neutrino in their final state (fig. 8.5a).
- **$M(Z)$:** Backgrounds which pass the isolated lepton requirement include one misidentified lepton. Since the events are from tt , the reconstructed invariant mass of the two selected isolated leptons is very different compared to signal events (fig. 8.5b).
- **$plmin$:** Since there is just one isolated charged lepton in the background final state the other misidentified lepton must be part of a jet. This lepton has a smaller momentum compared to isolated leptons. The smallest lepton momentum gives discriminative power for signal and backgrounds (fig. 8.5c).

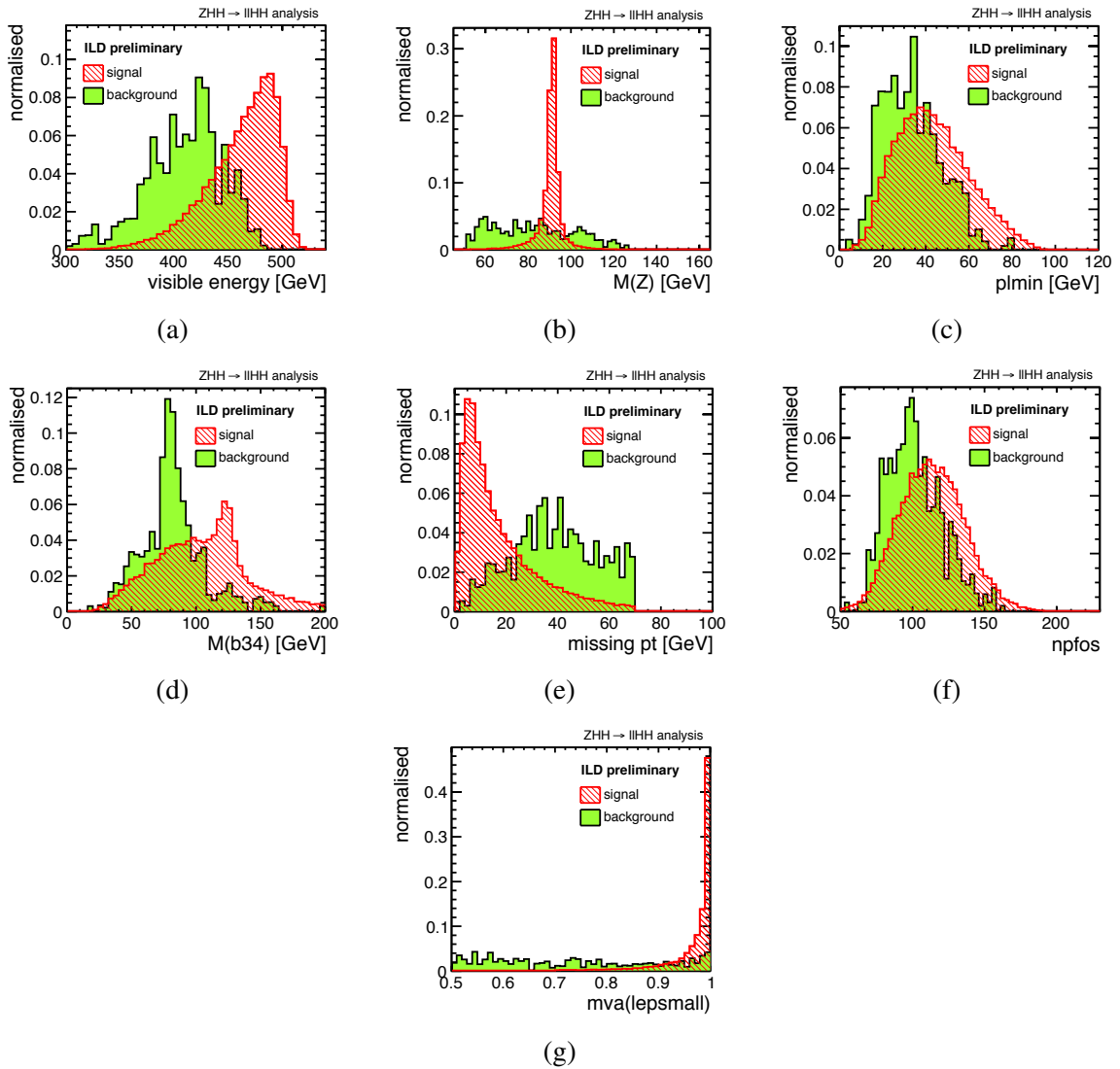


Figure 8.5: Inputs for $bdtg(lvbbqq)$ training. The descriptions can be found in the text.

- **$M(b_{34})$** : The four jets in the final state can be ordered from the largest to smallest b likeliness. The background includes two b jets and two light jets. Since the background comes from $t\bar{t}$ the two light jets are reconstructed as from a W decay. The invariant mass of the third and fourth jet is reconstructed as W boson (fig. 8.5d).
- **missing pt** : Since there is one neutrino in the final state of the background events, the missing transverse momentum is larger compared to the signal (fig. 8.5e).
- **$npfos$** : Generally, b quarks have larger multiplicities compared to light jets. Since the background events include only two b jets, the total number of PFOs in background events is smaller than in signal events (fig. 8.5f).
- **$mvasmall$** : The classifier output obtained in the developed isolated lepton strategy offers separation power. In the isolated lepton selection (sec. 6.1) leptons receive an MVA value and are selected as isolated if they pass the selection cuts on the

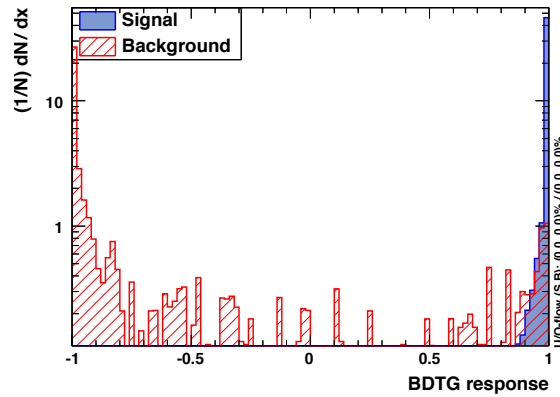


Figure 8.6: Classifier response of second BDTG: $lvbbqq$ vs. ZHH ($llbbbb$).

classifier outputs. In $llHH$, an isolated lepton pair is selected. Each of the two leptons receives an MVA value. The two values are sorted by size, which results in a larger and smaller MVA value. Both signal leptons have large MVA values, while $lvbbqq$ events have one large and one small value, which corresponds to the misidentified lepton. Therefore, the smaller MVA value is useful for background suppression. It provides one of the most important variables in training (fig. 8.5g).

The background statistics is very limited since the preceding selection cuts reduce the number of background events significantly. However, the BDTG training does not suffer from overtraining. Overtraining indicates that the output classifier is sensitive to statistical fluctuations of the training sample, which is often the case for limited statistics. Statistical fluctuations can lead to an overestimation of the discriminative power between signal and backgrounds. BDTGs are less sensitive to overtraining than MLPs. This is one aspect of using BDTGs in this analysis instead of MLPs as in [108].

The classifier response is shown in fig. 8.6. A clear signal and background separation is visible. The optimal cut value is 0.79 and is included in the training of the third BDTG. The selection cut on $bdtg(lvbbqq)$ is again optimised for the largest signal significance in both categories. The optimised thresholds are larger compared to the optimal cut suggested in training. For electron-type events the threshold reads $bdtg(lvbbqq) > 0.97$ (fig. 8.7a) and for muon-type events $bdtg(lvbbqq) > 0.85$ (fig. 8.7b). The optimised thresholds on $bdtg(lvbbqq)$ most likely are due to few statistics. More statistics is needed to study whether the tight cuts and the respective background rejection are reliable. At this stage of the event selection all other background processes have large statistics and small relative errors on the number of expected events (tab. 8.2).

Third BDTG: ZZH/ZZZ vs. $llHH$ ($llbbbb$)

The third dominant background includes processes which have the same particles in the final state as the signal. These backgrounds are ZZZ and ZZH . The cross sections of these

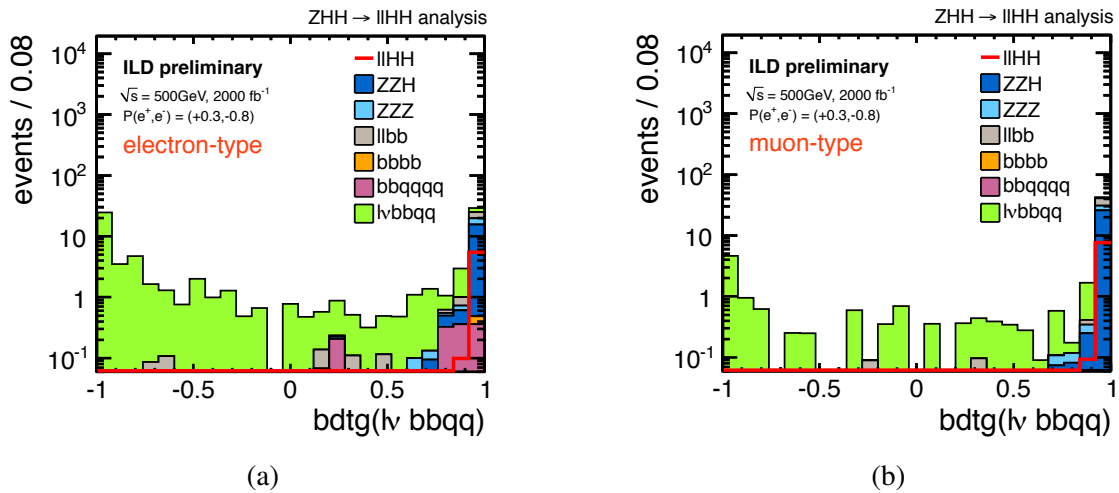


Figure 8.7: a) A cut of $bdtg(lvbbqq) > 0.97$ is imposed on electron-type events. b) A cut of $bdtg(lvbbqq) > 0.85$ is imposed on muon-type events.

processes are not large, but since they have the same final state as the signal they are more difficult to suppress. Especially in this case the discriminative power of the MVA output is very important. Mass distributions play an important role as input parameters for BDTG training. Hence, the kinematic fit results are taken into account and are evaluated.

At this stage of the analysis, the data samples used for BDTG training still have very large statistics, even after applying the foregoing cuts. The relative error on the expected number of background and signal events is below 1% after the cut on $bdtg(lvbbqq)$. In the following the input variables are discussed and the distributions are shown in fig. 8.8.

- χ^2_{ZHH} and χ^2_{ZZH} : As discussed in the preceding chapters, both variables are obtained from kinematic fits and are included in BDTG training. Both variables have shown an advanced signal and background separation. By adding these variables to the MVA, first investigations indicate a relative improvement of 20% in the event selection. However, the results are based on the kinematic fit without ISR treatment and without semi-leptonic correction. It needs to be confirmed for fit results including both effects since such fits give less discriminative power in signal and background separation (sec. 7.8). It turns out that in BDTG training the χ^2 distributions are the most important variables in ranking and separation (fig. 8.8a, fig. 8.8b).
- $M(H1)$ and $M(H2)$: The Higgs masses are important parameters to separate ZZH/Z from ZHH . The four jets are paired to form the signal bosons with eq. 5.4 (sec. 5.2) and by applying kinematic fits. Various combinations of Higgs masses have been tested as inputs. The fitted masses are highly correlated. The correlation is larger than 90%. The correlation degrades the separation power of the BDTG. By using only one Higgs mass the separation power is also decreased compared to the use of both masses before fit. Using both Higgs masses is useful, since ZZH/Z backgrounds cannot fulfil the two-Higgs hypothesis. Moreover, the fitted masses are

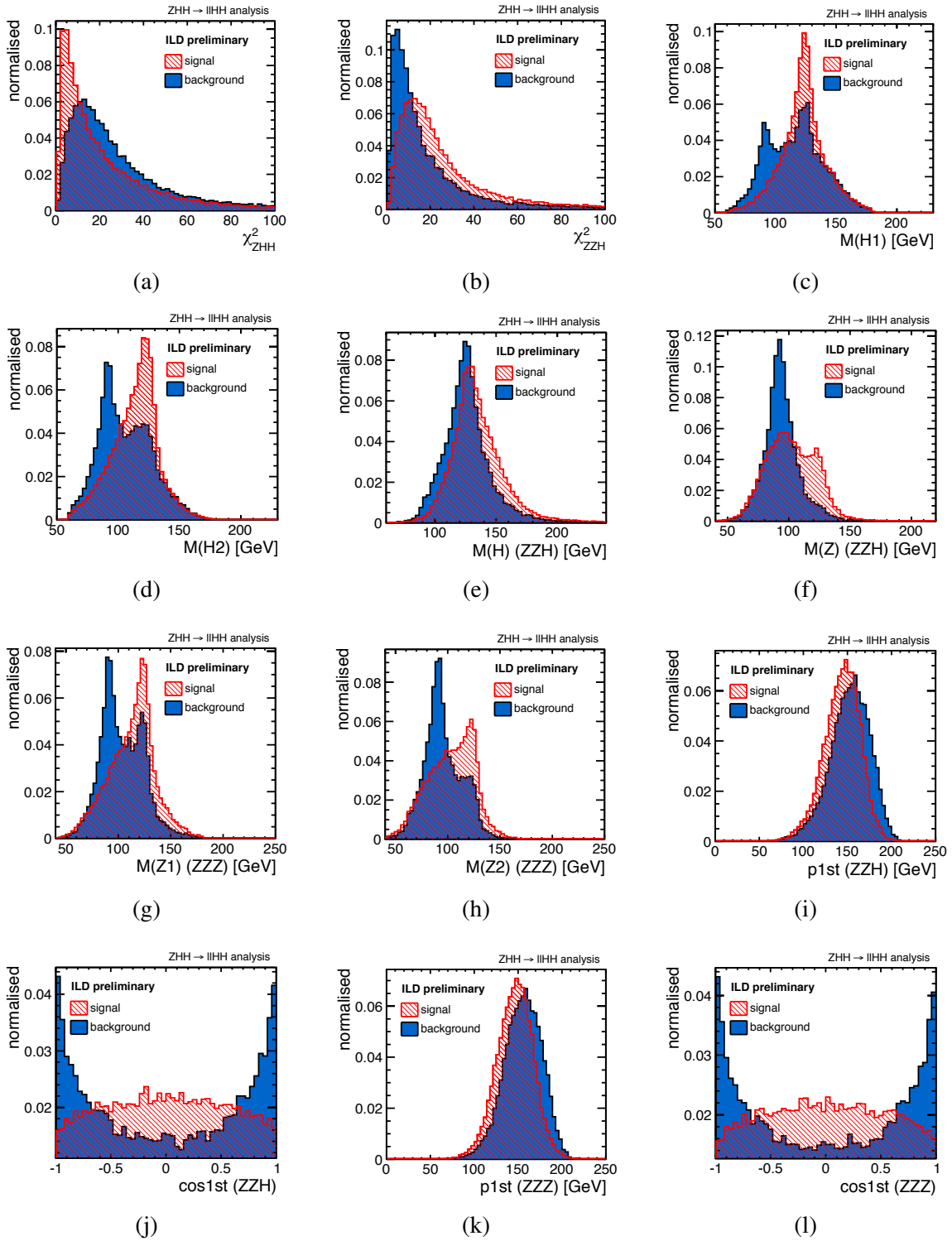


Figure 8.8: Inputs for $bdtg(llbbbb)$ training. The descriptions can be found in the text.

much more correlated to χ_{ZHH}^2 and χ_{ZZH}^2 , degrading the separation power of these variables in training. Hence, to assure the improvements by adding χ_{ZHH}^2 and χ_{ZZH}^2 , both masses without fitting are included even though the fitted masses give an enhanced background rejection (sec. 7.7.4) (fig. 8.8c, fig. 8.8d).

- **$M(H)$ (ZZH) and $M(Z)$ (ZZH):** The events are reconstructed according to the ZZH hypothesis. These boson masses are correlated to the ZHH final-state reconstruction, but give additional power to suppress ZZH . The Z and the Higgs masses are obtained without and with fitting. For the latter however, the hard-mass constraints used in the ZZH fit hypothesis fix the masses to a certain value. Nevertheless, the masses before fitting can be related to the fit results, by only considering the masses for the best jet permutation of the fit in every event. They are less correlated with $M(H1)$ and $M(H2)$ compared to the respective masses without fitting. This improves the separation power of the BDTG (fig. 8.8e, fig. 8.8f).
- **$M(Z1)$ (ZZZ) and $M(Z2)$ (ZZZ):** The events are reconstructed according to the ZZZ hypothesis. The masses are used to suppress the respective background. At this stage of the analysis, ZZZ is much smaller compared to ZZH . Various combinations of masses without and with fitting have been tested. Similar to the ZHH hypothesis, the fitted masses of the Z bosons are very correlated. Therefore, the Z -boson masses without fitting are used as inputs (fig. 8.8g, fig. 8.8h).
- **$p1st$ (ZZH) and $cos1st$ (ZZH):** ZZH includes a t -channel diagram with one Higgsstrahlung from a Z boson. The emitted bosons move very fast in forward direction. This property can be effectively used by reconstructing the events according to ZZH . The boson candidate with the largest momentum among the three bosons is identified. The largest boson momentum and its polar angle reflect the t -channel properties. They are less important in training, but excluding them from training still slightly decreases the separation power of the BDTG (fig. 8.8i, fig. 8.8j).
- **$p1st$ (ZZZ) and $cos1st$ (ZZZ):** Similar to ZZH , ZZZ includes a t -channel diagram with one Z strahlung from the electron line. Also in this case, the boson candidate with the largest momentum is identified and the largest boson momentum and its polar angle are used (fig. 8.8k, fig. 8.8l). The properties are correlated to $p1st$ (ZZH) and $cos1st$ (ZZH) ($\sim 80\%$), degrading the separation power.

The BDTG response is shown in fig. 8.9. Since the Higgs masses are the most discriminative quantities next to the χ^2 distributions from the kinematic fit, a cut on $bdtg(llbbbb)$ helps to suppress all other background processes as well. The overall relative improvement of the separation power of the BDTG response by adding the information obtained from the kinematic fit is about 5%. In total, a relative improvement of 20% can be achieved in the selection of $llHH$ by adding kinematic fit variables. This is discussed at the end of this chapter.

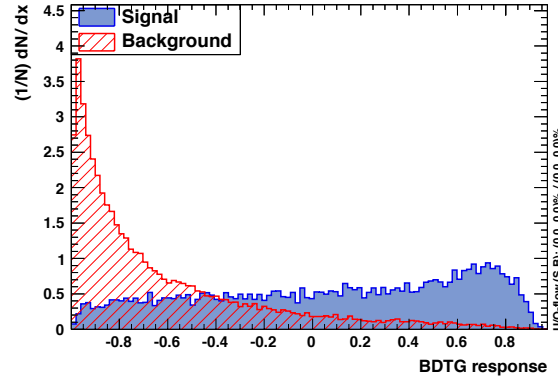


Figure 8.9: Classifier response of the third BDTG: ZHH/Z vs. ZHH ($llbbbb$).

The distribution of $bdtg(llbbbb)$ for electron-type and muon-type events is depicted in fig. 8.10. The absence of backgrounds at large $bdtg(llbbbb)$ for both lepton-types is visible. At this stage, the relative error on the expected number of events for ZZH and ZZZ is small. It reads 2% for ZZZ and 1% for ZZH in the electron-type category. In the muon-type category the relative error is 1% on ZZZ and ZZH , respectively. The selection cut is again optimised for both channels. In the electron channel, a threshold of $bdtg(llbbbb) > -0.41$ leads to 7.9 ± 0.6 background events in total. The largest contribution to the error is given by $evbbqq$. There are 4.03 ± 0.03 ZHH events remaining, 2.6 events of which are $ZHH \rightarrow eebbbb$ events. In the muon channel, a selection cut of $bdtg(llbbbb) > -0.28$ leads to 8.9 ± 0.5 background events in total and 5.1 ± 0.03 signal events, where 2.8 are $ZHH \rightarrow \mu\mu bbbb$ events. The final selection is listed in tab. 8.2.

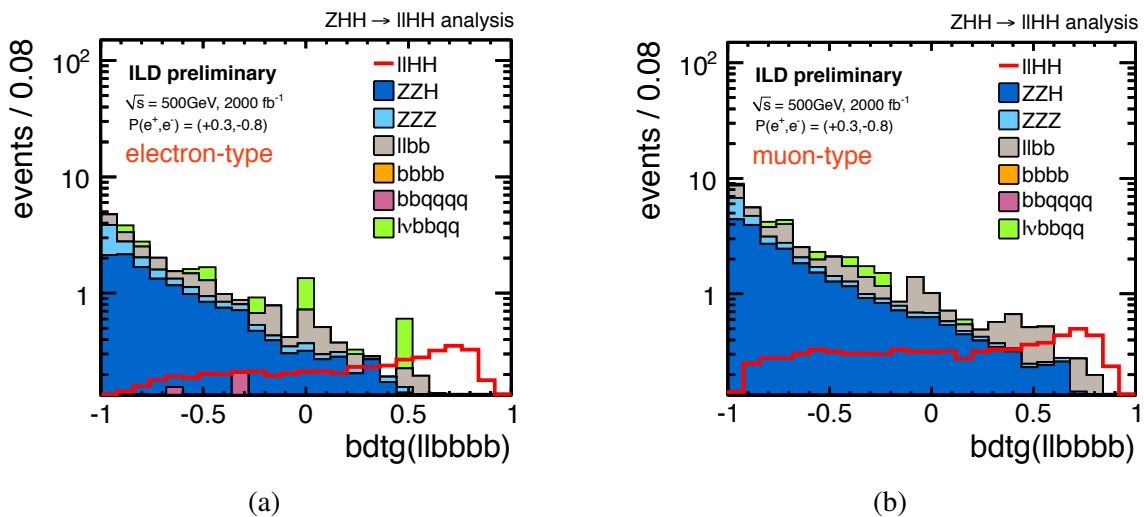
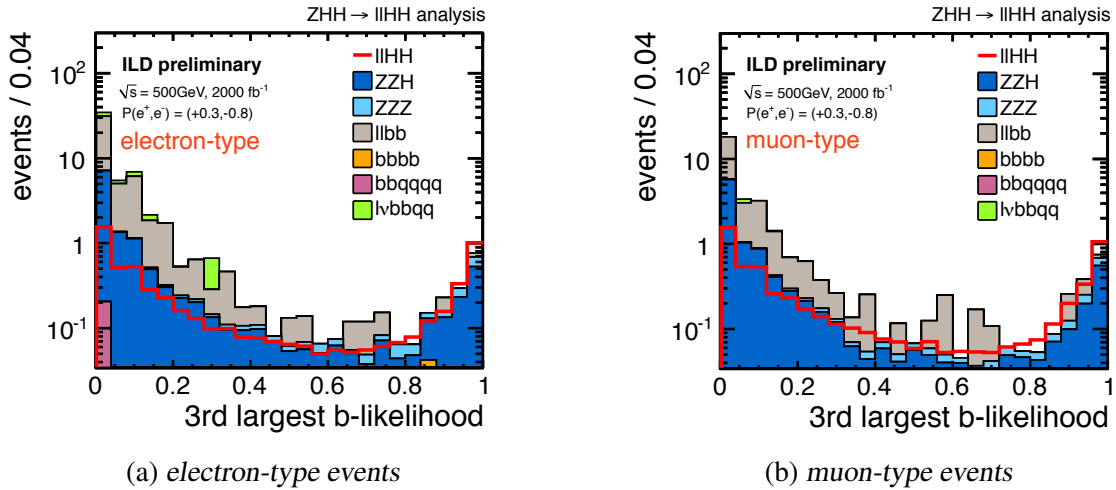


Figure 8.10: a) A cut of $bdtg(llbbbb) > -0.41$ is applied on electron-type events. b) A cut of $bdtg(llbbbb) > -0.28$ is imposed on muon-type events.

Figure 8.11: Jet with the third largest b likelihood.

8.1.3 Flavour Tag Information

So far, no flavour-tag information are used in the event selection. The backgrounds are well-suppressed by the BDTGs based on kinematic variables only. However, the number of background events is still larger than the number of signal events. One possibility to reject more events with two or even less b jets in the final state is given by flavour-tag information. This also refers to ZHH events, in which at least one of the Higgs bosons does not decay into a pair of b quarks. This allows to extract the desired $HH \rightarrow bbbb$ signal mode. To evaluate the flavour tag the four jets are ordered from largest to smallest b likelihood b_{max1} , b_{max2} , b_{max3} , and b_{max4} . Since all of the considered events contain at

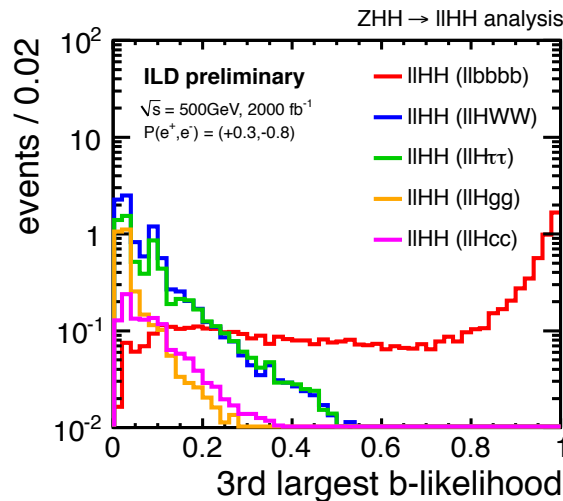


Figure 8.12: Jet with the third largest b likelihood for $ZHH \rightarrow lHH$ after preselection. Events with $H \rightarrow bb$ are present at small values. A tight cut on b_{max3} selects $ZHH \rightarrow llbbbb$ events.

least two b jets, $bmax1$ is large and $bmax4$ is small for signal and background events. The most discriminative variable is $bmax3$. The distributions for both lepton-type categories are shown in fig. 8.11. Only very soft cuts give an optimised signal significance at this stage of the analysis: $bmax3 > 0.03$ for electron-type (fig. 8.11a) and $bmax3 > 0.01$ for the muon-type (fig. 8.11b) events. The cuts do not have large effects on the background rejection, especially keeping in mind the limited statistics. Nevertheless, flavour-tag information can be used as optional feature to select $ZHH \rightarrow llbbbb$ events by applying a tight cut on $bmax3$. This is shown in fig. 8.12 for $llHH$ events after preselection. Events with one Higgs decaying into a channel other than $H \rightarrow bb$ are located only at small $bmax3$ values, while $HH \rightarrow bbbb$ peaks at large values. By increasing the selection threshold, more background events can be rejected and the desired signal mode can be selected. Since the optional b -tagging feature at the end gives a clear separation especially of $H \rightarrow WW, \tau\tau, bb$, the event selection strategy can serve the basis for further investigations of other Higgs decay modes.

8.2 Neutrino Channel

The important aspects of the optimised $\nu\nu HH$ event selection are discussed in the following. The event selection follows the same strategy as discussed for the lepton channel. First a preselection is applied to reduce the large background contribution. Then, separate BDTGs are trained for the dominant backgrounds. In every training the foregoing selection cuts are considered. Lastly, flavour-tag information are used in the selection. The cutflow for the entire selection is listed at the end of this section in tab. 8.3. The background events which contribute to $\nu\nu HH$ were discussed in sec. 5.2.

8.2.1 Preselection

The preselection of the neutrino channel follows the same strategy as in the lepton channel. In the lepton channel the most powerful preselection requirement is given by the isolated lepton selection, which rejects 95% of the total background contribution. In the neutrino channel, the isolated lepton selection is used as veto against events which contain at least one isolated lepton. Hardly any background considered in the neutrino channel includes isolated leptons. This requirement mainly reduces $lvbbqq$ events by almost 70%. The largest contribution to the remaining events is given by $\tau\nu bbqq$. Less than 10% of these events are from leptonic τ decays. A dedicated algorithm to identify hadronic τ decays could further improve the background suppression. The isolated lepton selection is optimised to find isolated e and μ . In 90% of $evbbqq$ and $\mu\nu bbqq$ one isolated lepton is found. Thus, the veto efficiency for events with one lepton is 90%. In the signal, roughly 22% of the events are rejected, only 3% which correspond to $ZHH \rightarrow \nu\nu bbbb$ (tab. 8.3). Mainly $H \rightarrow \tau\tau$ and $H \rightarrow WW$ events are suppressed. After jet pairing to reconstruct the signal bosons, the background contribution is suppressed by only 55% at this stage of

	$eebb$	$\mu\mu bb$	$e\nu bbq$	$\mu\nu bbq$	$\tau\nu bbq$	$bq\bar{q}q$	$b\bar{b}b\bar{b}$	$llbb\bar{b}\bar{b}$	$llq\bar{q}H$	Background	$llHH$ ($llbb\bar{b}\bar{b}$)
σ [fb]	142.1	24.8	124.2	123.0	123.0	312.0	20.1	0.03	0.08	869.1	0.02
expected events	$2.84 \cdot 10^5$	$4.95 \cdot 10^4$	$2.48 \cdot 10^5$	$2.46 \cdot 10^5$	$2.46 \cdot 10^5$	$6.24 \cdot 10^5$	$4.02 \cdot 10^4$	69.51	150.87	$1.734 \cdot 10^6$	40.51 (14.3)
total preselection	603 ± 7.5	287 ± 4.3	341 ± 9.1	45 ± 3.3	11.8 ± 1.5	3.7 ± 0.8	0.2 ± 0.09	11.5 ± 0.10	119.1 ± 0.44	1424 ± 13.1	21.4 ± 0.06 (7.7)

Electron-type Selection

$ltype = 11$	603 ± 7.5	0	341 ± 9.1	0.8 ± 0.4	10.9 ± 1.4	3.7 ± 0.8	0.2 ± 0.1	5.6 ± 0.07	57.9 ± 0.3	1024 ± 11.9	10.3 ± 0.04 (3.7)
$bdtg(llbb) > 0.87$	5.8 ± 0.7	0	51 ± 3.5	0.8 ± 0.4	1.9 ± 0.6	1.3 ± 0.5	0.2 ± 0.1	4.6 ± 0.06	16.1 ± 0.2	82 ± 3.7	5.8 ± 0.03 (3.6)
$bdtg(\nu bbq) > 0.97$	5.0 ± 0.7	0	2 ± 0.8	0	0.1 ± 0.2	0.4 ± 0.2	0.2 ± 0.1	3.9 ± 0.06	14.6 ± 0.2	27 ± 1.1	5.3 ± 0.03 (3.3)
$bdtg(llbb\bar{b}\bar{b}) > -0.41$	1.6 ± 0.4	0	1 ± 0.5	0	0	0	0	0.5 ± 0.02	4.2 ± 0.1	7.9 ± 0.7	4.0 ± 0.03 (2.6)
$bmax3 > 0.03$	1.5 ± 0.4	0	1 ± 0.5	0	0	0	0	0.5 ± 0.02	4.0 ± 0.1	7.0 ± 0.6	3.9 ± 0.03 (2.6)

Muon-type Selection

$ltype = 13$	0	287.7 ± 4.3	0	44.7 ± 3.2	0.9 ± 0.4	0	0	5.8 ± 0.07	61.2 ± 0.3	400 ± 5.4	11.0 ± 0.04 (3.9)
$bdtg(llbb) > 0.28$	0	10.1 ± 0.8	0	13.5 ± 1.8	0.3 ± 0.2	0	0	5.3 ± 0.07	26.7 ± 0.2	56 ± 1.9	8.0 ± 0.04 (3.9)
$bdtg(\nu bbq) > 0.85$	0	9.9 ± 0.8	0	2.7 ± 0.8	0	0	0	5.1 ± 0.07	26.3 ± 0.2	44 ± 1.2	7.7 ± 0.04 (3.8)
$bdtg(llbb\bar{b}\bar{b}) > -0.28$	0	2.8 ± 0.4	0	0.1 ± 0.1	0	0	0	0.4 ± 0.02	5.6 ± 0.1	8.9 ± 0.5	5.1 ± 0.03 (2.8)
$bmax3 > 0.01$	0	2.8 ± 0.4	0	0.1 ± 0.1	0	0	0	0.4 ± 0.02	5.6 ± 0.1	8.9 ± 0.5	5.1 ± 0.03 (2.8)

Table 8.2: Event selection results for the lepton channel, corresponding to a beam polarisation of $P(e^+e^-) = (0.3, -0.8)$ and an integrated luminosity of $\mathcal{L} = 2 \text{ ab}^{-1}$. If not stated otherwise, $l = e, \mu, \tau$. Also listed are the MC statistical errors on the number of events after every cut. The isolated lepton selection is not optimised for τ events. Only isolated e and μ pairs are selected. Hence, the preselection reduces the signal events by one third. The electron-type and muon-type selection is listed. The cut on $bmax3$ can be used to select $HH \rightarrow b\bar{b}\bar{b}\bar{b}$ events. The cut is optional and serves as example in this table, since it has no effect on the results.

the $\nu\nu HH$ preselection. In order to reduce backgrounds more effectively flavour-tag information are already included in the preselection. b_{max3} is the third largest b -tag value and is useful to suppress background events with less than three b jets. Moreover, as discussed in sec. 8.1.3, it allows to reject $\nu\nu HH$ events in which at least one Higgs does not decay into a pair of b quarks. A tight cut on b_{max3} gives access to $HH \rightarrow bbbb$ events. Therefore, $b_{max3} > 0.2$ is applied to the events, which rejects 99% of $\nu\nu bb$. Since this background has a large cross section roughly 2300 events pass the criteria. Additionally, 85% of $lvbbqq$ is suppressed. The largest contribution to $lvbbqq$ is given by $\tau\nu b b c s$ events. In this process the secondary vertices of the τ and c can make b tagging less effective. The total background is reduced by one order of magnitude (tab. 8.3). Since the flavour-tag efficiency scales to the power of the number of jets, improvements regarding flavour tagging have large effects on the analysis. The desired signal final state includes at least four b jets. Thus, by improving the b -tagging efficiency for the same purity by 5% would result in relative 20% more signal events after preselection.

Similar to $llHH$ additional cuts are applied before BDTG training, which represent properties of the signal mode. First, selection cuts are applied to $M(H1)$ (fig. 8.13a) and $M(H2)$ (fig. 8.13b). Both masses should satisfy values within 60 GeV and 180 GeV. This rejects ZZ and full-hadronic six-jet events from tt and WWZ . ZZ background can be suppressed by $thrust < 0.9$ (fig. 8.13c). In contrast to $llHH$, the two neutrinos in the neutrino channel cause a reduced visible energy and large missing transverse momentum. Therefore, the missing transverse momentum should satisfy $10 \text{ GeV} < m_{pt} < 180 \text{ GeV}$ (fig. 8.13d). Moreover, the visible energy in an event needs to fulfil $e_{vis} < 400 \text{ GeV}$ (fig. 8.13e). In signal events missing energy originates from $Z \rightarrow \nu\nu$ and ISR. Missing energy from semi-leptonic b and cascade c decays in the jets is corrected for and should not contribute largely. The visible energy requirement rejects full-hadronic backgrounds, in which the missing energy can only occur in the jets, i. e. $bbqqqq$ and $bbbb$. Moreover, the invariant mass of all reconstructed particles should be consistent with the mass of the two Higgs bosons $M(HH)$ (fig. 8.13f). Therefore, the events have to fulfil $M(HH) > 220 \text{ GeV}$. This requirement rejects $bbbb$ and $\nu\nu bb$ events. After applying the additional cuts the background contribution is again reduced by almost one order of magnitude and the signal efficiency is roughly 90% with respect to the preselection (tab. 8.3).

8.2.2 MVA Training and Final Selection

After preselection three separate MVAs are trained for the dominant backgrounds. Also in this channel using BDTGs instead of MVAs as in [108] gives 5% improvement on the $\nu\nu HH$ event selection results. At this stage the dominant backgrounds are again: (1) $bbbb$, (2) semi-leptonic background $lvbbqq$, and (3) ZZH/Z with the same final state as the signal $\nu\nu bbbb$. A summary of input variables and the corresponding distributions are listed in A.1. The important aspects of the final selection are discussed in the following.

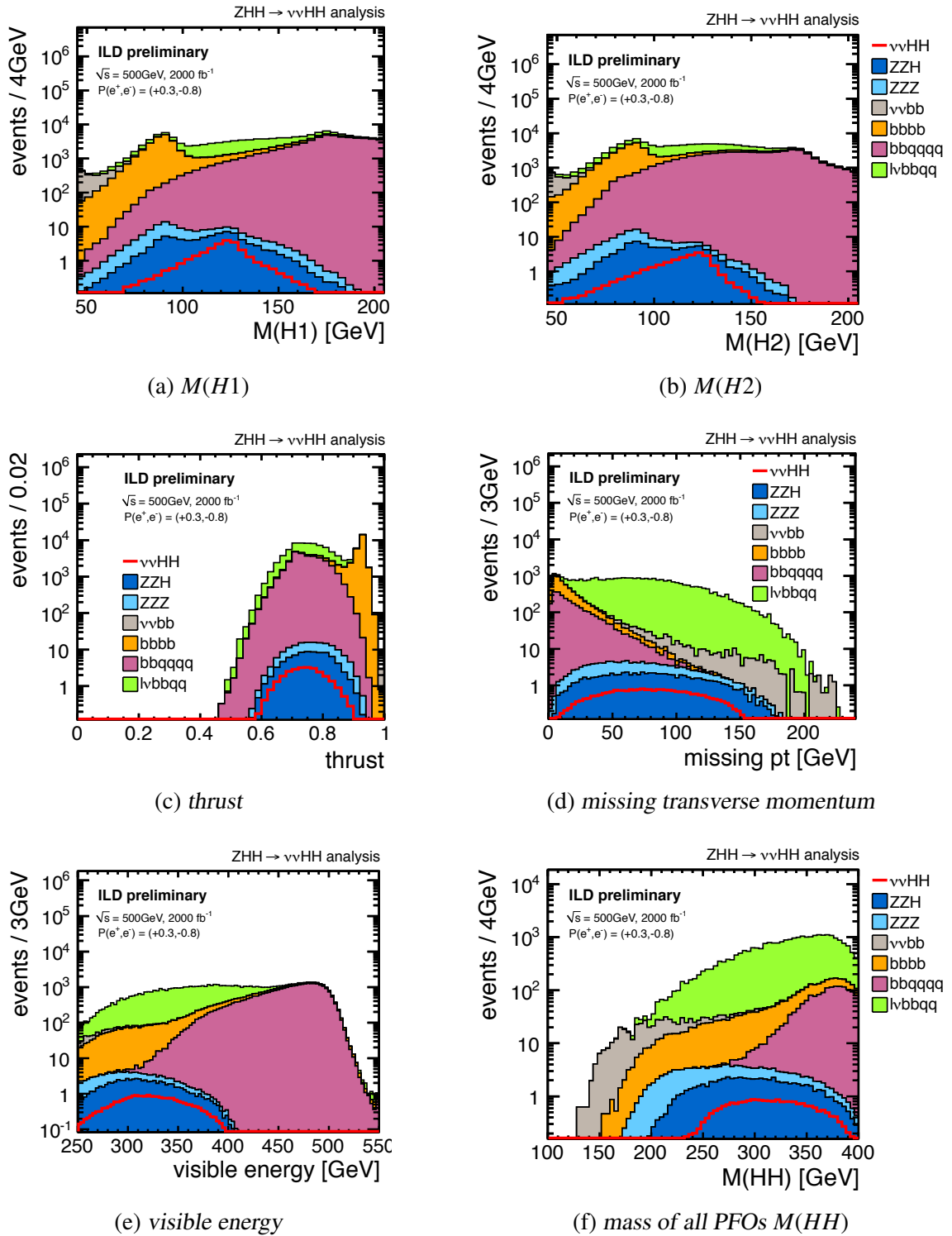


Figure 8.13: Preselection variables in the neutrino channel. All distributions are shown after having applied the respective previous cuts.

First BDTG: $bbbb$ vs. $\nu\nu HH$ ($\nu\nu bbbb$)

After preselection, the dominant background is $bbbb$. The b -tagging and missing energy requirements in the preselection were less effective for these events. Enough statistics is available for BDTG training after preselection. The relative error on background and signal events is less than 1%. The entire collection of input variables for training and the corresponding distributions are given in A.1.1. Especially important in the BDTG training are visible energy, missing transverse momentum and the thrust even though these variables have been used as precuts. Missing energy and transverse momentum in $bbbb$ can occur in the jets and from ISR. However, ISR photons do not carry transverse momentum since they are very forward and backward. Therefore, missing transverse momentum can only occur in the jets. Missing energy from semi-leptonic b and cascade c decays is corrected in the jets. Hence, the signal has larger missing energy and missing pt compared to the background (A.1.1).

The classifier response and the $bdtg(bbbb)$ distribution for signal and backgrounds after preselection are shown in fig. 8.14. The optimal cut suggested in training reads $bdtg(bbbb) > 0.81$. However, the threshold is optimised in the final selection with respect to the maximum signal significance $\sigma = \frac{s}{\sqrt{s+b}}$. The optimised selection cut reads $bdtg(bbbb) > 0.94$, since applying a more strict cut on $bdtg(bbbb)$ allows to suppress large amount of other backgrounds besides $bbbb$. The total background is suppressed by 60%, while keeping more than 70% of $\nu\nu HH$ and 80% of $ZHH \rightarrow \nu\nu bbbb$ with respect to the previous cut on $M(HH)$. 99% of $bbbb$ events do not pass this requirement and $lvbbqq$ is suppressed by 50%. The full-hadronic six-jet background does not satisfy the missing energy and momentum requirements and is suppressed by 95%. Hence, the properties of $bbbb$ used in training are very discriminative to select signal events and reject large amount of background. The optimised $bdtg(bbbb)$ cut is considered in the training of the second BDTG.

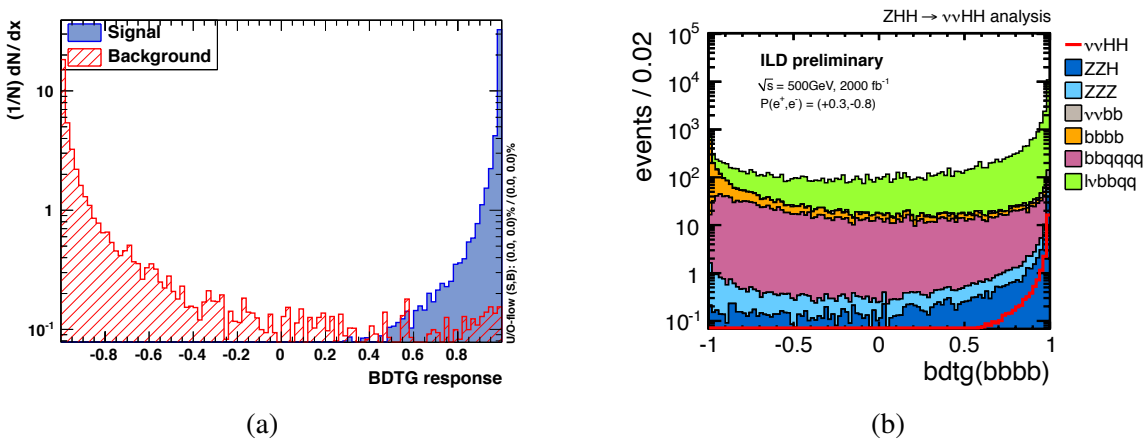


Figure 8.14: a) Classifier response of the first BDTG. b) $bdtg(bbbb)$ for signal and backgrounds after all foregoing cuts. $bdtg(bbbb) > 0.94$ is applied to the events.

Second BDTG: $lvbbqq$ vs. $\nu\nu HH$ ($\nu\nu bbbb$)

The largest background contribution is given by $lvbbqq$. The semi-leptonic background consists of $evbbcs$, $evbbud$ and the corresponding μ and τ modes. These processes come from tt and WWZ decays. So far, the $evbbqq$ and $\mu\nu bbqq$ processes are well suppressed by the selection. However, $\tau\nu bbqq$ events, especially $\tau\nu bbcs$ in which the τ and c jets can make b tagging less effective are very challenging. In order to discriminate $\tau\nu bbqq$, background variables are used as BDTG input which are obtained by reconstructing the events as five-jet events from $\tau\nu bbqq$. The jet with the smallest number of PFOs represents the τ jet. The remaining four jets are ordered by b likeliness. The two jets with the smallest b likeliness are reconstructed as W boson. The top mass is reconstructed by combining one of the b jets with the W -boson candidate, which results in two possible top-mass combinations. The top and W masses are used as inputs. Moreover, since some τ decay into a high-energetic charged π , the largest momentum of all PFOs can provide separation power. The entire collection of input variables and the corresponding distributions can be found in A.1.2. The classifier response and the $bdtg(lvbbqq)$ distribution for signal and backgrounds after all foregoing cuts are shown in fig. 8.15. The optimal cut value suggested in BDTG training reads $bdtg(lvbbqq) > 0.18$. However, the threshold is optimised with respect to the maximum signal significance. The optimised selection cut gives $bdtg(lvbbqq) > 0.67$. By applying this selection cut the total background is reduced by $\sim 95\%$, while keeping 70% of $\nu\nu HH$ with respect to the previous cut on $bdtg(bbbb)$. Relative 95% of $\tau\nu bbqq$ do not pass the selection cut. Nevertheless, the remaining 5% still correspond to 700 events. At this stage of the analysis the relative errors of some backgrounds become large, i. e. $\nu\nu bb$ obtains a relative error of 18% and $bbbb$ of 10%. To get a better picture on the suppression of the events, larger statistics is needed. To reduce the relative error on both background types to 5%, 20 times more statistics is needed for $\nu\nu bb$ and 60 times more for $bbbb$ with respect to the expected number of events.

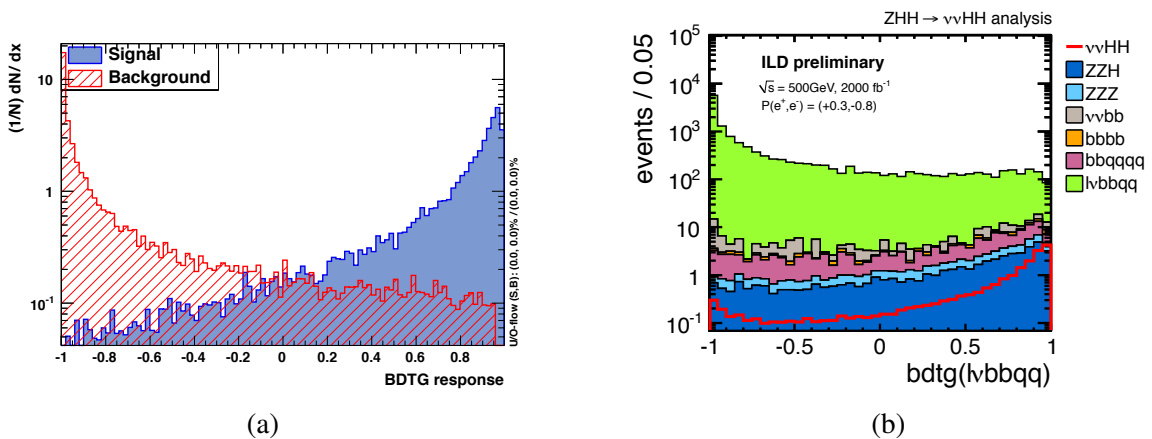


Figure 8.15: a) Classifier response of the second BDTG. b) $bdtg(lvbbqq)$ for signal and backgrounds after all foregoing cuts. $bdtg(lvbbqq) > 0.67$ is applied to the events.

Third BDTG: ZZH/Z vs. $\nu\nu HH$ ($\nu\nu bbbb$)

The third BDTG is trained for background processes as $ZZH/Z \rightarrow \nu\nu bbbb$. After the previous selection cuts, there is still enough statistics available for BDTG training. The relative error on the number of ZZH and ZZZ events is 1%, respectively. The relative error on the number of signal events is below 1%. The same input parameters are used in training as for $llHH$. Similar to $llHH$, the boson mass distributions without fitting are used in training to avoid large correlations between input variables, which degrade the separation power of χ^2_{ZHH} and χ^2_{ZZH} obtained from the fit. In the neutrino channel, missing four-momentum is carried away by $Z \rightarrow \nu\nu$. In order to be able to perform kinematic fits in this mode and to ensure that the fit is non-trivial, the $Z_{\text{invisible}}$ fit object was developed which is described in sec. 6.3.2. The $Z_{\text{invisible}}$ fit object automatically imposes one mass constraint of $M_{\nu\nu} = M_Z$ to the fit. The fit has to satisfy the Z -mass constraint parametrised by the missing energy. However, the application of the ISR photon fit object in combination to the $Z_{\text{invisible}}$ fit object had to be evaluated, since the ISR photon fit object is parametrised by the total missing p_z of an event. In fig. 8.16 $P(\chi^2)$ of the ZHH fit (fig. 8.16a) is exemplary shown for signal events, as well as the χ^2 scatter plot (fig. 8.16b) which is fed to the BDTG. The semi-leptonic correction provides improvements since less missing energy is present in the events. However, the missing energy in the events from either ISR or $Z \rightarrow \nu\nu$ cannot be distinguished. $P(\chi^2)$ indicates that the ISR consideration in the fit distorts the fit probability. The missing energy in the final state would require further developments for a successful ISR treatment. Hence, in the neutrino channel in the fit ISR is not considered. Nevertheless, the developed $Z_{\text{invisible}}$ fit object allows the application of kinematic fits without ISR consideration with very good fit performance. $P(\chi^2)$ is well-distributed. The classifier response and the $bdtg(\nu\nu bbbb)$ distribution for

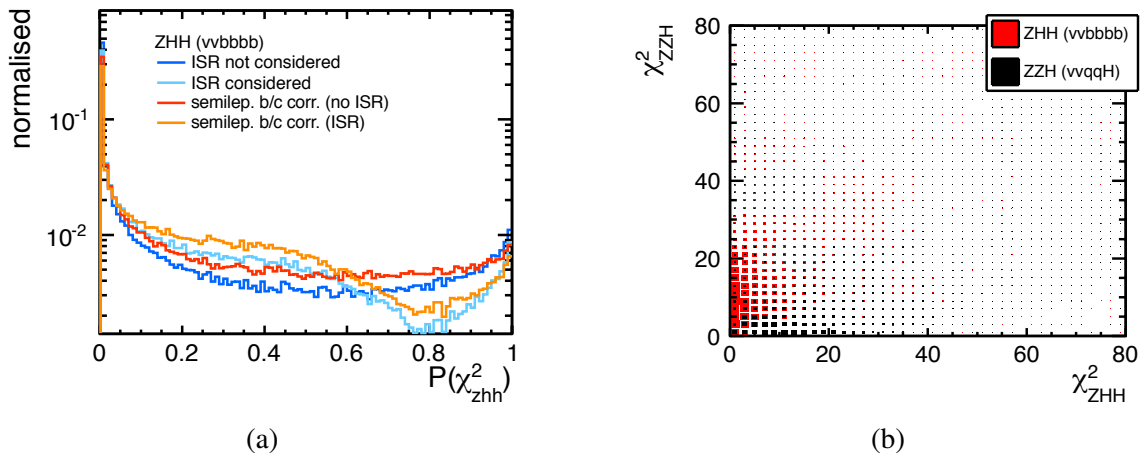


Figure 8.16: a) $P(\chi^2)$ of the ZHH fit for signal events. The semi-leptonic correction without ISR treatment gives an enhanced fit performance. b) χ^2_{zzh} vs. χ^2_{zhh} for fits without ISR consideration and with semi-leptonic energy correction. The developed $Z_{\text{invisible}}$ fit object allows the application of kinematic fits. However, the missing energy in the final state would require further developments for a successful ISR treatment.

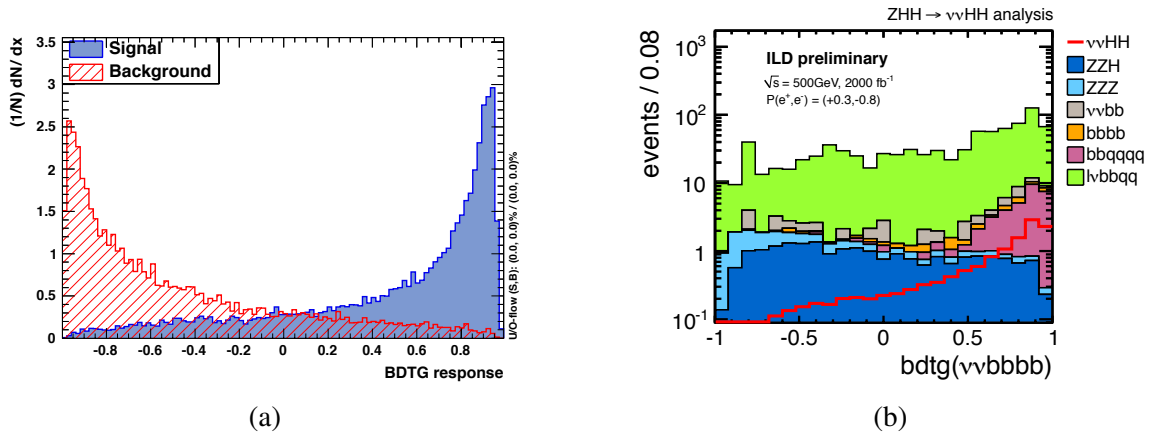


Figure 8.17: a) Classifier response of the third BDTG. b) $bdtg(vvbbbb)$ for signal and backgrounds after all foregoing cuts. $bdtg(vvbbbb) > 0.3$ is applied to the events.

signal and background events are shown in fig. 8.17. The selection cut is optimised to $bdtg(vvbbbb) > 0.3$. By applying this cut ZZH/Z is suppressed by roughly 80%. The total background is again suppressed by relative 42% after this cut.

8.2.3 Flavour Tag Information

Lastly, flavour-tag information are used to reject background events. After BDTG classification flavour tagging is crucial in this channel since there are still 525 ± 13 background events remaining, the majority of which is given by $\tau vbbqq$ events. At this stage of the event selection, the relative error on some background events is larger than 10%, i. e. $vvbb$ (20%), $evbbqq$ (12%), and $bbbb$ (12%). However, the error on $\tau vbbqq$ is small.

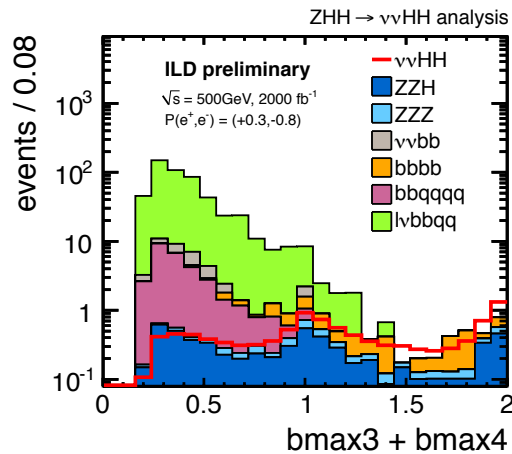


Figure 8.18: Sum of the third and fourth largest b tag after all cuts for background and signal events. $bmax3 + bmax4 > 1.08$ provides a very important threshold to suppress the majority of background events, especially full-hadronic and semi-leptonic backgrounds.

Events passing the selection so far are predominantly $\tau\nu b b c s$. The τ and c quarks can be misidentified as b jets and require large flavour-tagging efficiencies. The jets are ordered in descending order by b likeliness. The most discriminative variables are the third and fourth largest b likelihood, the sum of which is used in the selection. The distribution is shown in fig. 8.18. Due to the flavour-tagging requirement in the preselection, values $b_{max3} + b_{max4} < 0.2$ are not possible. At large values only signal events are present, next to $b b b b$ and $Z Z H / Z \rightarrow \nu b b b b$. Other backgrounds are populated at small values. The optimised cut reads $b_{max3} + b_{max4} > 1.08$, which reduces $\tau\nu b b q q$ from 414 ± 12 to 2.5 ± 0.9 events, which are given by $\tau\nu b b c s$. In total after this selection cut, 7 ± 1 background events pass the neutrino channel selection and 5.6 ± 0.04 $\nu\nu H H$ events, 5.5 events of which are $Z H H \rightarrow \nu b b b b$.

The b -tagging efficiency scales as ϵ^n , where n denotes the number of b jets in the signal final state. In the desired signal final state, there are at least four b jets. Therefore, improving the flavour tag could result in large relative enhancements of the selection. A relative improvement of 5% in the b -tagging efficiency would give relative 20% more signal events for the same purity. Thus, after the event selection, 6.8 signal events would pass the selection, 6.7 of which correspond to $Z H H \rightarrow \nu b b b b$. This would enhance the signal significance in this channel by relative 20%.

8.3 Hadron Channel

The hadron channel gives the largest contribution ($\sim 70\%$) to $Z H H$. Therefore, optimising this mode is very important. Providing a six-jet final state with at least four b jets poses high demands on the reconstruction software and detector technologies. In this channel, background processes are taken into account which have four or more quarks in the final state, at least two of which have to be b quarks. Also considered are $t t Z$ and $t t g$ backgrounds which can result in up to eight-jet final states. The basic analysis steps were discussed in sec. 5.2 and the strategy follows $l l H H$ and $\nu\nu H H$. In the following the challenging aspects of the selection are discussed.

The preselection includes an isolated lepton veto. The veto efficiency is 90% to reject events with one isolated lepton. Events with one or more isolated leptons are rejected. This allows to reduce semi-leptonic backgrounds $l\nu b b q q$ by 70%. The largest contribution to the events is given by $\tau\nu b b q q$. Less than 10% of these events are from leptonic τ decays, which could be suppressed by a dedicated algorithm to identify hadronic τ decays. This could further improve the background suppression. Next to the isolated lepton veto, the six jets are paired to form the signal bosons (eq. 5.4 in sec. 5.2). Jet pairing requires flavour-tag information as explained in the following.

	$\nu\nu bb$	$e\nu bbq$	$\mu\nu bbqq$	$\tau\nu bbqq$	$bbqqqq$	$bbbb$	$\nu\nu bbbb$	$\nu\nu qqH$	Background	$\nu\nu HH$ ($\nu\nu bbbb$)
σ [fb]	136.4	124.2	123.0	123.0	312.0	20.1	0.05	0.22	838.9	0.04
expected events	$2.73 \cdot 10^5$	$2.49 \cdot 10^5$	$2.46 \cdot 10^5$	$2.46 \cdot 10^5$	$6.24 \cdot 10^5$	$4.02 \cdot 10^4$	96.83	447.0	$1.68 \cdot 10^6$	80.14 (28.5)
Preselection Cuts										
$N_{isolep} = 0$	$2.7 \cdot 10^5 \pm 399$	$2.5 \cdot 10^4 \pm 72$	$2.4 \cdot 10^4 \pm 71$	$2.0 \cdot 10^5 \pm 270$	$6.1 \cdot 10^5 \pm 314$	$4.0 \cdot 10^4 \pm 53$	95 ± 0.4	392 ± 1.1	$1.2 \cdot 10^6 \pm 586$	62.4 ± 0.1 (27.9)
$ M_{ij} - M_{Hj} < 80$ GeV	$2.7 \cdot 10^4 \pm 126$	$1.9 \cdot 10^4 \pm 68$	$1.5 \cdot 10^4 \pm 58$	$2.0 \cdot 10^5 \pm 269$	$4.6 \cdot 10^5 \pm 273$	$3.7 \cdot 10^4 \pm 52$	93 ± 0.4	309 ± 1.0	$7.6 \cdot 10^5 \pm 416$	61.0 ± 0.1 (26.1)
$bmax3 > 0.2$	2290 ± 37	1807 ± 21	1423 ± 18	$3.6 \cdot 10^4 \pm 113$	$6.2 \cdot 10^4 \pm 100$	$3.1 \cdot 10^4 \pm 47$	82 ± 0.4	85 ± 0.5	$1.4 \cdot 10^5 \pm 165$	28.2 ± 0.1 (24.5)
Additional Precuts										
$60 < M_{H1} < 180$	1280 ± 27	1668 ± 20	1341 ± 18	$3.4 \cdot 10^4 \pm 110$	$3.8 \cdot 10^4 \pm 78$	$2.9 \cdot 10^4 \pm 46$	80 ± 0.4	84 ± 0.5	$1.1 \cdot 10^5 \pm 147$	27.8 ± 0.1 (24.3)
$60 < M_{H2} < 180$	634 ± 19	1619 ± 20	1299 ± 17	$3.3 \cdot 10^4 \pm 109$	$3.2 \cdot 10^4 \pm 72$	$2.8 \cdot 10^4 \pm 45$	76 ± 0.4	82 ± 0.5	$9.7 \cdot 10^4 \pm 142$	27.3 ± 0.1 (24.1)
$10 < m_{PT} < 180$	610 ± 19	1587 ± 20	1271 ± 17	$3.2 \cdot 10^4 \pm 107$	$1.7 \cdot 10^4 \pm 53$	$1.4 \cdot 10^4 \pm 32$	74 ± 0.4	81 ± 0.5	$6.7 \cdot 10^4 \pm 128$	27.0 ± 0.1 (23.9)
thrust < 0.9	446 ± 16	1572 ± 20	1254 ± 17	$3.2 \cdot 10^4 \pm 107$	$1.7 \cdot 10^4 \pm 53$	3404 ± 16	73 ± 0.4	80 ± 0.5	$5.6 \cdot 10^4 \pm 124$	26.8 ± 0.1 (23.7)
evs < 400 GeV	444 ± 16	1115 ± 16	1016 ± 15	$2.6 \cdot 10^4 \pm 96$	1841 ± 17	1783 ± 11	72 ± 0.4	80 ± 0.5	$3.2 \cdot 10^4 \pm 102$	26.6 ± 0.1 (23.6)
$M(HH) > 220$ GeV	161 ± 10	1073 ± 16	979 ± 15	$2.5 \cdot 10^4 \pm 94$	1799 ± 17	1656 ± 11	56 ± 0.3	75 ± 0.5	$3.0 \cdot 10^4 \pm 99$	25.7 ± 0.1 (21.5)
Final Selection Cuts										
$bdig(bbbb) > 0.94$	77 ± 7	621 ± 13	569 ± 11	$1.3 \cdot 10^4 \pm 69$	84 ± 4	17 ± 0.9	23 ± 0.2	49 ± 0.4	$1.5 \cdot 10^4 \pm 71$	18.8 ± 0.08 (17.1)
$bdig(lvbbqq) > 0.67$	18 ± 3	40 ± 3	62 ± 4	716 ± 16	28 ± 2	7 ± 0.7	10 ± 0.1	22 ± 0.3	902 ± 17	13.3 ± 0.07 (11.9)
$bdig(\nu\nu bbbb) > 0.3$	10 ± 2	25 ± 3	36 ± 3	414 ± 12	27 ± 2	5 ± 0.6	1 ± 0.05	6 ± 0.1	525 ± 13	10.5 ± 0.06 (9.5)
$bmax3 + bmax4 > 1.08$	0	0	0	2.5 ± 0.9	0	2 ± 0.4	0.5 ± 0.03	2 ± 0.1	7 ± 1	5.6 ± 0.04 (5.5)

Table 8.3: Selection table for the neutrino channel. The numbers correspond to an integrated luminosity of $\mathcal{L} = 2 \text{ ab}^{-1}$ and a beam polarisation of $P(e^+e^-) = (0.3, -0.8)$. The MC statistical error on the numbers of events after each selection cut are listed. After final selection 7 ± 1 background events and 5.6 ± 0.04 signal events remain, with 5.5 events of $ZHH \rightarrow \nu\nu bbbb$. The *biag* requirement is important to reject the very large $\tau\nu bbqq$ background at the end of the final selection.

8.3.1 Mass Reconstruction and Jet Pairing

The challenges in mass reconstruction have been discussed in sec. 5.2.2 in context of the event selection. While in both the lepton and neutrino channel only four jets need to be combined to form the two Higgs bosons, $ZHH \rightarrow qqbbbb$ is very challenging with its six-jet environment. There are 45 possible combinations to form the signal final state of ZHH . It is difficult to find the correct pairing, since many jet-pair combinations obtain small χ^2 . Hence, jet pairing is prone to errors due to combinatorics. A $btag$ requirement is used to support the jet pairing by choosing the permutation with smallest χ^2 (eq. 5.4). At least four jets in an event need to have a b likeliness larger than 0.16. These four jets are paired to form the Higgs bosons. If more than four jets in an event fulfil the requirement, the respective jet permutations are also evaluated as Higgs candidates. Since the dominant backgrounds predominantly contribute six-jet final states, the flavour-tag requirement rejects events which do not have four b jets in the final state. In this thesis, several $btag$ thresholds have been studied since the actually used requirement in [108] of four jets with $btag > 0.16$ rejects $\sim 15\%$ of desired $ZHH \rightarrow qqbbbb$ events. However, applying a more loose $btag$ degrades the mass resolution. This is shown in fig. 8.19 for two different flavour-tag requirements. The Higgs mass is obtained for the $ZHH \rightarrow qqbbbb$ hypothesis. Although both distributions are of similar shape, wrong jet pairings become mainly visible in the tails of the distributions. The tails to smaller or larger masses are reduced for $btag > 0.16$. Requiring $btag < 0.16$ leads to increasing tails especially to smaller masses, since events with semi-leptonically decaying W bosons from $H \rightarrow WW$ or with $H \rightarrow \tau\tau$ pass the requirement. Additionally, by requiring $btag < 0.16$ even more background events survive the selection, which then need to be suppressed with tight cuts in the final

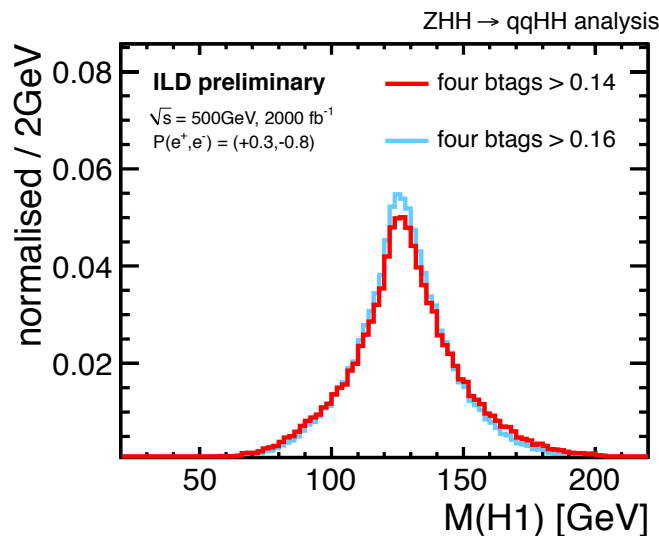


Figure 8.19: Normalised Higgs mass distribution $M(H1)$ for two different tag requirements in the jet pairing of $ZHH \rightarrow qqHH$ events with eq. 5.4. The wrong jet pairings are predominantly present in the tails to smaller or larger masses.

selection. As a consequence, the relative gain in the number of signal events is lost. At the end of an event selection, the larger background contributions and the degraded mass resolutions result in up to 20% relative degradation of the signal significance in the hadron channel. Especially here, a relative improvement of the flavour-tagging efficiencies could have large impact on the event selection. Assuming a relative improvement of 5% in the b -tagging efficiency for the same purity would lead to relative 20% more signal events after requiring four b tag larger than 0.16. Also kinematic fits suffer from combinatorics in case of $qqHH$ and the possible 45 jet permutations. This poses a challenge to the estimation of measurement resolution and the applied constraints in the fit hypothesis, which have to be chosen carefully to increase the chances of finding the correct permutation in six-jet final states. The effect of choosing wrong jet permutations is overwhelming especially in case of the equal-mass fit. In contrast to hard mass constraints, the equal-mass fit does not fix di-jet masses to a certain value. Many small χ^2 are obtained with very small differences. The semi-leptonic correction only gives a small improvement to the mass reconstruction in the fit of $qqHH$. Therefore, the discussed flavour-tag requirement has been implemented to the fit hypothesis which allows the reconstruction of boson masses in the six-jet configuration. The fit results are consistent with $llHH$ (sec. 7.7.4). Nevertheless, besides combinatorics at $\sqrt{s} = 500$ GeV, the invariant mass resolution of ZHH is dominated by jet-finding ambiguities rather than the jet-energy resolution.

8.3.2 Additional Preselection Cuts

After preselection, additional precuts are applied to reduce the number of background events before BDTG training. Apart from the b -tag requirement, the variables are identical to $llHH$. The preselection results are listed in tab. 8.4. All expected number of events are listed with the corresponding errors. In order to have a unified collection of precuts for all three signal channels, the two Higgs masses need to fulfil $60 \text{ GeV} < M(H1) < 180 \text{ GeV}$ (fig. 8.20a, fig. 8.20b) and $60 \text{ GeV} < M(H2) < 180 \text{ GeV}$ (fig. 8.20c, fig. 8.20d). The events have to fulfil missing $p_T < 70 \text{ GeV}$ (fig. 8.20e, fig. 8.20f). This cut reduces $lvbbqq$ events by almost 40% with respect to the previous cut. Additionally, the events need to satisfy a thrust value smaller than 0.9 (fig. 8.20g, fig. 8.20h). The requirement rejects 66% of $bbbb$. As a conclusion, after b -tag and isolated lepton requirement all other precuts are nearly 100% efficient on signal events and reduce the background by a factor of two.

8.3.3 MVA Training and Final Selection

After preselection the dominant backgrounds in the hadron channel are: (1) $bbbb$, (2) $bbqqqq$ (here: $q \neq b$), and (1) $qqbbbb$. The identification of six-jet background is crucial. It requires well-reconstructed masses, which are the most important variables in the signal and background separation. Moreover, flavour tagging is very important to suppress backgrounds as $bbcsc$. The identification rate of b and c jets has to be large.

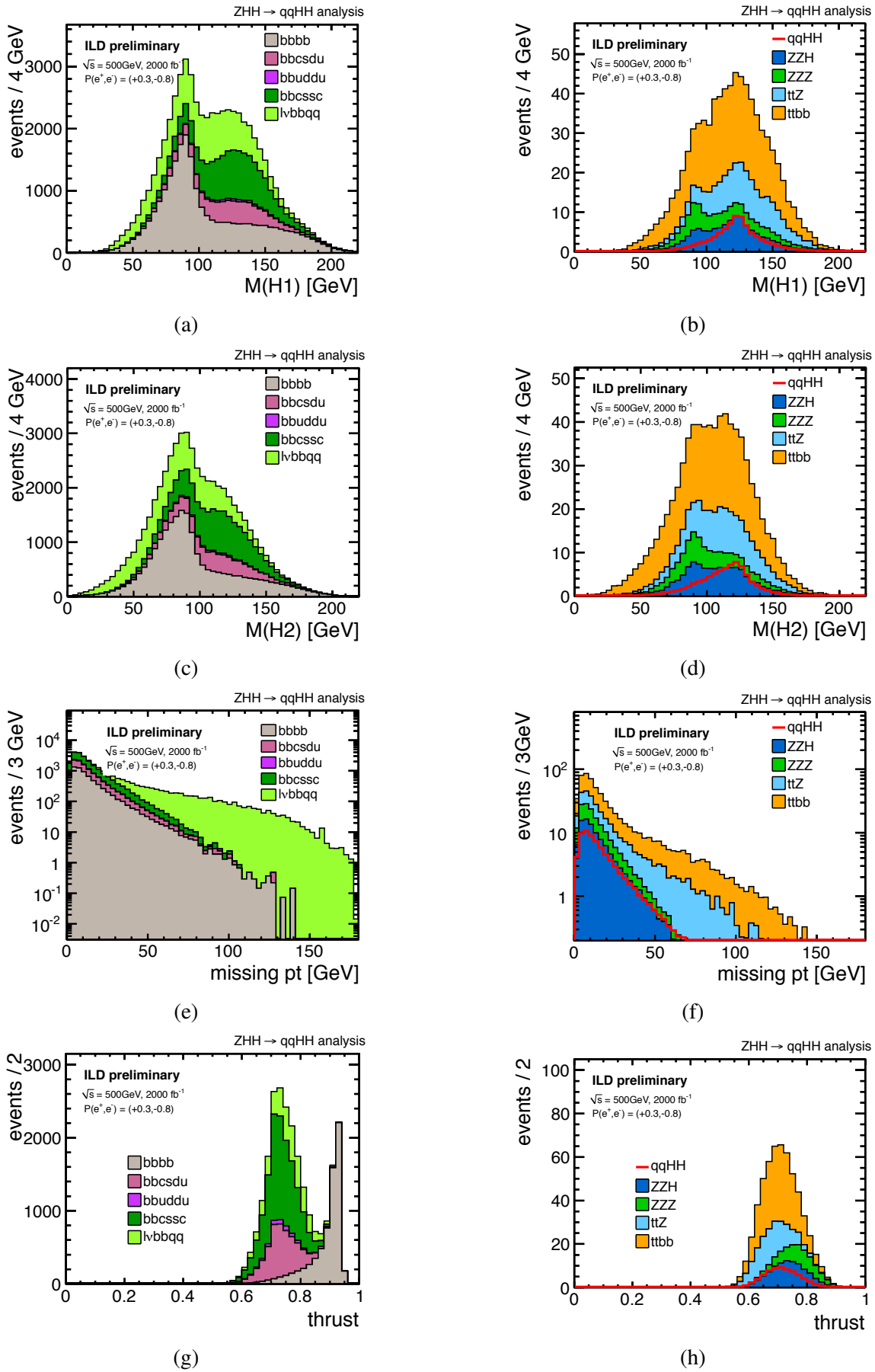


Figure 8.20: Preselection variables after having applied the respective foregoing cuts. The backgrounds with large cross sections (left) and smaller background processes plus signal (right) are shown in separate plots due to the different scales.

	$qqqH$	$qqbbbb$	$bbbb$	$bbcsc$	$bbcdu$	$bbuddu$	$lvbqq$	$t\bar{t}Z$	$t\bar{t}bb$	Background	$qqHH$ ($qqbbbb$)
σ [fb]	0.33	0.07	20.12	77.95	156	78.07	370	1.09	1.05	704.8	0.137
expected events	662.6	140.5	$4.02 \cdot 10^4$	$1.56 \cdot 10^5$	$3.12 \cdot 10^5$	$1.56 \cdot 10^5$	$7.40 \cdot 10^5$	2197	2109	$1.4 \cdot 10^6$	273.1 (99)
Preselection Cuts											
$N_{isollep} = 0$	583 ± 1.4	137 ± 0.4	$3.9 \cdot 10^4 \pm 53$	$1.5 \cdot 10^5 \pm 174$	$3.0 \cdot 10^5 \pm 270$	$1.5 \cdot 10^5 \pm 198$	$2.4 \cdot 10^4 \pm 222$	1322 ± 6	1271 ± 6	$6.7 \cdot 10^5 \pm 440$	214 ± 0.3 (82.0)
$btag > 0.16$	114 ± 0.6	84 ± 0.4	$2.4 \cdot 10^4 \pm 41$	$1.3 \cdot 10^4 \pm 51$	6167 ± 38	568 ± 12	$1.6 \cdot 10^4 \pm 57$	166 ± 2	429 ± 33	$6.0 \cdot 10^4 \pm 101$	81.7 ± 0.2 (59.7)
Additional Precuts											
$60 < M_{H1} < 180$	112 ± 0.6	82 ± 0.3	$2.2 \cdot 10^4 \pm 39$	$1.2 \cdot 10^4 \pm 50$	5955 ± 38	549 ± 12	$1.5 \cdot 10^4 \pm 55$	160 ± 2	412 ± 3	$5.6 \cdot 10^4 \pm 93$	80.5 ± 0.2 (59.0)
$60 < M_{H2} < 180$	109 ± 0.6	79 ± 0.3	$2.0 \cdot 10^4 \pm 36$	$1.2 \cdot 10^4 \pm 49$	5765 ± 37	526 ± 12	$1.2 \cdot 10^4 \pm 47$	156 ± 2	380 ± 3	$5.2 \cdot 10^4 \pm 86$	78.9 ± 0.2 (58.4)
missing $p_T < 70$	109 ± 0.6	79 ± 0.3	$1.9 \cdot 10^4 \pm 36$	$1.2 \cdot 10^4 \pm 49$	5752 ± 37	526 ± 12	7596 ± 37	143 ± 2	337 ± 3	$4.6 \cdot 10^4 \pm 82$	77.4 ± 0.2 (58.2)
thrust < 0.9	109 ± 0.6	78 ± 0.4	6492 ± 21	$1.2 \cdot 10^4 \pm 49$	5742 ± 37	525 ± 12	7487 ± 37	143 ± 2	337 ± 3	$3.3 \cdot 10^4 \pm 76$	77.3 ± 0.2 (58.2)

Table 8.4: Preselection results for the hadron channel. The numbers correspond to an integrated luminosity of $\mathcal{L} = 2 \text{ ab}^{-1}$ and a beam polarisation of $P(e^+e^-) = (0.3, -0.8)$. The MC statistical error on the numbers of events after each selection cut are listed. The mass reconstruction is very challenging in the six-jet final state. Flavour-tag information are needed. At least four jets of an event are required to have a $btag$ larger than 0.16. These jets are paired to form the two Higgs bosons. This requirement rejects 15% of the $ZHH \rightarrow qqbbbb$ events but imposing a more loose requirement on the $btag$ degrades the mass resolution and increases the background contribution since more backgrounds pass the selection cut. Investigations have shown that this results in up to 20% degradation of the signal significance in this channel. By improving the flavour-tagging efficiency by 5% for the same purity would lead to 20% more signal events after the selection. Conclusively, after b -tag and isolated lepton requirement all other precuts are nearly 100% efficient on signal events and reduce background events by a factor of two.

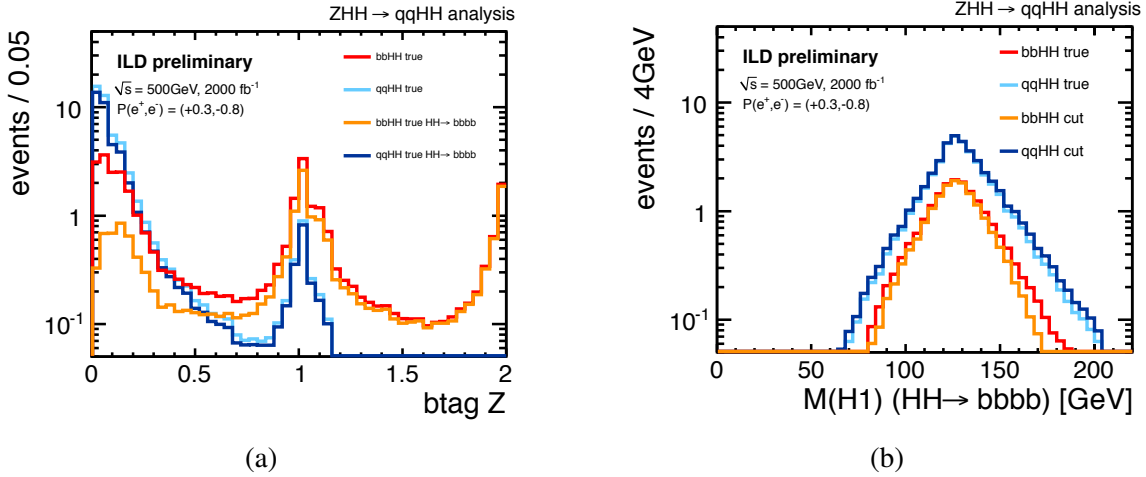


Figure 8.21: a) The combined flavour tag $b_{tag}Z$ of the two jets which are assigned to the Z -boson decay in the $qqHH$ channel. b) $M(H1)$ for $ZHH \rightarrow qqHH$. The masses of true $bbHH$ ($bbbbbb$) and $qqHH$ ($qqbbbb$) are compared to the distributions of reconstructed particles after applying the separation with $b_{tag}Z$.

Similar to the lepton channel, in the final selection all events are separated into two categories, called “ $bbHH$ dominant” and “light $qqHH$ dominant”, according to the flavour tag of the two jets from the Z -boson decay. The sum of b likelihood of the two jets which are assigned to the Z is illustrated in fig. 8.21a. The b likelihood is shown for true $bbHH$ and $qqHH$ events, as well as for true $HH \rightarrow bbbb$ events. At $b_{tag}Z \gtrsim 1.0$ the reconstructed events reproduce the true events well. At $b_{tag}Z \lesssim 1.0$ the true $bbHH$ and $bbbbbb$ events show different distributions. This is due to the jet-pairing requirement. Four jets with $b_{tag} > 0.16$ are assigned to the two Higgs bosons. The other two jets are assigned to the Z boson. Consequently, $b_{tag}Z$ is well-reproduced for Z decays into light jets, which obtain small b_{tag} values. For events with six jets with $b_{tag} > 0.16$, all permutations of possible jet pairings are tested for the three bosons. In such events the jet pairing is prone to errors due to combinatorics. Consequently, wrong jets can be assigned to the Z and the $b_{tag}Z$ at smaller values is different for $bbHH$ and $bbbbbb$ events. We have investigated that by optimising and performing the event selection without such a separation of $qqHH$, the signal significance is degraded by 10% compared to the evaluation of the two different categories. Therefore, this strategy [108] is also adapted in this study by using the threshold $b_{tag}Z > 0.54$ for “ $bbHH$ dominant” and $b_{tag}Z < 0.54$ for “light $qqHH$ dominant”. Different thresholds have been evaluated in this thesis. However, the original threshold gives the best results. This is shown in fig. 8.21b. The Higgs mass distribution of true $bbHH$ ($bbbbbb$) and $qqHH$ ($qqbbbb$) events are compared to the distributions of reconstructed particles after requiring a cut on $b_{tag}Z$. Similar to the lepton channel, the kinematic distributions look similar for both categories. Due to limited statistics, combined MVAs are trained. While the selection cut on the first MVA output ($bbbb$) should not differ for both categories, the cuts on the second ($bbqqqq$) and third ($qqbbbb$) MVA are optimised for the different categories. The signal-to-background ratio in “ $bbHH$

dominant” is better than in “light $qqHH$ dominant”, since the full-hadronic background $bbqqqq$ from tt and WWZ contribute to this category. Training separate MVAs could also enhance the signal selection. However, larger MC samples would be needed. The detailed list of input variables for training, the corresponding distributions, and the respective classifier response can be found in A.2. In the following the important aspects and optimisation steps for the three separate BDTGs are discussed. The final selection results of the two categories are listed in tab. 8.5 at the end of this section. The table also includes the errors on the number of events after each selection cut.

First BDTG: $bbbb$ vs. $qqHH$ ($qqbbbb$)

After preselection, the dominant background is $bbbb$. Enough statistics is available for BDTG training, even after having applied all foregoing selection cuts. The relative error on background and signal events is less than 1%. The collection of input variables can be found in A.2.1. A brief overview is given in the following.

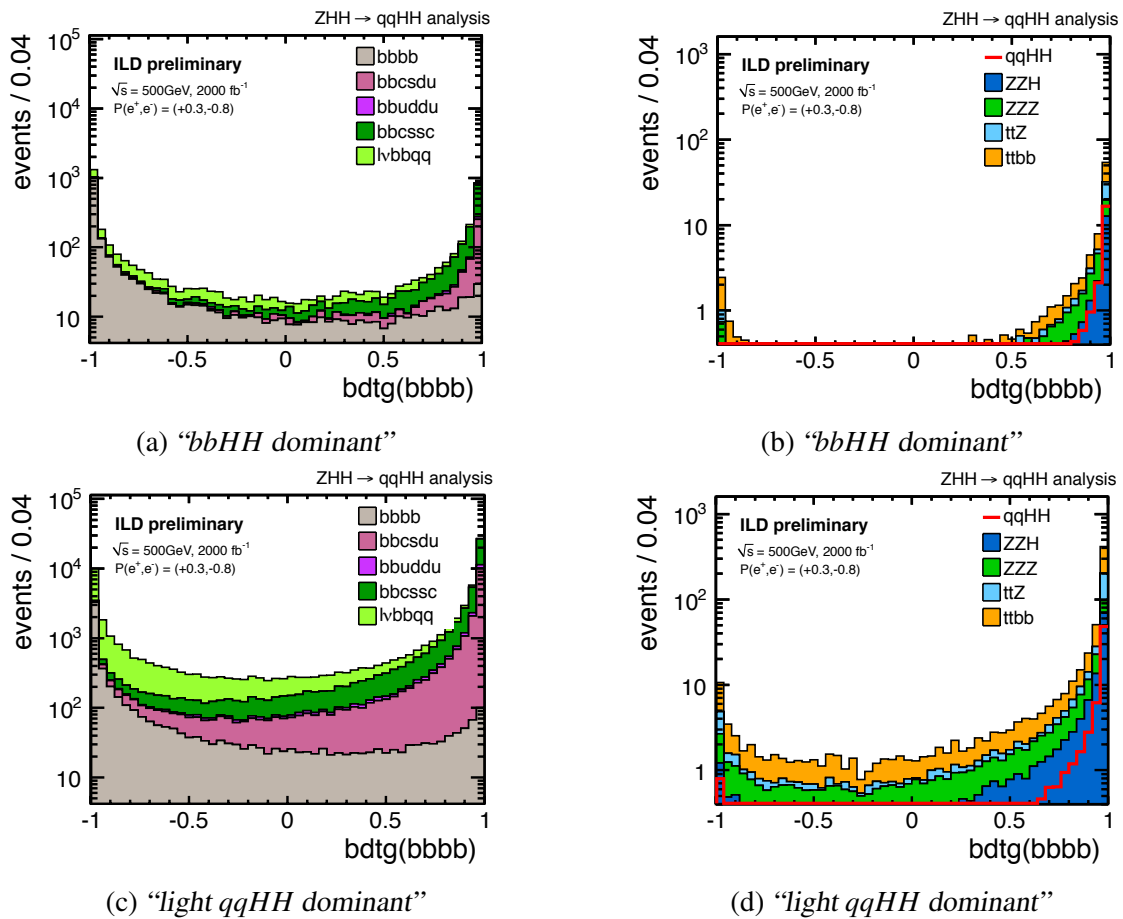


Figure 8.22: $bdtg(bbbb)$ after preselection for large backgrounds (left) and small backgrounds plus signal (right). $bdtg(bbbb) > 0.90$ is applied to the events in both categories.

Since $bbbb$ originates predominantly from ZZ , the thrust axis allows to separate signal and backgrounds. Moreover, the events are reconstructed as four-jet final states which represent the $bbbb$ background. The four jets are paired to form two Z bosons. The respective masses $M(Z1)$ and $M(Z2)$ are used as inputs, since signal events obtain much larger masses compared to the background. The largest jet momentum of the four-jet hypothesis and of the six-jet hypothesis also give overall smaller values for signal events compared to background events. Similar to the first BDTG in $llHH$, the total number of PFOs gives discriminative power, since the six-jet final state with at least four b jets has much larger multiplicities. Lastly, Durham parameters are used for various jet hypotheses. The optimal cut suggested in training reads $bdtg(bbbb) > 0.90$. This cut is taken into account in the training of the second BDTG. For signal and backgrounds $bdtg(bbbb)$ is shown in fig. 8.22 for “ $bbHH$ dominant” and “light $qqHH$ dominant”, respectively. In both categories the threshold is optimised with respect to the maximum signal significance after this cut. The optimised cut gives the same value of $bdtg(bbbb) > 0.9$ for both categories. The total background contribution is reduced by 70% in “ $bbHH$ dominant”, and by 55% in “light $qqHH$ dominant”. In both cases the signal efficiency reads 83%.

Second BDTG: $bbqqqq$ vs. $qqHH$ ($qqbbbb$)

The second dominant background after preselection are events with two b jets and four light jets in the final state. Such events are coming from ZZH , ZZZ , tt , and WWZ . The former two only give small contributions, since they have much smaller cross sections compared to tt and WWZ . tt and WWZ have very large cross sections. Even though the b -tag requirement in the preselection suppresses 97% of this background, it still gives the second largest contribution to the total background. At this stage of the analysis, the statistics is very large even after applying all foregoing cuts. While there is enough statistics to train a separate BDTG for “light $qqHH$ dominant” with a relative error of 1% on the number of background events, “ $bbHH$ dominant” requires more statistics. In total a relative error of 19% is present. The largest contribution to the relative error is given by $tt \rightarrow bbuddu$ ($\sim 18\%$). To train a separate BDTG for this category with a relative error of 1%, 40 times the MC data size is needed with respect to the expected number of events.

The discriminative power of the second and third BDTGs are very important in the event selection of $qqHH$, since they deal with six-jet final states. The entire list of input variables and the corresponding distributions can be found in A.2.2. Mass distributions play the dominant role as input parameters in training. Next to $M(H1)$ and $M(H2)$, the masses of tt (fig. 8.23a, fig. 8.23b) and the W bosons from $t \rightarrow bW$ (fig. 8.23c, fig. 8.23d) provide discrimination power. Like in the lepton channel, the two Higgs masses after kinematic fitting are highly correlated, which decreases the separation power of the classifier. The masses without fitting are used. In order to obtain the top and W masses the six jets are paired by choosing the best jet permutation with the smallest χ_{tt}^2

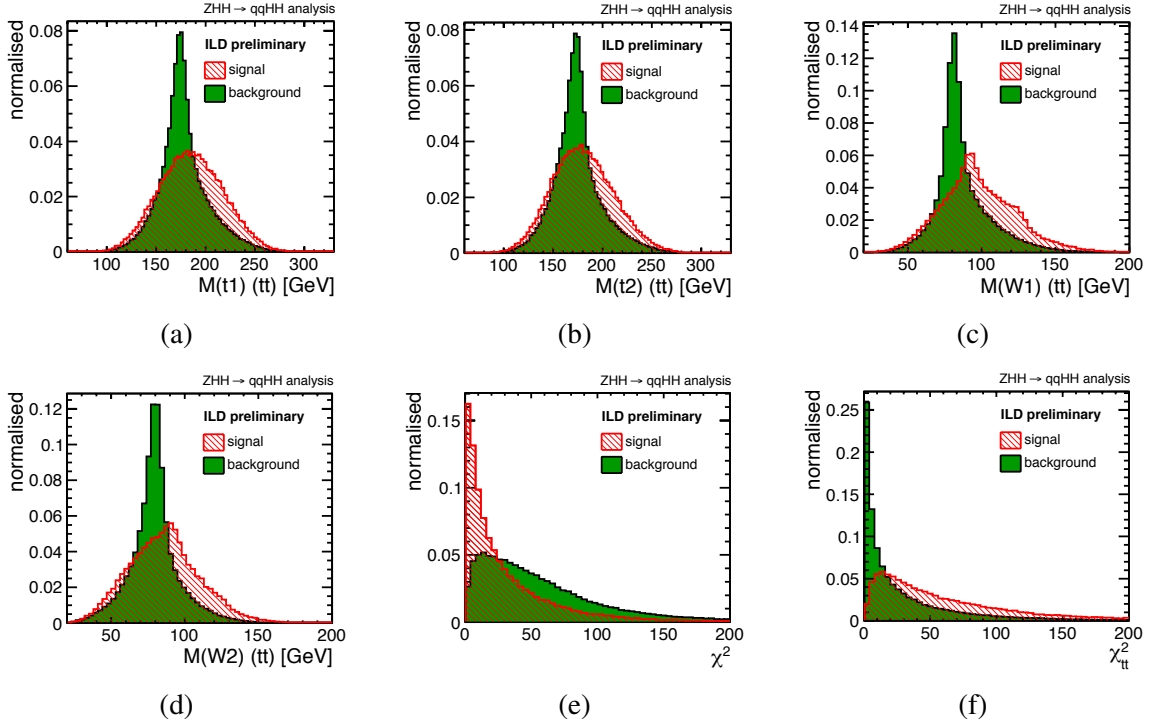


Figure 8.23: Optimised input variables for $bdtg(bbqqqq)$ training. The descriptions can be found in the text. The complete set of input variables is given in A.2.2.

$$\chi_{tt}^2 = \frac{(M(j_1 j_2) - M_W)^2}{\sigma_W^2} + \frac{(M(j_3 j_4) - M_W)^2}{\sigma_W^2} + \frac{(M(j_1 j_2 j_5) - M_t)^2}{\sigma_t^2} + \frac{(M(j_3 j_4 j_6) - M_t)^2}{\sigma_t^2}, \quad (8.1)$$

where j_5 and j_6 are the most-like b jets. $M(j_1 j_2)$ and $M(j_3 j_4)$ represent the W -boson masses ($M_W = 80.4$ GeV) and $M(j_1 j_2 j_5)$ and $M(j_3 j_4 j_6)$ the top masses ($M_t = 174$ GeV). Here, the W -mass resolution reads $\sigma_W = 4.8$ GeV and the top-mass resolution $\sigma_t = 20$ GeV. The smallest χ^2 (fig. 8.23e) from ZHH pairing and from χ_{tt}^2 (fig. 8.23f) are also used for separation.

Since tt is one of the dominant background processes in all three signal channels, investigating kinematic fits for the tt hypothesis can improve the signal and background separation. This should be performed and evaluated in the near future. In training, the respective χ^2 distributions from a kinematic fit can be less correlated to the masses without fitting. This can enhance the discriminative power of the classifier as it is the case for ZZH/Z backgrounds in the lepton channel. Investigating kinematic fits for tt events could lead to 5% relative improvement on the BDTG response.

The optimal cut value as suggested in the BDTG training reads $bdtg(bbqqqq) > 0.33$ and is considered in the training of the third BDTG. Nevertheless, this cut is again optimised for the two different categories with respect to the maximum signal significance. For “ $bbHH$ dominant” the optimised threshold reads $bdtg(bbqqqq) > 0.28$ and for “light $qqHH$ dominant” $bdtg(bbqqqq) > 0.61$ (fig. 8.24). Especially in “light $qqHH$ dominant”

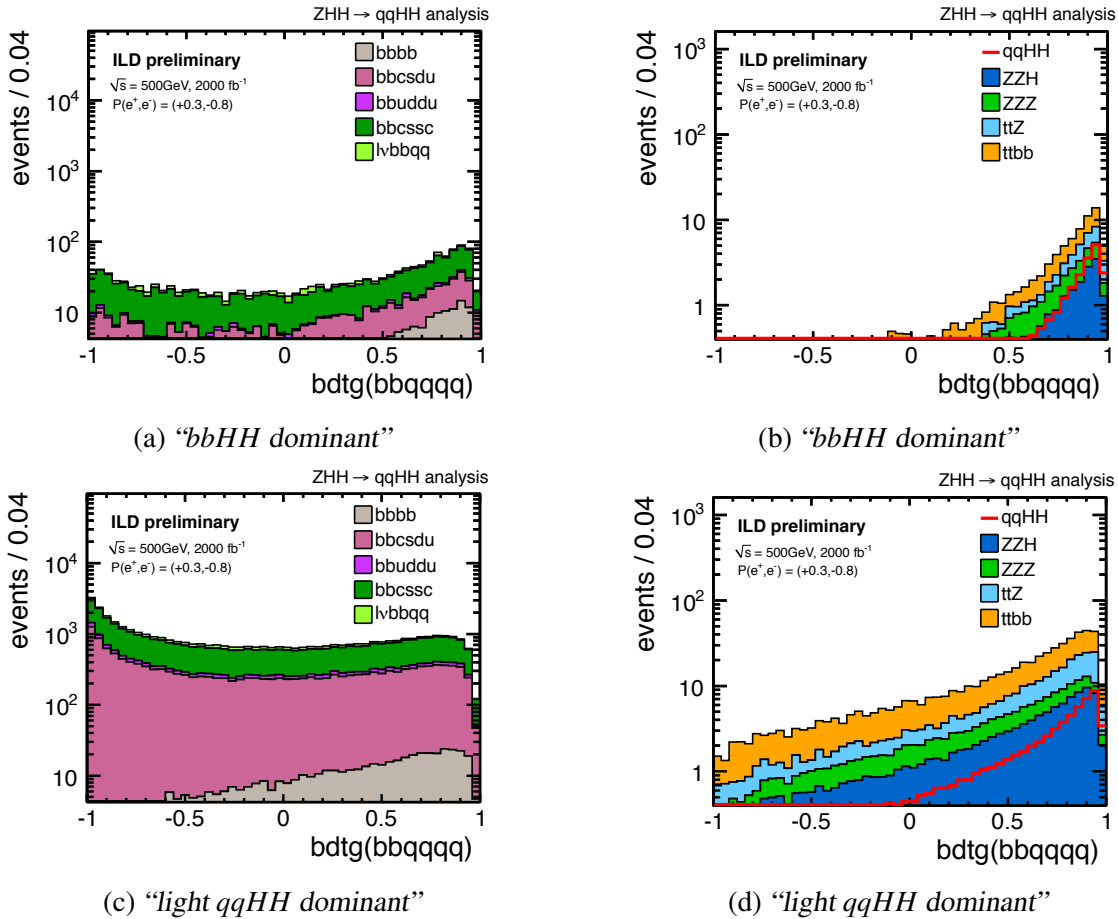


Figure 8.24: $bdtg(bbqqqq)$ after all foregoing cuts for large backgrounds (left) and small backgrounds plus signal (right). $bdtg(bbqqqq) > 0.28$ is applied to the events in “*bbHH* dominant” and $bdtg(bbqqqq) > 0.61$ to the events in “light *qqHH* dominant”.

this tight cut is important to reject the large background contribution since the signal-to-background ratio in this channel is much larger compared to “*bbHH* dominant”. In this category, the background is suppressed by $\sim 80\%$ and the signal by $\sim 30\%$.

Third BDTG: $qqbbbb$ vs. $qqHH$ ($qqbbbb$)

Like in the lepton channel a separate BDTG is trained for ZZH and ZZZ backgrounds. Despite of having rather small cross sections, these backgrounds are very difficult to suppress. At this stage of the analysis, the relative MC statistical error on the number of background events is roughly 1%. The same input variables are used as in $llHH$ and $\nu\nu HH$. The input variables and the corresponding distributions are listed in A.2.3. The kinematic fit results are evaluated in the context of this BDTG. As example the fit probabilities of the equal-mass fit are shown in fig 8.25. The semi-leptonic correction results in an enhanced fit performance with ISR consideration. Compared to the lepton channel χ^2_{ZHH} and χ^2_{ZZH} from the kinematic fit are less discriminative (fig. 8.25b). Nevertheless, next to $M(H1)$ (fig. 8.26c) and $M(H2)$ (fig. 8.26d) these variables represent the most important input

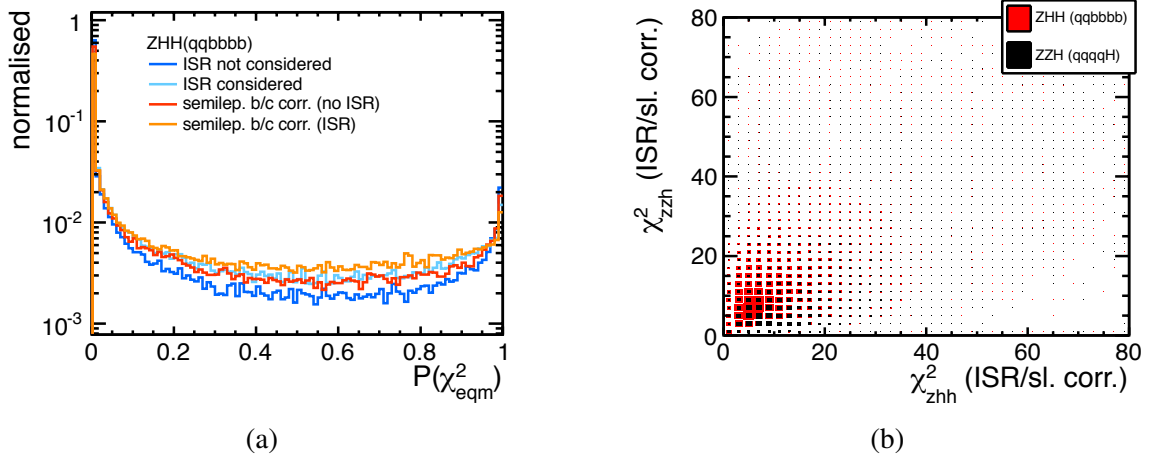


Figure 8.25: a) Fit probability for signal events in the equal-mass fit. The semi-leptonic correction with ISR treatment gives an enhanced fit performance. b) χ^2_{zzh} vs. χ^2_{zhh} scatter plot for the fit with ISR consideration and the semi-leptonic energy correction. The χ^2 distributions have less discriminative power compared to lHH .

variables in separation. As already discussed in sec. 8.1.2, the mass distributions without fitting are used to avoid large correlations between input variables which would degrade the separation power of the classifier output. As in the lepton channel, for $M(H)$ (ZZH) (fig. 8.26e) and $M(Z)$ (ZZH) (fig. 8.26f) the masses without fitting are linked to the best jet permutation obtained by the ZZH kinematic fit hypothesis. The optimal cut value for the combined BDTG is $bdtg(qqbbbb) > -0.10$. Optimising this value for both categories gives $bdtg(qqbbbb) > -0.25$ for “ $bbHH$ dominant” (fig. 8.27a) and $bdtg(qqbbbb) > 0.17$ for “light $qqHH$ dominant” (fig. 8.27a).

8.3.4 Flavour Tag Information

Similar to the previous channels the selection by BDTGs is followed by flavour-tag requirements. This is very difficult since the backgrounds include two to six b jets in the final state, as well as c jets. The discrimination between c and b flavours needs very large flavour-tagging efficiencies (sec. 4.3.1). Compared to b tagging, c tagging is limited due to the short lifetime and the low number of tracks from secondary vertices. In the flavour tagging (sec. 5.3.3) bc tagging was discarded as it showed no performance improvements.

The most discriminative flavour-tag threshold is given by the sum of the third and fourth largest b likelihood $bmax3 + bmax4$. The distributions for both categories are shown in fig. 8.28. At this stage of the analysis in “ $bbHH$ dominant” the largest contribution to the relative MC statistical error is given by $bbuddu$ (22%) and $lvbbqq$ (18%), while in “light $qqHH$ dominant” the relative errors on the number of events are below 5% for the various backgrounds. In “ $bbHH$ dominant” the optimal cut on the b tags is given by $bmax3 + bmax4 > 1.22$. This suppresses $ZZ \rightarrow bbbb$, and $bbsdu$ and $bbsc$ from tt and WWZ . Full-hadronic six-jet backgrounds from tbb and ttZ are also suppressed. In “light

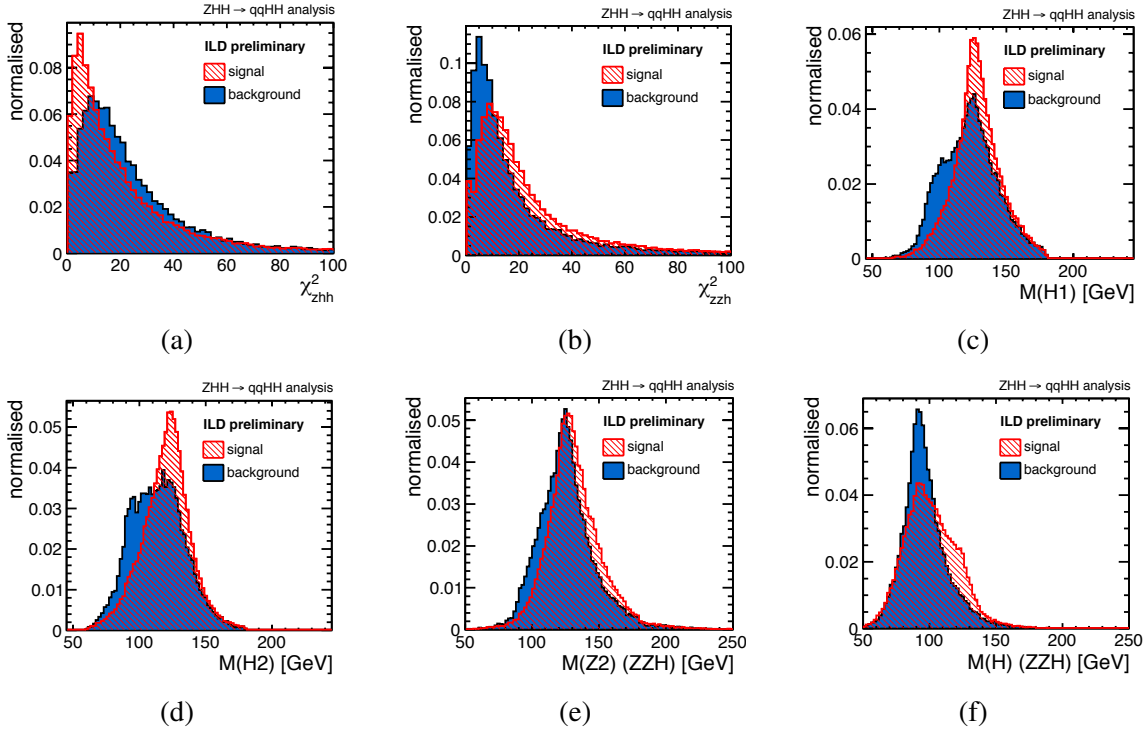


Figure 8.26: Optimised input variables for $bdtg(qqbbbb)$ training. The descriptions can be found in the text. The complete set of input variables is given in A.2.3.

$qqHH$ dominant” the optimal cut is given by $bmax3 + bmax4 > 1.18$. The requirement rejects 95% of $bbc.ssc$ and 93% of $bbc.sdu$ events, which give the largest contribution to the total background in this category. Nevertheless, only 82% of $bbuddu$ events are suppressed.

The results of the selection are listed in tab. 8.5. After having performed the basic event selection strategy 22 ± 1.3 background events and 8.5 ± 0.1 signal events pass the selection in “ $bbHH$ dominant”. 8.0 events of the signal correspond to $ZHH \rightarrow bbbbbb$. In this case a relative improvement of the b -tagging efficiency by 5% for the same purity would result in 10.2 signal events, 9.1 of which correspond to $ZHH \rightarrow bbbbbb$. This evaluation is made by scaling the efficiency for ϵ^n with $n = 4$ b jets. However, in the “ $bbHH$ dominant” channel, if ϵ^n with $n = 6$ is assumed, the number of signal events result in 12.2 events for the same purity, 10.9 of which are $ZHH \rightarrow bbbbbb$.

Opposed to this, a very large number of background events pass the selection in “light $qqHH$ dominant”. This is mainly due to the generally much larger signal-to-background ratio in this category compared to “ $bbHH$ dominant”. In total 261 ± 5.6 background events pass the selection. To reduce the large number of background events, additional cuts are evaluated. The additional cuts are applied to “light $qqHH$ dominant” only. They were tested in context of “ $bbHH$ dominant”, but no further signal and background separation was achieved. Especially, the application of additional cuts in “ $bbHH$ dominant” is questionable due to the large relative MC statistical errors at this stage of the analysis.

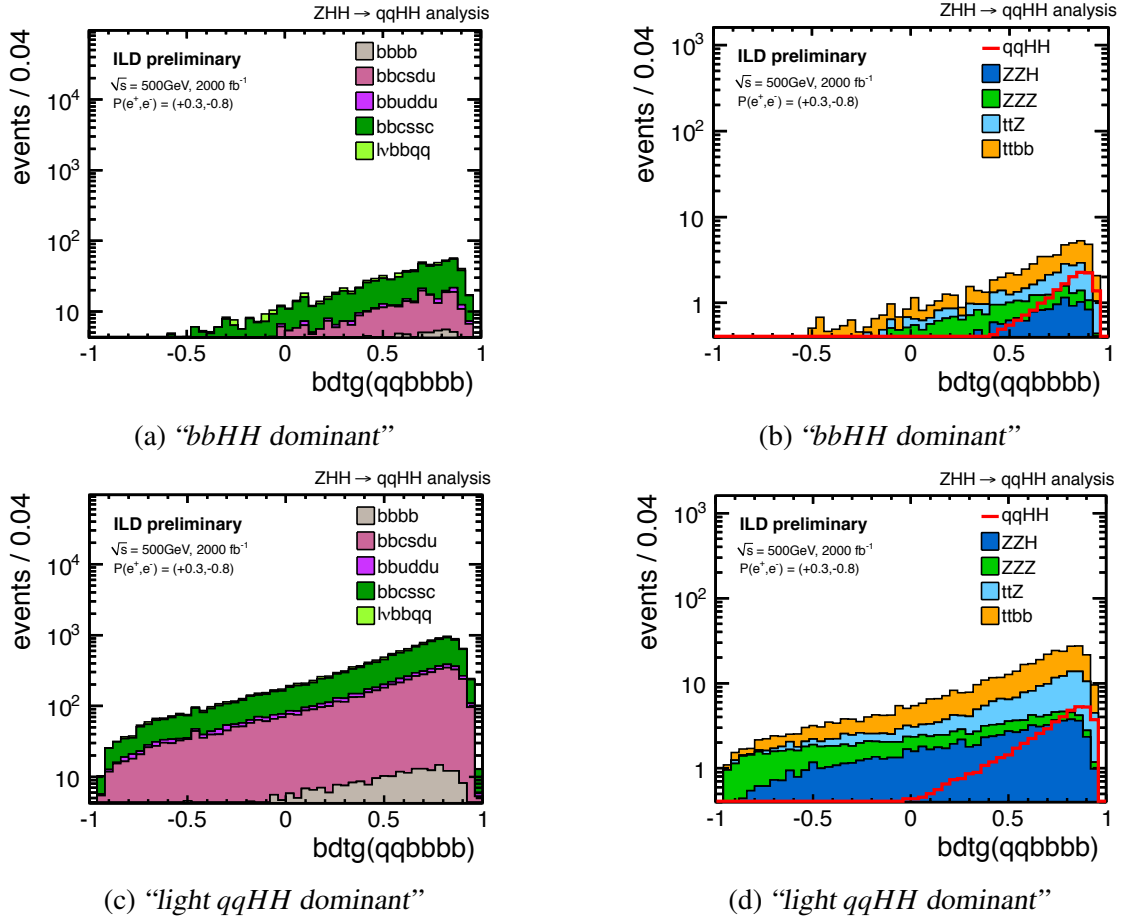


Figure 8.27: $bdtg(qqbbbb)$ after all foregoing cuts for large backgrounds (left) and small backgrounds plus signal (right). $bdtg(bbqqqq) > -0.28$ is applied to the events in “*bbHH* dominant” and $bdtg(bbqqqq) > 0.17$ to the events in “light *qqHH* dominant”.

The distributions of the selection variables can be found in A.2.4. Events are selected which have a b likeliness of $bmax3 > 0.85$, before additional cuts to the ZHH boson masses are applied to select events corresponding to the signal hypothesis. The Z -boson mass from ZHH pairing is very important in the selection of “light *qqHH* dominant”. It has not been used as input for BDTG training, since the distributions have different shapes in both categories (fig. A.11), which can be explained as follows: After having suppressed the $bbbb$ background with a cut on $bdtg(bbbb)$ the Z -mass distributions are dominated by $tt \rightarrow bbqqqq$, which obtain a large tail to smaller masses due to wrong jet pairing of tt background to form ZHH . Since “light *qqHH* dominant” includes 50 times more $bbqqqq$ events after the cut on $bdtg(bbbb)$ compared to “*bbHH* dominant”, the tail to smaller masses is very pronounced. Therefore, this variable is not used as input for $bbqqqq$ suppression. In this category, the events have to satisfy $40 \text{ GeV} < M(Z) < 110 \text{ GeV}$. This requirement suppresses $\sim 30\%$ of the total background and only $\sim 12\%$ of the signal. However, after this cut various backgrounds obtain large statistical errors, i. e. $bbcssc$ (7%), $bbcsdu$ (10%), $bbuddu$ (18%). Therefore, the results have to be taken with care in context of the following cuts on $M(H1)$ and $M(H2)$ of $90 \text{ GeV} < M(H1/2) <$

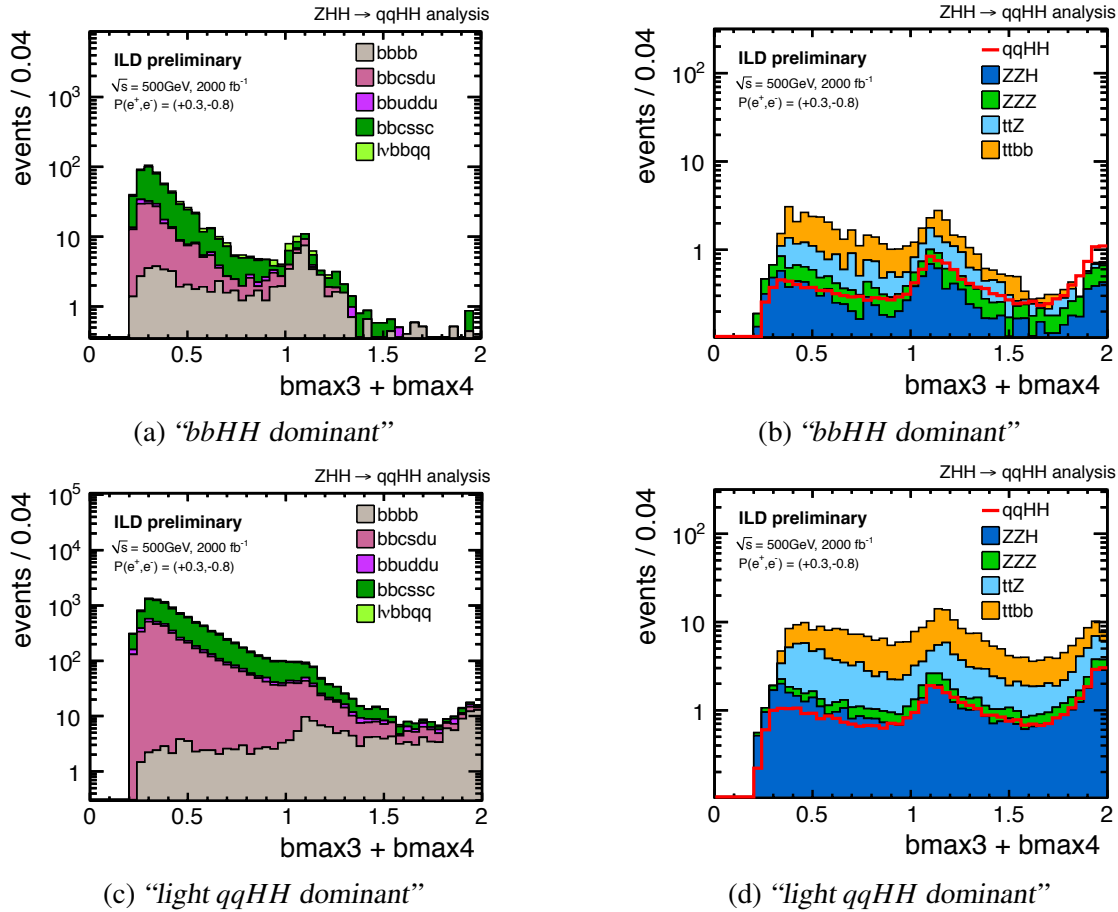


Figure 8.28: $b_{\max 3} + b_{\max 4}$ after all foregoing cuts for large backgrounds (left) and small backgrounds plus signal (right). $b_{\max 3} + b_{\max 4} > 1.22$ is applied to the events in “bbHH dominant” and $b_{\max 3} + b_{\max 4} > 1.18$ to the events in “light qqHH dominant”.

140 GeV. These allow to suppress the total background by additional 63%, while only losing 20% of the signal. Nevertheless, at this stage MC statistical fluctuations limit the realistic background suppression. The results of the hadron channel are listed in tab. 8.5. The additional cuts lead to 55 ± 2.0 background events and 12.6 ± 0.1 signal events in “light qqHH dominant”. Also in this case, by assuming 5% relative improvement in b -tag efficiencies, the number of signal events would increase by relative 20% for the same purity. Then, 15.3 signal events would pass the event selection.

8.4 Event Selection Summary

The event selection strategy was optimised and the achieved improvements of analysis techniques, i. e. isolated lepton finding, semi-leptonic energy correction, and kinematic fits, were included in the selection strategy. The results of the event selection are listed in tab. 8.6 and are discussed and summarised in the following.

	$qqqqH$	$qqbbbb$	$bbbb$	$bbscc$	$bbsdu$	$bbuddu$	$lvbbqq$	$t\bar{t}Z$	$t\bar{t}bb$	Background	$qqHH$ ($qqbbbb$)
expected events	662.6	140.5	$4.02 \cdot 10^4$	$1.56 \cdot 10^5$	$3.12 \cdot 10^5$	$1.56 \cdot 10^5$	$7.40 \cdot 10^5$	2197	2109	$1.4 \cdot 10^6$	273.1 (99)
preselection	109 ± 0.6	78 ± 0.4	6492 ± 21	$1.2 \cdot 10^4 \pm 49$	5742 ± 37	525 ± 12	7487 ± 37	143 ± 2	337 ± 3	$3.3 \cdot 10^4 \pm 76$	77.3 ± 0.2 (58.2)
$bbHH$ dominant Selection											
$btagZ > 0.54$	15 ± 0.2	14 ± 0.4	648 ± 6.8	242 ± 7	87 ± 5	11 ± 1.7	166 ± 6	16 ± 0.6	35 ± 0.9	1233 ± 12.7	18.8 ± 0.1 (16.1)
$bd\bar{t}g(bbbb) > 0.9$	11 ± 0.2	7 ± 0.1	25 ± 1.3	177 ± 6	65 ± 4	8 ± 1.5	16 ± 2	13 ± 0.6	25 ± 0.8	348 ± 7.8	15.7 ± 0.1 (13.7)
$bd\bar{t}g(bbqq) > 0.28$	10 ± 0.2	6 ± 0.1	22 ± 1.3	111 ± 5	45 ± 3	6 ± 1.2	12 ± 2	13 ± 0.6	23 ± 0.8	246 ± 6.5	14.6 ± 0.1 (13.0)
$bd\bar{t}g(qqbbb) > -0.25$	9 ± 0.2	5 ± 0.1	20 ± 1.2	105 ± 5	41 ± 3	5 ± 1.1	11 ± 2	12 ± 0.6	22 ± 0.7	231 ± 6.4	14.1 ± 0.1 (12.6)
$bmax3 + bmax4 > 1.22$	4 ± 0.1	2 ± 0.1	6 ± 0.6	4 ± 1	0	1 ± 0.3	0	2 ± 0.2	3 ± 0.3	22 ± 1.3	8.5 ± 0.1 (8.0)
Light $qqHH$ dominant Selection											
$btagZ < 0.54$	94 ± 0.6	65 ± 0.3	5845 ± 20.4	$1.2 \cdot 10^4 \pm 48$	5654 ± 37	514 ± 11.6	7321 ± 38.8	128 ± 1.8	302 ± 2.8	$3.1 \cdot 10^4 \pm 75.6$	58.5 ± 0.2 (42.1)
$bd\bar{t}g(bbbb) > 0.9$	71 ± 0.5	36 ± 0.2	208 ± 3.9	8571 ± 42	4219 ± 32	396 ± 10.2	521 ± 10.3	113 ± 1.7	244 ± 2.5	$1.4 \cdot 10^4 \pm 54.8$	48.5 ± 0.2 (36.5)
$bd\bar{t}g(bbqq) > 0.61$	42 ± 0.4	17 ± 0.2	80 ± 2.4	1599 ± 18	909 ± 15	98 ± 5.1	83 ± 4.1	71 ± 1.3	121 ± 1.8	3019 ± 24.4	32.5 ± 0.1 (25.5)
$bd\bar{t}g(qqbbb) > 0.17$	28 ± 0.3	8 ± 0.1	60 ± 2.1	1341 ± 16	746 ± 13	81 ± 4.6	70 ± 3.8	63 ± 1.3	102 ± 1.6	2499 ± 21.8	29.8 ± 0.1 (23.3)
$bmax3 + bmax4 > 1.18$	17 ± 0.2	5 ± 0.1	41 ± 1.7	57 ± 3	54 ± 4	16 ± 2.0	3 ± 0.8	27 ± 0.8	42 ± 1.0	261 ± 5.6	19.5 ± 0.1 (16.6)
$bmax3 > 0.85$	15 ± 0.2	5 ± 0.1	38 ± 1.6	36 ± 3	40 ± 3	13 ± 1.8	3 ± 0.7	24 ± 0.8	36 ± 1.0	209 ± 5.2	17.9 ± 0.1 (15.4)
$40 < M_Z < 110$	13 ± 0.2	4 ± 0.1	27 ± 1.4	27 ± 2	30 ± 3	7 ± 1.3	3 ± 0.7	15 ± 0.6	25 ± 0.8	151 ± 4.3	15.7 ± 0.1 (13.8)
$90 < M_{\pi 1} < 140$	8 ± 0.2	2 ± 0.1	16 ± 1.0	13 ± 2	17 ± 2	5 ± 1.1	2 ± 0.4	7 ± 0.5	14 ± 0.6	84 ± 3.2	13.0 ± 0.1 (11.9)
$90 < M_{\pi 2} < 140$	7 ± 0.2	2 ± 0.1	10 ± 0.8	8 ± 1	9 ± 1	4 ± 0.9	2 ± 0.4	5 ± 0.3	8 ± 0.5	55 ± 2.0	12.6 ± 0.1 (10.9)

Table 8.5: Final selection results for the hadron channel corresponding to an integrated luminosity of $\mathcal{L} = 2 \text{ ab}^{-1}$ and a beam polarisation of $P(e^+e^-) = (0.3, -0.8)$. The “ $bbHH$ dominant” and “light $qqHH$ dominant” categories are listed. Investigating one combined $qqHH$ channel degrades the event selection results by up to 20%. In “light $qqHH$ dominant” the baseline event selection strategy is not sufficient to suppress the large background contribution. Therefore, the flavour-tag requirement is followed by imposing tight cuts on preselection variables. The Z mass provides additional separation power. Relative 5% improvement of the b -tag efficiency for the same purity would give a relatively improved signal significance of 20% in both channels.

8.4.1 Signal Significance

So far a counting experiment was performed to determine the cross section of double Higgs-strahlung, in which ZHH was divided into statistically independent channels. In each channel n events are observed, which consist of signal n_s and background events n_b . The background events n_b are known, while the number of signal events n_s is unknown. These represent the new process, in this case double Higgs-strahlung, which needs to be observed to get access to information on the Higgs self-coupling. Two types of significances can be determined which indicate whether double Higgs-strahlung events can be observed in the respective signal channels. A procedure for searches with small statistics is applied, which allows the use of Poisson statistics [195].

Since n_s and n_b can be treated as independent Poisson random variables with mean s and b respectively, $n = n_s + n_b$ is also a Poisson random variable with mean $s + b$. The probability to observe n events is then given by

$$p(n; s, b) = \frac{(s + b)^n}{n!} \exp(-(s + b)). \quad (8.2)$$

Excess Significance

Typically, the question of interest is whether the observed number of events n_{obs} in data is due to statistical fluctuations of the background, assuming no signal is present. Hence this assumption (null hypothesis) represents a background-only experiment. This can be quantified by the probability (p value) that the background-only model gives statistical fluctuations equal to or exceeding the expected number of events n

$$p(n \geq n_{obs}) = \sum_{n=n_{obs}}^{\infty} p(n; s = 0, b) = 1 - \sum_{n=0}^{n_{obs}-1} \frac{b^n}{n!} \exp(-b). \quad (8.3)$$

The p value is independent of s . The “excess significance” σ_e is often defined as the number of standard deviations that a Gaussian variable would fluctuate in one direction to give the same p value

$$p(n \geq n_{obs}) = \int_{\sigma_e}^{\infty} \frac{1}{\sqrt{2\pi}} \exp(-x^2/2) dx = 1 - \Phi(\sigma_e), \quad (8.4)$$

where $\Phi(\sigma_e)$ denotes the Gaussian cumulative distribution [27]. The excess significance can be obtained with $\sigma_e = \Phi^{-1}(1 - p(n \geq n_{obs}))$. In the large statistics limit Gauss approximations give $\sigma_e = \frac{n-b}{\sqrt{b}}$ which leads to the well-known formula $\frac{s}{\sqrt{b}}$ [27].

Measurement Significance

Assuming an alternative hypothesis, in which signal and background exists, the p value of observing events equal or less than the expected number of events n is defined as in

<i>ZHH</i> channel	$s(HH \rightarrow bbbb)$	b	σ_e	σ_m
$eeHH$	3.9 ± 0.03 (2.6)	7 ± 0.6	1.29σ	1.07σ
$\mu\mu HH$	5.1 ± 0.03 (2.8)	9 ± 0.5	1.48σ	1.26σ
$\nu\nu HH$	5.6 ± 0.04 (5.5)	7 ± 1.0	1.78σ	1.50σ
$bbHH$	8.5 ± 0.10 (8.0)	22 ± 1.3	1.75σ	1.57σ
$qqHH$	12.6 ± 0.1 (10.9)	55 ± 2.0	1.65σ	1.55σ

Table 8.6: Results of the event selection corresponding to an integrated luminosity of $\mathcal{L} = 2 \text{ ab}^{-1}$ and a beam polarisation of $P(e^+e^-) = (0.3, -0.8)$. The number of signal events s , background events b , σ_e and σ_m for each signal channel are listed.

eq. 8.2. In this case the p value can also be expressed as

$$p(n \leq n_{obs}) = \sum_{n=n_{obs}}^{\infty} p(n; s, b) = \sum_{n=0}^{n_{obs}} \frac{(s+b)^n}{n!} \exp(-(s+b)). \quad (8.5)$$

The significance is determined similar to eq. 8.4 and is called ‘‘measurement significance’’ σ_m . In the large statistics limit the definition leads to the significance formula of $\frac{s}{\sqrt{s+b}}$ [27].

The combined signal excess significance is determined in the next chapter, giving indications on whether double Higgs-strahlung can be discovered or at least scientific evidence can be found with an integrated luminosity of $\mathcal{L} = 2 \text{ ab}^{-1}$ and a beam polarisation of $P(e^+e^-) = (0.3, -0.8)$ at a centre-of-mass energy of $\sqrt{s} = 500 \text{ GeV}$.

The event selection results and the corresponding measurement and excess significances in each channel are listed in tab. 8.6. The event selection results are summarised in the following. This includes a discussion of the achieved improvements in the event selection. The relative improvements, which are stated in the following, always refer to previous preliminary results of this thesis [197]. In total, σ_e and σ_m of the $llHH$ channel are improved by relative 25% in $\mu\mu HH$ and 15% in $eeHH$, respectively. In the neutrino channel an overall relative improvement of 10% is achieved, while almost 15% relative improvement is obtained in the results of the $qqHH$ category in the hadron channel. For $bbHH$ the yields are consistent with previous results.

8.4.2 Event Selection Improvements

MVA Classifier Training

Several MVA classifiers have been evaluated. The best classification is achieved with BDTGs. Compared to artificial neural nets, they provide a 10% relative improvement of the significances in the lepton channel and 5% in the neutrino channel. Decision trees are less sensitive to the amount of input variables, poorly discriminating variables and overtraining. Overtraining can result in an overestimation of the separation power between signal and backgrounds. It can be due to limited statistics in the training samples.

Due to the finite MC statistics separate BDTGs are trained for the dominant backgrounds in each signal channel. Training one BDTG for the entire background degrades the classifier performance since the strongest impact is given by the largest background process. Additionally, since the BDTGs are trained sequentially even more statistics is needed. This especially affects $bdtg(lvbbqq)$ training in the lepton channel. At this stage of the event selection, the relative MC statistical error on $evbbqq$ is 10%, on $\mu vbbqq$ 20%, and on $\tau vbbqq$ 35%. To obtain a relative statistical error of at least 5% before training, 8 times more $evbbqq$, 30 times more $\mu vbbqq$, and 180 times more $\tau vbbqq$ MC data sizes are needed with respect to the expected number of events. Moreover, in the lepton and hadron channel the events are separated into two categories. Without such a separation the respective event selection results are degraded by 10% compared to the evaluation of separated event categories. However, due to the limited statistics combined BDTGs are trained for the two categories. Training separate BDTGs for each category could enhance the event selection. However, even more statistics is required. In the hadron channel this concerns $tt \rightarrow bbqqqq$ events. At least 50 times larger MC data sizes for $bbuddu$ and 6 times for $bbcsc$ are required to obtain a relative error of 5% before BDTG training.

Isolated Lepton Selection

The isolated lepton selection strategy provides MVA variables which are used to suppress $lvbbqq$ backgrounds. The MVA variable of the second identified lepton is the most important variable in the training of $bdtg(lvbbqq)$ in the lepton channel. Moreover, the isolated lepton finder improves the background suppression by a factor of 10 for the same signal efficiency. The selection efficiency is larger than 90% for two isolated leptons in an event. Additionally, the isolated lepton strategy is used as veto in the neutrino and hadron channel. The veto efficiency is roughly 90% to find and reject events with at least one isolated lepton. However, the strategy is not optimised for τ events. Therefore, in $llHH$ only two third of the signal events pass the isolated lepton selection. Including a proper method for τ identification can be useful to select $\tau\tau HH$ signal events. Since less than 10% of τ decay leptonically, a dedicated algorithm to identify hadronic τ decays can also improve the background suppression.

By selecting $\tau\tau HH$ events in the lepton channel, the signal significance and the measurement precision on σ_{ZHH} can be improved. If similar results for $\tau\tau HH$ are achieved as in $\mu\mu HH$ and $ee HH$, this can lead to 8% relative improvement of the precision on σ_{ZHH} .

Flavour Tagging and Mass Reconstruction

Flavour tagging plays an important role in the event selection. In the lepton channel flavour-tag information can be used as optional feature to select $H \rightarrow WW, \tau\tau$ since the optimised strategy already provides a very large signal purity. The lepton channel selection can provide a foundation to select various Higgs decay modes.

In the neutrino channel, it is crucial to suppress the large amount of background events after separation using BDTGs. Before applying a flavour-tag requirement, the dominant background in this channel is $\tau\nu b b c s$, in which both the secondary vertices of the τ and the c quarks can make b tagging less effective. However, very high b -tagging efficiencies allow to reject the background by more than 99%.

In the hadron channel, flavour tagging already plays an important role in the boson mass reconstruction, by both the smallest χ^2 and the kinematic fit. $ZHH \rightarrow qqHH$ gives 45 possible combinations to form the signal bosons. Therefore, jet pairing is prone to errors due to combinatorics which can be solved by including flavour-tag information in jet pairing. This b -tag threshold is important since it already rejects large amount background events and has large impact on the mass resolution. A degradation of 20% on the signal significance in this channel is observed if 20% more soft b tags are used in jet pairing.

Moreover, improvements of the flavour-tagging efficiency would have large effects on the analysis, since the efficiency scales with the number of jets e^n . In the signal final state at least four b jets are considered. Since flavour-tag information play a crucial role in the event selection not only in the final selection but also in jet pairing of the hadron channel, optimising the b -tagging efficiencies by 5% for the same purity can enhance the significances in the neutrino channel and in the hadron channel by relative 20% and the precision on the measurement of σ_{ZHH} by relative 11%.

Kinematic Fits and Semi-leptonic Correction

The most important selection variables are invariant masses. Therefore, the impact of kinematic fits on mass resolutions have been investigated to suppress ZZH and ZZZ backgrounds. The semi-leptonic energy correction is applied to all jets in the analysis in which a lepton is found. This allows to enhance the reconstruction of final state particles, since the missing four-momentum is improved. The χ^2 distributions obtained from the fit are the most important input variables in BDTG training. By adding these variables to training the classifier response has been improved by relative 5%. In order to avoid a degradation of the separation power of these variables, the bosons masses without kinematic fitting are included in training, even though the fitted masses have better separation power. This way large correlations between input variables can be avoided, which degrade the discriminative power of the classifier. A relative improvement of 20% on the results is obtained.

One of the dominant backgrounds in all three signal channels is $t\bar{t}$. Especially in the hadron channel it is important to identify six-jet backgrounds. To identify $t\bar{t}$ backgrounds investigating kinematic fits for the $t\bar{t}$ hypothesis can improve the selection. The respective χ^2 distributions should be less correlated to the masses without fitting. This can enhance the discriminate power of the classifier as it is the case for ZZH/Z . Similar to the separation of ZZH/Z , investigating kinematic fits for $t\bar{t}$ could lead to 5% relative improvement of the BDTG response. This can improve the significance in the hadron channel by relative 5%.

Chapter 9

Analysis and Results

In this chapter, the achievable precisions for the measurement and observation of double Higgs-strahlung and the Higgs self-coupling are determined. Therefore, in sec. 9.1 the combined signal significance is calculated which indicates whether it is possible to obtain experimental evidence for the observation of double Higgs-strahlung at the ILC at $\sqrt{s} = 500$ GeV and $\mathcal{L} = 2$ ab⁻¹. Moreover, the Standard Model (SM) cross section σ_{ZHH} is determined in sec. 9.1.2 which gives information on the achievable precision on the Higgs self-coupling. In sec. 9.1.3 the achieved improvements are discussed in context of the analysis results. σ_{ZHH} is determined for various beam polarisations in sec. 9.1.4 which allows to estimate the expected measurement prospects for the full ILC running scenario in sec. 9.1.5. The results of the $\gamma\gamma$ overlay analysis are discussed in sec. 9.1.6. Finally, in sec. 9.2 the extraction of the Higgs self-coupling is outlined. Herein, the measurement prospects for the Higgs self-coupling are discussed in context of the SM and beyond the SM (BSM) physics. Finally, an outlook on additional improvements and ongoing efforts is given in sec. 9.3.

9.1 Prospects for Discovery and Measurement of Higgs-Pair Production

9.1.1 Combined Excess Significance

In the event selection ZHH is divided into statistically independent channels. For each mode, excess and measurement significances were calculated individually (tab. 8.6) using a procedure for searches with small statistics, which allows the use of Poisson statistics [195]. The determination of the combined signal significance is based on the same procedure. However, in this case a test statistic is calculated from the background-only and signal-plus-background hypotheses, which can be used to estimate how probable the observed result is with respect to the background-only hypothesis. The signal excess sig-

nificance for the combined ZHH process is determined with a standard likelihood ratio technique using Toy Monte-Carlo. The background-only experiment is simulated using Toy Monte-Carlo generated from the background-only measurement.

According to the Neyman-Pearson Lemma [186] the most powerful test statistic one can construct is the likelihood ratio of the signal-plus-background hypothesis (eq. 8.2) and the background-only hypothesis (eq. 8.3). In the respective likelihood function the different channels i are combined, which is performed as a product of their Poisson factors. The likelihood ratio reads

$$\frac{L(s+b)}{L(b)} = \prod_i \frac{(s_i + b_i)^{n_i} \exp(-(s_i + b_i))}{b_i^{n_i} \exp(-b_i)}, \quad (9.1)$$

in which the index i denotes the event selection results of each signal channel. Since usually the difference of the logarithms rather than the ratio itself is considered [27], the test statistics χ^2 reads

$$\chi^2 = -2\Delta \ln L = -2(\ln L(s+b) - \ln L(b)) = -2 \ln \left(\frac{L(s+b)}{L(b)} \right). \quad (9.2)$$

The likelihood ratio produced using a Toy Monte-Carlo is shown in fig. 9.1. χ^2 under the background-only hypothesis is shown in blue, and χ^2 under the signal-plus-background hypothesis is shown in red. The probability of the background-only hypothesis to fluctuate to the observed result in data is calculated by taking the median of the signal-plus-background hypothesis as the “observed” value. This is the maximum of the respective distribution as denoted by the black vertical line in fig. 9.1. The combined excess signif-

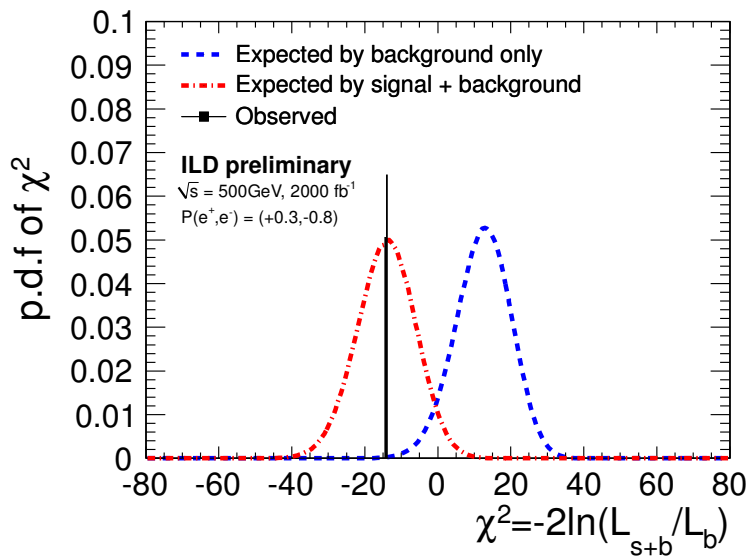


Figure 9.1: Results of the hypothesis test using the test statistic χ^2 . The blue and red lines correspond to the background-only and signal-plus-background hypothesis, respectively.

ificance of the observed value under the background-only hypothesis is $\sigma = 3.5\sigma$. Consequently, evidence to observe ZHH events at the ILC can be found for a Higgs boson with a mass of 125 GeV at 500 GeV centre-of-mass energy, using 2 ab^{-1} of data and a beam polarisation of $P(e^+e^-) = (0.3, -0.8)$.

9.1.2 Cross-section Measurement

As discussed in sec. 2.5.3, the measurement of double Higgs production provides direct access to information on the trilinear Higgs self-coupling. The ZHH cross section is directly related to the precision on the Higgs self-coupling (eq. 2.46). The cross-section measurement is performed in a parameter estimation using the standard minimum likelihood method [186]. The combined likelihood of the signal-plus-background hypothesis is defined by the product of eq. 8.2 of the signal channels i , in which only s_i is related to the cross section σ_{ZHH} as

$$s_i = N_{ZHH} \cdot BR_i \cdot \epsilon_i \cdot \sigma_i, \quad (9.3)$$

since $N_{ZHH} = \sigma_{ZHH} \cdot \mathcal{L}$, where \mathcal{L} denotes the integrated luminosity (here $\mathcal{L} = 2 \text{ ab}^{-1}$). BR_i denotes the branching ratio and ϵ_i the selection efficiency of mode i . σ_i represents the fusion contribution in channel i , which is not taken into account since it is negligible at $\sqrt{s} = 500 \text{ GeV}$. Therefore, the likelihood function contains only one unique parameter N_{ZHH} , which is determined by minimising

$$\chi^2 = -2 \ln \left(\frac{L(s+b)}{L(b)} \right). \quad (9.4)$$

This is shown in fig. 9.2. The errors on N_{ZHH} are given through $\chi_{min}^2 \pm 1$ as indicated by the horizontal line. The result reads

$$N_{ZHH} = 396.9_{-116}^{+125}. \quad (9.5)$$

Since $N_{ZHH} = \sigma_{ZHH} \cdot \mathcal{L}$, the cross-section measurement with an integrated luminosity of $\mathcal{L} = 2 \text{ ab}^{-1}$ and a beam polarisation of $P(e^+e^-) = (0.3, -0.8)$ results in

$$\sigma_{ZHH} = (0.198 \pm 0.060) \text{ fb}. \quad (9.6)$$

This corresponds to a measurement precision on the SM cross section of

$$\frac{\Delta\sigma_{ZHH}}{\sigma_{ZHH}} = 30.3\%. \quad (9.7)$$

The theoretical SM cross section for double Higgs-strahlung (sec. 5.1) reads $\sigma_{ZHH} = 0.198 \text{ fb}$ for a Higgs mass of 125 GeV and beam polarisation of $P(e^+e^-) = (0.3, -0.8)$. Assuming $\mathcal{L} = 2 \text{ ab}^{-1}$, in total 395 signal events are expected at $\sqrt{s} = 500 \text{ GeV}$. Consequently, the achieved result corresponds very well to the expected SM cross section.

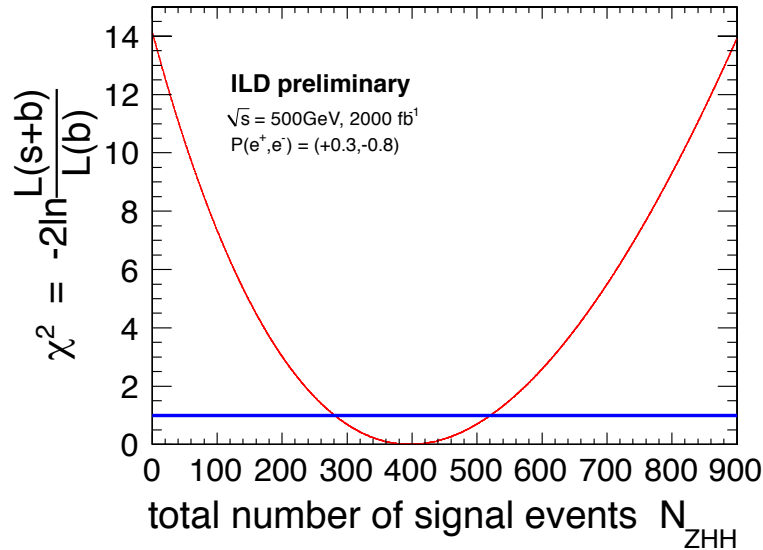


Figure 9.2: χ^2 as function of the total number of signal events N_{ZHH} , which should be consistent to $\sigma_{ZHH} \cdot \mathcal{L}$. The horizontal line represents the errors ($\chi_{min}^2 \pm 1$).

9.1.3 Effects of Analysis Improvements

The enhanced measurement prospects for double Higgs-strahlung by including the achieved improvements, which are obtained in this thesis, can be compared to

- the extrapolation of the results from the DBD full detector simulation for a Higgs boson with a mass of 120 GeV (sec. 2.5.5) [108].
- the results without taking into account the analysis improvements of the kinematic fit [196], by simply performing the basic analysis strategy for a Higgs mass of 125 GeV following [108]. The respective results already include the optimised isolated lepton strategy (sec. 6.1).

The extrapolation predicts a precision of roughly 33% on σ_{ZHH} . However, this assumption is rather optimistic since it includes only changes in the branching ratio and in σ_{ZHH} to larger Higgs masses. For $m_H = 125$ GeV the branching ratio of $BR(H \rightarrow bb)$ drops by relative 14% and σ_{ZHH} is 15% smaller compared to $m_H = 120$ GeV. The effects of changes in kinematic distributions are not taken into account. At $\sqrt{s} = 500$ GeV the ZHH events are produced near the kinematic threshold. Compared to $m_H = 120$ GeV, the jets are even less boosted and have significant overlap with each other. Besides the rather small cross section and the four-jet or six-jet final states, this poses large challenges on jet-clustering and flavour-tagging techniques. At $\sqrt{s} = 500$ GeV, the precision on σ_{ZHH} is significantly limited by jet-finding ambiguities rather than jet-energy resolution.

Despite of being rather optimistic, the extrapolation results are confirmed by preliminary results of this analysis, which only include improvements from isolated lepton find-

ing [196, 197]. A precision of 33% on σ_{ZHH} is achieved. By applying the improved analysis technique of kinematic fitting to the analysis and by optimising the event selection strategy, i. e. using BDTGs instead of MLPs, the result is enhanced to a precision of 30% on σ_{ZHH} , which corresponds to a 10% relative improvement. Consequently, the results of this thesis exceed the expected precision obtained from the rather optimistic extrapolations of former analysis results.

Even though a very large improvement was achieved in the lepton and neutrino channel, the results of the hadron channel dominate the accuracy of this measurement since it gives the largest contribution of events to the ZHH process. At $\sqrt{s} = 500$ GeV, the six-jet final state is dominated by jet-finding ambiguities. Further optimisations with respect to jet clustering and jet pairing are important. Moreover, since flavour-tag information play a crucial role in the event selection of this channel, not only in the final selection but also in jet pairing (sec. 8.3), optimising the b -tagging efficiencies by 5% for the same purity can enhance the precision on σ_{ZHH} by relative 11% to 27.2%. The result can also be enhanced by selecting $\tau\tau HH$ events in the lepton channel of ZHH . Assuming similar results for $\tau\tau HH$ as they are achieved in $\mu\mu HH$ and $ee HH$ can lead to 8% relative improvement. Then, σ_{ZHH} can be measured to a precision of 27.9%. By including both aspects to the ZHH analysis this would result in a total 19% relative improvement and would lead to a measurement precision of 25.5% on the double Higgs-strahlung cross section assuming an integrated luminosity of $\mathcal{L} = 2 \text{ ab}^{-1}$ and a beam polarisation of $P(e^+e^-) = (0.3, -0.8)$. This would correspond to a combined signal significance larger than 4σ .

9.1.4 Effect of different Beam Polarisations

The results of the SM cross-section measurement are estimated for various beam polarisations. The Higgs self-coupling analysis is performed with different polarisation weights (sec. 5.1). The respective results are based on the optimised selection cuts in the event selection for $P(e^+e^-) = (0.3, -0.8)$ which were discussed in chapter 8. The selection cuts have not been optimised individually for each beam polarisation. In tab. 9.1 the results for the different beam polarisations are listed, each of which corresponds to an integrated luminosity of $\mathcal{L} = 2 \text{ ab}^{-1}$. The electron beam polarisation is always taken as constant with $|P(e^-)| = 0.8$, while $|P(e^+)|$ is either increased from the ILC baseline polarisation of $|P(e^+)| = 0.3$ to $|P(e^+)| = 0.6$ or decreased to $|P(e^+)| = 0.0$.

In case of reversed polarisation signs, the results differ only by relative 3% in the precision on the σ_{ZHH} measurement. However, the combined significance is enhanced by on average 20% for $P(e^-) = +0.8$ configurations. This is expected, since for polarisation states with $P(e^-) = +0.8$ the relative cross section of backgrounds with a W boson, i. e. WWZ , are smaller compared to polarisation configurations with $P(e^-) = -0.8$, since the W boson cannot couple to right-handed electrons or left-handed positrons in the SM. Moreover, the Z -boson coupling does also depend on the weak isospin. Thus, the cross section of the signal and background processes including a Z boson, i. e. ZZH , are also reduced. Hence,

$P(e^+, e^-)$	ZHH channel	s ($HH \rightarrow bbbb$)	b	σ_e	σ_m
(0.3, -0.8)	$eeHH$	3.9 (2.6)	7.0	1.29σ	1.07σ
	$\mu\mu HH$	5.1 (2.8)	8.9	1.48σ	1.26σ
	$\nu\nu HH$	5.6 (5.5)	6.9	1.78σ	1.50σ
	$bbHH$	8.5 (8.0)	21.9	1.75σ	1.57σ
	$qqHH$	12.6 (10.9)	55.0	1.65σ	1.55σ
combined excess significance					3.5σ
measurement precision on σ_{ZHH}					30.3%
(-0.3, 0.8)	$eeHH$	2.9 (1.9)	4.2	1.18σ	0.92σ
	$\mu\mu HH$	3.8 (2.0)	5.3	1.37σ	1.10σ
	$\nu\nu HH$	3.6 (3.5)	1.1	2.72σ	1.54σ
	$bbHH$	5.9 (5.6)	7.0	1.89σ	1.58σ
	$qqHH$	8.3 (7.8)	16.0	1.85σ	1.64σ
combined excess significance					4.8σ
measurement precision on σ_{ZHH}					29.4%
(0.0, -0.8)	$eeHH$	3.1 (2.1)	5.6	1.08σ	0.86σ
	$\mu\mu HH$	4.2 (2.2)	7.6	1.30σ	1.08σ
	$\nu\nu HH$	4.5 (4.4)	5.6	1.59σ	1.28σ
	$bbHH$	6.7 (6.3)	17.0	1.45σ	1.30σ
	$qqHH$	9.6 (8.8)	43.1	1.38σ	1.27σ
combined excess significance					3.5σ
measurement precision on σ_{ZHH}					34.7%
(0.0, 0.8)	$eeHH$	2.3 (1.6)	3.5	0.96σ	0.70σ
	$\mu\mu HH$	3.1 (1.6)	4.4	1.19σ	0.93σ
	$\nu\nu HH$	3.1 (3.0)	1.2	1.94σ	1.30σ
	$bbHH$	4.7 (4.4)	6.1	1.59σ	1.32σ
	$qqHH$	7.1 (6.5)	15.1	1.63σ	1.44σ
combined excess significance					4.2σ
measurement precision on σ_{ZHH}					33.7%
(0.6, -0.8)	$eeHH$	4.7 (3.1)	8.5	1.39σ	1.17σ
	$\mu\mu HH$	6.3 (3.4)	11.7	1.62σ	1.40σ
	$\nu\nu HH$	6.8 (6.7)	8.9	1.95σ	1.67σ
	$bbHH$	10.2 (9.7)	26.6	1.81σ	1.64σ
	$qqHH$	14.1 (13.0)	69.6	1.60σ	1.52σ
combined excess significance					4.2σ
measurement precision on σ_{ZHH}					28.7%
(-0.6, 0.8)	$eeHH$	3.4 (2.2)	4.9	1.26σ	1.01σ
	$\mu\mu HH$	4.3 (2.3)	6.1	1.45σ	1.20σ
	$\nu\nu HH$	4.3 (4.2)	1.1	2.68σ	1.81σ
	$bbHH$	6.5 (6.2)	7.5	2.03σ	1.68σ
	$qqHH$	9.7 (8.8)	18.9	2.00σ	1.79σ
combined excess significance					5.5σ
measurement precision on σ_{ZHH}					27.8%

Table 9.1: Results for different beam polarisations. The number of signal events s , the number of background events b , and the excess σ_e and measurement σ_m significance for each signal channel are listed, as well as the combined signal significance and the achieved precision on σ_{ZHH} . The results for each beam polarisation correspond to an integrated luminosity of $\mathcal{L} = 2 \text{ ab}^{-1}$.

the background contamination is much smaller for polarisations with $P(e^-) = +0.8$. Increasing $|P(e^+)|$ results in a relative improvement of roughly 6% of the precision on σ_{ZHH} and the combined signal excess significance. Decreasing $|P(e^+)|$ degrades the precision on σ_{ZHH} and the signal significance by relative 15%. This is not the case with respect to the signal significance of $P(e^+e^-) = (0.3, -0.8)$. The event selection is optimised for this polarisation in contrast to the other results. Optimising the selection for the other polarisation states, i. e. BDTG training with the correct polarisation weights, could lead to even better results.

9.1.5 Prospects for the Full ILC Running Scenario at 500 GeV

In the preferred ILC running scenario (sec. 3.3) a total integrated luminosity of 4 ab^{-1} is planned to be collected at 500 GeV. Data taking is proposed to be shared between the two opposite-sign helicity configurations of the foreseen beam polarisations of $|P(e^-)| = 0.8$ and $|P(e^+)| = 0.3$. Therefore, by combining the results of the respective reversed-sign polarisation states, a measurement precision on σ_{ZHH} of 21.1% and a combined signal significance of 5.94σ is achieved, which indicates a large discovery potential for double Higgs-strahlung at the ILC after the full running scenario. The measurement prospects for $|P(e^+)| = 0.6$ even lead to a measurement precision on σ_{ZHH} of 19.9% and to a combined signal significance of 6.92σ .

For a Higgs mass of 125 GeV the second most dominant Higgs decay mode is $H \rightarrow WW$. Next to this thesis using $HH \rightarrow bbbb$, the Higgs self-coupling analysis at $\sqrt{s} = 500 \text{ GeV}$ is performed for ZHH events with the final state $HH \rightarrow bbWW$ [125]. By combining both channels, additional 20% relative improvement of the precision on σ_{ZHH} can be achieved. This results in a precision of 16.8% on σ_{ZHH} after the full ILC running scenario and corresponds to a roughly 8σ discovery for the observation of double Higgs-strahlung, which establishes a non-zero Higgs self-coupling in the SM.

9.1.6 Effect of Overlay

The effect of the $\gamma\gamma$ overlay on the measurement has not been studied so far in previous Higgs self-coupling analyses and provides a significant hint on whether the DBD overlay removal (sec. 5.3.2) works satisfactory or whether more advanced strategies are needed. For DBD benchmark analyses [130] the $\gamma\gamma$ -overlay removal strategy did not have large impact on the measurement results.

The removal strategy has been optimised for this analysis, as discussed in sec. 6.2. The results of the analysis with $\gamma\gamma$ overlay are given in tab. 9.2 corresponding to an integrated luminosity of $\mathcal{L} = 2 \text{ ab}^{-1}$ and a beam polarisation of $P(e^+e^-) = (0.3, -0.8)$. A combined signal significance of 3.4σ is achieved. The precision on the SM cross section σ_{ZHH} reads 35.8%. Hence, the $\gamma\gamma$ overlay leads to a relative degradation of $\sim 15\%$ compared to the results without overlay. However, one should keep in mind that this degradation refers

ZHH channel	$s (HH \rightarrow bbbb)$	b	σ_e	σ_m
$eeHH$	$3.5 \pm 0.02 (2.4)$	10 ± 0.8	1.10σ	0.93σ
$\mu\mu HH$	$3.9 \pm 0.03 (2.5)$	7 ± 0.4	1.29σ	1.07σ
$\nu\nu HH$	$5.2 \pm 0.04 (5.1)$	8 ± 1.0	1.57σ	1.34σ
$bbHH$	$8.5 \pm 0.06 (8.0)$	23 ± 1.4	1.61σ	1.46σ
$qqHH$	$6.8 \pm 0.06 (6.1)$	33 ± 1.8	1.13σ	1.03σ
combined excess significance				3.4σ

Table 9.2: Results of the event selection corresponding to an integrated luminosity of $\mathcal{L} = 2 \text{ ab}^{-1}$ and a beam polarisation of $P(e^+e^-) = (0.3, -0.8)$. The $\gamma\gamma$ overlay is added in the simulation and the standard DBD overlay removal is applied in the analysis. Signal s and background events b , σ_e and σ_m for each signal channel are listed.

to only small changes in the number of events after the selection. Moreover, the results are rather pessimistic since at the time of MC production an overestimated number of $\langle N \rangle = 1.7$ background events was statistically laid over the simulated events per bunch crossing, instead of the expected $\langle N \rangle = 1.2$ at 500 GeV. Nevertheless, the observation indicates that the DBD overlay removal using the exclusive k_t jet clustering algorithm is not sufficient for this analysis and that more advanced techniques need to be developed.

Next to the rather small cross section, the ZHH events result in four-jet or six-jet final states, since for the investigated Higgs mass of 125 GeV the decay channel $H \rightarrow bb$ is dominant. The jets are hardly boosted and have significant overlap with each other, since the events are produced near the kinematic threshold at $\sqrt{s} = 500 \text{ GeV}$. In the exclusive k_t clustering algorithm particles are clustered into hard-interaction jets and additional very forward beam jets (sec. 5.3.2). The particles in the beam jets are removed from the reconstructed particle list to recover the bare events without overlay. Hence, in case of the less boosted and rather overlapping jets from ZHH , reconstructed particles other than overlaid background events are removed from the particle list and falsify the event properties. More sophisticated tools are required which include a detailed modelling of the background and exploit the full power of high-granularity detectors. Since the respective investigations are ongoing (sec. 9.3) we focus on the results without overlay.

9.2 Determination of the Higgs Self-coupling

9.2.1 Extracting λ_{SM} at 500 GeV

The measurement of double Higgs production provides direct access to information on the trilinear Higgs self-coupling. The precision on σ_{ZHH} is directly related to the precision on the Higgs self-coupling (eq. 2.46). The sensitivity of double Higgs production processes to λ was discussed in detail in sec. 2.5.3. In the SM the relation of the measurement

precision on σ_{ZHH} and λ for double Higgs-strahlung reads (eq. 2.47)

$$\frac{\Delta\lambda}{\lambda} = 1.62 \cdot \frac{\Delta\sigma}{\sigma}, \quad (9.8)$$

for a Higgs boson mass of 125 GeV and a centre-of-mass energy of $\sqrt{s} = 500$ GeV. This factor is based on the event-weighting method, which was introduced in sec. 2.5.3. Without weighting the sensitivity factor reads 1.73 for double Higgs-strahlung in the SM. The precision of 30% on the SM ZHH cross section leads to a precision of 49% on λ_{SM} , assuming $\mathcal{L} = 2 \text{ ab}^{-1}$ and $P(e^+e^-) = (0.3, -0.8)$. The combined measurements for the two reversed-sign polarisation states of $|P(e^-)| = 0.8$ and $|P(e^+)| = 0.3$, each of which corresponds to $\mathcal{L} = 2 \text{ ab}^{-1}$, achieve a precision of 34% on λ_{SM} .

After the full ILC running scenario (sec. 3.3) at 500 GeV and with a total integrated luminosity of 4 ab^{-1} , the ILC provides a measurement precision of 16.8% on σ_{ZHH} which leads to a precision of 26.6% on λ_{SM} . The achieved precision corresponds to an evidence larger than 3σ for the existence of λ_{SM} . The results are based on the combination of the dominant channels $HH \rightarrow bbbb$ and $HH \rightarrow bbWW$. Extrapolating these results in view of the anticipated 19% relative improvement due to $\tau\tau HH$ and 5% enhanced flavour-tag efficiencies, this would result in a measurement precision of 21.5% on λ_{SM} .

9.2.2 Prospects for λ_{SM} after Energy Upgrade

An energy upgrade to $\sqrt{s} = 1$ TeV should also be considered. At this energy, the WW -fusion production becomes accessible (sec. 2.3.1). The WW -fusion process is also studied and updated for $m_H = 125$ GeV for $HH \rightarrow bbbb$ and $HH \rightarrow bbWW$ in detailed full detector simulations for $\sqrt{s} = 1$ TeV, respectively [197]. Combining the respective results leads to a measurement precision of 16% on λ_{SM} , assuming $\mathcal{L} = 2 \text{ ab}^{-1}$. Moreover, the Higgs self-coupling precision can reach 10% in case of $\mathcal{L} = 5 \text{ ab}^{-1}$ [135]. The discussed Higgs self-coupling projections take into account the expected relative improvement due to the enhanced analysis techniques. The results are based on the analyses without $\gamma\gamma$ overlay since the efforts of modelling and understanding the $\gamma\gamma$ overlay are ongoing [198].

9.2.3 Measurement Prospects for $\lambda \neq \lambda_{SM}$ at the ILC

So far, the results are based on the assumption of a solely SM theory. However, λ is one of the most important discriminative quantities to reveal new physics (sec. 2.5.2). In various extended Higgs sectors, λ can deviate by significantly more than a few percent from SM predictions. In such cases, next to large deviations from the SM prediction, it is also possible to measure λ with much better precision. This is due to the complementary behaviour of WW -fusion and ZHH cross sections in their sensitivity to new physics with respect to changes in λ , which results from the sign of the interference terms of the additional diagrams in the respective final states (sec. 2.5.3). New physics can give sizeable

enhancements to the double Higgs production cross sections, which can be directly observed in the cross-section measurement. For each production mechanism, extrapolated measurement precisions on the Higgs self-coupling are illustrated in fig. 9.3 as a function of λ/λ_{SM} for $\mathcal{L} = 4 \text{ ab}^{-1}$. The extrapolation is based on the λ_{SM} results of this thesis for a Higgs mass of $m_H = 125 \text{ GeV}$ before implementing the achieved analysis improvements. The results are combined with the results of the channel $HH \rightarrow bbWW$ [125], which leads to additional 20% relative improvement. The changes in the cross sections with respect to λ are shown in fig. 2.25 (sec. 2.5.3).

As an example and without focussing on a particular BSM model, if $\lambda = 2\lambda_{SM}$ (fig. 9.3a) the Higgs self-coupling can already be measured to very high precision at the ILC at 500 GeV with ZHH , while at 1 TeV WW fusion would not give sufficient precision especially in the region of $1.25 < \lambda/\lambda_{SM} < 1.75$. In the $\lambda = 2\lambda_{SM}$ scenario, the sensitivity factor for ZHH would improve from 1.73 to approximately 1.08 without weighting method, and from 1.62 to roughly 1.02 with weighting method [111], since for $\lambda > \lambda_{SM}$ the Higgs self-coupling and interference diagrams become more dominant than the additional diagrams in the ZHH final state. Assuming a total integrated luminosity of 4 ab^{-1} and a beam polarisation of $P(e^+e^-) = (0.3, -0.8)$, which is reasonable according to the ILC running scenario (sec. 3.3), σ_{ZHH} is enhanced by 60% compared to the SM. This leads to a measurement precision of 14% on λ which represents a 7σ discovery and 3σ deviation from the SM value [111]. Including the analysis improvements to the extrapolation leads to a measurement precision of 13% on λ at $\sqrt{s} = 500 \text{ GeV}$. The same precision can be achieved in case of $\lambda = 0.5\lambda_{SM}$ with WW fusion at $\sqrt{s} = 1 \text{ TeV}$ using 5 ab^{-1} (fig. 9.3b).

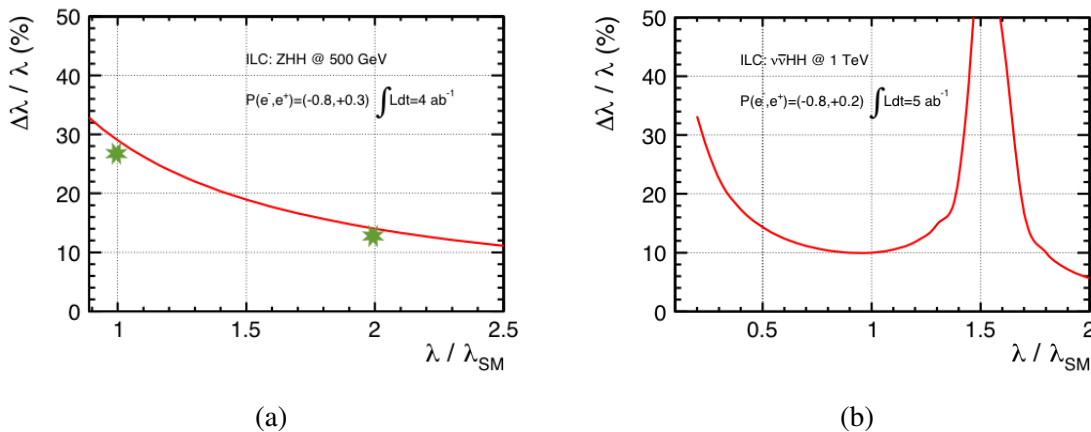


Figure 9.3: Extrapolated accuracies of λ , combined with the results of the channel $HH \rightarrow bbWW$ [125] as function of λ/λ_{SM} . The figures are based on the results of the full detector simulation for a Higgs mass of $m_H = 125 \text{ GeV}$ before implementing the achieved analysis improvements. a) for ZHH at $\sqrt{s} = 500 \text{ GeV}$. The improvements of this analysis are indicated as green stars. For $\lambda > \lambda_{SM}$, the Higgs self-coupling can be measured to high precision with ZHH already at 500 GeV. b) for WW fusion at $\sqrt{s} = 1 \text{ TeV}$. For $\lambda < \lambda_{SM}$, the Higgs self-coupling can be measured very precisely with WW fusion, which requires high energies. Figures are modified and taken from [111].

Models of electroweak baryogenesis in the 2HDM (sec. 2.5) expect minimal deviations of 20% from SM predictions. In the parameter region of the 2HDM in which electroweak baryogenesis is possible, λ could even be twice as large as in the SM. The latter corresponds to the example for $\lambda > \lambda_{SM}$ which was discussed in the foregoing. In scenarios with electroweak baryogenesis the expected deviation in the Higgs self-coupling from the SM value results in a larger cross section for double Higgs-strahlung and in a smaller cross section for the WW-fusion process. Thus, scenarios with electroweak baryogenesis are possible to be observed to a very high precision with double Higgs-strahlung at a centre-of-mass energy of $\sqrt{s} = 500$ GeV at the ILC.

As a result, the observation of double Higgs production and the Higgs self-coupling are possible at the ILC. The results of this analysis show that it is possible to observe double Higgs production and obtain scientific evidence of the existence of the SM Higgs self-coupling. With regard to new physics models, which predict deviations from λ_{SM} , the ILC provides great discovery potential already at an energy of $\sqrt{s} = 500$ GeV.

9.3 Outlook on further Ideas for Improvement

The expected precision on λ_{SM} obtained from the measurement of σ_{ZH} is illustrated in fig. 9.4 as a function of the centre-of-mass energy \sqrt{s} . The results correspond to the preferred ILC full running scenario (sec. 3.3). A total integrated luminosity of $\mathcal{L} = 4 \text{ ab}^{-1}$ is assumed, which is reasonable according to the ILC running scenario. During data taking, the beam polarisations of $P(e^+e^-) = (\pm 0.3, \mp 0.8)$ are considered. The red distribution indicates the theoretical precision by assuming 100% signal efficiency and no background. The blue distribution illustrates the realistic precision obtained from full-simulation studies based on the λ_{SM} results of this thesis for a Higgs mass of $m_H = 125$ GeV before implementing the achieved analysis improvements. The results are combined with the channel $HH \rightarrow bbWW$ [199]. The achieved improvements of this thesis are indicated by the green star. At $\sqrt{s} = 500$ GeV the perfect analysis gives 6% precision on λ_{SM} . The previous full simulation results led to a precision on λ_{SM} of 30%. The improvements achieved in this thesis result in a precision of 26% on λ_{SM} for the full ILC running scenario (green star). The gap between the perfect scenario without background and 100% signal efficiency and the results obtained in this thesis indicates possible room for further improvements [200]. There are a lot of efforts ongoing in detector optimisation and event reconstruction. The Higgs self-coupling analysis is very complex and could benefit from any improvement. Several ongoing investigations are briefly discussed in the following.

Matrix Element Method

The sensitivity of double Higgs production cross sections to the Higgs self-coupling is degraded by additional diagrams, which do not include the Higgs self-coupling vertex (sec. 2.5.3). For double Higgs-strahlung the sensitivity factor reads 1.62 with weighting

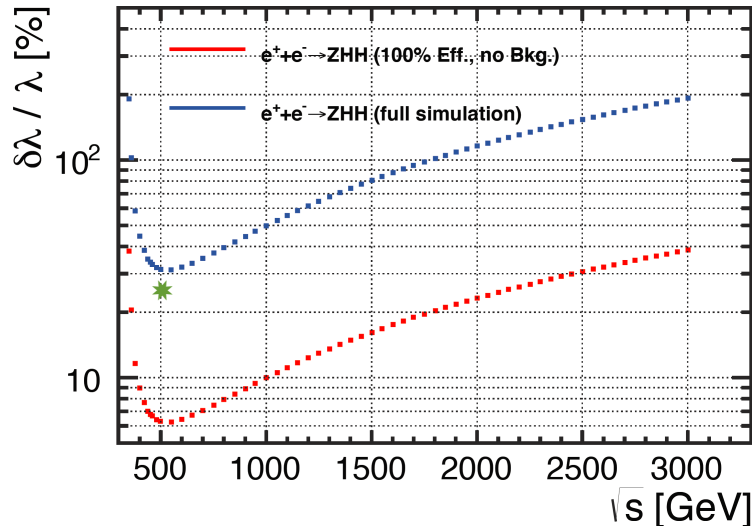


Figure 9.4: Accuracies of λ_{SM} for a Higgs mass of 125 GeV as function of the centre-of-mass energy \sqrt{s} . The results correspond to the preferred ILC full running scenario. A total integrated luminosity of $\mathcal{L} = 4 \text{ ab}^{-1}$ is considered, which is reasonable according to the preferred ILC running scenario. A beam polarisation of $P(e^+e^-) = (0.3, -0.8)$ is considered. The improvements achieved in this thesis result in a relative 10% improvement and lead to a precision on λ_{SM} of 26% for the full ILC running scenario (green star). A perfect scenario without background and 100% signal efficiency indicates the potential for further improvements (red line). Figure is modified and taken from [200].

at 500 GeV. Without the degrading effects of the additional diagrams the sensitivity factor would read 0.5. In this case, the achieved measurement precision of 30% on the SM cross section σ_{ZHH} would lead to a precision of 15% on λ_{SM} for an integrated luminosity of $\mathcal{L} = 2 \text{ ab}^{-1}$ and $P(e^+e^-) = (0.3, -0.8)$. With respect to the full ILC running scenario this would lead to a precision of 10.6% on λ_{SM} for $HH \rightarrow bbbb$ and even of 8.6% in combination with the channel $HH \rightarrow bbWW$. Therefore, a significant improvement of the measurement precision on λ_{SM} can be reached by optimising the analysis strategy for the Higgs self-coupling diagram instead of ZHH in general. One possibility is given by the application of the so-called matrix element method. A matrix element tool [201,202] was developed within `Marlin`, which provides libraries to calculate matrix elements for specific channels. For calculation only the four-momenta of the final state particles are required. The libraries include the amplitudes of the additional diagrams of ZHH . The corresponding matrix element can be used to weight the results with respect to the Higgs self-coupling diagram. This would allow to optimise the analysis strategy for the Higgs self-coupling diagram only instead of ZHH and could minimise the degrading effects of the additional amplitudes.

Moreover, the matrix element tool provides the amplitude calculation of several background processes. According to the Neyman-Pearson Lemma [186], the likelihood ratio of matrix elements from different processes is expected to provide large discriminative power between signal and backgrounds and can be included in the event selection.

Jet Clustering

In this study, jet-clustering ambiguities rather than jet-energy resolution dominate the ZHH event reconstruction. At $\sqrt{s} = 500$ GeV the events are produced near the kinematic threshold and thus, the jets are less collimated and have significant overlap. Therefore, mis-clustering represents one important limiting factor of the measurement precision. By assuming perfect jet clustering the precision on the cross section of double Higgs-strahlung, and thus the Higgs self-coupling can be improved by relative $\sim 40\%$. Consequently in case of perfect jet clustering, the achieved 30% precision on σ_{ZHH} would be improved to absolute 18% for an integrated luminosity of $\mathcal{L} = 2 \text{ ab}^{-1}$ and $P(e^+e^-) = (0.3, -0.8)$. For the full ILC running scenario, this would lead to a precision of 12.8% on σ_{ZHH} for $HH \rightarrow bbbb$ for $\mathcal{L} = 4 \text{ ab}^{-1}$, shared between the polarisation configurations of $|P(e^-)| = 0.8$ and $|P(e^+)| = 0.3$. Combined with $HH \rightarrow bbWW$, this would give 10.1% precision on σ_{ZHH} and 16.5% on λ_{SM} .

However, the development of new jet-clustering algorithms is very difficult. Investigations show, that the Durham jet-clustering algorithm (sec. 5.3.1) starts having clustering issues when the number of the remaining mini-jets is ~ 20 . Advanced clustering algorithms need to be developed to combine these mini-jets. The main idea to improve the jet clustering is to reconstruct the entire parton-shower history of the hard process by using perturbative QCD. Investigations are ongoing [203].

Flavour Tagging

Flavour tagging plays an important role in the analysis. If the b -tagging efficiencies were improved by 5% for the same purity, this would lead to an 11% relative improvement of the precision on σ_{ZHH} and λ_{SM} . In this case, the achieved precision on the cross section of 30% can be enhanced to 27% for an integrated luminosity of $\mathcal{L} = 2 \text{ ab}^{-1}$ and $P(e^+e^-) = (0.3, -0.8)$. The combined signal significance can be improved by almost 15% to 4.0σ . After the full ILC running scenario, this would lead to a measurement precision of 19% on σ_{ZHH} for $HH \rightarrow bbbb$ and even of 15.2% on σ_{ZHH} in combination with $HH \rightarrow bbWW$.

In context of detector technologies such an improvement of flavour-tagging efficiencies depends on the impact parameter resolution. The decay products of heavy quarks do not point back to the primary vertex. The impact parameter is the minimal transverse distance between the track and the expected interaction point (sec. 4.3.1). So far, b and c jets can be identified if the distance between the primary vertex and the decay vertex is sufficiently large. Both flavours are discriminated based on the lifetime and the invariant mass of the charged decay products. Hence, momentum resolution and particle identification down to low momenta are important for flavour tagging.

Since the ZHH events with predominantly $H \rightarrow bb$ are hardly boosted compared to two-body processes i. e. ZZ or ZH at $\sqrt{s} = 500$ GeV, the displaced vertices of the b quarks are shorter and more difficult to reconstruct. For such events the flavour-tagging performance

can be enhanced by improving the impact parameter resolution of the vertex detector. This can be done by bettering the point resolution of the vertex detector, or by moving the vertex detector closer to the interaction point. However, this would give rise to much larger occupancies due to pair background. Higher occupancies would degrade the tracking and flavour-tagging performance. To reduce the larger occupancies the timing resolution needs to be improved to reduce the integrated number of bunch crossings. Neither of the current readout technologies (sec. 4.3.1) can provide very good spatial point and timing resolutions at the same time. Therefore, the combination of different technologies would allow to benefit from the advantages of each technology.

Nevertheless, since the physics studies are based on an interplay between detector performance and analysis techniques, improvements of the flavour-tagging software LCFIPlus (sec. 5.3.3) are ongoing [204]. The use of isolated leptons from semi-leptonic decays can provide further discriminative power between heavy-flavoured and light-flavoured jets. This requires very good particle identification, which is closely linked to high tracking efficiencies and low track fake rates to correctly identify tracks which belong to secondary vertices. The TPC contributes largely to particle identification with a declared goal of a dE/dx resolution of 5% [130]. Moreover, the mass reconstruction from the charged vertices can benefit from recovering neutral jet components. Two third of the jet content is composed of charged particles, i. e. π^\pm , and neutral hadrons, i. e. K_L . One third of the jet is carried by π^0 , which decay into $\gamma\gamma$ and leave most of their energy in the ECAL. In total, 95% of the photons in a jet originate from these π^0 decays. Therefore, the $\pi^0 \rightarrow \gamma\gamma$ reconstruction is the key for improvements in the vertex mass recovery. Several investigations are ongoing [204, 205].

Isolated Lepton Tagging

The isolated lepton selection or rejection is an important tool in the event selection. In the developed strategy in this thesis the background suppression is bettered by a factor of 10 for the same signal efficiency. Nevertheless, the strategy is optimised for e and μ . Therefore, the biggest loss in the signal efficiency occurs in the isolated lepton selection in the lepton mode of ZHH . An efficient τ finder would allow to properly select $\tau\tau HH$ events in the analysis. If similar results were achieved as in $\mu\mu HH$ and $ee HH$, this could improve the precision of σ_{ZHH} by relative 8%. Since less than 10% of the τ decay leptonically, a hadronic τ finder could also enhance the background suppression. Investigations are ongoing, based on methods which rely on the accurate knowledge of the τ production vertex and the precise measurement of its decay products [206]. The prospects of identifying τ decays at the ILD are very good, since the dominant decay modes are $\tau \rightarrow \pi^\pm \pi^0 \nu_\tau$, $3\pi^\pm \nu_\tau$, $\pi^\pm \nu_\tau$. The charged π can be measured very precisely in the tracker, while the identification of $\pi^0 \rightarrow \gamma\gamma$ is possible in high-granularity calorimeters.

Particle Flow Concept in Kinematic Fitting

The kinematic fit is a tool to improve mass resolutions by taking into account the measurement resolutions of the fitted objects. At the ILC the mass resolution relies on the particle flow performance (sec. 4.3.4) and the achievable jet-energy resolution σ_E (sec. 4.1.1), which is limited by the detector performance. The current parametrisation of the jet-energy resolution is applied to all jets in the events independent of their particle content. σ_E is determined from the measured jet energy. In this thesis, the missing energy of semi-leptonic b and c decays in the jets is included in the definition of σ_E (eq. 7.12), as explained in sec. 7.5. Further enhancement can be achieved by calculating the jet-energy resolution σ_E individually for each jet, based on its particle content. This would exploit the full power of the particle flow and high-granularity detectors (sec. 4.2).

The jet-energy resolution of charged particles can be calculated by the covariance matrix. σ_E of photons is determined using the ECAL energy resolution $\frac{\sigma_E}{E} = \frac{16\%}{\sqrt{E}} \oplus 2\%$ [130] while σ_E of neutral hadrons is determined using the HCAL resolution $\frac{\sigma_E}{E} = \frac{50\%}{\sqrt{E}} \oplus 1\%$ [130]. The overall jet-energy resolution is defined by eq. 4.6. This study is currently ongoing [207]. The key to optimal particle flow performance is cluster separation in the calorimeters to limit degrading effects as confusion.

Since jets are mostly composed of charged hadrons as π^\pm the tracking performance is crucial which is directly linked to particle identification. One third of the jet energy is carried by π^0 which decay into $\gamma\gamma$ and thus leave most of their energy in the ECAL. Since about 95% of the photons in a jet originate from these π^0 decays, the origin of the pions and photons needs to be reconstructed precisely, i. e. $K_s \rightarrow \pi^0\pi^0$, $\Delta \rightarrow n\pi^0$. Particle identification tools with large identification efficiencies and small fake rates (sec. 7.6), as well as high-granularity calorimeters are crucial to separate low momentum μ and π . Software reconstruction efforts are ongoing [192, 193, 205].

Overlay Removal

For all DBD benchmark analyses [130] the $\gamma\gamma$ overlay did not have large impact on the measurement results. The effect of this background on the Higgs self-coupling analysis was investigated in this thesis. The overlaid events need to be identified and removed from the reconstructed particle list to recover the original events. Therefore, the DBD overlay removal was optimised for this study (sec. 6.2). As a result, the degradation of the analysis yields was minimised to absolute 15%. Nevertheless, the observation indicates, that more advanced removal strategies are needed in the Higgs self-coupling analysis, which require a detailed modelling of the background and exploit the full power of high-granularity detectors as the ILD.

To identify the products from the $\gamma\gamma$ collisions an explicit reconstruction of the events is needed. One of the most dominant subprocesses in the $\gamma\gamma$ overlay is given by vector-meson dominance in which the photons predominantly oscillate into a neutral ρ meson

$\gamma\gamma \rightarrow \rho^0\rho^0$ [170]. For example, the neutral vector mesons can convert into charged π as $\rho^0 \rightarrow \pi^+\pi^-$. The reconstruction of the decay products would allow to exclude the respective overlay events. However, investigations have shown that the simulation of the DBD $\gamma\gamma$ -overlay events are neither representing the state-of-the art nor an updated description of the expected model. Therefore, a new description and precise simulation of the overlay events have to be developed before a realistic investigation of the effects of the overlay on the Higgs self-coupling measurement is possible. Efforts of better modelling and understanding the $\gamma\gamma$ overlay are ongoing [198].

Moreover, the detailed simulation of the overlay events would allow to exploit the vertex information, and thus determine the vertex position of the background particles to identify the events. The overlay events have a shifted interaction point in z direction along the length of the bunch compared to the primary interaction point of signal events. The bunch spread in z direction is $\sim 300 \mu\text{m}$ at the ILC and the track impact parameter resolution $\sim 10 \mu\text{m}$ (sec. 3.4). Therefore, efficient low-momentum tracking and vertex finding would allow to reconstruct the interaction point of the $\gamma\gamma$ -overlay events when the shift is several $10 \mu\text{m}$.

Chapter 10

Conclusion

The discovery of the Higgs boson candidate in 2012 was a milestone in the history of particle physics. One of the most important tasks in nowadays particle physics is the investigation of its properties and its role in the Standard Model (SM). This requires a precise investigation and model-independent reconstruction of the electroweak symmetry breaking sector (EWSB). Any deviation of SM predictions could be an indication to new physics beyond the SM (BSM). The Higgs mechanism is the cornerstone in the SM EWSB sector. The Higgs potential is a characteristic feature in the SM and needs to be measured to establish the Higgs mechanism experimentally. This requires not only a precise measurement of the Higgs mass, but also of the Higgs self-coupling λ_{SM} . At particle collider experiments, it needs to be investigated if the measured value is represented by the SM prediction. To establish a non-zero Higgs self-coupling, Higgs-pair production needs to be observed in a model-independent cross-section measurement. Indications to BSM can already be given from this measurement since new physics can give sizeable enhancements to the cross section.

Therefore, the prospects of observing Higgs-pair production at the International Linear Collider (ILC) at $\sqrt{s} = 500$ GeV have been investigated in this thesis. The analysis is performed for a Higgs mass of 125 GeV. It is based on a full ILD detector simulation and on ILC beam parameters according to the Technical Design Report. At the ILC, λ can be measured directly in double Higgs-strahlung predominantly with $HH \rightarrow bbbb$ at $\sqrt{s} = 500$ GeV. Very small production cross sections and multi-jet final states pose challenges on the detector performance and event reconstruction. Boson mass distributions play an essential role in the event selection. Therefore, the jets have to be reconstructed as precisely as possible and paired to form the signal bosons. In reality, the reconstruction of primary quarks by measuring jet properties is limited by errors in fragmentation and hadronisation, undetected particles, jet mis-clustering, and limited detector resolutions.

A tool to improve the invariant mass resolutions are kinematic fits, which have been investigated in detail. Their application to events with heavy-flavoured jets has required a detailed study of missing energy from $Z \rightarrow \nu\nu$, initial-state radiation (ISR), and semi-

leptonic decays of b and cascade c quarks. Since energy and momentum conservation is the most powerful constraint in kinematic fitting, all mentioned aspects degrade the fit performance. The analysis has been performed by dividing ZHH into statistically independent modes with respect to the decay of the Z boson ($Z \rightarrow ll, \nu\nu, qq$). Therefore, a strategy has been developed to consider $Z \rightarrow \nu\nu$ in kinematic fits, which allows to successfully apply kinematic fitting to the signal final state $\nu\nu HH$.

The signal final state with $HH \rightarrow bbbb$ can suffer from missing four-momentum from semi-leptonic decays of the b and cascade c quarks. The additional missing four-momenta cause a mis-reconstruction of jet momenta in the fit, and thus do not allow an automatic ISR recognition as provided for light jets. Therefore, two strategies have been developed which deal with the ISR treatment in the fit of heavy-jet final states.

The first strategy allows to work around the issues by treating ISR in the fit on an event-by-event classification using ISR characteristics. This does not provide an automatic ISR recognition but is a simple approach to decide whether to include the ISR photon treatment in the fit for certain events. The developed strategy yields an optimised mass resolution. A more sophisticated approach has been developed in which semi-leptonic decays are considered. Missing energy from such decays has been corrected for in the jets by adding a fraction of the energy carried by the charged lepton, which accompanies the neutrino in semi-leptonic decays and the energy of which can be measured to very high precision. The energy correction results in a tremendous improvement regarding the fit performance, since non-Gaussian tails are taken into account in the jet-energy resolution. Moreover, it enables an automatic ISR recognition as for light jets. This leads to improved mass resolutions, which give an enhanced signal and background separation by more than 10% compared to the masses without fitting. The semi-leptonic jet-energy correction has been applied to events independent of kinematic fitting, since correcting semi-leptonic decays in the jets can enhance the jet-pairing procedure.

Additionally, several fit hypotheses have been studied in terms of new variables, i. e. the fit probability and the goodness of the fit, which provide an enhanced signal and background separation. These variables have been added to the event selection. Relative improvements of up to 20% in the event selection of the signal channels have been achieved by including the variables to the strategy.

Isolated lepton finding is another important tool in the analysis, which requires large efficiencies and purities in the signal selection of $llHH$ and in the background suppression of all signal channels. A neural-net based isolated lepton strategy has been developed. For the same signal efficiency, the background suppression is enhanced by a factor of 10. Moreover, it provides parameters which can be used in the event selection.

Optimising the analysis strategy using boosted decision trees (BDTG) results in additional improvements. Since BDTGs are less sensitive to non-discriminating input variables and overtraining, relative betterments of 10% in $llHH$ and 5% in $\nu\nu HH$ are achieved. Combined with the achievements in kinematic fitting and isolated lepton tagging, relative improvements are obtained in $llHH$ of 25% in $\mu\mu HH$ and 15% in $ee HH$, as well as 10% in

$\nu\nu HH$, and 15% in $qqHH$ ($q \neq b$), while equal results are achieved for $bbHH$. The results of this thesis lead to a 10% relative improvement of the measurement precision on the double Higgs-strahlung cross section σ_{ZHH} . For the SM scenario, an evidence of 3.5σ for the observation of double Higgs-strahlung and a measurement precision of 30% on σ_{ZHH} is achieved, assuming an integrated luminosity of $\mathcal{L} = 2 \text{ ab}^{-1}$ and the beam polarisation of $P(e^+e^-) = (0.3, -0.8)$.

Prospects for the achievable measurement precision after the full ILC running scenario have been provided by the investigation of various beam polarisations. After the full running scenario and a collected integrated luminosity of $\mathcal{L} = 4 \text{ ab}^{-1}$, a precision of 21% on σ_{ZHH} is achieved, which corresponds to a 5.9σ discovery of double Higgs-strahlung. Moreover, a precision of even 16% on σ_{ZHH} is achieved in combination with the $HH \rightarrow bbWW$ channel. This leads to a precision of 26% on λ_{SM} after the full ILC running scenario. The results of this study exceed the expected precision obtained from extrapolations of former analysis results, which even were very optimistic since they did not take into account effects of kinematic distributions for a Higgs mass of 125 GeV.

Moreover, λ is one of the most important quantities to reveal new physics models. WW fusion and ZHH are complementary in their sensitivity to new physics. Both processes behave differently with respect to changes in λ . At $\sqrt{s} = 500 \text{ GeV}$, double Higgs-strahlung can provide measurements of new physics scenarios with $\lambda > \lambda_{SM}$. Models of electroweak baryogenesis in the 2HDM expect deviations from λ_{SM} of at least 20%. In this theory, λ can even be twice as large as in the SM. In such a scenario, the improvements of this thesis provide a precision of 12% on σ_{ZHH} after the full ILC running scenario. This leads to a precision of 13% on λ , which represents a 7σ discovery combined with $HH \rightarrow bbWW$.

The effect of the $\gamma\gamma \rightarrow \text{low-}p_T$ hadrons background has also been studied, which has not been considered in previous Higgs self-coupling studies. By optimising the standard removal strategy, the degradation of the results was minimised to 15%. However, this indicates that more sophisticated removal strategies are needed, which include a precise modelling of the background and exploit the full power of high-granularity detectors.

Moreover, since the results of the analysis are based on the interplay of an excellent detector performance and event reconstruction, more ideas have been discussed which provide improvements of the measurement precisions, i. e. flavour tagging, jet clustering, or the application of matrix element methods to enhance the cross-section sensitivity to the Higgs self-coupling vertex.

To summarise, the results of this thesis show that it is possible to observe double Higgs production and obtain scientific evidence of the existence of the SM Higgs self-coupling at the ILC at an energy of 500 GeV. Continuing the efforts in detector optimisation and event reconstruction provide possibilities for large improvements of the measurement precisions of σ_{ZHH} and λ . In this thesis a relative improvement of 10% leads to a precision on σ_{ZHH} of 16% and of 26% on λ_{SM} after the full ILC running scenario. Moreover, with regard to new physics models the ILC provides a great discovery potential already at a centre-of-mass energy of 500 GeV using ZHH events.

Appendix A

Appendix

A.1 Neutrino Channel

A.1.1 Input variables of first BDTG

The first BDTG in the neutrino channel is trained for $bbbb$ background events against $\nu\bar{\nu}HH$ ($\nu\bar{\nu}bbbb$) signal events. The input variables are shown in fig. A.1.

- **visible energy:** Since the signal has missing four-momentum in the final state, the visible energy can offer separation power. Missing energy can occur from semi-leptonic b and cascade c decays in the jets. However, this is corrected for in the analysis by applying the semi-leptonic energy correction. Nevertheless, missing energy can also be caused by ISR in the events (fig. A.1a).
- **missing p_T :** Similar to the visible energy, missing transverse momentum offers discrimination power. However, in this case ISR does not carry transverse momentum since the ISR photons are very forward and backward. Missing transverse momentum can only occur in the jets in $bbbb$ (fig. A.1b).
- **thrust:** The thrust reflects the anisotropy of an event, indicating if there is a special direction is favoured by the event. Since the $bbbb$ originates from a two-body decay, most of the PFOs in each event are very forward and backward and therefore the thrust value is close to one. The signal is a three-boson decay. The thrust of the background is larger compared to the signal (fig. A.1c).
- **p_{jmax} :** The largest jet momentum of the six-jet hypothesis gives overall smaller values for signal events compared to background events and thus provides separation power (fig. A.1d).
- **$M(Z1)$ and $M(Z2)$:** The four jets are paired to form two Z bosons, representing the background. The respective masses $M(Z1)$ and $M(Z2)$ are used as inputs, since

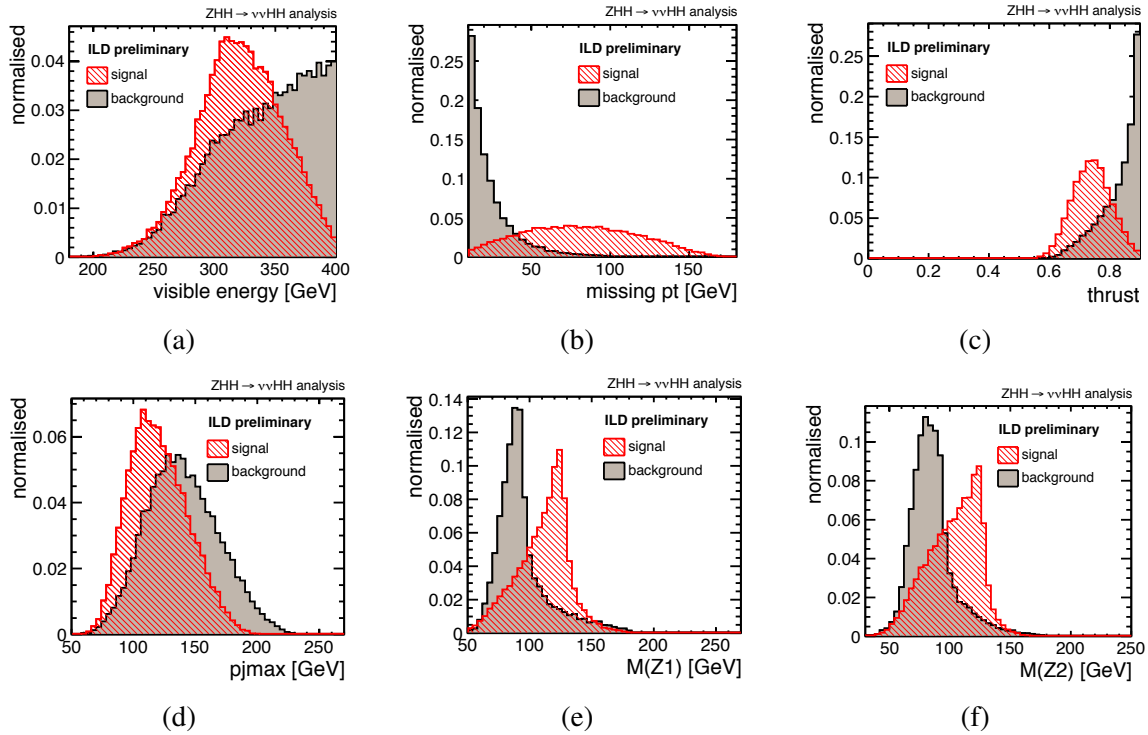


Figure A.1: *Input variables of the first BDTG training $bdtg(bbbb)$ in the neutrino channel. The descriptions can be found in the text.*

signal events obtain much larger masses compared to the background (fig. A.1e, fig. A.1f).

A.1.2 Input variables of second BDTG

In the neutrino channel, the second BDTG is trained to suppress $lvbbqq$ background events. The input variables are shown in fig. A.2. Since $\tau vbbqq$ gives the dominant background contribution to the semi-leptonic background at this stage of the analysis, the BDTG includes many variables which describe properties of the τ decay.

- **npfos**: The signal consists of four b jets in the final state, while the background includes only two b jets. Since b jets have very large multiplicities compared to light jets the total number of PFOs is larger for signal events compared to background events (fig. A.2a).
- **missing $M(Z)$** : In the signal the total missing invariant mass should be consistent with the Z -boson mass. However, the line shape is skewed by beamstrahlung and ISR. The missing energy from semi-leptonic decays in the jets is corrected for and should not contribute (fig. A.2b).

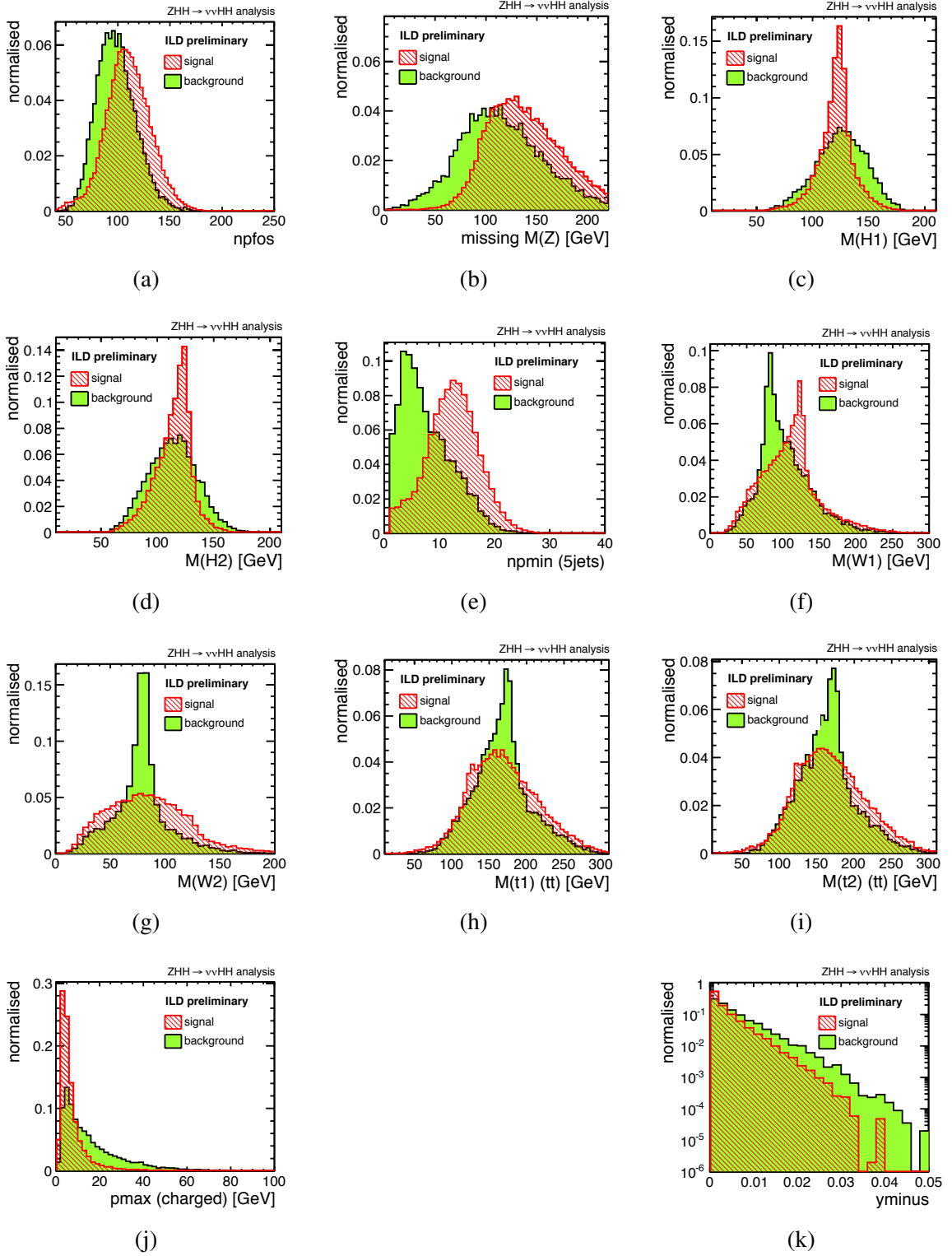


Figure A.2: Input variables of the second BDTG training $bdtg(lvbbqq)$ in the neutrino channel. The descriptions can be found in the text.

- $M(H1)$ and $M(H2)$: The reconstructed invariant masses of the two Higgs bosons provide separation power. The Higgs masses without kinematic fitting are used in BDTG training (fig. A.2c, fig. A.2d).
- **npfosmin**: The events are reconstructed as five-jet events from $\tau\nu bbbq$. The jet with the smallest number of PFOs represents the τ jet (fig. A.2e).
- $M(W1)$ and $M(W2)$: Since the jet with the smallest number of PFOs is identified as τ jet, the remaining four jets are ordered by b likeliness. The jets with the smallest b likeliness are reconstructed as W bosons (fig. A.2f, fig. A.2g).
- $M(t1)$ (tt) and $M(t2)$ (tt): The top mass is reconstructed by combining one of the b jets with the reconstructed W -boson candidate. This results in two possible top-mass combinations (fig. A.2h, fig. A.2i).
- **pcmax**: Since some τ decay into a high-energetic charged π , the largest momentum of charged PFOs can provide separation power (fig. A.2j).
- **yminus**: The Durham parameter for the five-jet hypothesis indicates whether the event is consistent with the clustered number of jets. The signal receives much smaller values since it is not compatible to the five-jet final state (fig. A.2k).

A.1.3 Input variables of third BDTG

The third BDTG in the neutrino channel is trained for $\nu\nu bbbb$ events from ZZH/Z background processes, which give the same final state particles as the signal. Since the same input variables are used for training as in the lepton channel (sec. 8.1.2), we spare the repetition of the variable descriptions. The corresponding figures are shown in fig. A.3.

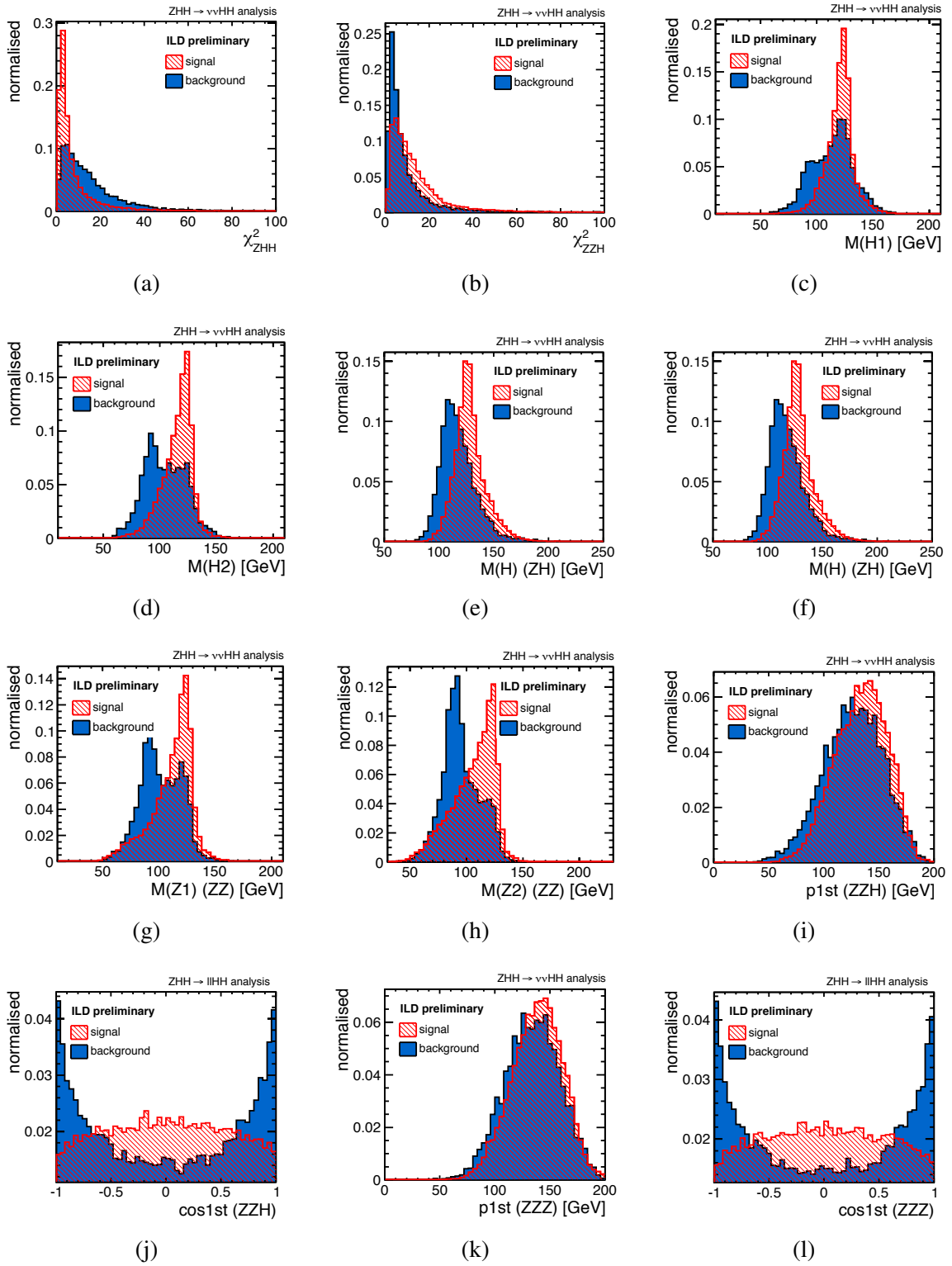


Figure A.3: Input variables of the third BDTG training $bdtg(vvbbb)$ in the neutrino channel.

A.2 Hadron Channel

A.2.1 Input variables of first BDTG

The first BDTG in the hadron channel is trained for $bbbb$ background events against $qqHH$ ($qqbbbb$) signal events. The input variables are shown in fig. A.4. The BDTG classifier response is shown in fig. A.5.

- ***costhrust***: Since $ZZ \rightarrow bbbb$ is a two-body decay, the events are very forward-peaked. Since these events are much closer to beam direction compared to the signal, the polar angle of the thrust axis provides separation power (fig. A.4a).
- ***pjmax (6jets)***: The signal events are produced near kinematic threshold at 500 GeV. Compared to the background, the signal events are less boosted. Therefore, the largest jet momentum offers separation power (fig. A.4b).
- ***yminus***: Several Durham parameters are used as input for BDTG training since the jet multiplicity is different for the $bbbb$ background than for the signal. The Durham parameters Y_{65} (*yminus*), Y_{54} and Y_{43} offer discriminative power. Since these parameters are of similar shape only one example is shown (fig. A.4c).
- ***npfos***: The signal gives a six-jet final state with at least four b jets. Therefore, the total number of PFOs is larger compared to the background (fig. A.4d).
- ***npfosmin***: The smallest number of particles in a jet when reconstructing the events as six-jet final state offers separation power. Since the four-jet of background is clustered into six-jet final states, the background obtains smaller values compared to the signal (fig. A.4e).
- ***M(Z1) (4jets)*** and ***M(Z2) (4jets)***: The events are reconstructed as four-jet final states representing the background. The four jets are paired to form the two Z bosons. While the background peaks at the nominal Z mass, the signal obtains much larger masses (fig. A.4f, fig. A.4g).
- ***pjmax (4jets)***: The largest jet momentum in the four-jet final-state hypothesis provides additional discrimination power. The largest jet momentum for background events is much larger, since the ZZ events are much more boosted at 500 GeV compared to the signal (fig. A.4h).
- ***cosjmax (4jets)***: Since the background events are more boosted than the signal, the polar angle of the jet with the largest momentum in the in the four-jet hypothesis offers discrimination power (fig. A.4i).

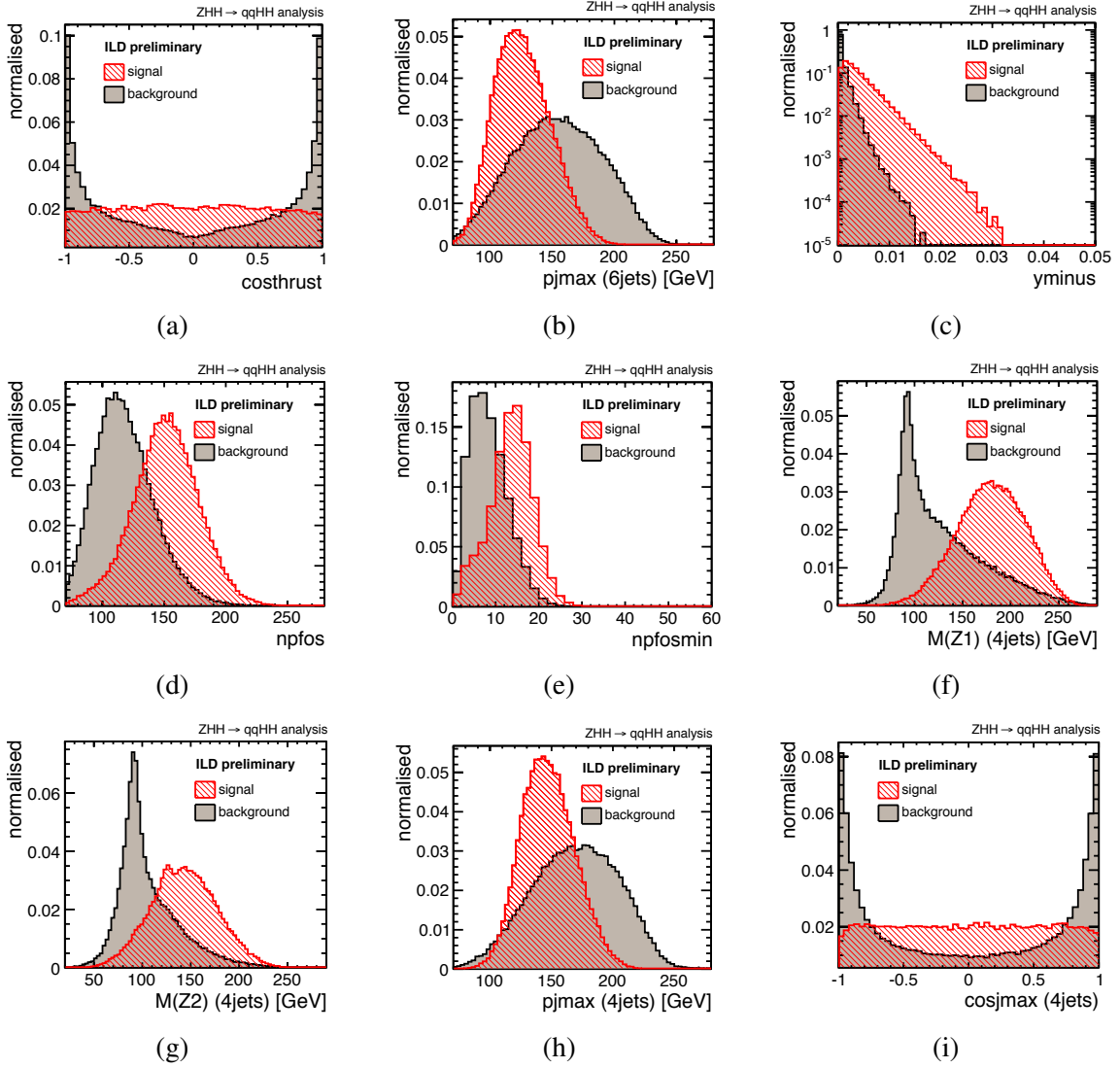


Figure A.4: Input variables of the first BDTG training $bdtg(bbbb)$ in the hadron channel. The descriptions can be found in the text.

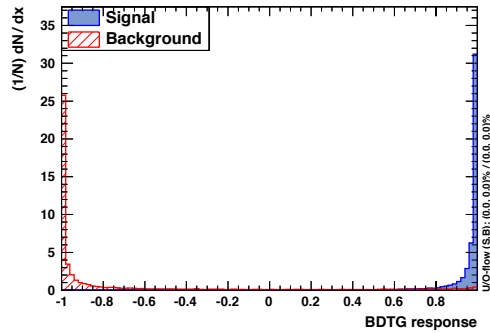


Figure A.5: Classifier response of the first BDTG in the hadron channel: $bbbb$ vs. ZHH ($qqbbbb$).

A.2.2 Input variables of second BDTG

In the hadron channel, the second BDTG is trained to suppress $bbqqqq$ background events from tt , WWZ , ZZH , and ZZZ . The latter have very small cross sections compared to tt and WWZ and therefore do not contribute largely. The BDTG classifier response is shown in fig. A.6. The input variables are shown in fig. A.7.

- Several variables have been discussed in sec. 8.3.3. This concerns $M(t1)$ (tt) and $M(t2)$ (tt) (fig. A.7a, fig. A.7b), $M(W1)$ (tt) and $M(W2)$ (tt) (fig. A.7c, fig. A.7d), and χ^2 and χ^2_{tt} (fig. A.7e, fig. A.7f).
- $M(H1)$ and $M(H2)$: The Higgs masses without fitting are used, since they offer discriminative power to suppress $bbqqqq$ backgrounds (fig. A.7g, fig. A.7h).
- $npfos$: The total number of PFOs is larger for the signal, since signal events include at least four b jets (fig. A.7i).
- $pjmax$ (**6jets**): The largest jet momentum of the six-jets final-state hypothesis is smaller than for tt background events, since ZHH is less boosted at 500 GeV (fig. A.7j).
- $cosbmax$: The cosine of the angle between the two most-like b jets offers separation power (fig. A.7k).
- $M(Z)$: The reconstructed Z -boson mass of ZHH is not used in training but listed in here, since it would provide additional separation power. The tails to smaller masses in the backgrounds results from the pairing of tt events to the signal final state. Since more tt events contribute to “light $qqHH$ dominant”, the distribution is much more pronounced for this signal category. Since in “ $bbHH$ dominant” just few tt events are present, the bump to smaller masses is less pronounced for this category. Since one combined BDTG is trained, the distributions which look different for the two categories are excluded (fig. A.7l). Training separate BDTGs would allow the use of this variable.

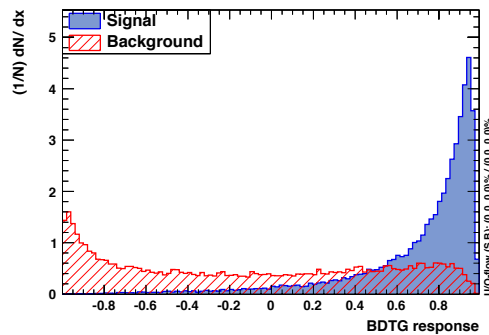


Figure A.6: Classifier response of the second BDTG in the hadron channel: $bbqqqq$ vs. ZHH ($qqbbbb$).

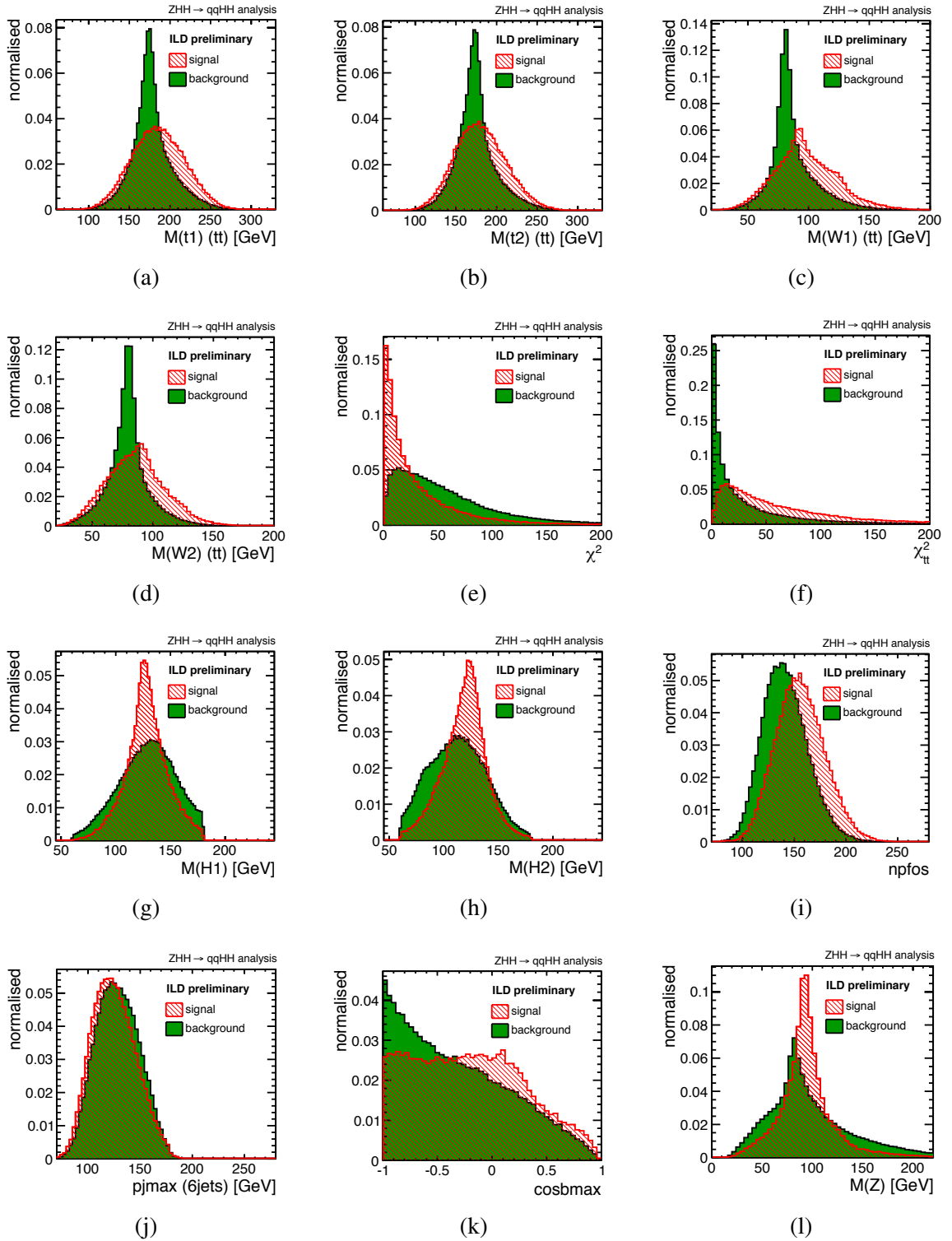


Figure A.7: Input variables of the second BDTG training $bdtg(bbqqq)$ in the hadron channel. The descriptions can be found in the text.

A.2.3 Input variables of third BDTG

The third BDTG in the hadron channel is trained for $qqbbbb$ events, which give the same final state particles as the signal. Since the same input variables are used as in the lepton and neutrino channel we waive the variable descriptions. The BDTG classifier response is shown in fig. A.8. The corresponding figures are shown in fig. A.9.

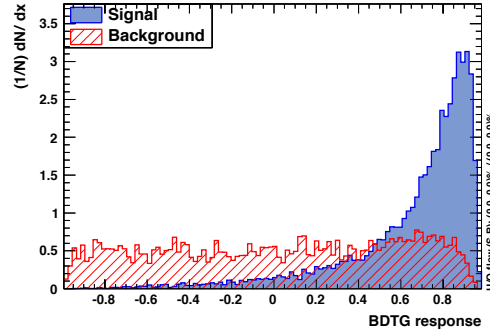


Figure A.8: Classifier response of the third BDTG in the hadron channel: $qqbbbb$ vs. ZHH ($qqbbbb$).

A.2.4 Final selection variables

In “light $qqHH$ dominant” after the basic selection strategy further cuts have to be applied to reduce the large background contribution. The distributions after final selection are shown in fig. A.10.

1. Events are selected which have a b likeliness of $bmax3 > 0.85$, before additional cuts to the ZHH boson masses are applied to select events corresponding to the signal hypothesis (fig. A.10a, fig. A.10b).
2. The Z -boson mass from ZHH pairing has not been used as input for BDTG training, since the distributions are of different shape for both categories as explained in sec. A.2.2. In “light $qqHH$ dominant”, the events have to satisfy $40 \text{ GeV} < M(Z) < 110 \text{ GeV}$ (fig. A.10c, fig. A.10d).
3. After the cut on $M(Z)$ various backgrounds obtain large statistical errors, i. e. $bbcsc$ (7%), $bbcdu$ (10%), $bbuddu$ (18%). Therefore, the results have to be taken with care in context of the following cuts on $M(H1)$ and $M(H2)$ of $90 \text{ GeV} < M(H1/2) < 140 \text{ GeV}$ (fig. A.10e, fig. A.10f, fig. A.10g, fig. A.10h).

The additional cuts lead to 55 ± 2.0 background events and 12.6 ± 0.1 signal events after the final selection in “light $qqHH$ dominant”.

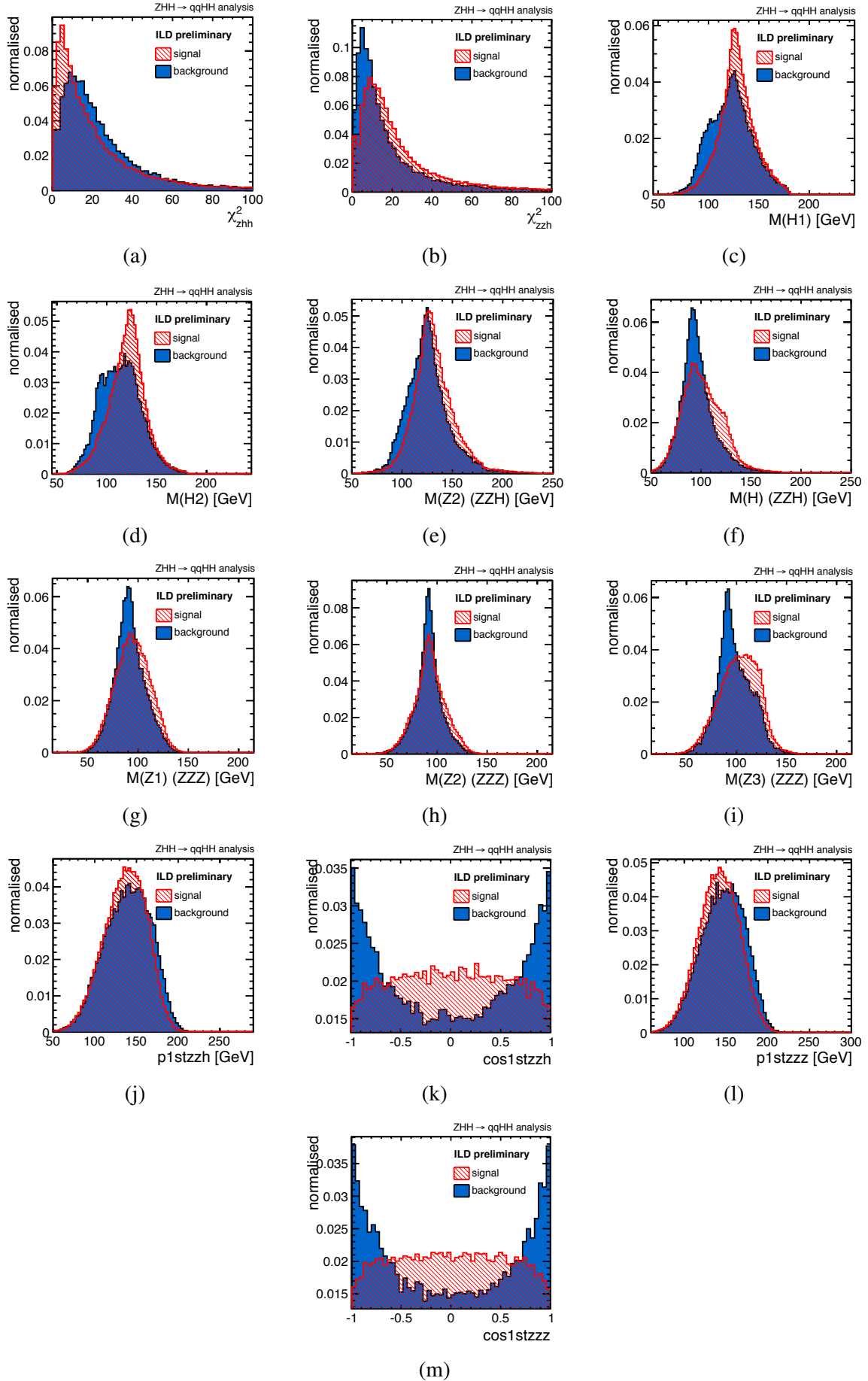


Figure A.9: Input variables of the third BDTG training $bdtg(qqbbb)$ in the hadron channel.

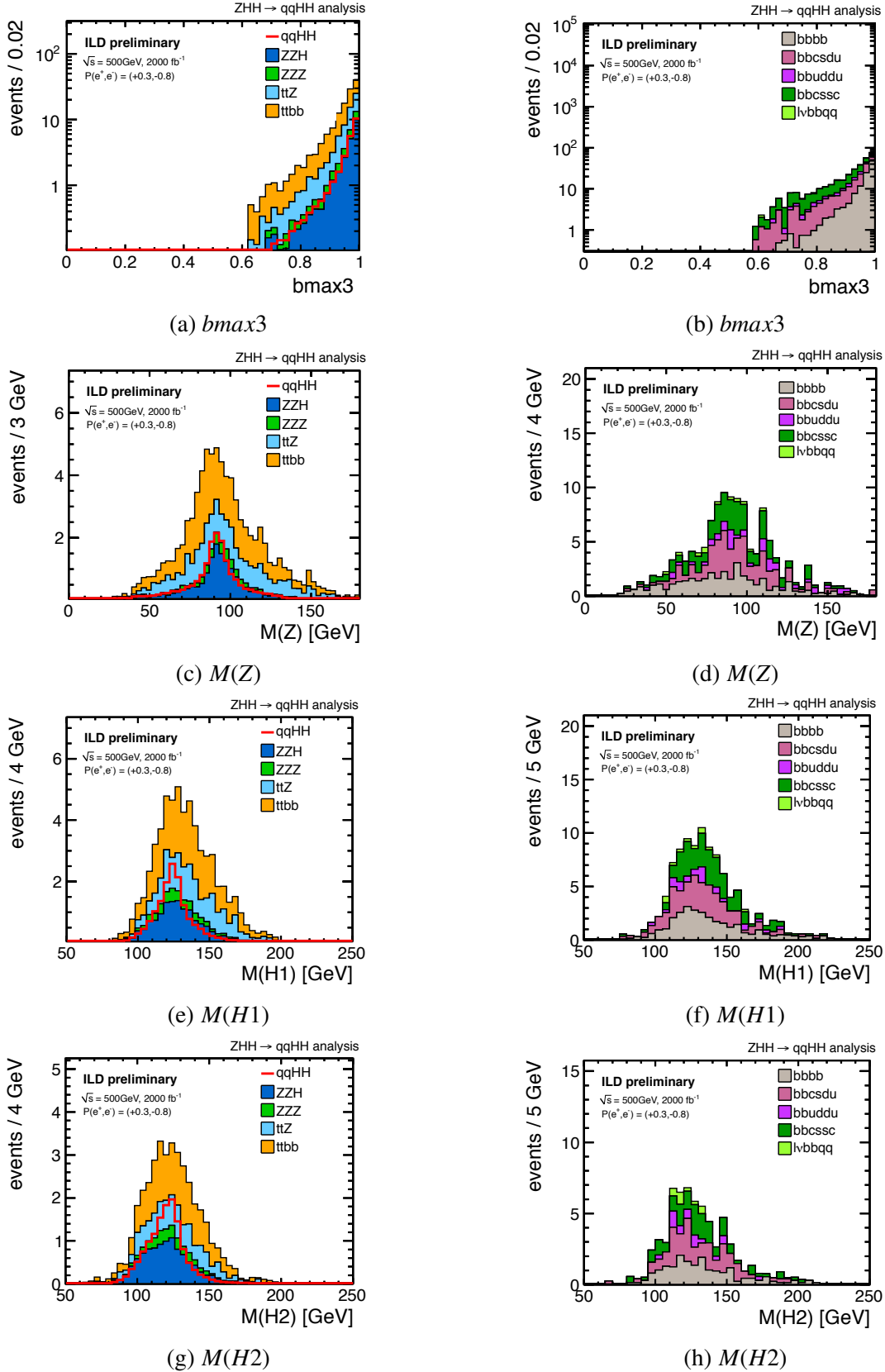


Figure A.10: Additional separation variables for “light $qqHH$ dominant”. Each distribution is shown for signal and small backgrounds (left) and large backgrounds (right) after having applied the respective foregoing cuts.

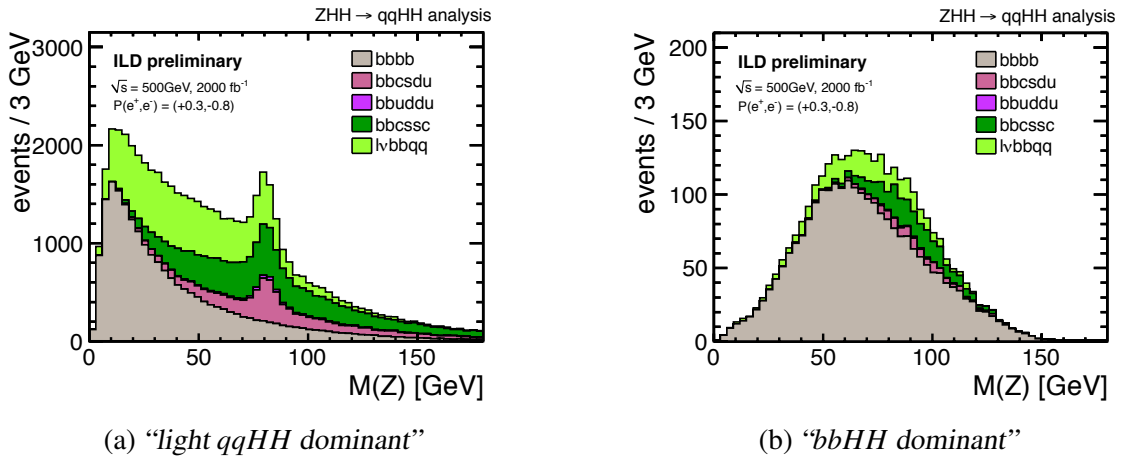


Figure A.11: Reconstructed Z-boson mass after isolated lepton rejection and b-tag requirement in jet pairing for the background processes giving the largest contribution.

A.3 Results for Analysis with Overlay

The tables for the analysis with $\gamma\gamma$ overlay can be found on the following pages.

- The preselection results of the lepton channel are listed in tab. A.1.
- The final selection results of the lepton channel are listed in tab. A.2.
- The complete selection results of the neutrino channel are listed in tab. A.3.
- The preselection results of the hadron channel are listed in tab. A.4.
- The final selection results of the hadron channel are listed in tab. A.5.

	<i>eebb</i>	<i>$\mu\mu bb$</i>	<i>evbbqq</i>	<i>$\mu\nu bbqq$</i>	<i>$\tau\nu bbqq$</i>	<i>bbqqqq</i>	<i>bbbb</i>	<i>llbbbb</i>	<i>llqqH</i>	Background	<i>llHH (llbbbb)</i>
σ [fb]	142.1	24.8	124.2	123.0	123.0	312.0	20.1	0.03	0.08	869.1	0.02
generated events	$3.03 \cdot 10^6$	$6.49 \cdot 10^5$	$1.38 \cdot 10^6$	$1.18 \cdot 10^6$	$1.41 \cdot 10^6$	$3.89 \cdot 10^6$	$9.14 \cdot 10^5$	$7.89 \cdot 10^4$	$9.45 \cdot 10^4$		$2.33 \cdot 10^5$
expected events	$2.84 \cdot 10^5$	$4.95 \cdot 10^4$	$2.48 \cdot 10^5$	$2.46 \cdot 10^5$	$2.46 \cdot 10^5$	$6.24 \cdot 10^5$	$4.02 \cdot 10^4$	69.51	150.87	$1.73 \cdot 10^6$	$40.51 (14.3)$
Preselection Cuts											
$N_{\text{isolep}} \geq 2$	$6.4 \cdot 10^4 \pm 77$	$2.1 \cdot 10^4 \pm 40$	1911 \pm 19	226 \pm 7	195 \pm 6	26 \pm 2	2.4 \pm 0.3	22 \pm 0.1	135 \pm 0.5	$8.8 \cdot 10^4 \pm 89$	$25.2 \pm 0.07 (7.9)$
$ M_{H_1} - M(Z) < 40$ GeV	$3.4 \cdot 10^4 \pm 56$	$1.6 \cdot 10^4 \pm 35$	558 \pm 10	77 \pm 4	33 \pm 2	5 \pm 0.8	0.4 \pm 0.1	15 \pm 0.1	133 \pm 0.4	$4.3 \cdot 10^4 \pm 67$	$24.0 \pm 0.06 (7.9)$
exclusive k_T	$2.7 \cdot 10^4 \pm 50$	$1.3 \cdot 10^4 \pm 31$	552 \pm 10	74 \pm 4	32 \pm 2	3 \pm 0.7	0.3 \pm 0.1	13 \pm 0.1	133 \pm 0.4	$4.1 \cdot 10^4 \pm 60$	$22.6 \pm 0.06 (7.4)$
$ M_{H_1} - M_{H_2} < 80$ GeV	3163 \pm 17	1772 \pm 12	533 \pm 10	70 \pm 4	29 \pm 2	3 \pm 0.7	0.3 \pm 0.1	12 \pm 0.1	130 \pm 0.4	5713 \pm 24	$22.5 \pm 0.06 (7.4)$
Additional Precuts											
60 GeV $< M_{H_1} < 180$ GeV	2265 \pm 14	1254 \pm 10	510 \pm 10	63 \pm 4	29 \pm 2	2.9 \pm 0.7	0.3 \pm 0.1	12 \pm 0.1	127 \pm 0.4	4264 \pm 20	$21.5 \pm 0.06 (7.3)$
60 GeV $< M_{H_2} < 180$ GeV	1401 \pm 11	756 \pm 8	445 \pm 9	54 \pm 3	26 \pm 2	2.7 \pm 0.7	0.3 \pm 0.1	11 \pm 0.1	122 \pm 0.4	2828 \pm 17	$20.6 \pm 0.06 (7.1)$
missing $p_T < 70$ GeV	1384 \pm 11	754 \pm 8	327 \pm 8	40 \pm 3	16 \pm 2	2.7 \pm 0.7	0.3 \pm 0.1	11 \pm 0.1	118 \pm 0.4	2654 \pm 16	$19.1 \pm 0.06 (7.0)$
thrust < 0.9	804 \pm 9	482 \pm 6	325 \pm 8	40 \pm 3	16 \pm 2	2.7 \pm 0.7	0.2 \pm 0.1	11 \pm 0.1	118 \pm 0.4	1802 \pm 14	$19.1 \pm 0.06 (7.0)$

Table A.1: Preselection results of the lepton channel. The $\gamma\gamma$ overlay is included. The numbers correspond to an integrated luminosity of $\mathcal{L} = 2 \text{ ab}^{-1}$ and $P(e^+e^-) = (0.3, -0.8)$. If not stated otherwise $l = e, \mu, \tau$.

	$eebb$	$\mu\mu bb$	$e\nu bbqq$	$\mu\nu bbqq$	$\tau\nu bbqq$	$b\bar{b}qqqq$	$b\bar{b}bb$	$llbbbb$	$llqqH$	Background	$llHH$	$llbbbb$
σ [fb]	142.1	24.8	124.2	123.0	123.0	312.0	20.1	0.03	0.08	869.1	0.02	0.02
expected events	$2.84 \cdot 10^5$	$4.95 \cdot 10^4$	$2.48 \cdot 10^5$	$2.46 \cdot 10^5$	$2.46 \cdot 10^5$	$6.24 \cdot 10^5$	$4.02 \cdot 10^4$	69.51	150.87	$1.734 \cdot 10^6$	40.51 (14.3)	40.51 (14.3)
preselection	804.8 ± 8.68	482.1 ± 6.06	325.6 ± 7.65	40.0 ± 2.89	16.2 ± 1.68	2.7 ± 0.66	0.2 ± 0.09	11.4 ± 0.10	118.7 ± 0.42	1802 ± 14	19.1 ± 0.06	19.1 ± 0.06
Electron-type Selection												
$ltype = 11$	804.8 ± 8.68	0	325.6 ± 7.65	0.5 ± 0.31	14.1 ± 1.57	2.7 ± 0.66	0.2 ± 0.09	5.6 ± 0.07	57.8 ± 0.29	1211 ± 11.7	9.0 ± 0.04	9.0 ± 0.04
$bdig(lbb) > 0.95$	8.9 ± 0.91	0	54.0 ± 3.12	0	3.5 ± 0.78	0.6 ± 0.32	0.1 ± 0.07	4.3 ± 0.06	15.6 ± 0.15	86.9 ± 3.36	4.8 ± 0.03	4.8 ± 0.03
$bdig(l\nu bbqq) > 0.96$	6.1 ± 0.76	0	3.0 ± 0.73	0	0.3 ± 0.23	0	0	3.5 ± 0.05	13.8 ± 0.14	26.7 ± 1.09	4.2 ± 0.03	4.2 ± 0.03
$bdig(llbbbb) > -0.52$	2.2 ± 0.45	0	2.0 ± 0.59	0	0	0	0	0.6 ± 0.02	5.7 ± 0.09	10.4 ± 0.75	3.5 ± 0.2	3.5 ± 0.2
$bmax3 > 0.01$	2.2 ± 0.45	0	2.0 ± 0.59	0	0	0	0	0.6 ± 0.02	5.7 ± 0.09	10.4 ± 0.75	3.5 ± 0.02	3.5 ± 0.02
Muon-type Selection												
$ltype = 13$	0	482.1 ± 6.06	0	39.6 ± 2.88	2.1 ± 0.60	0	0	5.7 ± 0.07	60.9 ± 0.30	590 ± 6.74	10.3 ± 0.04	10.3 ± 0.04
$bdig(llbb) > 0.93$	0	7.9 ± 0.78	0	6.6 ± 1.17	0	0	0	4.4 ± 0.06	17.6 ± 0.16	36.6 ± 1.42	5.7 ± 0.03	5.7 ± 0.03
$bdig(l\nu bbqq) > 0.42$	0	7.9 ± 0.78	0	1.1 ± 0.48	0	0	0	4.3 ± 0.06	17.4 ± 0.16	30.8 ± 0.93	5.6 ± 0.03	5.6 ± 0.03
$bdig(llbbbb) > -0.26$	0	2.3 ± 0.42	0	0	0	0	0	0.4 ± 0.02	4.2 ± 0.08	7.0 ± 0.43	3.9 ± 0.03	3.9 ± 0.03
$bmax3 > 0.01$	0	2.3 ± 0.42	0	0	0	0	0	0.4 ± 0.02	4.2 ± 0.08	7.0 ± 0.43	3.9 ± 0.03	3.9 ± 0.03

Table A.2: Event selection results of the lepton channel. The $\gamma\gamma$ overlay is considered. The numbers correspond to an integrated luminosity of $\mathcal{L} = 2 \text{ ab}^{-1}$ and $P(e^+e^-) = (0.3, -0.8)$.

	$\nu b b$	$e \nu b b q q$	$\mu \nu b b q q$	$\tau \nu b b q q$	$b b q q q q$	$b b b b$	$\nu \nu b b b b$	$\nu \nu q q H$	Background	$\nu H H$ ($\nu \nu b b b b$)
σ [fb]	136.4	124.2	123.0	123.0	312.0	20.1	0.05	0.22	838.9	0.04
generated events	$4.59 \cdot 10^5$	$1.38 \cdot 10^6$	$1.18 \cdot 10^6$	$9.28 \cdot 10^5$	$3.83 \cdot 10^6$	$4.14 \cdot 10^5$	$5.45 \cdot 10^4$	$1.49 \cdot 10^5$	$1.68 \cdot 10^6$	$2.29 \cdot 10^5$
expected events	$2.73 \cdot 10^5$	$2.49 \cdot 10^5$	$2.46 \cdot 10^5$	$2.46 \cdot 10^5$	$6.24 \cdot 10^5$	$4.02 \cdot 10^4$	96.83	447.0	$1.68 \cdot 10^6$	80.14 (28.5)
Preselection Cuts										
$N_{i, \text{selected}} = 0$	$2.5 \cdot 10^5 \pm 380$	$2.5 \cdot 10^4 \pm 66$	$2.4 \cdot 10^4 \pm 69$	$2.2 \cdot 10^5 \pm 242$	$6.2 \cdot 10^5 \pm 241$	$4.0 \cdot 10^4 \pm 61$	96 ± 0.4	392 ± 1.1	$1.2 \cdot 10^6 \pm 523$	62.5 ± 0.15 (28.0)
$ M_{ij} - M_{\mu i} < 80$ GeV	$2.8 \cdot 10^4 \pm 127$	$1.9 \cdot 10^4 \pm 57$	$1.5 \cdot 10^4 \pm 55$	$2.1 \cdot 10^5 \pm 234$	$5.5 \cdot 10^5 \pm 229$	$3.7 \cdot 10^4 \pm 59$	95 ± 0.4	320 ± 1.0	$8.5 \cdot 10^5 \pm 365$	60.9 ± 0.15 (25.3)
$b_{\text{max}3} > 0.2$	2619 ± 39	961 ± 13	854 ± 13	$3.6 \cdot 10^4 \pm 98$	$3.8 \cdot 10^4 \pm 79$	$3.5 \cdot 10^4 \pm 58$	95 ± 0.4	107 ± 0.6	$1.1 \cdot 10^5 \pm 145$	28.9 ± 0.10 (22.6)
Additional Precuts										
$60 < M_{H1} < 180$	1489 ± 30	879 ± 13	807 ± 13	$3.3 \cdot 10^4 \pm 93$	$2.4 \cdot 10^4 \pm 62$	$3.1 \cdot 10^4 \pm 55$	92 ± 0.4	105 ± 0.6	$9.4 \cdot 10^4 \pm 130$	28.6 ± 0.10 (22.4)
$60 < M_{H2} < 180$	744 ± 21	851 ± 12	778 ± 13	$3.3 \cdot 10^4 \pm 93$	$2.1 \cdot 10^4 \pm 58$	$3.2 \cdot 10^4 \pm 56$	88 ± 0.4	103 ± 0.6	$8.7 \cdot 10^4 \pm 126$	28.1 ± 0.10 (22.2)
missing $p_T < 180$ GeV	702 ± 20	838 ± 12	762 ± 13	$3.2 \cdot 10^4 \pm 92$	$1.2 \cdot 10^4 \pm 44$	$1.6 \cdot 10^4 \pm 40$	86 ± 0.4	101 ± 0.5	$6.2 \cdot 10^4 \pm 113$	27.7 ± 0.09 (21.9)
thrust < 0.9	493 ± 17	831 ± 12	754 ± 13	$3.2 \cdot 10^4 \pm 92$	$1.2 \cdot 10^4 \pm 44$	5150 ± 22	85 ± 0.4	101 ± 0.5	$5.1 \cdot 10^4 \pm 107$	27.6 ± 0.09 (21.8)
evts < 400 GeV	490 ± 17	588 ± 10	603 ± 11	$2.5 \cdot 10^4 \pm 82$	1813 ± 17	2264 ± 15	85 ± 0.4	99 ± 0.5	$3.1 \cdot 10^4 \pm 87$	27.2 ± 0.09 (21.5)
$M(HH) > 220$ GeV	183 ± 10	564 ± 10	579 ± 11	$2.4 \cdot 10^4 \pm 80$	1775 ± 17	2102 ± 14	65 ± 0.3	93 ± 0.5	$3.0 \cdot 10^4 \pm 84$	26.1 ± 0.09 (21.0)
Final Selection Cuts										
$bdtg(bbbb) > 0.95$	76 ± 7	323 ± 8	338 ± 8	$1.3 \cdot 10^4 \pm 59$	94 ± 3.9	20 ± 1.4	26.8 ± 0.2	59 ± 0.4	$1.4 \cdot 10^4 \pm 60$	19.8 ± 0.08 (16.0)
$bdtg(\nu b b q q) > 0.38$	25 ± 4	54 ± 3	62 ± 3	1293 ± 19	43 ± 2.6	11 ± 1.0	15.7 ± 0.2	34 ± 0.3	1541 ± 19	14.9 ± 0.07 (13.0)
$bdtg(\nu \nu b b b b) > 0.39$	6 ± 2	31 ± 2	34 ± 3	683 ± 13	40 ± 2.5	6 ± 0.8	1.4 ± 0.1	8 ± 0.2	810 ± 14	10.7 ± 0.06 (9.4)
$b_{\text{max}3} + b_{\text{max}4} > 1.12$	0	0	0	2.3 ± 0.8	0	2.5 ± 0.5	0.5 ± 0.03	3 ± 0.1	8 ± 1	5.2 ± 0.04 (5.1)

Table A.3: Event selection table of the neutrino channel with $\gamma\gamma$ overlay. The numbers correspond to an integrated luminosity of $\mathcal{L} = 2 \text{ ab}^{-1}$ and $P(e^+e^-) = (0.3, -0.8)$.

	$qqqqH$	$qqbbbb$	$bbbb$	$bbcsc$	$bbcscdu$	$bbuddu$	$lvbbqq$	ttZ	$ttbb$	Background	$qqHH$ ($qqbbbb$)
σ [fb]	0.33	0.07	20.12	77.95	156	78.07	370	1.09	1.05	704.8	0.137
generated events	$2.94 \cdot 10^5$	$1.30 \cdot 10^5$	$7.19 \cdot 10^5$	$1.16 \cdot 10^6$	$1.27 \cdot 10^6$	$8.67 \cdot 10^5$	$3.56 \cdot 10^6$	$8.43 \cdot 10^4$	$8.35 \cdot 10^4$		$5.58 \cdot 10^5$
expected events	662.6	140.5	$4.02 \cdot 10^4$	$1.56 \cdot 10^5$	$3.12 \cdot 10^5$	$1.56 \cdot 10^5$	$7.40 \cdot 10^5$	2197	2109	$1.4 \cdot 10^6$	273.1(99)
Preselection Cuts											
$N_{isolep} = 0$	583 ± 1.4	138 ± 0.4	$3.9 \cdot 10^4 \pm 53$	$1.5 \cdot 10^5 \pm 175$	$3.0 \cdot 10^5 \pm 272$	$1.5 \cdot 10^5 \pm 151$	$2.4 \cdot 10^5 \pm 223$	1227 ± 5.6	1274 ± 5.6	$8.8 \cdot 10^5 \pm 423$	214 ± 0.3 (84.0)
$btag > 0.16$	118 ± 0.6	85 ± 0.4	$2.4 \cdot 10^4 \pm 42$	$1.5 \cdot 10^4 \pm 55$	8415 ± 45	562 ± 9	$1.9 \cdot 10^4 \pm 63$	179 ± 2	447 ± 3	$6.8 \cdot 10^4 \pm 104$	83.2 ± 0.2 (60.3)
Additional Precuts											
60 GeV <M(H1) < 180 GeV	115 ± 0.6	83 ± 0.3	$2.2 \cdot 10^4 \pm 40$	$1.4 \cdot 10^4 \pm 53$	8092 ± 45	539 ± 9	$1.7 \cdot 10^4 \pm 59$	173 ± 2	429 ± 3	$6.3 \cdot 10^4 \pm 100$	81.4 ± 0.2 (59.0)
60 GeV <M(H2) < 180 GeV	113 ± 0.6	81 ± 0.3	$2.0 \cdot 10^4 \pm 38$	$1.4 \cdot 10^4 \pm 53$	7842 ± 44	515 ± 9	$1.4 \cdot 10^4 \pm 54$	168 ± 2	397 ± 3	$5.7 \cdot 10^4 \pm 96$	80.1 ± 0.2 (58.4)
missing $p_T < 70$ GeV	112 ± 0.6	81 ± 0.3	$2.0 \cdot 10^4 \pm 38$	$1.4 \cdot 10^4 \pm 53$	7820 ± 44	514 ± 9	8803 ± 43	153 ± 2	352 ± 3	$5.1 \cdot 10^4 \pm 90$	78.4 ± 0.2 (58.2)
thrust <0.9	112 ± 0.6	80 ± 0.3	6391 ± 21	$1.4 \cdot 10^4 \pm 53$	7813 ± 44	513 ± 9	8731 ± 43	153 ± 2	352 ± 3	$3.8 \cdot 10^4 \pm 84$	78.3 ± 0.2 (58.2)

Table A.4: Preselection results of the hadron channel with $\gamma\gamma$ overlay. The numbers correspond to an integrated luminosity of $\mathcal{L} = 2 \text{ ab}^{-1}$ and $P(e^+e^-) = (0.3, -0.8)$.

	<i>qqqgH</i>	<i>qqbbbb</i>	<i>bbbb</i>	<i>bbcsc</i>	<i>bcbcd</i>	<i>bbudd</i>	<i>lvbbqg</i>	<i>ttZ</i>	<i>ttbb</i>	Background	<i>qqHH (qqbbbb)</i>
expected events	662.6	140.5	$4.02 \cdot 10^4$	$1.56 \cdot 10^5$	$3.12 \cdot 10^5$	$1.56 \cdot 10^5$	$7.40 \cdot 10^5$	2197	2109	$1.4 \cdot 10^6$	273.1 (99)
preselection	112 ± 0.6	80 ± 0.3	6391 ± 21	$1.4 \cdot 10^4 \pm 53$	7813 ± 44	513 ± 9	8731 ± 43	153 ± 2	352 ± 3	$3.8 \cdot 10^4 \pm 84$	$78.3 \pm 0.2 (58.2)$
<i>bHH</i> dominant Selection											
<i>btgZ > 0.54</i>	16 ± 0.2	14 ± 0.1	653 ± 7	375 ± 9	162 ± 6	11 ± 1	274 ± 8	17 ± 1	38 ± 1	1561 ± 15	$19.5 \pm 0.1 (16.5)$
<i>btg(bbhb) > 0.48</i>	13 ± 0.2	10 ± 0.1	21 ± 1	311 ± 8	133 ± 6	9 ± 1	44 ± 3	15 ± 1	30 ± 1	587 ± 10	$17.3 \pm 0.1 (15.1)$
<i>btg(bbqqq) > -0.74</i>	13 ± 0.2	10 ± 0.1	20 ± 1	274 ± 8	117 ± 5	8 ± 1	42 ± 3	15 ± 1	30 ± 1	530 ± 10	$17.2 \pm 0.1 (15.0)$
<i>btg(qqbbb) > -0.08</i>	10 ± 0.2	6 ± 0.1	15 ± 1	222 ± 7	92 ± 5	6 ± 1	33 ± 3	13 ± 1	26 ± 1	424 ± 9	$15.6 \pm 0.1 (13.7)$
<i>bmax3 + bmax4 > 1.25</i>	4 ± 0.1	3 ± 0.1	4 ± 1	5 ± 1	2 ± 1	0	0.4 ± 0.3	2 ± 0.2	3 ± 0.3	23 ± 1	$8.5 \pm 0.1 (8.0)$
Light <i>qqHH</i> dominant Selection											
<i>btgZ < 0.54</i>	96 ± 0.6	66 ± 0.3	5738 ± 20	$1.3 \cdot 10^4 \pm 52$	7650 ± 43	503 ± 9	8456 ± 42	135 ± 2	314 ± 3	$3.6 \cdot 10^4 \pm 82$	$58.8 \pm 0.2 (41.7)$
<i>btg(bbhb) > 0.38</i>	81 ± 0.5	46 ± 0.3	196 ± 4	$1.1 \cdot 10^4 \pm 47$	6531 ± 40	443 ± 8	1280 ± 16	125 ± 2	273 ± 3	$2.0 \cdot 10^4 \pm 64$	$51.8 \pm 0.2 (38.3)$
<i>btg(bbqqq) > -0.03</i>	58 ± 0.4	27 ± 0.2	129 ± 3	4131 ± 29	2590 ± 25	203 ± 6	514 ± 10	100 ± 2	189 ± 2	7942 ± 40	$43.1 \pm 0.1 (32.5)$
<i>btg(qqbbb) > 0.35</i>	29 ± 0.3	9 ± 0.1	69 ± 2	2624 ± 23	1581 ± 20	122 ± 4	313 ± 8	72 ± 2	123 ± 2	$4941 \pm$	$33.0 \pm 0.1 (25.8)$
<i>bmax3 + bax4 > 1.34</i>	12 ± 0.2	4 ± 0.1	32 ± 2	28 ± 2	33 ± 3	7 ± 1	4 ± 1	17 ± 1	24 ± 1	161 ± 4	$14.9 \pm 0.1 (12.8)$
<i>bmax3 > 0.92</i>	10 ± 0.2	3 ± 0.1	28 ± 1	15 ± 2	20 ± 2	5 ± 1	2 ± 1	14 ± 1	18 ± 1	115 ± 4	$13.1 \pm 0.1 (11.3)$
$40 < M_Z < 110$	8 ± 0.2	2 ± 0.1	17 ± 1	9 ± 1	14 ± 2	2 ± 1	2 ± 1	9 ± 1	11 ± 1	74 ± 3	$10.3 \pm 0.1 (9.1)$
$90 < M_{H1} < 140$	6 ± 0.1	1 ± 0.1	9 ± 1	5 ± 1	9 ± 2	1 ± 0.4	1 ± 0.4	5 ± 0.4	6 ± 0.4	45 ± 2	$7.8 \pm 0.1 (7.0)$
$90 < M_{H2} < 140$	5 ± 0.1	1 ± 0.1	6 ± 1	3 ± 1	7 ± 1	1 ± 0.4	1 ± 0.4	4 ± 0.3	4 ± 0.3	33 ± 2	$6.8 \pm 0.1 (6.1)$

Table A.5: Final selection results of the hadron channel with $\gamma\gamma$ overlay. The “*bHH* dominant” and “light *qqHH* dominant” categories are listed. The numbers correspond to an integrated luminosity of $\mathcal{L} = 2 \text{ ab}^{-1}$ and $P(e^+e^-) = (0.3, -0.8)$.

Bibliography

- [1] P. W. Higgs, “Broken Symmetries and the Masses of Gauge Boson”, *Phys. Rev. Lett.* **13** (1964) 508-509.
- [2] P. W. Higgs, “Broken symmetries, massless particles and gauge fields”, *Phys. Lett.* **12** (1964) 132-133.
- [3] F. Englert and R. Brout, “Broken Symmetry and the Mass of Gauge Vector Mesons”, *Phys. Rev. Lett.* **13** (1964) 321-323.
- [4] G. Aad et al. [ATLAS Collaboration], “Observation of a new particle in the search for the Standard Model Higgs boson with the ATLAS detector at the LHC”, *Phys. Lett. B* **716** (2012) 1, arXiv:1207.7214 [hep-ex].
- [5] S. Chatrchyan et al. [CMS Collaboration], “Observation of a new boson at a mass of 125 GeV with the CMS experiment at the LHC”, *Phys. Lett. B* **716** (2012) 30, arXiv:1207.7235 [hep-ex].
- [6] R. S. Gupta, H. Rzehak and J. D. Wells, “How well do we need to measure the Higgs boson mass and self-coupling?”, *Phys. Rev. D* **88** (2013) 055024, arXiv:1305.6397 [hep-ph].
- [7] S. Kanemura, E. Senaha, T. Shindou and T. Yamada, “Electroweak phase transition and Higgs boson couplings in the model based on supersymmetric strong dynamics”, *JHEP* **1305** (2013) 066, arXiv:1211.5883 [hep-ph].
- [8] S. Glashow, “Partial Symmetries of Weak Interaction”, *Nucl. Phys.* **22**, 579-588 (1961).
- [9] A. Salam and J. C. Ward, “On a Gauge Theory of Elementary Interactions”, *Nuovo Cim.* **19**, 165-170 (1961).
- [10] A. Salam and J. C. Ward, “Electromagnetic and weak interactions”, *Phys. Lett.* **13** (1964) 168.
- [11] S. Weinberg, “A Model of Leptons”, *Phys. Rev. Lett.* **19** (1967) 1264.
- [12] S. Weinberg, “Conceptual Foundations of the Unified Theory of Weak and Electromagnetic Interactions”, *Rev. Mod. Phys.* **52** (1980) 515.
- [13] E. Fermi, “Zur Quanteln des idealen einatomigen Gases,” German, *Zeitschrift für Physik* 36.11-12 (1926) 902-912, ISSN: 0044-3328.
- [14] P. A. M. Dirac, “On the Theory of Quantum Mechanics,” *Proceedings of the Royal Society of London A: Mathematical, Physical and Engineering Sciences*, 112.762 (1926) 661-667, ISSN: 0950-1207.

- [15] Bose, “Plancks Gesetz und Lichtquantenhypothese,” German, *Zeitschrift für Physik* **26.1** (1924) 178-181, ISSN: 0044-3328.
- [16] A. Einstein, “Quantentheorie des einatomigen idealen Gases”, *Sitzungsberichte der Preussischen Akademie der Wissenschaften* (1924) 261-267.
- [17] F. Halzen and A. D. Martin, “Quarks & Leptons: An Introductory Course in Modern Particle Physics”, John Wiley & Sons, 1984.
- [18] Ta-Pei Cheng and Ling-Fong Li, “Gauge theory of elementary particle physics”, Oxford University Press, 1984.
- [19] J. Goldstone, A. Salam and S. Weinberg, “Broken Symmetries”, *Phys. Rev.* **127** (1962) 965.
- [20] M. E. Peskin and D. V. Schroeder, “An introduction to Quantum Field Theory”, Westview Press, 1995.
- [21] M. Drewes, “The Phenomenology of Right Handed Neutrinos”, *Int. J. Mod. Phys. E* **22** (2013) 1330019, arXiv:1303.6912 [hep-ph].
- [22] E. Majorana, “Theory of the Symmetry of Electrons and Positrons”, *Nuovo Cim.* **14** (1937) 171.
- [23] C. Giunti and M. Laveder, “Neutrino mixing”, hep-ph/0310238.
- [24] S. M. Bilenky, “Neutrino in Standard Model and beyond”, *Phys. Part. Nucl.* **46** (2015) 4, 475, arXiv:1501.00232 [hep-ph].
- [25] S. M. Bilenky and S. T. Petcov, “Massive Neutrinos and Neutrino Oscillations”, *Rev. Mod. Phys.* **59** (1987) 671.
- [26] J. Schechter and J. W. F. Valle, “Neutrino Masses in $SU(2) \times U(1)$ Theories”, *Phys. Rev. D* **22** (1980) 2227.
- [27] K. A. Olive et al. [Particle Data Group], “Review of Particle Physics”, *Chin. Phys. C*, **38** 090001 (2014) and 2015 update.
- [28] H. M. Georgi, S. L. Glashow, M. E. Machacek and D. V. Nanopoulos, “Higgs Bosons from Two Gluon Annihilation in Proton Proton Collisions”, *Phys. Rev. Lett.* **40** (1978) 692.
- [29] Z. Kunszt, S. Moretti and W. J. Stirling, “Higgs production at the LHC: An Update on cross-sections and branching ratios”, *Z. Phys. C* **74** (1997) 479, hep-ph/9611397.
- [30] M. Spira, “QCD effects in Higgs physics”, *Fortsch. Phys.* **46** (1998) 203, hep-ph/9705337.
- [31] R. N. Cahn and S. Dawson, “Production of Very Massive Higgs Bosons”, *Phys. Lett. B* **136** (1984) 196 [*Phys. Lett. B* **138** (1984) 464].
- [32] S. L. Glashow, D. V. Nanopoulos and A. Yildiz, “Associated Production of Higgs Bosons and Z Particles”, *Phys. Rev. D* **18** (1978) 1724.
- [33] Z. Kunszt, “Associated Production of Heavy Higgs Boson with Top Quarks”, *Nucl. Phys. B* **247** (1984) 339.

- [34] T. Plehn, M. Spira and P. M. Zerwas, “Pair production of neutral Higgs particles in gluon-gluon collisions”, Nucl. Phys. B **479** (1996) 46 [Nucl. Phys. B **531** (1998) 655], hep-ph/9603205.
- [35] A. Abbasabadi, W. W. Repko, D. A. Dicus and R. Vega, “Single and Double Higgs Production by Gauge Boson Fusion”, Phys. Lett. B **213** (1988) 386.
- [36] V. D. Barger, T. Han and R. J. N. Phillips, “Double Higgs Boson Bremsstrahlung From W and Z Bosons at Supercolliders”, Phys. Rev. D **38** (1988) 2766.
- [37] R. Frederix, S. Frixione, V. Hirschi, F. Maltoni, O. Mattelaer, P. Torrielli, E. Vryonidou and M. Zaro, “Higgs pair production at the LHC with NLO and parton-shower effects”, Phys. Lett. B **732** (2014) 142, arXiv:1401.7340 [hep-ph].
- [38] A. Djouadi, H. Haber, and P. Zerwas, “Multiple production of MSSM neutral Higgs bosons at high-energy e^+e^- colliders”, Phys. Lett. B **375** (1996) 203, hep-ph/9602234.
- [39] G. Gounaris, D. Schildknecht, and F. Renard, “Test of Higgs Boson Nature in $e^+e^- \rightarrow HHZ$ ”, Phys. Lett. B **83** (1979) 191.
- [40] V. Ilyin, A. Pukhov, Y. Kurihara, Y. Shimizu, and T. Kaneko, “Probing the H^{**3} vertex in e^+e^- , γe and $\gamma\gamma$ collisions for light and intermediate Higgs bosons”, Phys. Rev. D **54** (1996) 6717, hep-ph/9506326.
- [41] V. D. Barger and T. Han, “Double Higgs Boson Production via WW Fusion in Tev e^+e^- Collisions”, Mod. Phys. Lett. A **5** (1990) 667.
- [42] A. Djouadi, W. Kilian, M. Muhlleitner and P. M. Zerwas, “The Reconstruction of trilinear Higgs couplings”, In *2nd ECFA/DESY Study 1998-2001* 791-811, hep-ph/0001169.
- [43] A. Denner, S. Heinemeyer, I. Puljak, D. Rebuszi, and M. Spira, “Standard Model Higgs-Boson Branching Ratios with Uncertainties“, Eur. Phys. J. **C71** (2011) 1753, arXiv:1107.5909 [hep-ph].
- [44] D. Kohler, B. A. Watson, and J. A. Becker, “Experimental search for a low-mass scalar boson“, Phys. Rev. Lett. **33** (1974) 1628.
- [45] R. Barbieri and T. E. O. Ericson, “Evidence against the existence of a low mass scalar boson from neutron-nucleus scattering”, Phys. Lett. B **57** (1975) 270-272.
- [46] J. Ellis, M. K. Gaillard, and D. V. Nanopoulos, “A Historical Profile of the Higgs Boson”, CERN-PH-TH-2012-009 (2012).
- [47] T. Yamazaki et al., “Search For A Neutral Boson In A Two-body Decay Of $K^+ \rightarrow \pi + \Xi^0$ “, Phys. Rev. Lett. **52** (1984) 1089.
- [48] M. S. Atiya et al., “Search for the Decay $K^+ \rightarrow \pi^+$ Neutrino Anti-neutrino”, Phys. Rev. Lett. **64** (1990) 21.
- [49] G. D. Barr et al. [NA31 Collaboration], “Search for a Neutral Higgs Particle in the Decay Sequence $K_L^0 \rightarrow \pi^0 H^0$ and $H^0 \rightarrow e^+e^-$ ”, Phys. Lett. B **235** (1990) 356.
- [50] M. S. Alam et al. [CLEO Collaboration], “Search for a Neutral Higgs Boson in B Meson Decay”, Phys. Rev. D **40** (1989) 712 [Phys. Rev. D **40** (1989) 3790].

- [51] M. Althoff et al. [TASSO Collaboration], “Production and Muonic Decay of Heavy Quarks in e^+e^- Annihilation at 34.5-GeV”, *Z. Phys. C* **22** (1984) 219.
- [52] B. Grinstein, L. J. Hall and L. Randall, “Do B meson decays exclude a light Higgs?”, *Phys. Lett. B* **211** (1988) 363.
- [53] J. R. Ellis, G. L. Fogli and E. Lisi, “Bounds on $M(H)$ from electroweak radiative corrections”, *Phys. Lett. B* **274** (1992) 456.
- [54] F. del Aguila, M. Martinez and M. Quiros, “Precision bounds on $m(H)$ and $m(t)$ ”, *Nucl. Phys. B* **381** (1992) 451, hep-ph/9203210.
- [55] F. Abe et al., “Observation of top quark production in $p\bar{p}$ collisions with the collider detector at Fermilab”, *Phys. Rev. Lett.* **74** (1995) 2626-2631.
- [56] R. Barate et al. [LEP Working Group for Higgs boson searches and ALEPH and DELPHI and L3 and OPAL Collaborations], “Search for the standard model Higgs boson at LEP”, *Phys. Lett. B* **565** (2003) 61, hep-ex/0306033.
- [57] Tevatron New Physics Higgs Working Group and CDF and D0 Collaborations, “Updated Combination of CDF and D0 Searches for Standard Model Higgs Boson Production with up to 10.0 fb^{-1} of Data”, arXiv:1207.0449 [hep-ex].
- [58] G. Aad et al. [ATLAS Collaboration], “Combined search for the Standard Model Higgs boson in pp collisions at $\sqrt{s} = 7 \text{ TeV}$ with the ATLAS detector”, *Phys. Rev. D* **86** (2012) 032003, arXiv:1207.0319 [hep-ex].
- [59] S. Chatrchyan et al. [CMS Collaboration], “Combined results of searches for the standard model Higgs boson in pp collisions at $\sqrt{s} = 7 \text{ TeV}$ ”, *Phys. Lett. B* **710** (2012) 26, arXiv:1202.1488 [hep-ex].
- [60] G. Aad et al. [ATLAS Collaboration], “Measurements of Higgs boson production and couplings in diboson final states with the ATLAS detector at the LHC”, *Phys. Lett. B* **726** (2013) 88 [*Phys. Lett. B* **734** (2014) 406], arXiv:1307.1427 [hep-ex].
- [61] S. Chatrchyan et al. [CMS Collaboration], “Measurement of the properties of a Higgs boson in the four-lepton final state”, *Phys. Rev. D* **89** (2014) 092007, arXiv:1312.5353 [hep-ex].
- [62] G. Aad *et al.* [ATLAS and CMS Collaborations], “Combined Measurement of the Higgs Boson Mass in pp Collisions at $\sqrt{s} = 7$ and 8 TeV with the ATLAS and CMS Experiments,” *Phys. Rev. Lett.* **114** (2015) 191803 [arXiv:1503.07589 [hep-ex]].
- [63] J. N. Bahcall et al., “Solar Neutrinos: The First Thirty Years”, Westview, Boulder, CO (2002).
- [64] V. Barger, D. Marfatia, and K. L. Whisnant, “The Physics of Neutrinos”, Princeton University Press, 2012.
- [65] L. Canetti, M. Drewes and M. Shaposhnikov, “Matter and Antimatter in the Universe”, *New J. Phys.* **14** (2012) 095012, arXiv:1204.4186 [hep-ph].
- [66] A. D. Sakharov, “Violation of CP Invariance, c Asymmetry, and Baryon Asymmetry of the Universe”, *Pisma Zh. Eksp. Teor. Fiz.* **5** (1967) 32.

- [67] M. B. Gavela, P. Hernandez, J. Orloff and O. Pene, “Standard model CP violation and baryon asymmetry”, *Mod. Phys. Lett. A* **9** (1994) 795, hep-ph/9312215.
- [68] M. E. Shaposhnikov, “Baryon Asymmetry of the Universe in Standard Electroweak Theory”, *Nucl. Phys. B* **287** (1987) 757.
- [69] C. Grojean, G. Servant, and J. D. Wells, “First-order electroweak phase transition in the standard model with a low cutoff”, *Phys. Rev. D* **71** (2005) 036001, hep-ph/0407019.
- [70] M. Aoki, S. Kanemura, and O. Seto, “Neutrino mass, Dark Matter and Baryon Asymmetry via TeV-Scale Physics without Fine-Tuning”, *Phys. Rev. Lett.* **102** (2009) 051805, arXiv:0807.0361 [hep-ph].
- [71] A. G. Cohen, D. Kaplan, and A. Nelson, “Progress in electroweak baryogenesis”, *Ann. Rev. Nucl. Part. Sci.* **43** 27 (1993), hep-ph/9302210.
- [72] M. Quiros, “Field theory at finite temperature and phase transitions”, *Helv. Phys. Acta* **67** (1994) 451.
- [73] V. Rubakov and M. Shaposhnikov, “Electroweak baryon number nonconservation in the early universe and in high-energy collisions”, *Usp. Fiz. Nauk* **166** (1996) 493 [*Phys. Usp.* **39** (1996) 461], hep-ph/9603208.
- [74] P. A. R. Ade et al. [Planck Collaboration], “Planck 2013 results. XVI. Cosmological parameters”, *Astron. Astrophys.* **571** (2014) A16, arXiv:1303.5076 [astro-ph.CO].
- [75] F. Zwicky, “Die Rotverschiebung von extragalaktischen Nebeln”, *Helv. Phys. Acta* **6** (1933) 110.
- [76] N. Kaiser and G. Squires, “Mapping the dark matter with weak gravitational lensing”, *Astrophys. J.* **404** (1993) 441.
- [77] G. Bertone, D. Hooper and J. Silk, “Particle dark matter: Evidence, candidates and constraints”, *Phys. Rept.* **405** (2005) 279, hep-ph/0404175.
- [78] D. Huterer and M. S. Turner, “Prospects for probing the dark energy via supernova distance measurements”, *Phys. Rev. D* **60** (1999) 081301, astro-ph/9808133.
- [79] A. G. Riess et al. [Supernova Search Team Collaboration], “Observational evidence from supernovae for an accelerating universe and a cosmological constant”, *Astron. J.* **116** (1998) 1009, astro-ph/9805201.
- [80] P. J. E. Peebles and B. Ratra, “The Cosmological constant and dark energy”, *Rev. Mod. Phys.* **75** (2003) 559, astro-ph/0207347.
- [81] J. A. Frieman, C. T. Hill, A. Stebbins and I. Waga, “Cosmology with ultra-light pseudo Nambu-Goldstone bosons,” *Phys. Rev. Lett.* **75** (1995) 2077 [astro-ph/9505060].
- [82] P. J. E. Peebles and B. Ratra, “Cosmology with a Time Variable Cosmological Constant,” *Astrophys. J.* **325** (1988) L17.
- [83] B. W. Lee, C. Quigg and H. B. Thacker, “Weak Interactions at Very High-Energies: The Role of the Higgs Boson Mass”, *Phys. Rev. D* **16** (1977) 1519.

- [84] B. Herberg, “Measuring hadronic jets at the ILC”, Ph.D. thesis, Universität Hamburg, 2015.
- [85] S. Kanemura, Y. Okada, E. Senaha, and C.-P. Yuan, “Higgs coupling constants as a probe of new physics”, *Phys. Rev. D* **70** (2004) 115002, hep-ph/0408364.
- [86] S. Kanemura, S. Kiyoura, Y. Okada, E. Senaha, and C.-P. Yuan, “New physics effect on the Higgs selfcoupling”, *Phys. Lett. B* **558** (2003) 157, hep-ph/0211308.
- [87] G. Degrandi, S. Di Vita, J. Elias-Miro, J. R. Espinosa, G. F. Giudice, G. Isidori and A. Strumia, “Higgs mass and vacuum stability in the Standard Model at NNLO”, *JHEP* **1208** (2012) 098, arXiv:1205.6497 [hep-ph].
- [88] S. Alekhin, A. Djouadi and S. Moch, “The top quark and Higgs boson masses and the stability of the electroweak vacuum”, *Phys. Lett. B* **716** (2012) 214, arXiv:1207.0980 [hep-ph].
- [89] M. Vos *et al.*, “Top physics at high-energy lepton colliders”, arXiv:1604.08122 [hep-ex].
- [90] T. Appelquist and J. Carazzone, “Infrared Singularities and Massive Fields”, *Phys. Rev. D* **11** (1975) 2856.
- [91] S. Kanemura, Y. Okada, and E. Senaha, “Electroweak baryogenesis and quantum corrections to the triple Higgs boson coupling”, *Phys. Lett. B* **606** (2005) 361, hep-ph/0411354.
- [92] S. Kanemura, T. Shindou, and K. Yagyu, “Non-decoupling effects in supersymmetric Higgs sectors”, *Phys. Lett. B* **699** (2011) 258, arXiv:1009.1836 [hep-ph].
- [93] M. Aoki, S. Kanemura, and O. Seto, “A Model of TeV Scale Physics for Neutrino Mass, Dark Matter and Baryon Asymmetry and its Phenomenology”, *Phys. Rev. D* **80** (2009) 033007, arXiv:0904.3829 [hep-ph].
- [94] Daniel. J. H. Chung, Andrew J. Long and Lian-Tao Wang, “125 GeV Higgs boson and electroweak phase transition model classes”, *Phys. Rev. D* **87** (2013) 023509.
- [95] S. W. Ham and S. K. Oh, “Electroweak phase transition and Higgs self-couplings in the two-Higgs-doublet model”, hep-ph/0502116.
- [96] A. Noble and M. Perelstein, “Higgs self-coupling as a probe of electroweak phase transition”, *Phys. Rev. D* **78** (2008) 063518, arXiv:0711.3018 [hep-ph].
- [97] S. Kanemura, E. Senaha, and T. Shindou, “Decoupling Property of SUSY Extended Higgs Sectors and Implication for Electroweak Baryogenesis”, arXiv:1203.0430 [hep-ph].
- [98] Tomislav Prokopec, “Lecture notes for Cosmology”, www.staff.science.uu.nl/~proko101/2cm.pdf.
- [99] L. Fromme, S. J. Huber and M. Seniuch, “Baryogenesis in the two-Higgs doublet model”, *JHEP* **0611** (2006) 038, hep-ph/0605242.
- [100] A. T. Davies, C. D. Froggatt, G. Jenkins and R. G. Moorhouse, “Baryogenesis constraints on two Higgs doublet models”, *Phys. Lett. B* **336** (1994) 464.

- [101] J. M. Cline, K. Kainulainen and A. P. Vischer, “Dynamics of two Higgs doublet CP violation and baryogenesis at the electroweak phase transition”, *Phys. Rev. D* **54** (1996) 2451, hep-ph/9506284.
- [102] G. D. Kribs, T. Plehn, M. Spannowsky, and T. M. Tait, “Four generations and Higgs physics”, *Phys. Rev. D* **76** (2007) 075016, arXiv:0706.3718 [hep-ph].
- [103] R. Fok and G. D. Kribs, “Four Generations, the Electroweak Phase Transition, and Supersymmetry”, *Phys. Rev. D* **78** (2008) 075023, arXiv:0803.4207 [hep-ph].
- [104] S. W. Ham, S. K. Oh and D. Son, “Electroweak phase transition in the MSSM with four generations”, *Phys. Rev. D* **71** (2005) 015001, hep-ph/0411012.
- [105] Y. Kikukawa, M. Kohda and J. Yasuda, “The Strongly coupled fourth family and a first-order electroweak phase transition. I. Quark sector”, *Prog. Theor. Phys.* **122** (2009) 401, arXiv:0901.1962 [hep-ph].
- [106] E. Asakawa, D. Harada, S. Kanemura, Y. Okada, and K. Tsumura, “Higgs boson pair production in new physics models at hadron, lepton, and photon colliders”, *Phys. Rev. D* **82** (2010) 115002, arXiv:1009.4670 [hep-ph].
- [107] J. Baglio, A. Djouadi, R. Gröber, M. M. Mühlleitner, J. Quevillon and M. Spira, “The measurement of the Higgs self-coupling at the LHC: theoretical status”, *JHEP* **1304** (2013) 151, arXiv:1212.5581 [hep-ph].
- [108] J. Tian, “Study of Higgs self-coupling at the ILC based on the full detector simulation at $\sqrt{s} = 500$ GeV and $\sqrt{s} = 1$ TeV”, LC-REP-2013-003.
- [109] J. Baglio, A. Djouadi et al., “The Measurement of the Higgs self-coupling at the LHC: theoretical status”, arXiv:1212.5581v2[hep-ph], 2013.
- [110] J. Tian, Presentation for LCWS 2012.
- [111] J. Tian, “Higgs projections”, presentation at the Asian Linear Collider workshop at KEK, Tsukuba (Japan), April 2015.
- [112] D. de Florian and J. Mazzitelli, “Higgs Boson Pair Production at Next-to-Next-to-Leading Order in QCD”, *Phys. Rev. Lett.* **111** (2013) 201801, arXiv:1309.6594 [hep-ph].
- [113] W. Yao, “Studies of measuring Higgs self-coupling with $HH \rightarrow b\bar{b}\gamma\gamma$ at the future hadron colliders”, arXiv:1308.6302 [hep-ph].
- [114] V. Barger, L. L. Everett, C. B. Jackson and G. Shaughnessy, “Higgs-Pair Production and Measurement of the Triscalar Coupling at LHC(8,14)”, *Phys. Lett. B* **728** (2014) 433, arXiv:1311.2931 [hep-ph].
- [115] ATLAS Collaboration, “Prospects for measuring Higgs pair production in the channel $H(\rightarrow \gamma\gamma)H(\rightarrow b\bar{b})$ using the ATLAS detector at the HL-LHC”, ATLAS-PHYS-PUB-2014-019 (2014), <http://cds.cern.ch/record/1956733>.
- [116] ATLAS Collaboration, “Higgs Pair Production in the $H(\rightarrow \tau\tau)H(\rightarrow b\bar{b})$ channel at the High-Luminosity LHC”, ATLAS-PHYS-PUB-2015-046 (2015), <http://cds.cern.ch/record/2065974>.

- [117] CMS Collaboration, “Technical Proposal for the Phase-II Upgrade of the Compact Muon Solenoid”, CERN-LHCC-2015-010 (2015), <https://cds.cern.ch/record/2020886>.
- [118] C. Castanier, P. Gay, P. Lutz and J. Orloff, “Higgs self coupling measurement in e^+e^- collisions at center-of-mass energy of 500GeV”, In *2nd ECFA/DESY Study 1998-2001* 1362-1372, hep-ex/0101028.
- [119] T. Barklow, “Higgs self-coupling measurement”, Presentation for LCWS07.
- [120] Y. Takubo, “Analysis of Higgs Self-coupling with ZHH at ILC”, arXiv:0907.0524 [hep-ph].
- [121] J. Tian, K. Fujii and Y. Gao, “Study of Higgs Self-coupling at ILC”, arXiv:1008.0921 [hep-ex].
- [122] S. Yamashita, “A study of Higgs self-coupling measurement at about 1TeV”, Presentation for LCWS04.
- [123] M. F. Giannelli, “Sensitivity to the Higgs Self-coupling Using the ZHH Channel”, arXiv:0901.4895 [hep-ex].
- [124] T. Behnke *et al.* [ILC Collaboration], “ILC Reference Design Report Volume 4 - Detectors,” arXiv:0712.2356 [physics.ins-det].
- [125] M. Kurata, T. Tanabe, J. Tian, K. Fujii and T. Suehara, “The Higgs Self Coupling Analysis Using The Events Containing $H \rightarrow WW^*$ Decay”, LC-REP-2013-025.
- [126] T. Behnke, J. E. Brau, B. Foster, J. Fuster, M. Harrison, J. M. Paterson, M. Peskin and M. Stanitzki *et al.*, “The International Linear Collider Technical Design Report - Volume 1: Executive Summary”, arXiv:1306.6327 [physics.acc-ph].
- [127] H. Baer, T. Barklow, K. Fujii, Y. Gao, A. Hoang, S. Kanemura, J. List and H. E. Logan *et al.*, “The International Linear Collider Technical Design Report - Volume 2: Physics”, arXiv:1306.6352 [hep-ph].
- [128] C. Adolphsen, M. Barone, B. Barish, K. Buesser, P. Burrows, J. Carwardine, J. Clark and H. M. Durand *et al.*, “The International Linear Collider Technical Design Report - Volume 3.I: Accelerator R&D in the Technical Design Phase”, arXiv:1306.6353 [physics.acc-ph].
- [129] C. Adolphsen, M. Barone, B. Barish, K. Buesser, P. Burrows, J. Carwardine, J. Clark and H. M. Durand *et al.*, “The International Linear Collider Technical Design Report - Volume 3.II: Accelerator Baseline Design”, arXiv:1306.6328 [physics.acc-ph].
- [130] T. Behnke, J. E. Brau, P. N. Burrows, J. Fuster, M. Peskin, M. Stanitzki, Y. Sugimoto and S. Yamada *et al.*, “The International Linear Collider Technical Design Report - Volume 4: Detectors”, arXiv:1306.6329 [physics.ins-det].
- [131] C. Berger *et al.* [PLUTO Collaboration], “Evidence for Gluon Bremsstrahlung in e^+e^- Annihilations at High-Energies”, Phys. Lett. B **86** (1979) 418.
- [132] D. P. Barber *et al.*, “Discovery of Three Jet Events and a Test of Quantum Chromodynamics at PETRA Energies”, Phys. Rev. Lett. **43** (1979) 830.

- [133] S. Schael *et al.* [ALEPH and DELPHI and L3 and OPAL and SLD and LEP Electroweak Working Group and SLD Electroweak Group and SLD Heavy Flavour Group Collaborations], “Precision electroweak measurements on the Z resonance”, Phys. Rept. **427** (2006) 257, hep-ex/0509008.
- [134] B. Richter, “Very High-Energy electron-Positron Colliding Beams for the Study of the Weak Interactions”, Nucl. Instrum. Meth. **136** (1976) 47.
- [135] K. Fujii *et al.*, “Physics Case for the International Linear Collider”, arXiv:1506.05992 [hep-ex].
- [136] T. Barklow, J. Brau, K. Fujii, J. Gao, J. List, N. Walker and K. Yokoya, “ILC Operating Scenarios”, arXiv:1506.07830 [hep-ex].
- [137] H. Li *et al.* [ILD Design Study Group Collaboration], “ HZ Recoil Mass and Cross Section Analysis in ILD”, 1202.1439.
- [138] N. Walker, “Accelerator ILC”, Lecture, 2013.
- [139] N. Phinney, N. Toge and N. Walker, “ILC Reference Design Report Volume 3 - Accelerator”, arXiv:0712.2361 [physics.acc-ph].
- [140] K. Fujii, D. J. Miller, and A. Soni, “Linear collider physics in the new millennium”, Advanced series on directions in high energy physics, World Scientific, New Jersey, 2005, p. 499.
- [141] A. Vogel, “Beam-Induced Backgrounds in Detectors at the ILC”, Ph.D. thesis, Universität Hamburg, 2008.
- [142] ILD generator group, private communication, 2013.
- [143] S. Boogert *et al.*, “Polarimeters and energy spectrometers for the ILC Beam Delivery System”, *JINST* **4** (2009) P10015.
- [144] B. Vormwald, “Polarisation and Beam Energy Measurement at a Linear e^+e^- Collider”, *JINST* **9** (2014) C08012, arXiv:1406.3636 [physics.ins-det].
- [145] H. Abramowicz, A. Abusleme, K. Afanaciev, J. Aguilar, P. Ambalathankandy, *et al.*, “Forward Instrumentation for ILC Detectors”, *JINST* **5** (2010) P12002, arXiv:1009.2433 [physics.ins-det].
- [146] M. Thomson, “Measurements of the mass of the W boson at LEP”, Eur. Phys. J. C **33** 689 (2004).
- [147] F. Müller, “Development of a Triple GEM Readout Module for a Time Projection Chamber + Measurement Accuracies of Hadronic Higgs Branching Fractions in $\nu\nu H$ at a 350 GeV ILC”, Ph. D. thesis, Universität Hamburg, 2016.
- [148] J. S. Marshall and M. A. Thomson, “Pandora Particle Flow Algorithm”, arXiv:1308.4537 [physics.ins-det].
- [149] M. A. Thomson, “Particle Flow Calorimetry and the PandoraPFA Algorithm”, Nucl. Instrum. Meth. A **611** (2009) 25, arXiv:0907.3577 [physics.ins-det].
- [150] I. G. Knowles and G. D. Lafferty, “Hadronization in Z^0 decay”, J. Phys. G **23** (1997) 731, hep-ph/9705217.
- [151] The ILD Concept Group, “The International Large Detector: Letter of Intent”, arXiv:1006.3396v1 [hep-ex], 2010.

- [152] H. Aihara, P. Burrows, M. Oreglia, “SiD Letter of Intent”, arXiv:0911.0006v1 [physics.ins-det], 2009.
- [153] Rey.Hori, “ILC / Structural view of ILD detector”, [image], 2011, available online at http://www.linearcollider.org/images/pid/1000890/gallery/15_ILC_ILD.jpg; accessed on August 4th 2015.
- [154] G. G. Voutsinas [ILD and SiD groups Collaborations], “Vertexing Software and Methods for the ILC”, PoS Vertex **2014** (2015) 040.
- [155] C. Hu-Guo *et al.*, “First reticule size MAPS with digital output and integrated zero suppression for the EUDET-JRA1 beam telescope”, Nucl. Instrum. Meth. A **623** (2010) 480.
- [156] Y. Sugimoto, “Fine Pixel CCD Option for the ILC Vertex Detector”, eConf C **050318** (2005) 0804.
- [157] J. J. Velthuis *et al.*, “DEPFET, a monolithic active pixel sensor for the ILC”, Nucl. Instrum. Meth. A **579** (2007) 685.
- [158] J. Strube, “FPCCD Flavor Tagging”, talk in Americas Workshop on Linear Colliders, May 2014, Fermilab (USA).
- [159] S. Agostinelli *et al.* [GEANT4 Collaboration], “GEANT4: A Simulation toolkit”, Nucl. Instrum. Meth. A **506** (2003) 250.
- [160] F. Gaede, S. Aplin, R. Glattauer, C. Rosemann and G. Voutsinas, “Track reconstruction at the ILC: the ILD tracking software”, J. Phys. Conf. Ser. **513** (2014) 022011.
- [161] T. Mori, D. Kamai, A. Miyamoto, Y. Sugimoto, A. Ishikawa, T. Suehara, E. Kato and H. Yamamoto, “Study of Tracking and Flavor Tagging with FPCCD Vertex Detector”, arXiv:1403.5659 [physics.ins-det].
- [162] ILCSoft project web page, URL: <http://ilcsoft.desy.de/portal>.
- [163] W. Kilian, T. Ohl and J. Reuter, “WHIZARD: Simulating Multi-Particle Processes at LHC and ILC”, Eur. Phys. J. C **71** (2011) 1742, arXiv:0708.4233 [hep-ph].
- [164] T. Ohl, “O’Mega & WHIZARD: Monte Carlo event generator generation for future colliders”, AIP Conf. Proc. **578** (2001) 638, hep-ph/0011287.
- [165] M. Moretti, T. Ohl and J. Reuter, “O’Mega: An Optimizing matrix element generator”, In *2nd ECFA/DESY Study 1998-2001* 1981-2009, hep-ph/0102195.
- [166] T. Sjostrand, S. Mrenna and P. Z. Skands, “PYTHIA 6.4 Physics and Manual”, JHEP **0605** (2006) 026, hep-ph/0603175.
- [167] M. Berggren, “Tuning PYTHIA”, (2010).
- [168] F. Gaede, T. Behnke, N. Graf and T. Johnson, “LCIO: A Persistency framework for linear collider simulation studies”, eConf C **0303241** (2003) TUKT001, physics/0306114.
- [169] P. Mora de Freitas and H. Videau, “Detector simulation with MOKKA / GEANT4: Present and future”, LC-TOOL-2003-010.

- [170] P. Chen, T. L. Barklow and M. E. Peskin, “Hadron production in $\gamma\gamma$ collisions as a background for e^+e^- linear colliders”, *Phys. Rev. D* **49** (1994) 3209 [hep-ph/9305247].
- [171] F. Gaede, “Marlin and LCCD: Software tools for the ILC”, *Nucl. Instrum. Meth. A* **559** (2006) 177.
- [172] T. Suehara and T. Tanabe, “LCFIPlus: A Framework for Jet Analysis in Linear Collider Studies”, *Nucl. Instrum. Meth. A* **808** (2016) 109, arXiv:1506.08371 [physics.ins-det].
- [173] MarlinReco project page, URL: http://ilcsoft.desy.de/portal/software_packages/marlinreco.
- [174] R. Brun and F. Rademakers, “ROOT - An Object Oriented Data Analysis Framework”, Proceedings AIHENP 96 Workshop, Lausanne, Sep. 1996, *Nucl. Inst. & Meth. in Phys. Res. A* **389** (1997) 81-86.
- [175] ROOT homepage, url: <http://root.cern.ch>.
- [176] A. Hocker et al., “TMVA - Toolkit for Multivariate Data Analysis”, PoS ACAT (2007) 040, physics/0703039 [PHYSICS].
- [177] T. Hastie, R. Tibshirani, and J. Friedman, “The Elements of Statistical Learning”, Springer Series in Statistics, Springer New York Inc., 2009.
- [178] J. H. Friedman, “Stochastic gradient boosting”, *Computational Statistics & Data Analysis* 38.4 (2002), *Nonlinear Methods and Data Mining* 367-378, url: <http://www.sciencedirect.com/science/article/pii/S0167947301000652>.
- [179] S. Catani, Y. L. Dokshitzer, M. Olsson, G. Turnock and B. R. Webber, “New clustering algorithm for multi-jet cross-sections in e^+e^- annihilation”, *Phys. Lett. B* **269** (1991) 432.
- [180] S. Moretti, L. Lonnblad and T. Sjostrand, “New and old jet clustering algorithms for electron - positron events”, *JHEP* **9808** (1998) 001, hep-ph/9804296.
- [181] S. Catani, Y. L. Dokshitzer, M. H. Seymour and B. R. Webber, “Longitudinally invariant K_t clustering algorithms for hadron hadron collisions”, *Nucl. Phys. B* **406** (1993) 187.
- [182] S. D. Ellis and D. E. Soper, “Successive combination jet algorithm for hadron collisions”, *Phys. Rev. D* **48** (1993) 3160, hep-ph/9305266.
- [183] M. Cacciari, G. P. Salam and G. Soyez, “FastJet User Manual”, *Eur. Phys. J. C* **72** (2012) 1896, arXiv:1111.6097 [hep-ph].
- [184] M. Cacciari, G. P. Salam and G. Soyez, “The Anti- k_t jet clustering algorithm”, *JHEP* **0804** (2008) 063, arXiv:0802.1189 [hep-ph].
- [185] B. List, J. List, “MarlinKinfit: An Object-Oriented Kinematic Fitting Package”, LC-TOOL-2009-001, 2009, <http://www-flc.desy.de/lcnotes/>.
- [186] A. G. Froedsen, O. Skeggstad and H. Tøfte, “Probability and Statistics in Particle Physics”, Universitetsforlaget, 1979.

- [187] M. Beckmann, “Verbesserung der WW/ZZ-Unterscheidung am ILC durch Berücksichtigung von Photoabstrahlung in kinematischen Fits”, Diploma thesis, Leibniz Universität Hannover, DESY, May 2009.
- [188] R. J. Barlow, “Statistics: A Guide to the Use of Statistical Methods in the Physical Sciences”, The Manchester Physics Series, John Wiley & Sons, Chichester, 1989.
- [189] L. Demortier, L. Lyons, “Everything you always wanted to know about pulls”, Technical Report CDF/ANAL/PUBLIC/5776, CDF, February 2002.
- [190] O. Behnke, K. Kröniger, T. Schörner-Sadenius and G. Schott, “Data analysis in high energy physics : A practical guide to statistical methods”, Wiley-VCH (2013), ISBN: 9783527410583.
- [191] J. List, “Suche nach assoziierter Produktion von Higgs- und Z^0 -Bosonen mit Zerfall in Quarks oder Gluonen am OPAL-Experiment”, Ph.D. thesis, RWTH Aachen, August 2000, PITHA 00/16.
- [192] M. Kurata, “High Level Reconstruction Tools”, University of Tokyo, presentation at the Asian Linear Collider Workshop 2015 (ALCW15), Tsukuba, Japan.
- [193] M. Kurata, “Particle ID Study and its Application”, University of Tokyo, presentation at the Asian Linear Collider Workshop 2015 (ALCW15), Tsukuba, Japan.
- [194] S. Lukic, “PID Tools”, University of Belgrade, presentation at ILD software & reconstruction workshop, Hamburg, Germany, 2016.
- [195] T. Junk, “Confidence level computation for combining searches with small statistics”, Nucl. Instrum. Meth. A **434** (1999) 435 [hep-ex/9902006].
- [196] C. Dürig et al., “Higgs self-coupling measurement at the ILC”, DESY, presentation at the American Workshop of Linear Colliders, Fermilab USA, 2014.
- [197] C. Dürig et al., “Update on Higgs self-coupling analyses for ILD”, presentation at the Asian Linear Collider workshop at KEK, Tsukuba (Japan), April 2015.
- [198] S. Sasikumar, *private communication*, DESY Hamburg, Germany, 2016.
- [199] M. Kurata et al., “Higgs self-coupling Analyses at ILC”, University of Tokyo, presentation at the International Linear Collider Workshop 2015 (LCWS15), Whistler, Canada.
- [200] J. Tian, K. Fujii, “Prospects of the Higgs self-coupling measurement at the linear colliders”, KEK, presentation at the 15th Regular Meeting of the New Higgs Working Group, Toyama University, 2015.
- [201] J. Tian, K. Fujii, “Matrix Element Method and its Application for ILC Physics Analysis”, KEK, presentation at the Tokusui Workshop, 2014.
- [202] J. Tian, K. Fujii, “Matrix Element Method for ILC physics Analysis”, KEK, presentation at the ILD Software and Analysis Meeting, 2016.
- [203] J. Tian, K. Fujii, “Jet Reconstruction at the ILC”, KEK, presentation at the Workshop on Top physics at the LC, IFIC, Valencia, 2015.

-
- [204] M. Kurata, “LCFIPlus - Basic idea and towards improvement”, University of Tokyo, presentation at the Tokusui Workshop, 2015.
 - [205] G. Wilson, “Mass Constrained Fitting of Di-Photons”, University of Kansas, presentation at ILD software& reconstruction workshop, Hamburg, Germany, 2016.
 - [206] D. Jeans, “Tau lepton reconstruction at collider experiments using impact parameters”, Nucl. Instrum. Meth. A **810** (2016) 51, arXiv:1507.01700 [hep-ex].
 - [207] A. Ebrahimi, *private communication*, DESY Hamburg, Germany, 2016.

Acknowledgements

Finally, I would like to thank a few people for their support during the last years. Without them, this thesis would not have been possible.

First of all, I would like to thank Jenny List for giving me the opportunity to write my thesis under her supervision, for her sound advice and patience, and for her inexhaustible help in word and deed. I don't think one could wish for a better supervisor. I would also like to thank my PhD committee for agreeing to act as my referees, especially Erika Garutti for always providing a helping hand. I would also like to thank my mentor Kerstin Tackmann for always giving me good advice and the PIER graduate school for their support, which gave me the opportunity to gain new experiences.

I would like to thank the entire research group at KEK, especially Keisuke Fujii, Akiya Miyamoto, Constantino Calancha and Junping Tian for their support and giving me the opportunity to visit and work with them in Japan. I don't want to miss one single day. I am very grateful to Junping Tian for providing such a huge support from the other side of the world. Without your constant, and daytime-independent advice, the outcome of this thesis would not have been the same.

Of course, I would like to thank the entire FLC group for providing such a nice environment and for lending a helping hand when it was needed. Even though I never joint lunch, I really enjoyed being part of the group. In particular, I would like to thank my fellow PhD colleagues and former group members: Benjamin Hermberg, Benedikt Vormwald, Hale Sert, Annika Vauth, Moritz Habermehl, Suvi-Leena Lehtinen, Swathi Sasikumar, and Madalina Chera for all the conversations, memories and trips that we shared. Most importantly I would like to thank Coralie Neubüser for becoming a friend and being the best office mate one can imagine. It would not have been the same without you.

And of course a special thanks to Felix Müller for everything...

While I was writing this thesis it seemed to me that I had no life outside the office. However, and less surprisingly, this is not true. Without the support of many special friends it would have been much harder to survive. Among other, I am grateful to Christina Wilhelm for her longstanding friendship (I cannot wait for more years to come) and Lena Fischer for fixing me when it was needed. You are a magician. Of course, I would also like to thank the most amazing group of girls for their endless support, for reading some chapters of this thesis without falling asleep, and for enduring all my frustrations and moods especially during the last months! I am so lucky to have you in my life!

Lastly, and most importantly, I wish to thank my family - my brother Oliver and my parents - for the unfailing encouragement, the endless support and for loving me throughout my life. I know that wherever life brings me, I have you. Olli, just knowing you are there makes life better. Dad, you are in my heart as an inspiration and a guide, and there is much of you in this thesis, as there is in all that I do. Mum, this thesis is dedicated to you, and you know why... I would not have done this without you.

Eidesstattliche Versicherung

Hiermit erkläre ich an Eides statt, dass ich die vorliegende Dissertationsschrift selbst verfasst und keine anderen als die angegebenen Quellen und Hilfsmittel benutzt habe.

Hamburg, July 2016

Claude Dürig

